Current Density Compression of Intense Ion Beams

Adam Bennett Sefkow

A Dissertation
Presented to the Faculty
of Princeton University
in Candidacy for the Degree
of Doctor of Philosophy

Recommended for Acceptance
by the Department of
Astrophysical Sciences

September 2007

Abstract

Current density compression of intense ion beams in space and time is required for heavy ion fusion, in order to achieve the necessary intensities to implode an inertial confinement fusion target. Longitudinal compression to high current in a short pulse is achieved by imposing a velocity tilt upon the space-charge-dominated charge bunch, and a variety of means exist for simultaneous transverse focusing to a coincident focal plane. Compression to the desired levels requires sufficient neutralization of the beam by a pre-formed plasma during final transport. The physics of current density compression is studied in scaled experiments relevant for the operating regime of a heavy ion driver, and related theory and advanced particle-in-cell simulations provide valuable insight into the physical and technological limitations involved.

A fast Faraday cup measures longitudinal compression ratios greater than 50 with pulse durations less than 5 ns, in excellent agreement with reduced models and sophisticated simulations, which account for many experimental parameters and effects. The detailed physics of achieving current density compression in the laboratory is reviewed. Quantitative examples explore the dependency of longitudinal compression on effects such as the finite-size acceleration gap, voltage waveform accuracy, variation in initial beam temperature, pulse length, intended fractional velocity tilt, and energy uncertainty, as well as aberration within focusing elements and plasma neutralization processes. In addition, plasma evolution in experimental sources responsible for the degree of beam neutralization is studied numerically, since compression stagnation occurs under inadequate neutralization conditions, which may excite nonlinear collective excitations due to beam-plasma interactions.

The design of simultaneous focusing experiments using both existing and upgraded hardware is provided, and parametric variations important for compression physics are investigated. Current density compression factors from 10^3 to over 10^5 can be realized, depending on the optimization of various sensitive components for a given set of experimental constraints and system parameters. Since a heavy ion beam driver becomes more compact and cost-effective than previously envisioned as the amount of compression increases, the physics foundation of simultaneous beam focusing has near-term applicability to warm dense matter studies, and heavy ion fusion in the longer term.

To Elizabeth,

"You know you're in love when you can't fall asleep because reality is finally better than your dreams."

— Dr. Seuss

Acknowledgments

This research was supported by the U.S. Department of Energy under the auspices of the Heavy Ion Fusion Science Virtual National Laboratory.

I am gratefully indebted to my primary thesis advisor, Ronald C. Davidson, for his tireless efforts on behalf of my graduate education. His affable and supportive personality has made this experience fruitful and memorable. For anyone who has the pleasure to work with him, it goes without saying that Ron's inspiring leadership and work ethic deserve the highest esteem.

I would like to offer sincere thanks and appreciation to my effective co-advisors Phil Efthimion, Dale Welch, and Simon Yu for their scientific support. In addition, I am much obliged to Sam Cohen and Hong Qin for devoting time to the reading of this thesis, as well as providing access to their commendable knowledge and wisdom. Sam Cohen in particular deserves extra recognition for his role as my faculty advisor, as does Cynthia Phillips for her role on my thesis committee.

Many thanks are due to Nat Fisch and Barbara Sarfaty for welcoming me into the Program in Plasma Physics, and providing assistance and encouragement throughout these graduate school years. The faculty of the Princeton Plasma Physics Laboratory (PPPL) devote large amounts of time to our foundational courses each year and are worthy of much recognition.

The Beam Physics and Nonneutral Plasma Division of PPPL has been a friendly and productive group of individuals, within which I have enjoyed participating. In addition to Ron, Phil, and Hong, I'd like to acknowledge the group members Andy Carpe, Moses Chung, Erik Gilson, Larry Grisham, Igor Kaganovich, and Ed Startsev.

In particular, Igor selflessly shared huge amounts of time and thought in order to help me with my research and education, and for that I am grateful. Erik has also shared large amounts of time for both calculated and random discussions on a moment's notice, but I will most fondly remember him as a worthy volleyball adversary; I hope he finds happiness from a new spiking-and-blocking nemesis.

My colleagues at Lawrence Berkeley and Lawrence Livermore National Laboratories deserve high praise for their roles in the success of both the experimental and computational efforts towards intense ion beam compression. Their feedback and support were invaluable throughout my involvement in our mutual projects. Those members who deserve special thanks for their direct involvement and help are John Barnard, Frank Bieniosek, Josh Coleman, Shmuel Eylon, Alex Friedman, Wayne Greenway, Enrique Henestroza, Joe Kwan, B. Grant Logan, Prabir Roy, Peter Seidl, David Vanecek, and Will Waldron.

Summer internships are responsible for sparking my initial interest in nuclear fusion-related science. Therefore, I would like to acknowledge the key advisory influences of John Edwards, Jan Egedal, Ambrogio Fasoli, and Richard London for helping to direct me towards a graduate education in plasma physics.

Life is about friends and family. To all my friends, past and present (you know who you are): thank you for all the good times so far, and for those yet to come. Without a life outside of studying, most students would go mad.

My parents-in-law, Joan and Joe Marques, are incredible for wholeheartedly welcoming me into their family and supporting me through their kindness and love.

To my brother Ryan and sister Elizabeth: thanks for being the amazing people I am proud to call my siblings. Ryan is my go-to guy for most things technical. Special thanks to Liz for not trying to collect that $100 I owe her, because I really needed it in graduate school.

To my loving parents, Susan and Tom: I obviously owe you a debt I can never fully repay. You two were there every step of the way, from the first literal step to the point where you couldn't help me with homework anymore, and beyond. Not only did you give birth to me and raise me to value an education, but you also taught me to never give up on anything. Especially multiplication tables. For the record, let it be known that you really did know what was best.

Finally, no words can express my profound appreciation and love for my wife, Elizabeth. She's my blue sky and sunny day, without whom this world would be much darker.

Contents

List of Figures

List of Tables

Chapter 1

Introduction

Nuclear fusion is the process which powers stars. The controlled exploitation of fusion as a source of energy on Earth, without the confining aid of massive gravitational forces, has remained an unanswered challenge to the scientific community for over six decades. Since the global population and its consumption of energy are both rapidly increasing, the development of long-term and environment-friendly power sources for electrical use is prudent. Power plants that economically harness nuclear fusion are an attractive possible contribution to the future energy portfolio.

The advantages of fusion power, especially as they relate to fission power, include waste disposal, safety, and proliferation considerations. There exists worldwide availability of an essentially inexhaustible low-cost fuel, the absence of combustion products which have detrimental environmental impact, and an estimated cost of electricity similar to other long-term energy options. Tapping the potential of fusion energy as a power source has proven to be a challenging task, and the only terrestrial examples of using fusion reactions to create much more energy than required to initiate them are found in thermonuclear weapons.

Demonstration of energy gain in the laboratory requires that the fuel be confined at high densities and temperatures long enough for it to fuse, which results in the destruction of mass in order to release energy. The fusion reaction requiring the lowest temperature to realize involves deuterium and tritium. In a power plant, some energy released by the reaction assists in the fusion of additional reactants (a self-sustaining chain reaction called *ignition*), and some of the energy is harnessed to continue the operation of the power plant as well as generate electricity.

Stars confine fusion products by means of enormous gravitational forces, and a different mechanism for confinement must be utilized for controlling fusion in a power plant. Confinement is necessary for achieving fusion because of the need to overcome the repulsive Coulomb force between positively charged nuclei. Two of the most intensely studied methods for sustaining fusion conditions without the aid of gravity are magnetic confinement and inertial confinement. The magnetic fusion energy approach seeks to employ strong magnetic fields to confine plasma, whose constituents are electrons and fuseable ions, in devices operating in (or near) steady state. Configurations of current-carrying coils produce magnetic field topologies in devices such as tokamaks, spheromaks, field-reversed configurations, and stellarators, in order to attempt the confinement of fusion fuel using the electromagnetic force. The world's largest tokamak is currently under construction in France; the International Thermonuclear Experimental Reactor will be a global effort to demonstrate ignition in the laboratory using the magnetic confinement concept. The primary competing method proposed to create fusion conditions in the laboratory is the inertial confinement fusion concept; the National Ignition Facility under construction at the Lawrence Livermore National Laboratory also seeks to demonstrate ignition, but by an alternative means.

1.1 Inertial confinement fusion

One of the reasons inertial confinement fusion (ICF) is under investigation is to assess the feasibility of inertial fusion energy as an alternative to magnetic fusion energy power production. The promise and subsequent advent of high intensity lasers garnered interest in electromagnetic radiation as a source of compression (called the *driver*), in order to scale down a thermonuclear explosion to a manageable size in the laboratory, and whose energy could be harnessed for civilian use. Inertial confinement fusion relies on the inertia of a spherical capsule, which contains fusion fuel and is rapidly compressed in an implosion process, in order to provide confinement. The implosion of the target capsule may be driven by the bombardment of intense lasers, ion beams, or x-rays. As the target compresses, the interior can reach sufficient density and temperature for rapid and efficient thermonuclear burning of the fuel. The target physics of the approach is highlighted in Fig. 1.1. The implosion velocity of the target capsule largely determines the minimum energy requirements of the driver. The envisioned plan for inertial fusion energy requires that the driver be pulsed with a repetition rate (similar to a combustion engine), which depends on the energy gain of the target and efficiency of the power plant.

Two methods that couple the driver energy to the target are the direct-drive and indirect-drive approaches. In the direct-drive approach [Nuckolls *et al.*, 1972], the driver energy (in the form of lasers, ion beams, or x-rays) is symmetrically focused directly onto the target, which resides at the center of a target chamber, resulting in the efficient coupling of driver energy to target compression. Symmetric implosions are necessary in order to maximize the conversion of the target's kinetic energy into compression and heating of the fusion fuel. However, direct-drive is sensitive to the quality

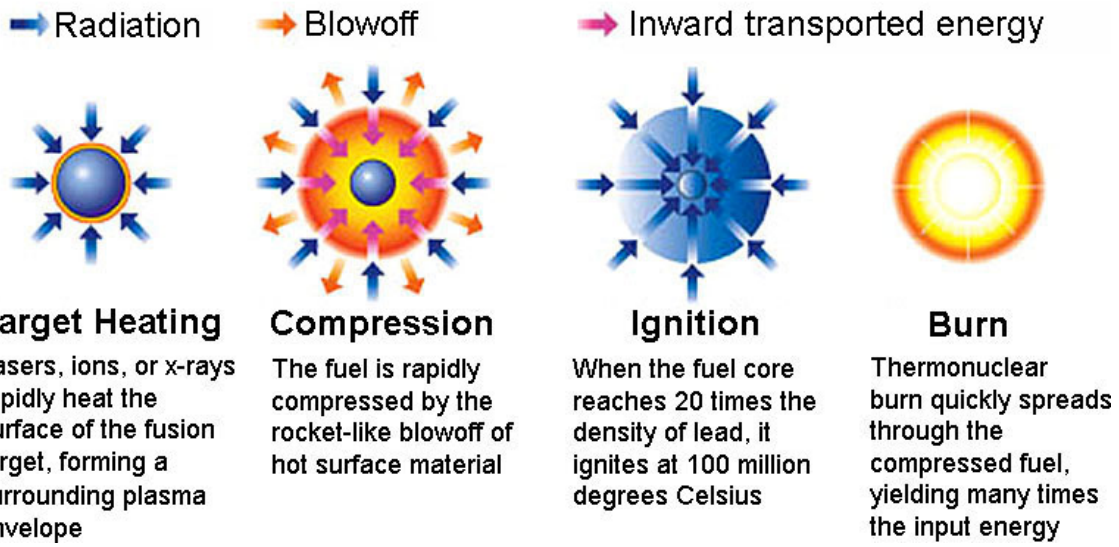

Figure 1.1: (Color) The target physics behind the inertial confinement fusion concept.

of the driving beams as well as to hydrodynamic instability [Chandrasekhar, 1961].

In the indirect-drive approach [Lindl, 1995] (which is currently the preferred approach in the United States), the driver energy is instead incident upon a high-Z enclosure called a hohlraum, which surrounds the target capsule, as shown in Fig. 1.2; the hohlraum absorbs much of the driver energy, heats into the plasma state, and radiates intense x-rays, which symmetrically bathe the target and cause it to implode. The x-ray temperature is limited by coupling issues such as driver absorption by the hohlraum, x-ray conversion, and energy transport. The temporal profile of the laser power is shaped in such a way as to maintain a low adiabat during compression, in order to form a hot-spot at the center of the target. Due to the high densities and temperatures in the hot-spot, the fusion fuel ignites, a burn wave propagates radially away from the core, and fusion occurs throughout a significant fraction of the remaining colder fuel. Indirect-drive is less efficient, but the requirements on beam uniformity and issues surrounding hydrodynamic instability are reduced. The driver

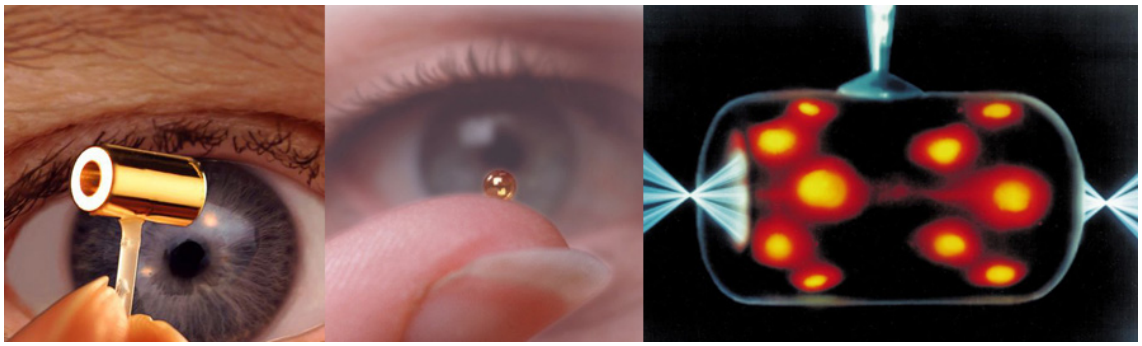

Figure 1.2: (Color) Photograph of a gold plated hohlraum for indirect-drive ICF (left) and a target capsule (middle). Laser-driven indirect-drive ICF in a cylindrical hohlraum bathes the fusion target with intense x-rays (right).

for the indirect-drive approach may be powerful lasers, ion beams, or z-pinch wire arrays, and the physics of the imploding target is largely independent from the driver. Topics under active research in the inertial confinement fusion community include hohlraum design, radiation transport, high-gain target design, implosion symmetry, compression and ignition physics, laser-plasma interactions, and hydrodynamic instability, to name a few.

The 192 modular beams of the National Ignition Facility will become the world's most powerful laser, and configurable for direct-drive as well as indirect-drive experiments. Nominally capable of producing 1.8 MJ and 500 TW of flashlamp-pumped Nd:glass laser light, it is expected to access hohlraum temperatures of approximately 300 eV and target implosion velocities approaching 4×10^7 cm s^{-1}, thereby allowing it to conduct the first successful target ignition experiments. However, the laser-driven inertial fusion energy concept suffers from a few major obstacles. First, the efficiency of flashlamp-pumped laser generation using current technology is quite low (a few percent, at best). Second, the necessary repetition rates are generally $0.1 - 10$ Hz, depending on fusion yield, and are not met by current laser technology. Third,

damage to the optics is a concern for high intensity lasers, as well as mitigating the danger of fusion products and debris impacting the final focus optic, which directly faces the explosion at the center of the target chamber. Two types of lasers under active research, the diode-pumped solid-state laser [Orth *et al.*, 1996] and the Krypton Fluoride laser [Sethian *et al.*, 2004], offer the potential of providing higher efficiencies and repetition rates required for laser-driven inertial fusion energy.

One of the main two alternative concepts to laser-driven inertial fusion energy is the pulsed-power Z machine, which is the world's largest x-ray producer, at Sandia National Laboratories. Z is capable of producing and discharging up to 20 MA of electrical current and 290 TW of power into a cylindrical array of thin parallel wires, which are rapidly heated, vaporized, and ionized into plasma. The strong magnetic field generated by the discharge implodes the plasma in what is known as a z-pinch ($-F_r \sim J_z \times B_\theta$), from which the machine derives its name. The imploded plasma produces an intense x-ray pulse, which can be shaped and directed onto a target capsule for fusion energy applications. Research is underway to achieve symmetric target capsule implosions by using double-pinch-driven hohlraums [Cuneo *et al.*, 2006]. Z is also undergoing a refurbishment in order to discharge up to 26 MA of current and 350 TW of power, producing 2.7 MJ worth of x-ray energy. Traditionally, pulsed power systems like the Z machine tend to be energy-rich but power-poor; therefore, the challenge has been to concentrate the large amount of available energy into a small enough volume, so as to create high enough x-ray radiation temperature within the holhraum and provide the necessary conditions for target implosion and inertial confinement fusion.

1.2 Heavy ion fusion

The other main alternative to laser-driven inertial fusion involves the use of energetic charged particle beams [Reiser, 1994, Miller, 1994] as the driver. The use of intense ion beams for fusion energy applications is called heavy ion fusion (HIF); scientists around the world collaborate with active HIF research programs, which exist in the United States [Logan *et al.*, 2004], Russia [Sharkov *et al.*, 2005], Japan [Kikuchi *et al.*, 2006], Germany [Meyertervehn *et al.*, 1990], as well as France [Lifschitz *et al.*, 2006]. In heavy ion fusion schemes, a spherical target is imploded (directly or indirectly) in much the same way as described earlier, except intense pulses composed of energetic ions are used instead of photons. Most of the hohlraum dynamics, radiation transport, and implosion physics learned in laser-driven inertial confinement simulations and experiments are directly applicable to heavy ion-driven hohlraums [Lindl, 1998]. Advantageously, ion-driven inertial fusion energy concepts sidestep the three primary drawbacks of their laser-driven counterparts: heavy ion accelerators are robust and efficient ($25-40\%$), already can achieve the necessary repetition rates, and final focus "optics" (magnets) are not susceptible to damage from target chamber exposure. The magnets can be placed out of direct line-of-sight with the target, and fast-closing valves and differential pumps can maintain accelerator vacuum isolation relative to the target chamber.

The development of heavy ion drivers for inertial confinement fusion has been heralded by the National Academy of Sciences [NAS, 1990], the Fusion Policy Advisory Committee [FPAC, 1990], and the Fusion Energy Advisory Committee [FEAC, 1993] as the candidate with the greatest potential for inertial fusion power production, due to advantages in efficiency, durability, and repetition rate. Also, intense ion beams

are relatively easy to create and control. However, heavy ion driver technology is currently the least mature and least funded of the various driver options mentioned earlier; in spite of this, innovative progress has been made throughout the years [Davidson *et al.*, 2006, Logan *et al.*, 2007].

A substantial barrier to heavy ion fusion is the cost of accelerating ion beams to the high energy densities that are required for the implosion of a target. Indeed, the driver would be the most costly item and steps to reduce driver requirements, such as the development of closely coupled targets [Callahan-Miller and Tabak, 1999], have a significant impact on the associated economics. Most of the ion-driven inertial confinement research has centered around the indirect-drive approach because of the attractiveness of two sided illumination, as well as increased radiation uniformity and target stability. The use of the word "heavy" in heavy ion fusion is presently a misnomer because, whereas original designs called for uranium beams, current research focuses on mid-Z ions, in order to balance accelerator cost (cheaper for lighter ions) with performance (beam energy, peak power, and ion range in the target).

Charged particle beam physics [Davidson and Qin, 2001] has a wide range of applications in modern scientific research, such as nuclear physics, particle physics, coherent radiation generation by intense electron beams, neutron sources, advanced accelerator concepts, pulsed power technology, high-voltage diodes, and inertial fusion energy. Space-charge-dominated beams are characterized by strong electric self-fields and, in the high-current case, magnetic self-fields; in particular, the nonlinear effects of intense self-fields play a significant role in the equilibrium, stability, and transport dynamics of a charge bunch. A charged particle beam is a many-body collection of ions or electrons, can exhibit a wide range of collective phenomena such as

plasma waves and instabilities, and is actually a one-component nonneutral plasma [Davidson, 2001] when considered in the beam frame. Therefore, much of the literature on laboratory-confined nonneutral plasmas, which exhibit complex collective and nonlinear dynamics, is directly relevant to the study of intense charged particle beam propagation [Davidson and Qin, 2001].

Indeed, research related to the development of a heavy ion driver for inertial fusion energy and high-energy-density physics applications is relevant for many fields of currently active research, including nonneutral plasma physics, magnetic fusion plasma physics, advanced nonlinear dynamics, atomic physics, and advanced computing. Some of the benefits to those fields and for the aforementioned applications include theoretical techniques, accelerator physics and technology, warm dense matter studies, beam-plasma interactions, diagnostics, chaotic dynamics, collective effects research, evaluation of ionization and stripping cross sections, and the development of novel particle-in-cell and hybrid numerical simulation approaches.

A schematic of a typical design for heavy ion fusion is shown in Fig. 1.3. In a heavy ion driver, many facets of accelerator physics and technology must be brought to bear in order to achieve high-power ion beams on target. The design of a MJ-scale driver needs to demonstrate the satisfaction of all constraints put on it by the complexities of beam generation, acceleration and focusing, target physics requirements, and the engineering issues surrounding the target chamber. Compact ion sources and injectors capable of generating high-current, space-charge-dominated beams need to be realized. After the initial injection, the beams need to be matched into an accelerator region, which not only increases the kinetic energy of the intense beams up to the GeV scale, but also transports, combines and compresses them via electric

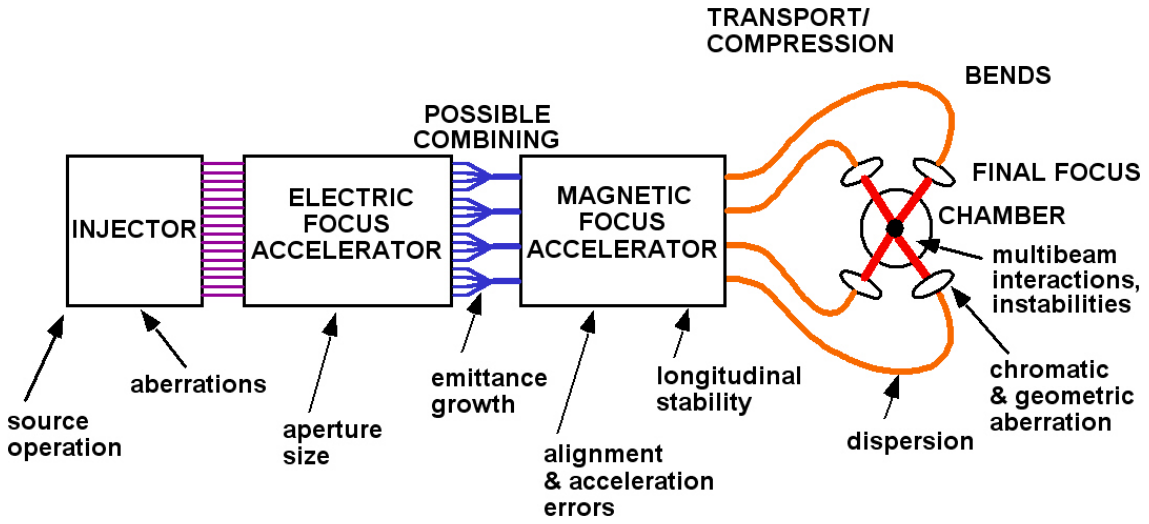

Figure 1.3: (Color) Schematic of the various physical and technological issues surrounding the construction of a heavy ion driver [HIFS-VNL, 2001].

and magnetic focusing. As the beams near the end of the device, they enter the final-focus region, which is responsible for the focusing and transportation of multiple beams to the center of the target chamber, where each of the beams (usually 16 total) needs to carry up to 10 kA of current inside a 2 mm beam radius with pulse duration less than 10 ns, for a power total of approximately 500 TW. Estimates of the final beam density near the target are in the $n_b \sim 10^{13} - 10^{14}$ cm^{-3} range (for each beam). Once the beams traverse the target chamber to its center, they impinge upon the target directly (in the case of direct-drive) or strike the walls of a hohlraum in order to generate x-rays (in the case of indirect-drive). In order to protect the walls of the chamber and beamline from the intense flux of neutrons, x-rays, and debris ejected in the controlled thermonuclear explosion of the target, jets of molten salt ($2LiF - BeF_2$) or ceramic granules (Li_2O) are envisioned for use to create an absorbing liquid blanket or wall [Meier *et al.*, 1991]; the heat stored in the flowing

wall can then be transferred to a conventional generator for the production of electricity. Other key scientific issues remaining to be addressed include the optimization of fusion targets with necessary gain and hohlraum symmetry, which must be robust to beam aiming errors and suitable for mass production, as well as the development of attractive fusion chamber concepts that minimize materials development needs.

Technological issues under active research include source operation and injector development, the role of aperture size in the electric and magnetic focusing sections, alignment and acceleration errors in the beamline, longitudinal stabilization of the beam over large distances, dispersion of the beam in the final transport and compression sections, and aberrations induced in the final transverse and longitudinal focusing elements. Several key physics issues which affect the propagation of the intense ion beam are also under active investigation, such as the generation of high-quality beams (suitable for acceleration and focusing) in the injection and matching region, ionization of the beam and background gas in the target chamber, stray electron cloud effects, multi-beam interactions, and the evaluation of various instabilities.

Current heavy ion fusion research also investigates the possibility of using ion beams as fast ignition drivers [Logan *et al.*, 2006], rather than ultraintense, short-pulse lasers. In the fast ignition concept [Tabak *et al.*, 1994], the compression and heating stages are decoupled from one another and the resulting driver requirements are significantly reduced. Rather than hot-spot ignition, a primary driver (laser, ion, or z-pinch) provides initial compression of the target without a series of shocks. A secondary PW-class beam would then be employed to ignite the compressed fuel on the ps timescale. Advantages of this method include higher gains, lack of shock timing necessity, compression of more fuel for the same driver energy, and easing of

the implosion symmetry requirements. Ignition energy requirements using an efficient ion driver can be even lower than in traditional fast ignition, due to more favorable energy deposition characteristics. The main challenges of the approach are in the transportation of the energetic electron beam through the coronal plasma to the target (in the case of laser drivers), and in the acceleration and focusing of the ion beam to the necessary ultra high levels (in the case of ion drivers).

1.3 Motivation for neutralized compression of intense ion beams

Of the challenges encountered in creating heavy ion drivers, one of the most significant is found in the final transport section leading to the target [Yu *et al.*, 1979, Olson, 1980], where ion beam compression in space and time is required in order to achieve the necessary high intensities for striking the target. In other words, intense ion beam pulses must undergo simultaneous transverse and longitudinal bunch compression to a coincident focal plane in order to meet the requisite beam power on target. Heavy ion drivers can deliver more intensity to the target per unit length of accelerator by greatly compressing intense ion charge bunches over short distances.

The most comprehensive study of final-focusing for heavy ion drivers was HIBALL-II [Badger *et al.*, 1984], which assumed that the vacuum in the target chamber would be good enough so that converging beam ions would experience no forces during the final transport, save their own collective space-charge forces. Numerical simulations [Sharp *et al.*, 2003] and scaled experiments [MacLaren *et al.*, 2002] agreed on the feasibility of the so-called *ballistic* transport in driver-scale systems [Olson, 1980],

which were designed by carefully choosing the species, current, and energy of the beams in order to reduce the effects of space-charge on propagation (such as enlarging the focal spot and pulse duration). Since HIBALL-II, ballistic chamber transport has become unsuitable for heavy ion fusion applications due to a number of reasons. Driver economics is more favorable for beams with lower kinetic energies and higher currents; far too many beams would be required to sufficiently reduce space-charge effects to allow ballistic transport [HENESTROZA *et al.*, 2004]. Also, the use of molten salt jets to form thick liquid walls [MOIR *et al.*, 1994], capable of protecting the target chamber from the explosion and debris, introduces a vapor pressure high enough for collisional ionization to transform the singly-charged ion beams into a wide range of charge states, so they become more sensitive to self-fields and difficult to focus. Lastly, distributed-radiator targets [TABAK and CALLAHAN-MILLER, 1998, CALLAHAN-MILLER and TABAK, 1999] put more stringent constraints on beam focusing, since fusion energy gain reduces appreciably if the beam radii are greater than 2 mm as they strike the hohlraum, implying the need for using beams with low temperature and net charge. Therefore, the move away from ballistic transport to beams with less energy and higher currents (and space-charge) was made.

In recent conceptual designs of a heavy ion driver [YU *et al.*, 2003], intense charge bunches are transported from a final-focus magnet system to the target chamber, where they must transversely focus onto the target with a final diameter of a few millimeters or less [CALLAHAN, 1996, LOGAN and CALLAHAN, 1998]. After the intense ion beams leave the final-focus magnet system, they must drift without further external focusing to the target at the center of the chamber, a distance of about 6 m. When the ion beams arrive, the current of each must be on the order of 10 kA with

pulse length < 10 ns. Therefore, the ion beams also need to be focused longitudinally in order to achieve large beam currents in short pulse durations. Maximizing both the transverse and longitudinal current density compression offers the potential of accessing higher levels of energy deposition within a target per unit length of accelerator. Compression also allows shorter accelerators and transport lines to be used as drivers, making them more compact and cost-effective than previously envisioned.

In order to focus an intense ion beam to the small spot size (few mm) and short pulse duration (< 10 ns) required, the majority of the beam's space-charge and current must be neutralized during the final transport stage [Kaganovich *et al.*, 2001, Rose *et al.*, 2001, Kaganovich *et al.*, 2007], thereby overcoming the defocusing self-field forces of a positively-charged ion beam. A recent driver study [Yu *et al.*, 2003] called for a high-density plasma to be positioned between the final-focus magnets and the target chamber, in order to provide an unbound electron population to be trapped by the potential well of the beam propagating in the drift region; such an implementation is called a *neutralized* ballistic transport scheme. Here, "high-density" means the plasma density n_p is much greater than the beam density n_b throughout the drift region, so that the presence of the beam is only a perturbation to the plasma (generally requiring $n_p \sim 10^{10} - 10^{14}$ cm^{-3}, depending on the beam compression parameters). With adequate neutralization of the beam supplied by the background plasma, the intense beam can be focused beyond the traditional space-charge limit for quiescent propagation, relieving the issues of ballistic focusing. Numerical simulations support the claim that effective space-charge neutralization, leading to dramatically improved focal spots, will take place if each beam is passed through a dense plasma after the final-focus magnets [Welch *et al.*, 2001, Welch *et al.*, 2003a].

1.4 Neutralized Transport Experiment

Transverse compression of the beam radius r_b helps meet the requisite beam intensities desired at the target by greatly increasing the current density ($J_z \sim r_b^{-2}$). To experimentally verify the quantitative predictions of theory and simulation, the Heavy Ion Fusion Science Virtual National Laboratory (a formal collaboration between Lawrence Berkeley National Laboratory, Lawrence Livermore National Laboratory, and Princeton Plasma Physics Laboratory scientists) constructed the Neutralized Transport Experiment (NTX) [Henestroza *et al.*, 2004]. The NTX was designed to study the neutralized transport physics, on a reduced scale, required by beams with high space-charge to achieve small spot sizes.

The NTX device consisted of three main sections: the beam source and injector section, magnetic transport section, and neutralized drift section. A photograph of the NTX is shown in Fig. 1.4. Vacuum pressure was maintained throughout the device to levels of $10^{-5} - 10^{-7}$ Torr. The experiment was equipped with an injector capable of generating a high-brightness, low-emittance, and variable-perveance K^+ ion beam with $E_b \leq 400$ keV of directed energy. A beam's brightness is loosely defined as the ratio of its current to the square of its emittance, where the beam's emittance [Reiser, 1994] is a measure of its area in phase space, and is related to its internal temperature according to

$$\epsilon_n^{4\,rms} = 2\, r_b \sqrt{\frac{T_\perp}{m_i\, c^2}}\,, \tag{1.1}$$

for a nonrelativistic, uniform round beam with a Maxwellian velocity distribution, where r_b is the beam radius, $T_\perp$ is the transverse temperature, and $m_i\, c^2$ is the rest

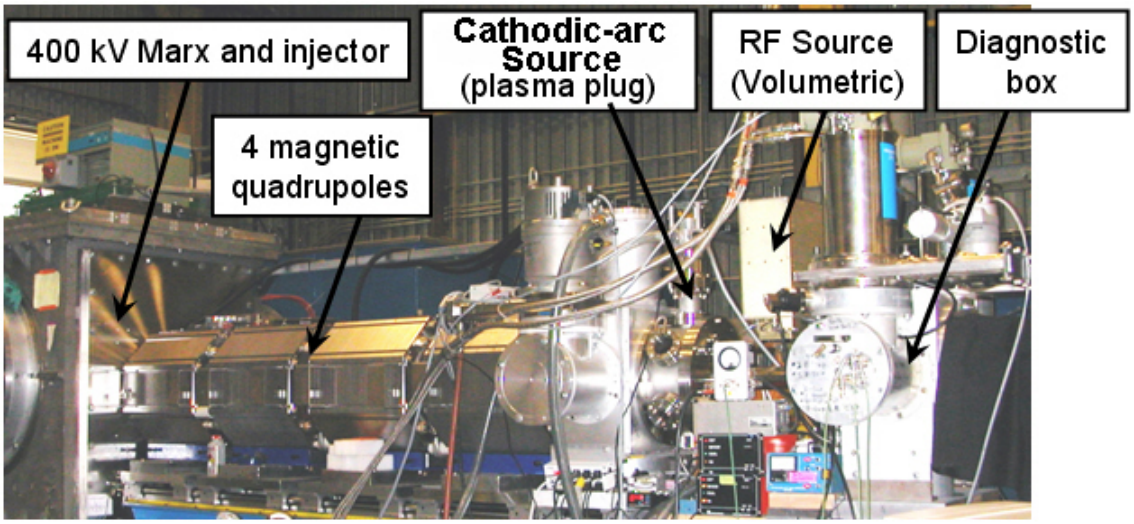

Figure 1.4: (Color) A photograph of the components in the Neutralized Transport Experiment [Henestroza *et al.*, 2004] at Lawrence Berkeley National Laboratory.

energy of the beam. The normalized four-times-rms transverse effective emittance is given by Eq. (1.1) in units of m-rad (although typically quoted in cm-mrad or mm-mrad). The longitudinal emittance is similarly defined by replacing $T_\perp$ with the longitudinal temperature $T_\parallel$ and r_b with z_b, the axial bunch length. Liouville's theorem ensures that the normalized emittance is conserved in the absence of nonlinear forces and coupling forces between different coordinate directions; in practice, Eq. (1.1) is a theoretical lower limit because nonlinear dynamics, focusing aberrations, collisions, instabilities, and other effects can cause beam emittance growth in experiments [Reiser, 1994]. Beams with low emittances are desirable because they suffer less from aberration during the focusing process. If one can neglect space-charge (such as when the beam is very well neutralized by a background plasma), the focusing of the beam is said to be emittance-dominated. After generation, the NTX ion beam was passed through a magnetic-focusing section, comprised of four pulsed solenoids or quadrupoles, in order to study magnet tuning physics and its effects on phase-space

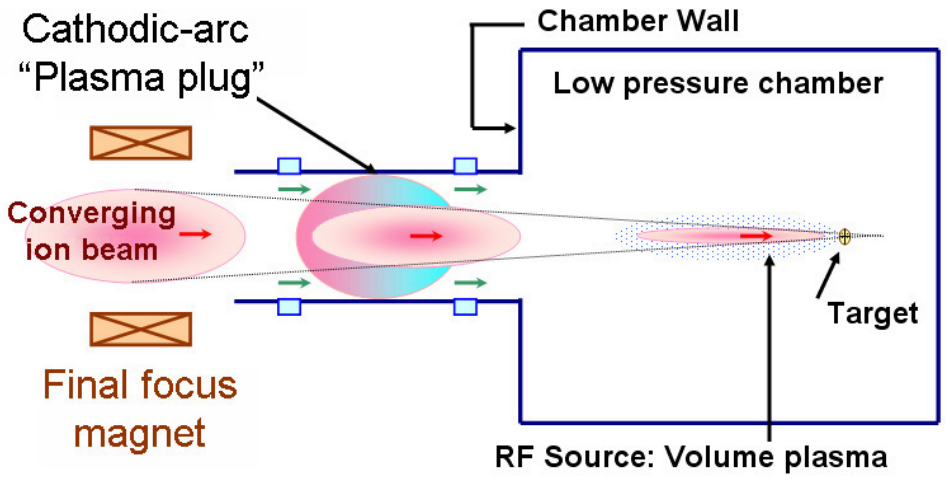

Figure 1.5: (Color) The physics of the two plasma sources in the Neutralized Transport Experiment. After acquiring an initial convergence angle, the intense ion beam passed through a high-density "plasma plug", which allowed the beam to transversely focus to small spot size. A radio-frequency plasma source represented the additional photoionized plasma near the target in an ion driver.

evolution of the beam. The final magnet was used to give the beam a convergent angle just before the beam entered the drift region, which contained background plasma.

Two plasma sources were utilized in the experiment to study final spot size dependence on various neutralization conditions during transverse beam compression, as illustrated in Fig. 1.5. The first was a pulsed cathodic-arc source, which acted as a "plasma plug" in the drift region; in a heavy ion driver, the "plasma plug" is the injected plasma between the final-focus magnet and the target chamber. The second was a pulsed, volumetric radio-frequency plasma source [Efthimion *et al.*, 2003], which was installed near the end of the neutralized transport section. The radio-frequency source was intended to mock-up the additional neutralization provided by photoionization of background gas in the target chamber [Langdon, 1992], due to thermal radiation given off by the target during preheat (from lower-current "foot" pulses preceding the main pulse).

The Neutralized Transport Experiment was a scaled, proof-of-principle experiment [Roy *et al.*, 2004]; although the beam energies and currents were far lower than parameters found in heavy ion driver designs, the experiment's operating regime was extremely relevant to the physics of an actual, full-scale driver in terms of the transverse beam dynamics and neutralization physics. The key dimensionless scaling parameter for intense beam transport is called *perveance* [Lawson, 1958]. The perveance determines the degree to which space-charge plays a role in the charge bunch dynamics, is loosely defined as the ratio of the beam's space-charge potential energy to its kinetic energy, and is given in SI units for a nonrelativistic beam by

$$K = \frac{Z\, e\, I_b}{2\,\pi\,\epsilon_0\, m_i\, v_i^3}\ , \tag{1.2}$$

where I_b is the beam current and Z, m_i, and v_i are the charge state, mass, and velocity of the beam ions, respectively. Ion trajectories of a charge bunch are nearly ballistic, meaning space-charge defocusing effects are negligible, up to a perveance limit of approximately $K \sim 10^{-5}$ [Olson, 1980, Olson, 2001].

Early heavy ion fusion designs called for $K \leq 10^{-6}$, whereas recent designs typically utilized perveances in the $K \sim 10^{-4}$ range and clearly required neutralized transport to offset space-charge effects for achieving acceptable focal-spot radii with short pulse lengths. The experimental injector was designed to produce ion beams of variable-perveance up to $K \sim 10^{-3}$ [Henestroza *et al.*, 2004]. Therefore, the physics studied on the device was driver-relevant, since the dimensionless quantity of importance was chosen to be similar to values found in driver designs. The other scaled dynamical quantities were the reduction of the emittance and initial beam radius (by the ratio of magnetic lattice lengths), and the final-focus magnetic fields

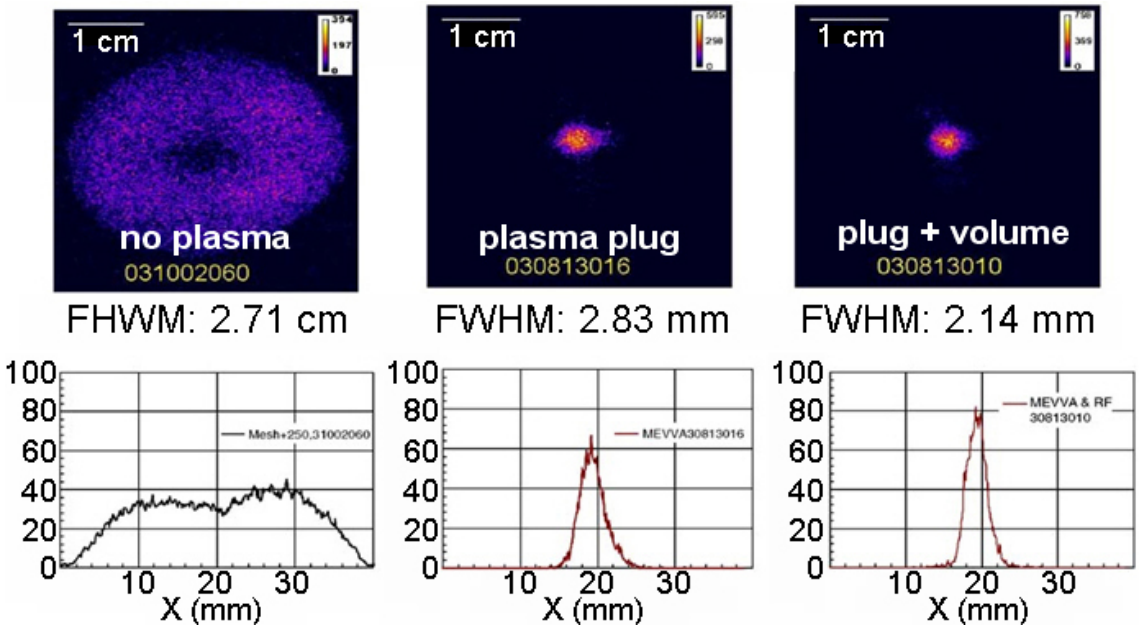

Figure 1.6: (Color) Optical intensity images and slices from transverse beam focusing experiments without a neutralizing plasma (left), with only a plasma plug (middle), and with both plasma sources (right) [Roy *et al.*, 2005a].

(according to ion mass and energy). Some issues could not be studied in a single-beam, scaled experiment [Henestroza *et al.*, 2004], such as beam-gas collisional effects (cross sections are energy-dependent), converging effects near the target from multiple overlapping beams, high-current effects such as magnetic self-focusing and filamentation, and beam photoionization by target x-ray radiation.

Experiments [Henestroza *et al.*, 2004, Roy *et al.*, 2004, Roy *et al.*, 2005a] and related simulations [Welch *et al.*, 2001, Thoma *et al.*, 2005] demonstrated that a plasma whose density satisfied $n_p >> n_b$ (where n_p and n_b are the plasma and beam densities, respectively) and was positioned "upstream" of the target chamber, provided a sufficient electron population to neutralize the beam's space-charge and current. When the proper convergent angle was applied by the final-focus magnet, the

beam transversely focused, during final transport in the device, beyond the space-charge limit to a full-width, half-maximum diameter of ~ 2 mm at the focal plane, corresponding to a transverse compression in density of approximately 400. The important role of the plasma in achieving small spot sizes with space-charge-dominated beams is clearly highlighted in Fig. 1.6; a camera captured the optical images of the transverse profiles from a scintillator plate, which was placed within the diagnostic box at the end of the beamline (refer to Fig. 1.4).

The objectives of the Neutralized Transport Experiment were successfully met. A more detailed description of the beamline system [Henestroza *et al.*, 2004], results of the transverse compression physics [Roy *et al.*, 2004], comparisons to detailed $3D$ particle-in-cell simulations [Thoma *et al.*, 2005], and other important experimental topics addressed by the experiments [Roy *et al.*, 2005a] were published.

1.5 Neutralized Drift Compression Experiment

Experiments successfully demonstrated the ability to transversely focus an ion beam by passing it through a background plasma, and results were in agreement with quantitative predictions by simulations. However, focusing an ion beam in the transverse direction is only part of the challenge. In order to achieve the requirement that the pulse length be < 10 ns at the focal plane, each ion beam pulse in a heavy ion driver must also undergo longitudinal compression, in the axial direction of propagation. Longitudinal bunch compression also helps the ion beam meet the requisite beam intensities desired at the target by increasing the current density ($J_z \sim \lambda$).

In order to validate that ion beams with high current compression and short pulse durations can be achieved on target, there is a need for an experiment to determine

the physical and technological limits of longitudinal focusing. Longitudinal bunch compression occurs by imposing a time-dependent, axial velocity tilt onto the beam, and subsequently allowing it to drift through plasma, thereby neutralizing the beam's space-charge and current as the pulse length compresses [Welch *et al.*, 2005]. The current density, and therefore relative power, of the charge bunch grows in the intermediate region of the applied tilt while the beam drifts through a pre-formed plasma column. This process is explicitly referred to in the name "neutralized drift compression," and the upgrade of the NTX facility is called the Neutralized Drift Compression Experiment (NDCX) [Roy *et al.*, 2005b, Roy *et al.*, 2007]. Longitudinal compression of intense ion beams without the aid of background plasma has also been studied [Qin *et al.*, 2004, Sharp *et al.*, 2005].

A schematic of the experiment is shown in Fig. 1.7 [Roy *et al.*, 2005b]. The primary component addition compared to the previous experiment is the induction module, which is a linear induction accelerator [Christofilos *et al.*, 1964] with one acceleration gap. The induction accelerator is the type preferred by the U.S. heavy ion beam community (as opposed to a radio-frequency linear accelerator) because of its simplicity and ability to handle high-current beams; it is a non-resonant (low-Q) device whose purpose is to induce a pulsed electric field along the accelerator axis by changing the magnetic flux in a ferromagnetic core encircling the beam pipe. It is responsible for the impression of the axial velocity tilt on the beam pulse by means of a time-dependent voltage waveform. In effect, the induction core is a one-turn transformer, with the beam acting as the secondary winding. The pulse modulators used to drive the magnetic flux, the induction core, and the acceleration gap across which the electric field is produced are together called an *induction module*. Refer to

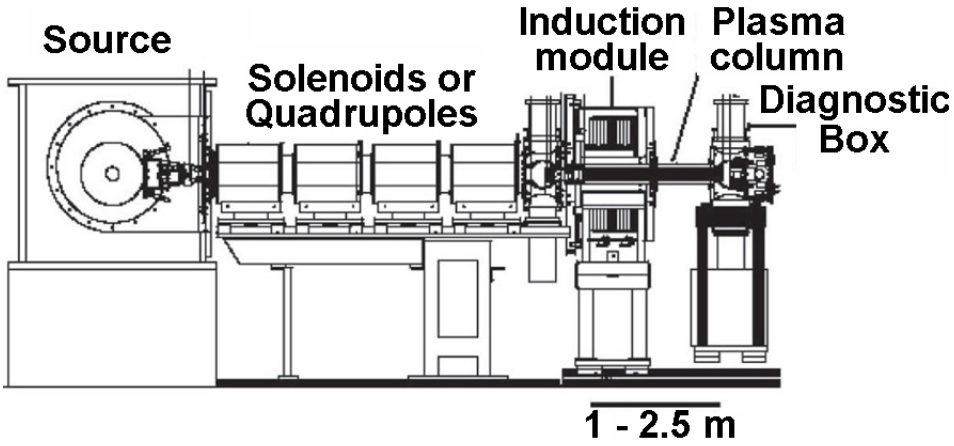

Figure 1.7: Schematic of the Neutralized Drift Compression Experiment [Roy *et al.*, 2005b]. The primary component addition compared to the previous experiment (NTX) is the induction module.

Appendix A for more details on a single-gap linear induction accelerator. The time-dependent voltage waveform has two extrema and changes polarity in the middle, such that the first half of the beam pulse (the "head") experiences a net decelerating electric force, and the second half of the beam pulse (the "tail") experiences a net accelerating electric force. Thus, the charge bunch acquires a head-to-tail velocity tilt immediately before it drifts through a 1 to 2.5 m-long region containing plasma; the tilt causes the tail of the beam to meet the head of the beam at the longitudinal focal plane, where maximum current is reached near the end of the plasma column.

The secondary upgrade compared to the previous experiment is a ferroelectric plasma source [Rosenman *et al.*, 2000, Efthimion *et al.*, 2005b] that was designed, constructed, and tested at the Princeton Plasma Physics Laboratory, and integrated into the experiment in the Fall of 2006. The ferroelectric source enjoys a few major advantages over the previous cathodic-arc and radio-frequency plasma sources, due to the method by which the plasma is created and fills the volume of the drift region for

beam compression experiments. Simulations and further discussion on the cathodic-arc and ferroelectric plasma sources will follow in Chapter 5.

The main issues to be addressed by the Neutralized Drift Compression Experiment are the determination of (1) the fundamental physical and technological limits of longitudinal compression (and how accurately it can be measured), (2) the non-ideal experimental aspects of neutralized drift compression, and (3) the integrated system architecture by testing small systems individually. The experiments will provide the knowledge to design and construct the "next-step" facility, which will employ intense ion beams of greater kinetic energy with the necessary equipment designs for facilitating large amounts of total (transverse and longitudinal) current density compression, in order to study warm dense matter and high-energy-density physics, on the path to a heavy ion fusion driver.

1.6 Simultaneous transverse and longitudinal ion beam focusing

The Neutralized Transport Experiment demonstrated the feasibility of transverse compression of an intense ion beam by applying a radial focusing angle to it prior to neutralizing the beam's space-charge and current in a plasma-filled drift region. The radial defocusing effect of the charge bunch's self electric field, which arises due to its positive potential, was negated by the presence of neutralizing electrons in the high-density plasma. When the plasma density n_p was much larger than the beam density n_b throughout the drift region, quasineutrality was maintained and the beam focused ballistically to a small spot (few mm). When the level of neutralization was very high,

the focusing was emittance-dominated, meaning only the inherent initial temperature of the beam limited the final beam radius r_b, due to chromatic aberration.

The Neutralized Drift Compression Experiment currently studies longitudinal compression in a similar way, by providing plasma to neutralize the beam as it focuses in the axial direction. The primary difference between the experiments is the addition of the induction module, which modifies the longitudinal velocity profile of the beam in order to decrease its initial pulse length. The plasma source assists the compression of the beam by neutralizing the defocusing effect of the charge bunch's self electric field, which inhibits the transverse and longitudinal compression. Longitudinal focusing can also be emittance-dominated, provided that the accuracy of the imposed velocity tilt and the level of neutralization are each very high.

In order to meet the requisite beam intensities desired at the target for various applications, space-charge-dominated charge bunches must take advantage of both types of focusing. In other words, they must undergo simultaneous transverse and longitudinal bunch compression. While trying to achieve optimal simultaneous compression, the vast majority of the ion beam's greatly increasing space-charge and current must remain neutralized as the beam focuses during the final transport to the target. Upcoming experiments of neutralized drift compression will attempt to transversely focus a beam with an axial velocity tilt to a sub-mm spot size coincident with the longitudinal focal plane. Numerical simulations and future experiments seek to optimize the amount of simultaneous transverse and longitudinal current density compression, given a set of experimental constraints (including drift length, which is 1 to 2.5 m for the NDCX device, and would be longer for more energetic beams).

The neutralization provided by the plasma is critical in determining the total

achievable transverse and longitudinal compression of the beam pulse. Theory and simulation predict total current density compression factors of 10^3 to 10^5 over a few m in experiments, provided that sufficient amounts of plasma density are supplied. The peak beam density n_b sets a lower bound on the local plasma density n_p required for optimal beam compression, since the beam's self-fields can become important in the focusing dynamics if the greatly increased n_b encroaches upon the available n_p near the focal plane. Longitudinal compression increases the beam current as a function of time, therefore the perveance of the beam increases and, in cases of large amounts of compression, it becomes crucial to provide sufficient neutralization near the simultaneous focal plane for optimal focusing. One might expect compression stagnation, decreased amounts of overall compression, and complex collective behavior in the background plasma to occur if significant charge and current density perturbations are created in the beam-plasma system due to inadequate neutralization.

1.7 Thesis objective and outline

An outline of the objectives of this thesis is provided below.

As discussed in Chapter 1, neutralized drift compression offers the promise of compressing heavy ion beams to very high current densities. Achieving the requisite beam intensity is the central issue of heavy ion accelerators for use as drivers. This thesis studies the issues which determine the effective limits concerning the simultaneous transverse and longitudinal compression of intense charge bunches, since the maximum current density compression that can be achieved determines the amount of power delivered to the target. More intensity per unit length of accelerator can

be delivered to the target than previously envisioned by greatly compressing space-charge-dominated ion beams over short distances, while providing neutralization with plasma sources. The primary uncertainties for a given accelerator design include the minimum achievable spot size and pulse duration; a particular design for ion-driven inertial fusion energy should plan to confidently run close to its optimized state, in order to avoid prohibitively raising the cost associated with providing conservative beam specifications. Optimizing the compression under the appropriate experimental constraints offers the potential of allowing more compact and cost-effective accelerators to be used as heavy ion drivers, making them more attractive than previously considered.

In Chapter 2, the design, simulation, fabrication, and calibration of a diagnostic for the fast and accurate measurement of the absolute current and short pulse length of a longitudinally compressed beam are described. The so-called fast "pinhole" Faraday cup is shown to accurately recover the absolute beam current in the presence of plasma, where standard Faraday cup diagnostics fail, and therefore its development was critical for the success of longitudinal compression experiments. Sophisticated particle-in-cell simulations of intense ion beam propagation through plasma are in excellent agreement with data acquired by the fast Faraday cup, which demonstrate successful current compression to pulse lengths < 5 ns in duration.

Chapter 3 provides derivations and discussions of the various theoretical frameworks employed in the following Chapter to model intense charge bunch propagation and compression in a background plasma. In support of the neutralized drift compression experiments, several theoretical models of intense ion beam propagation are expanded upon by accounting for some of the non-ideal parameters and effects found

in charge bunch compression experiments. The Klimontovich-Maxwell description is first derived as a starting point for the further derivation of the plasma kinetic equation and nonlinear Vlasov equation. The macroscopic warm-fluid description is derived by evaluating velocity moments of the Vlasov equation, and closing the system of equations by assuming an equation of state. The particle-in-cell code LSP is discussed as a method to self-consistently incorporate many effects of beam compression in plasma, and compare to the reduced model descriptions.

Theory and numerical simulation are provided in Chapter 4 to investigate many non-ideal experimental effects involved in longitudinal ion beam focusing. Reduced theoretical models and particle-in-cell simulations are shown to realistically describe longitudinal compression dynamics, and contribute detailed understanding to the forefront of ion beam compression research. Many assumptions on solution-type and uniformity are relaxed in the analysis, such as the inclusion of nonuniform and asymmetric density and axial velocity profiles, acceleration gap size and voltage waveform, space-charge and perveance, beam temperature effects, focusing aberrations, beam energy uncertainties due to technological limitations, and beam propagation through a plasma which incompletely neutralizes the beam.

The derivation of the ideal velocity tilt is provided, as well as the voltage waveform that produces it. The warm-fluid model is a tractable computational tool for realistically predicting the dynamic evolution of the compressing beam, and it is used to demonstrate the velocity and line density pulse-shaping ability of the acceleration gap. A Vlasov formalism explores the physics of the central portion of the beam with an approximate linear velocity tilt, which most effectively contributes to the main compressed pulse at focus. In order to study how surrounding regions of pedestal

current form, a hybrid combination of the fluid and Vlasov models is developed, since such a hybrid implementation combines the advantages of both methods. However, ion beam trajectories generally need to be evaluated numerically by particle-in-cell simulation, in order to account for the (normally intractable) effects that determine the quality of the focal plane. The successful comparison between measurements and the numerical models of longitudinal compression is also reported in Chapter 4.

The detailed physics and implications of acceleration gap effects and focusing aberration on optimum longitudinal compression are quantitatively reviewed, with dependency on most of the system parameters examined. For example, the finite-size gap effects are shown to result in compression reduction, due to an increase in effective longitudinal temperature imparted to the beam and decrease in intended fractional tilt. Sensitivity to initial beam temperature and resulting aberration of the focal plane is explored, where slower particles are shown to suffer increased levels of aberration (and contribute more current to the pre-pulse) compared to faster particles. An analytical equation for the minimum temporal pulse length of an ideally-tilted beam with finite initial temperature, accounting for the variation in aberration, is derived. The compression ratio and pulse length at focus are demonstrated to decrease and increase, respectively, with square root dependence on the initialized beam temperature, which is the limiting physics on longitudinal bunch compression using optimized waveforms and plentiful plasma supply.

Axial compression dependence on initial pulse length and intended fractional tilt is also investigated in Chapter 4, since they comprise the two voltage waveform parameters adjustable by the experimenter. A plateau effect in initial pulse length is shown to occur, where aberrations due to longer drift lengths dominate increases in

compression, indicating a trade-off consideration between current compression and pulse duration. The dependence on intended fractional tilt is discussed and agrees well with theory. A balance between longer initial pulse lengths and larger fractional tilts is discussed, since both increase the compression ratio, but have opposite effects on the pulse length, drift length, and aberration. Quantitative examples are outlined that explore the dependency of longitudinal compression on initial kinetic energy and thermal distribution. Simulations warn that small constant differences and temporal drifts in directed energy cause significant departure from the optimum compression parameters. It is also demonstrated that experimental beam energy scans to align the plane of the diagnostic with a peak compression result, while holding the waveform fixed, do not unambiguously determine the optimum compression, and a method for doing so is provided.

Chapter 5 outlines the execution of large-space scale and long-time scale plasma flow simulations, in order to study the spatial and temporal evolution of plasma parameters from two different types of source used in the laboratory. The results help assess the neutralization conditions in experiments, and can be employed in additionally sophisticated compression simulations, which previously ignored the dynamical nature of the provided plasma.

Three-dimensional simulations of the cathodic-arc plasma source show the coupling efficiency of the plasma flow from the source to the drift region depends on many geometrical factors, as well as the plasma properties and magnetic field topology. The non-uniform magnetic topology complicates the well-known general analytic considerations for evaluating guiding-center drifts, and particle-in-cell simulations provide self-consistent evaluation of the physics in an otherwise challenging scenario.

Plasma flow profiles of the ferroelectric source demonstrate that the required plasma densities are provided over the drift length for longitudinal compression experiments, and are in good agreement with measurements. Situations involving azimuthally-asymmetric plasma creation conditions observe that symmetric profiles are nevertheless achieved at the time of peak on-axis plasma density. Also, ferroelectric plasma expands upstream on the thermal expansion time scale, and therefore avoids the possibility of plasma penetration far upstream into the acceleration gap and transport sections, where partial neutralization would raise the beam emittance.

Upcoming experiments will use the magnetic fields in a strong final-focus solenoid in order to transversely focus the axially-compressing beam to a sub-mm spot coincident with the longitudinal focal plane. In order to fill a final-focus solenoid with the high-density plasma necessary for beam neutralization, simulations in Chapter 5 predict that supersonically-injected plasma from the low-field region will penetrate the high-field region of the solenoid. Simulations indicate the final-focus solenoid becomes partially-filled with plasma, and the on-axis plasma density depends on the supersonic injection velocity as well as the magnetic field strength.

The design details and considerations for achieving simultaneous transverse and longitudinal focusing in the laboratory are presented in Chapter 6. The acceleration gap is shown to time-dependently defocus the radially-converging trajectories of the beam ions. The resulting beam radius $r_b(t)$ depends on the beam parameters, acceleration gap, and $-dV(t)/dt$ of the voltage waveform, but, by giving the beam an exaggerated initial convergence angle, the "over-focused" trajectories are shown to balance the excess divergence given to the beam in the gap. In the absence of plasma, the intense self-fields of the beam cause it to radially expand and potentially strike

the chamber wall. The cumulative effects of partial neutralization, caused by partially exposed beam potential within the drift length, on charge bunch compression at the simultaneous focal plane are explored. Simulations demonstrate that reduced plasma densities and increased plasma temperatures are harmful to compression, since neutralization physics occurs on the Debye-length scale λ_D.

Simultaneous compression simulations involving beams with various initial $J_z(t)$ and $r_b(t)$ are also discussed in Chapter 6, and the various profiles are shown to result in different amounts of compression due to focusing aberration. The profiles approximately achieving the maximum amount of compression, by minimizing the aberration, are provided. The design of a simultaneous focusing experiment using existing hardware and a $B_z = 80.5$ kG final-focus solenoid is given, in support of upcoming planned experiments. In addition, simulations indicate that a 400 keV K^+ ion beam can be transversely and longitudinally compressed in current density by a factor greater than 10^5 over a distance of $L_d \sim 2.5$ m using upgraded hardware, including an induction module with more Volt-second capability, a $B_z = 150$ kG final-focus solenoid, and plasma sources capable of densities above $n_p \sim 10^{14}$ cm^{-3}. The optimization of simultaneous focusing, for a given set of experimental constraints, is shown to be a sensitive function of nearly all of the system parameters.

Ultimately, the transverse compression of the beam is largely determined by the strength and length of the final-focus solenoid, along with its position in the drift region and the amount of plasma provided for neutralization. Neutralization of the beam within the final-focus solenoid is critical for adequate compression. If remnant magnetic fields at the focal plane are not desired, the reverse-aligned solenoid configuration is a viable alternative to the single final-focus solenoid, since it has many

inherent advantages. The plasma must sufficiently neutralize the beam throughout the focusing process, otherwise compression stagnation and loss of optimal compression occurs, since the peak beam density n_b is demonstrated to set a lower bound on the local plasma density n_p required near the focal plane to recover near-ballistic focusing. Beam-plasma interactions, due to partial neutralization effects in the presence of a strong solenoidal magnetic field near the focal plane, deleteriously affect the compression physics and lead to the formation of nonlinear wave excitations in the plasma.

Chapter 7 summarizes the major results of the thesis, while discussing important ramifications for intense ion beam compression experiments. Suggestions for future work are also discussed in detail. Lastly, an epilogue that reiterates the importance of ion beam current density compression in space and time is provided, along with how this thesis contributes to long-term heavy ion fusion goals.

Chapter 2

Diagnostic Design

The Neutralized Drift Compression Experiment (NDCX) [Roy *et al.*, 2005b] at the Lawrence Berkeley National Laboratory is used to determine the effective limits of neutralized drift compression, which occurs due to an imposed longitudinal velocity tilt on the drifting beam and subsequent neutralization of the beam's space-charge and current in a drift region filled with high-density plasma. As mentioned in Sec. 1.5, the primary issue to be addressed by the NDCX device is to determine the fundamental physical and technological limits of longitudinal compression, as well as how accurately the current compression ratio and final pulse length can be measured. Simulations predict a final pulse length of a few ns with approximately ≤ 1 A cm^{-2} of current density at peak compression for experiments involving only longitudinal compression [Sefkow *et al.*, 2005a, Sefkow *et al.*, 2005b].

The accurate and temporally-resolved measurement of the ion beam's current and pulse length, which has been longitudinally compressed to a few ns in duration at its focal plane, is critical for the success of neutralized drift compression experiments.

This Chapter describes the design, simulation, fabrication, calibration, and experimental results for a fast and accurate ion beam diagnostic, which reliably measures the absolute compressed beam current as a function of time at the longitudinal focal plane, in the presence of a neutralizing background plasma. The reason a re-designed diagnostic is necessary for longitudinal compression experiments is explained in Sec. 2.1. The particle-in-cell LSP code [LSP, 1999, HUGHES *et al.*, 1999] is used in Sec. 2.2 to simulate the so-called fast "pinhole" Faraday cup [SEFKOW *et al.*, 2006], which is designed to operate properly within a plasma environment. The details surrounding the construction and calibration of the diagnostic are described in Sec. 2.3. In Sec. 2.4, measurements of longitudinal compression in the laboratory using the fast Farday cup are shown. Additional modifications to increase the temporal resolution of the diagnostic, as well as comparison to particle-in-cell simulations of longitudinal compression, are provided in Sec. 2.5. A brief summary and discussion of the diagnostic design and implementation concludes the Chapter in Sec. 2.6.

2.1 The need for a redesigned diagnostic

The ion beam probe that is designed to measure the time-dependent beam current $I_b(t)$, while operating in the presence of high-density plasma within the beamline, is a modified Faraday cup. In Fig. 2.1, a schematic of a standard Faraday cup is shown. Generically, a Faraday cup consists of a negatively-biased, electron-repelling ring located "upstream" of a positively-biased collector cup and enclosed in a grounded housing such that various particle populations in the system are controlled. A standard Faraday cup design that admits the compressed ion beam in its entirety is inadequate for the purposes of neutralized drift compression experiments because of

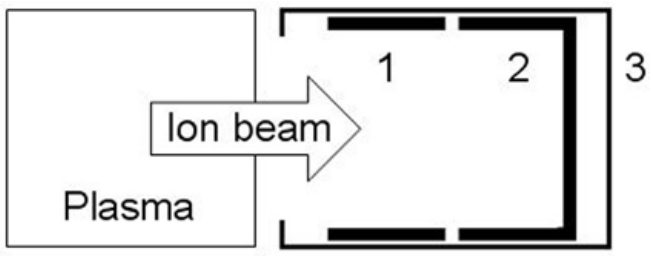

Figure 2.1: A standard Faraday cup includes a negatively-biased electron-repelling ring (1), a positively-biased collector cup (2), and a grounded enclosure (3).

the complex plasma and secondary electron behavior within such a probe. Particle-in-cell simulations show that, if high-density plasma is allowed to enter the probe, the plasma can shield the applied potentials which are meant to reject all particles from measurement except the beam ions, allowing plasma electrons (and ions) to penetrate the probe and be detected, thereby reducing (and increasing) the corresponding signal measured at the collector. Thus, if plasma particles are not controlled, the signal due to beam ions alone cannot reliably be determined. Ideally, an experimenter would prefer that the collector only measure a signal proportional to the ion beam current.

Therefore, a fast "pinhole" Faraday cup diagnostic for measuring the absolute beam current in the presence of plasma at the focal plane as a function of time is designed, fabricated, and incorporated into the Neutralized Drift Compression Experiment (NDCX) [Sefkow *et al.*, 2006]. The fast Faraday cup diagnostic is corroborated by optical measurements made with a fast phototube arrangement [Bieniosek *et al.*, 2005b], which measures light intensity created by beam bombardment on a scintillator. However, the limitation of such an optical measurement is that it cannot measure the actual ion beam current, whereas the fast Faraday cup diagnostic can.

2.2 Fast "pinhole" Faraday cup design

The successful characterization of neutralized drift compression requires accurate measurements of the time-dependent compressed ion beam current $I_b(t)$ and pulse length at the focal plane, near the end of the plasma region. Several probe designs based on numerical simulations are tested to measure the beam parameters in the presence of high-density plasma. The use of the LSP code is one method for simulating an ion beam pulse propagating through background plasma. LSP is an advanced $3D$ electromagnetic particle-in-cell simulation code, designed for complex plasma simulations, and can be execute in multiple coordinate systems and geometries. The code is utilized in order to realistically predict the evolution of the ion beam as it acquires a velocity tilt and drifts through the plasma to the longitudinal focal plane. The code is also employed to determine the diagnostic requirements for an accurate measurement of the beam current using a probe residing in a plasma environment.

The five key requirements that must be met in order to accurately measure the true beam current $I_b(t)$ or current density $J_b(t)$ include (1) plasma ions and beam ions must not shield the negatively-biased electron-repelling ring, (2) co-moving plasma electrons that neutralize the beam's potential must be completely rejected from the probe, (3) beam ions must not be allowed to strike the electron-repelling ring and create secondary electrons which would foul the measurement at the collector, (4) secondary electrons created by ion bombardment on the collecting surface must be trapped, otherwise artificially high signals would be measured at the collector, and (5) large beam current densities must be measured at the collector with sub-ns time resolution.

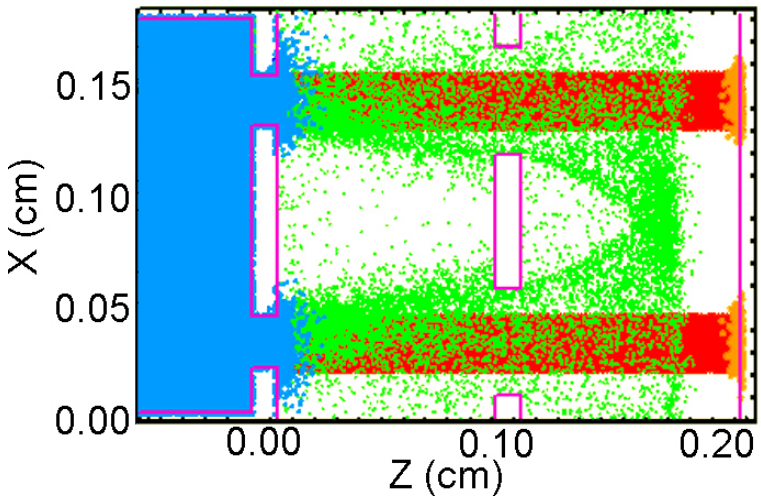

Figure 2.2: (Color) The particle-in-cell simulation of the fast "pinhole" Faraday cup diagnostic for measuring $I_b(t)$ includes particles for the K^+ ion beam particles (red), plasma electrons (blue), plasma Al^+ ions (green), and secondary electrons (orange). The grounded frontplate ($z = 0.0$ cm), the negatively-biased electron-repelling backplate ($z = 0.1$ cm), and the positively-biased collector cup ($z = 0.2$ cm) are shown. Secondary electrons created by plasma ion bombardment on the backplate are not shown for clarity reasons.

In order for the diagnostic to operate properly in a plasma environment, simulations indicate that the standard Faraday cup design should be modified such that it includes a grounded frontplate containing plasma Debye-length-size holes, replaces the electron-repelling ring with an electron-repelling plate containing slightly larger holes, and replaces the collector cup with a collector plate, as shown in the particle plot of Fig. 2.2 (only a fraction of the total number of particles are plotted for clarity reasons). The aligned holes of the frontplate and electron-repelling plate (also called the backplate) provide a geometric shadow to the probe, thereby allowing only a fraction of the compressed beam pulse to enter the diagnostic and simplifying the control of the five important processes mentioned earlier. The frontplate and backplate of the diagnostic are similar in design and purpose to grids normally found in a

gridded-energy analyzer [HUTCHINSON, 2002].

The $2D$ $\{x, z\}$ PIC simulation models five species of particles, including (1) the plasma electrons, (2) the plasma ions (Al^+), (3) the beam ions (K^+), (4) secondary electrons created on the frontplate and collector by ion beam bombardment, and (5) secondary electrons created on the frontplate and backplate by plasma ion bombardment (however, due to the design requirements outlined earlier, beam ions do not strike the backplate and plasma ions do not strike the collector). In the simulations, all species are treated as kinetic, explicit, and energy-conserving particles, the electrostatic field equations are solved (meaning the $\partial\mathbf{E}/\partial t$ terms and $\partial\mathbf{B}/\partial t$ terms are ignored), and a cloud-in-cell interpolation scheme is used in order to reduce particle noise [BIRDSALL and LANGDON, 1985]. In addition, a stimulated secondary electron emission package (included in LSP) is used in order to model the ejection of electrons from conducting surfaces when beam ion or plasma ion particles strike any of the surfaces (the frontplate, backplate, and collector).

The primary difference between the standard Faraday cup and the "pinhole" design is found in the nature of the negatively-biased, electron-repelling backplate. In the standard Faraday cup design, shown in Fig. 2.1, the electron-repelling ring only exists out at some large radius (greater than the ion beam's radius) and does not adequately deflect all of the co-moving plasma electrons. Instead, shielding by the various charged particle populations occurs, and the applied potential near the axis is not adequate to effectively remove the ion charge bunch from the plasma. Therefore, the signal detected at the collector is not proportional to the beam current alone, but is reduced by any plasma and secondary electron current detected. Also, plasma

ions are accelerated into the diagnostic by the negative bias applied to the electron-repelling ring. Plasma ions can eject secondary electrons and simulations show that such electrons can be accelerated by the ring and also detected, further complicating the signal at the collector [so it is not solely proportional to the $I_b(t)$].

In the "pinhole" Faraday cup design shown in Fig. 2.2, a grounded frontplate with plasma Debye-length-size holes ($n_p \sim 10^{10}$ cm^{-3}, $T_p \sim 3$ eV) admits only a small fraction of the beam, while also limiting the effective entry locations for the plasma ions and electrons. Since the entrance holes are on the order of the plasma Debye length λ_D, the ion beamlets (created by the shadow of the frontplate) are each stripped of their neutralizing, co-moving plasma electrons because each frontplate hole has some corresponding negatively-biased, electron-repelling backplate in close proximity. The backplate with slightly larger holes (to accommodate diverging beam ions and avoid creation of secondary electrons by ion beam bombardment) replaces the electron-repelling ring of the standard Faraday cup, and is effective at resisting the introduction of plasma electrons into the diagnostic. Thus, plasma electrons (as well as secondary electrons created on the frontplate by ion beam bombardment) are secluded outside of the probe, due to the electric field created between the frontplate and backplate. Plasma ions are accelerated into the probe by such an electric field, but are repelled from detection by an applied positive bias on the collector plate, which creates a stronger, reversed electric field between the backplate and the collector, as shown in Fig. 2.3. The positive bias on the collector also traps secondary electrons, created by energetic ion beam bombardment, on the collector plate so the measured signal is proportional to $I_b(t)$ (and not artificially high, due to secondary electron loss from the detector). The frontplate is grounded to ensure its potential relative to the

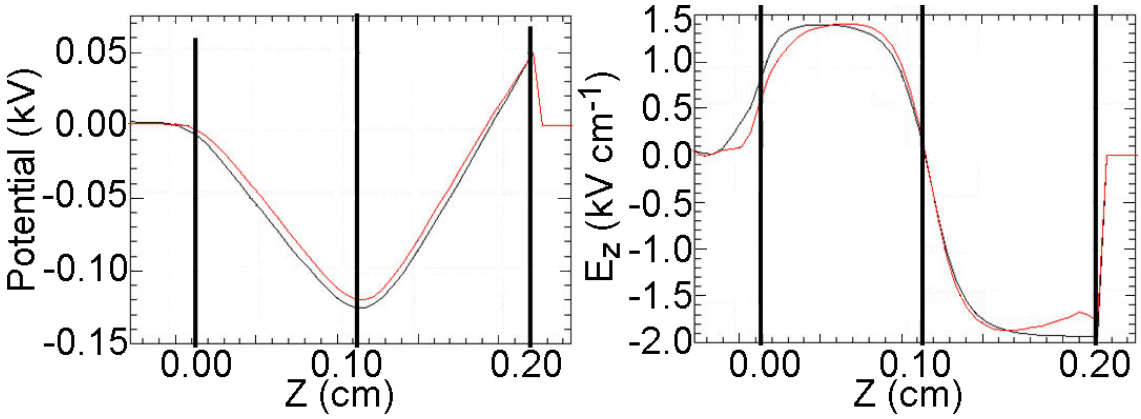

Figure 2.3: (Color) Axial coordinate slice plots of electrostatic potential (left) and axial electric field (right) through an entrance hole in the fast Faraday cup when no beam is present (black) and when the expected peak beam density from longitudinal compression is present (red). The vertical black lines represent the locations of the frontplate, backplate, and collector. The various charged particle populations within the diagnostic do not shield the applied biases.

backplate and collector. The ion beamlets pass into the diagnostic largely unaffected by the biases on the backplate and collector, since the applied potentials in the probe are about 5×10^{-4} lower than the directed energy of the K^+ ions. The trajectories of the beam ions are expected to be unperturbed by sheath effects.

Since the frontplate holes are comparable in size to the plasma Debye length λ_D, and because the plasma ions are modeled with only thermal and no directed energy (plasmas with axial drift momentum can be repelled using higher biases), the densities associated with the plasma ions penetrating into the diagnostic are predicted to be two to three orders-of-magnitude lower ($n_{pi} \sim 10^7 - 10^8$ cm^{-3}) than the bulk plasma density n_p outside of the probe. Therefore, any image-current effects and detection of secondary electron currents created by (low energy) plasma ion bombardment on the backplate are expected to be negligible ($< 10^{-3}$ compared to I_b). Thus, all three possible sources of secondary electron current in the diagnostic

are controlled (ion beam and plasma ion bombardment on the backplate, as well as ion beam bombardment on the collector), and their negative side effects on the measurement process are mitigated. The fourth source of secondary electrons, the ion beam bombardment on the frontplate, is simulated as well, however those electrons are completely rejected from the probe by the same mechanism which rejects the plasma electrons.

The beam ions, plasma ions, secondary electrons created on the backplate by plasma ion bombardment, and secondary electrons created on the collector by ion beam bombardment do not significantly shield the potentials on the backplate and collector (refer to Fig. 2.3), due to the close (0.1 cm) spacings between the three plates (the associated λ_D lengths for these species are > 0.1 cm, due to their low densities). The 0.1 cm gaps are chosen to reduce the bias-shielding capability of the beam ions, and to minimize induced image-current effects at the collector. Therefore, the entire beam (less some transmission factor, due to the geometric shadow cast by the frontplate) is admitted into the probe and the collector accurately measures the total beam current $I_b(t)$ before the beam has sufficient time to decompress due to space-charge forces. This configuration is shown in simulation to be ideal for controlling the two most important electron populations: if all co-moving plasma electrons are not rejected from detection, the signal on the collector plate underestimates $I_b(t)$, and if all secondary electrons created on the collector by ion beam bombardment are not trapped, the signal on the collector plate overestimates $I_b(t)$.

2.3 Calibration of the fast "pinhole" Faraday cup

The diagnostic used in initial longitudinal compression experiments consists of a frontplate with hole radii approximately a plasma Debye length in size ($n_p \sim 10^{10}$ cm^{-3}, $T_p \sim 3$ eV), followed $\Delta z = 0.1$ cm "downstream" by a backplate with larger hole radii, and a collector plate another $\Delta z = 0.1$ cm "downstream" of the backplate [Sefkow *et al.*, 2005b]. Table 2.1 shows the hole radius, horizontal hole-to-hole separation, and applied bias for each of the plates. The vertical hole-to-hole separation is $\sqrt{3}/2$ times the horizontal separation, and each row of holes is staggered with respect to the adjacent rows, giving an hexagonal arrangement. Such an arrangement ensures the holes are equidistant and provides increased structural integrity to the thin plate. The frontplate and backplate are each 102 μm thick ($< 2\, r_{hole}$), made of stainless steel, and contain over $2,000$ holes. Due to the geometrical shadow cast by the aligned holes of the plates, the signal measured at the collector must be multiplied by the transmission factor in order to determine $I_b(t)$. The probe biases are chosen so the diagnostic operates properly under the harshest conditions expected in longitudinal compression experiments ($n_p^{peak} \sim 10^{11}$ cm^{-3}, $n_b^{foc} \sim 10^{10}$ cm^{-3}).

A photograph of the fast "pinhole" Faraday cup is shown in Fig. 2.4. Prior to installation, the outer perimeter of the diagnostic is wrapped with kapton tape and clear acrylic paint, in order to electrically isolate the components from the plasma.

Table 2.1: Fast "pinhole" Faraday cup specifications

Plate	r_{hole}	**Hole-to-hole**	**Bias**
Front	114 μm	1016 μm	Grounded
Back	241 μm	1016 μm	-150 V
Collector	N/A	N/A	$+50$ V

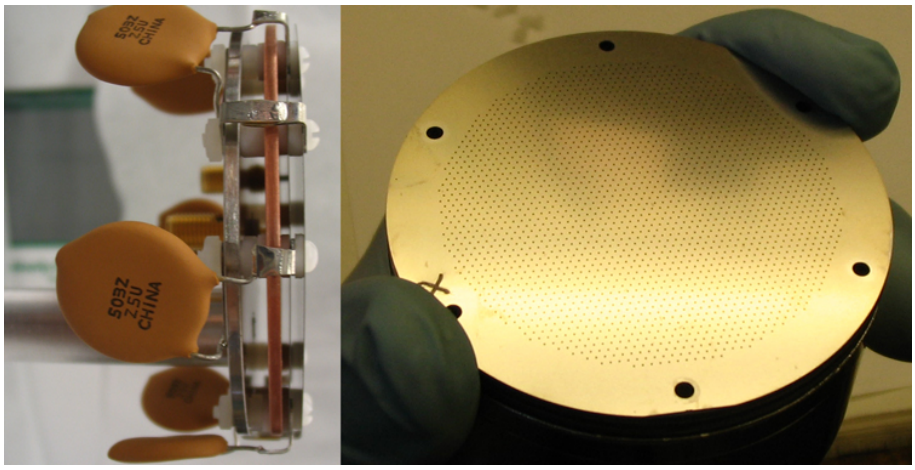

Figure 2.4: (Color) Photographs of the fast "pinhole" Faraday cup before installation. The copper collector is visible behind the frontplate and backplate in the left picture. The small holes in the frontplate are visible in the right picture.

The signal measured at the collector plate is expected to be very close to the true $I_b(t)$. Error levels associated with measuring the beam particles are expected to be $< 1\%$, except for contributions from system noise (which is not included in the model). Therefore, signal fidelity, instrumentation response, and various sources of system noise are expected to be the chief sources of error for beam current measurements.

Measurements made with the redesigned diagnostic show that, when only plasma is present, the collector plate draws no current and the backplate draws < 0.2 mA of plasma ion current, in agreement with simulations assuming a plasma density of $n_p \sim 10^{10}$ cm^{-3}. The ion beam injector is capable of producing uniform K^+ charge bunches with initial pulse lengths $t_p \sim 5 - 10\,\mu$s, energies $E_0 = 200 - 400$ keV, and beam radii $r_b = 1 - 2$ cm, which travel in the $+\hat{z}$ direction through the magnetic transport and plasma drift sections. The beam current is measured by the diagnostic at the longitudinal focal plane, near the end of the plasma drift column.

In order to calibrate the diagnostic, measurements of $I_b(t)$ are recorded with the

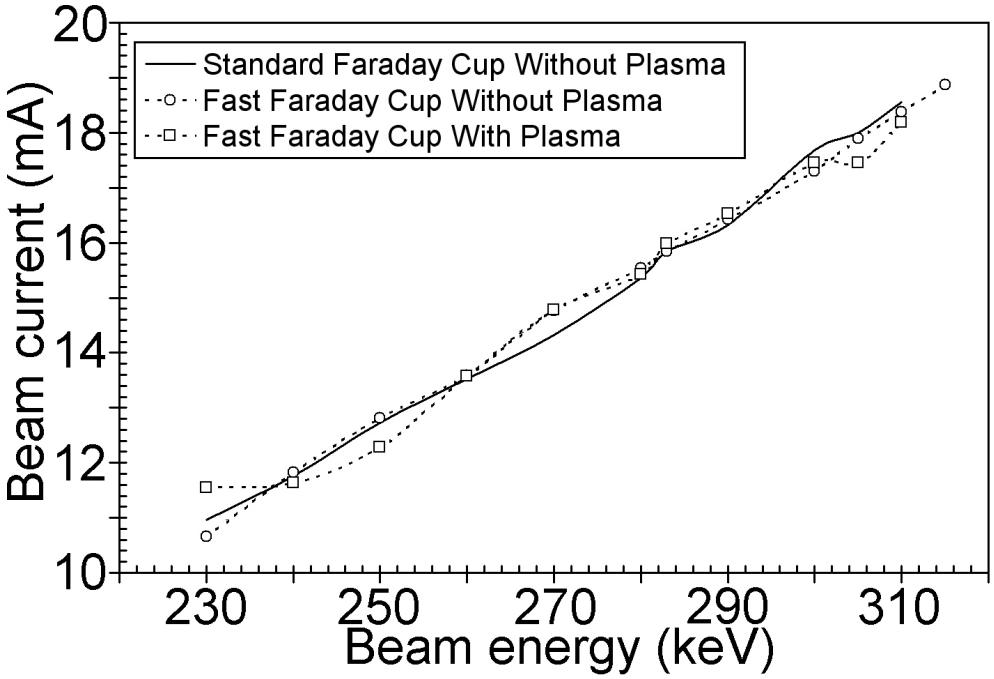

Figure 2.5: Uncompressed ion beam current I_b as a function of beam energy E_0 using the standard Faraday cup without plasma (solid line), fast Faraday cup without plasma (circles), and fast Faraday cup with plasma (squares). As intended, the fast Faraday cup functions reliably in the presence of plasma.

collector plate of the fast Faraday cup and compared to previous measurements using the standard Faraday cup (without plasma present). Very good agreement between the fast and standard Faraday cups is shown in Fig. 2.5 when the (uncompressed) beam current is measured without a background plasma, over a wide range of beam energies. Note this is the only regime where the standard cup accurately measures $I_b(t)$ (it cannot in the presence of plasma, as mentioned earlier). The measurements are repeated with the fast Faraday cup in the presence of plasma, in order to test whether the diagnostic operates properly in such an environment.

Figure 2.5 clearly demonstrates that the fast Faraday cup measures the true $I_b(t)$ magnitude in the presence of plasma. The $V^{3/2}$ voltage dependence of the beam

current for space-charge-limited flow is only slightly noticeable in the figure, due to the small range of beam energies involved. The calibration of the fast Faraday cup is satisfactory since the error is measured to be $< 3\%$ over most of the range, compared to standard Faraday cup measurements (especially at higher energies, where most compression data is taken).

2.4 Longitudinal compression measurements using the fast Faraday cup

In order to compress the ion beam in the longitudinal direction, the time-dependent voltage swing across the $\Delta z = 3$ cm acceleration gap of the linear induction module [Christofilos *et al.*, 1964] is adjusted to create an electric field whose direction is initially in the $-\hat{z}$ direction, and changes polarity to point in the $+\hat{z}$ direction later in time. Therefore, the head of the energetic ion charge bunch is decelerated, and the tail is subsequently accelerated, relative to the initial beam velocity.

A representative voltage waveform $V(t)$ used in experiments, in order to impose an approximately linear velocity tilt on the beam as it passes the gap, is shown in Fig. 2.6. The region of the waveform responsible for longitudinal compression of the charge bunch has a negative $[dV(t)/dt < 0]$ slope in the convention used here (from $t \sim 220 - 550$ ns in Fig 2.6). Positive voltages across the gap correspond to negative axial electric fields in the gap, and negative voltages correspond to the opposite. The shape and slope of the voltage waveform can be appropriately tailored, as they are determined by 12 independently-timed high-power pulse modulators (refer to Appendix A). The timing of the voltage swing relative to the generation of the ion

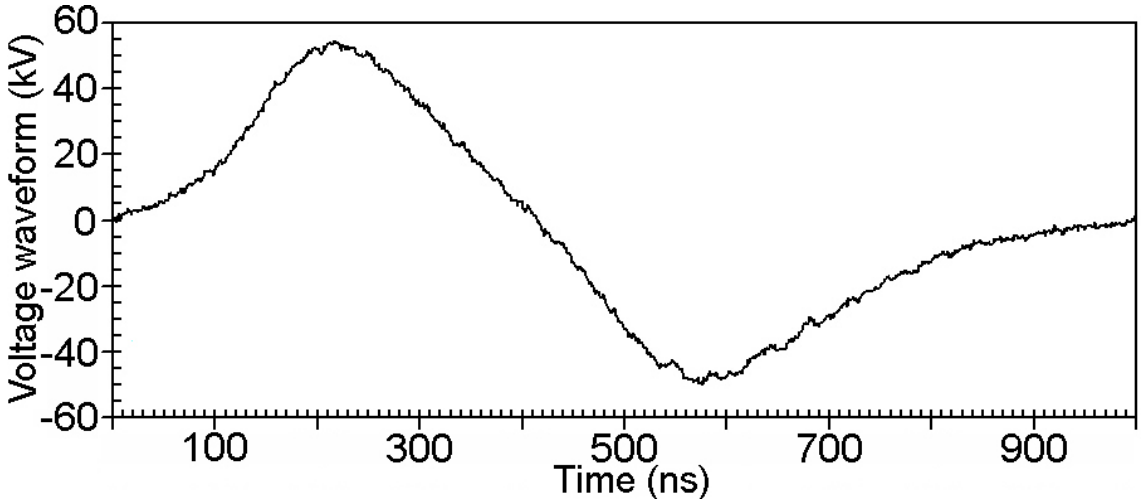

Figure 2.6: Typical voltage waveform $V(t)$ used by the induction module in order to perform neutralized drift compression experiments. The timing is arbitrary.

beam is arbitrary; in practice, a beam of initial pulse length $t_p \sim 5 - 10$ μs is injected into the NDCX device and the timing of the voltage waveform is adjusted so as to "carve out" the central portion of the beam to undergo longitudinal compression.

Once the velocity tilt is imposed, the ion beam drifts through a plasma column until a focal plane in current density J_z is reached between 1 and 2.5 m downstream of the gap (the length of the plasma column is a variable in experiments). Neutralization of the beam's space-charge by plasma is required in order to compress the beam to current densities of interest for warm dense matter, high-energy-density physics, and heavy ion fusion applications. The location of the longitudinal focal plane is determined by the slope of the voltage waveform and the energy of the ion beam.

In these experiments, the voltage waveform is timed to act near the middle 1 μs of the beam's initial pulse length $t_p \sim 6$ μs. The fast Faraday cup is located at the far end of the plasma region such that the longitudinal focal plane coincides with the plane of the collector. The collector plate measures the ion beam current $I_b(t)$, as shown in

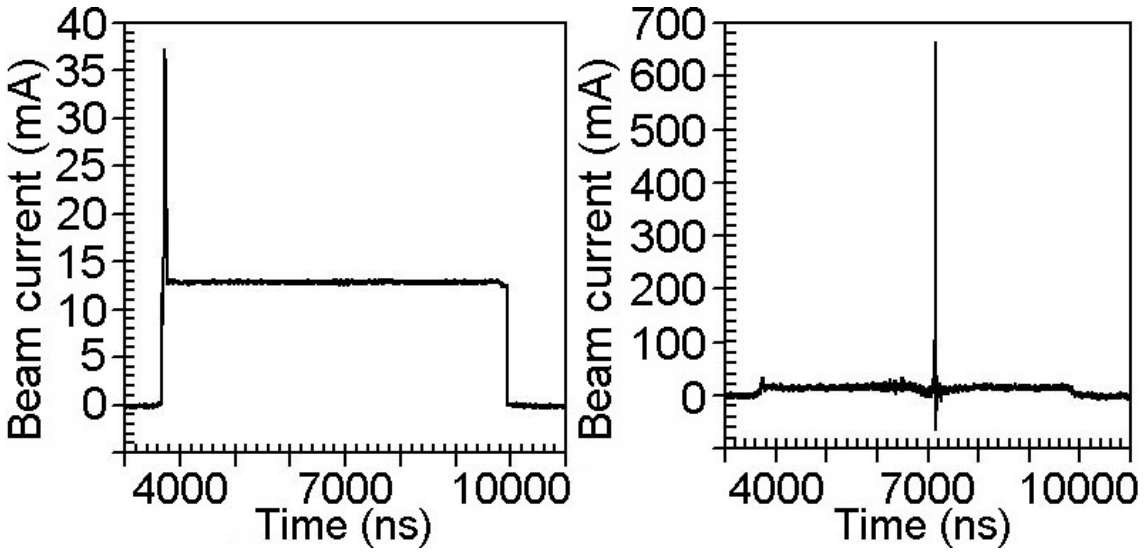

Figure 2.7: An average of 11 shots of uncompressed ion beam current $I_b(t)$ (left) and average of 9 shots of longitudinally compressed $I_b(t)$ over a drift length of approximately $L_d \sim 1.4$ m, showing a compression ratio of 50 (right). Notice the large difference in peak current between the two.

Fig. 2.7. The left plot illustrates the level of noise latent in the uncompressed beam signal once the data is averaged over multiple shots (and accounts for the transmission factor); the right plot is a representative measurement of longitudinal compression occurring due to the imposition of a velocity tilt. The current compression is defined as the ratio of the peak compressed I_b to the uncompressed value (a compression ratio of 50 is shown in Fig. 2.7). Time is measured from the trigger of the voltage pulse on the source injector, so the rise of the signal on the collector plate also measures the transit time of the beam particles from injector to diagnostic. The sharp peak measured early in time is a commonly-seen feature primarily associated with the pile-up of the slower particles in the head of the pulse, created by the finite amount of rise-time in the source voltage; the feature is also associated with effects such as image-current and latent capacitance in the diagnostic.

2.5 Probe modifications and comparison to PIC simulation

Measurements of neutralized drift compression by the fast Faraday cup in the initial experiments [Sefkow *et al.*, 2005b] reveal the need for electronic modifications to ensure faster temporal response by the diagnostic, which must accurately track the beam's fast-rising and fast-falling signal. The probe design under discussion has limited ability to resolve signals on the few ns time scale, due to circuit and construction details, so the fifth key requirement (refer to Sec. 2.2) to accurately measure the beam current $I_b(t)$ is not yet satisfied. Thus, a number of electronic modifications for improving the high-frequency response are investigated. Some of the modifications adopted are similar to those used in probes also requiring ns temporal resolution [Rawnsley, 2000], but are used in different applications [Rawnsley, 2005].

The necessary modifications to the fast "pinhole" Faraday cup diagnostic first described in [Sefkow *et al.*, 2005b] include the following. First, the collector plate's material is changed from stainless steel to copper, and the coaxial cable connection is moved from the circumference of the collector to the center. Both changes lower the effective impedance encountered by the beam signal. Second, a new housing design is employed to increase the distance between the grounded housing and the plates, in order to avoid creating a lumped element capacitance, which deteriorates the response time by increasing the associated time constant. Third, all signal-bearing cables to the three plates are replaced with well-insulated, shielded wires in order to avoid inducing or measurement of high-frequency signals. Fourth, the backplate is coupled to the grounded housing by six $C \sim 50$ nF capacitors in parallel, effectively leaving

the biased backplate at AC ground, in order to ensure isolation from RF signals in the GHz range (and maintain a constant DC bias). Fifth, the coupling box in the circuit between the oscilloscope and diagnostic is modified to reduce its inductance and capacitance, in order to decrease the temporal lag on the beam signal. Sixth, circumferential delrin spacers between the plates are replaced with small teflon washers around the support rods of the probe, in order to further decrease the amount of geometrical capacitance between the frontplate, backplate, and collector. The three plates are required to be close together in order to (1) diminish image-current effects from the ion beam on the collector, (2) achieve the desired electric field strengths for controlling the various charged particle populations, and (3) ensure that the beam doesn't have enough time to decompress under its own space-charge forces before measurement. However, an important side effect is the presence of some latent capacitance in the system due to the geometrical arrangement of the plates. The effect is believed to be one of the limiting factors of this design for measuring sub-ns signals.

In addition, other considerations are also addressed in the fast Faraday cup design. Larger, more closely-spaced holes reduce the signal noise and increase the statistical sampling of the beam, at the cost of higher biases in the probe to control the plasma and secondary behavior, as well as reduced structural integrity of the frontplate and backplate. Due to the spacings of the holes in the frontplate, the question arises as to whether sub-millimeter-scale fluctuations in current are lost to the frontplate and averaged over. Measurements made while the probe is in slightly different vertical positions illustrate that there are no sub-mm fluctuations of importance in the longitudinal compression experiments.

The role of desorbed gas from the frontplate and collector due to ion beam bombardment is also considered, but its effect on the measurement is concluded to be small. The estimated total surface charge density at the focal plane (where the diagnostic resides) for the $t_p \sim 6\,\mu$s of ion charge bunch, with uncompressed initial current $I_b = 0.02$ A and final radius $r_b = 0.3$ cm, is $\sigma < 2.2 \times 10^{-8}$ C cm^{-2} (accounting for the transmission factor). Estimating that approximately 3000 gas molecules are liberated from the collector plate per impacting beam ion and the probe fills with desorbed gas at a flow rate of $v_g \sim 1$ mm/μs [Bieniosek *et al.*, 2005a], the peak gas density is expected to be $n_g < 4 \times 10^{15}$ cm^{-3}. The corresponding gas pressure is approximately 1.5×10^{-4} atm, which is well below the bottom of the Paschen curve ($p \times d = 7.62 \times 10^{-3}$ mm atm), implying that gas breakdown by the applied electric field in the 0.1 cm gap between the backplate and collector is unlikely. Also, the mean free path for beam-gas collisions is estimated to be significantly longer than the 0.2 cm length of the diagnostic, therefore the probability of desorbed gas ionization by incoming beam ions is also small (which would otherwise decrease the beam signal at the collector due to the drawn electron current). Lastly, the small fraction of the beam that is longitudinally compressed to higher current density is only a minor addition to the gas density estimation above, because the compressed pulse is a factor of $< 10^{-3}$ shorter in duration than the original $t_p \sim 6\,\mu$s charge bunch. In support of these estimates, measurements taken with the fast Faraday cup are found to be clear of any detectable gas effects.

In order to test the fast Faraday cup design, a set of longitudinal compression experiments are conducted to achieve a large amount of longitudinal compression with short temporal pulse length. An $E_0 = 320$ keV K^+ beam with initial radius $r_b = 2$

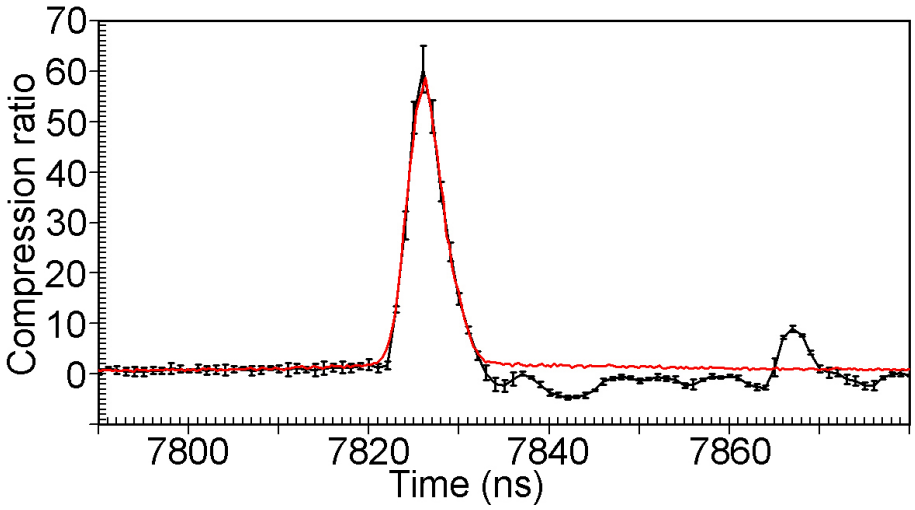

Figure 2.8: (Color) Longitudinal current compression ratio as measured with the fast "pinhole" Faraday cup (black) and simulated using the LSP code (red) [Sefkow *et al.*, 2006].

cm and current $I_0 = 19$ mA [corresponding to a perveance of 4.3×10^{-4}, according to Eq. (1.2)] is injected into the NDCX device. An approximate 15% axial velocity tilt (defined as $\Delta v_b/v_0$) is applied to the beam across the 3 cm acceleration gap, using the voltage waveform shown in Fig. 2.6, and the beam drifts approximately $L_d \sim 2.4$ m through a plasma of density $n_p \sim 10^{10} - 10^{11}$ cm^{-3}. The experimental result in Fig. 2.8 [Sefkow *et al.*, 2006] shows an average of the four best shots measured with the fast Faraday cup at the focal plane, with a range in compression ratios (defined as I_b^{max}/I_0) from 55 to 65. The compressed ion beam signal is normalized to the initial beam current (measured without an applied velocity tilt) and expanded around the location of peak compression in order to show the error bars. The error bars for the experiment are 95% confidence intervals in the mean of the four shots. Ringing reflections are measured in the beam current $I_b(t)$ signal *after* the compressed beam pulse, due to impedance mismatch in the 50Ω circuit.

In order to compare to experiment, the measured voltage waveform from experiment (refer to Fig. 2.6) and beam parameters mentioned in the previous paragraph are used in particle-in-cell simulation, the longitudinal compression result from which is also plotted in Fig. 2.8 [SEFKOW *et al.*, 2006]. In the $2D$ $\{r, z\}$ numerical simulation, the ion beam is initialized approximately $\Delta z = -10$ cm upstream of the acceleration gap with a $T_b = 0.2$ eV Maxwellian temperature in both the transverse and longitudinal directions [corresponding to a normalized effective emittance of 9.3×10^{-3} cm-mrad, according to Eq. (1.1)], and the initial plasma density and temperature are $n_p = 5 \times 10^{10}$ cm^{-3} and $T_p = 3$ eV, respectively. Particle-in-cell simulation predicts a compression ratio of 60 with a full-width, half-maximum pulse length of approximately $t_{fwhm} \sim 4.5$ ns, in excellent agreement with the fast Faraday cup measurement. In addition, the simulated beam reaches a peak on-axis density of approximately $n_b^{foc} \sim 1.8 \times 10^{10}$ cm^{-3} at the focal plane with a minimum radius $(1/e)$ of $r_b \sim 1$ cm. The drift length to the longitudinal focal plane downstream of the gap is approximately $L_d \sim 2.4$ m, and the corresponding overall current density compression factor is approximately 240. Without the plasma present, a compression ratio of only 20 is measured (also in agreement with simulation), largely because the radial electric self-field of the unneutralized beam modifies the charge bunch dynamics over the drift distance: the beam expands radially and is lost to the chamber walls prior to the intended focal plane, where the diagnostics reside.

As will be discussed in Chapter 4, simulations [SEFKOW *et al.*, 2005b] and theory [SEFKOW and DAVIDSON, 2006] illustrate that the shortest achievable pulse lengths of the compressed ion beams in these experiments are limited by the accuracy of the voltage waveform; there exists an ideal voltage waveform (derived in Sec. 4.1)

that would result in the application of an ideal velocity tilt onto the beam, and experimental deviations from that waveform are expected to dominate the minimum achievable pulse length in these experiments. If the beam had an ideal velocity tilt, chromatic aberration due to longitudinal beam temperature effects are expected to dominate the minimum achievable pulse length, as will be discussed in Chapter 4. Other interesting experimental results and simulations pertaining to the Neutralized Drift Compression Experiment, especially as they relate to the need for precise control over the voltage waveform, have been published [Roy *et al.*, 2005b].

2.6 Summary and conclusions

The Neutralized Drift Compression Experiment studies the physical and technological limits of current density compression. In this Chapter, a diagnostic was introduced for the fast and accurate measurement of neutralized drift compression in the laboratory. Since simulations predicted final pulse lengths of a few ns at the longitudinal focal plane, a diagnostic capable of measuring ion beam current, current density, and pulse length with fast temporal resolution needed to be employed, and its development was critical for the success of the experiment.

The standard Faraday cup design commonly used in ion beam experiments was inadequate for measuring longitudinal compression, because of (1) the complex charged particle behavior within such a probe, (2) its inability to differentiate signals due to the compressed charge bunch alone, and (3) its nominally poor temporal resolution (Sec. 2.1). Therefore, the so-called fast "pinhole" Faraday cup was designed and simulated using the LSP particle-in-cell code (Sec. 2.2). Essentially, the diagnostic removed the longitudinally compressing ion beam from the plasma (within 0.2 cm of

the focal plane) by rejecting the plasma from detection at the collector plate using two biased (and aligned) holeplates within the probe; such an arrangement was expected to accurately measure the absolute ion beam current $I_b(t)$ within a plasma environment.

The fast "pinhole" Faraday cup diagnostic was designed, simulated, fabricated, installed, and calibrated successfully in the Neutralized Drift Compression Experiment, and was shown to accurately recover the absolute beam current in the presence of plasma (as intended), where the standard Faraday cup diagnostic failed (Sec. 2.3). Corroborative experiments using an optical system, composed of a scintillator and fast phototube arrangement, verified the integrity of the fast Faraday cup measurements.

Measurements of longitudinal current compression using the fast Faraday cup demonstrated the successful compression of space-charge-dominated ion beams by ratios of final-to-initial current greater than 50 with full-width, half-maximum pulse lengths $t_{fwhm} < 5$ ns in duration (Sec. 2.4). The diagnostic was modified to ensure accurate and fast temporal resolution for further experiments (Sec. 2.5). Sophisticated particle-in-cell simulations involving the measured voltage waveform and beam parameters, and a plasma column satisfying $n_p >> n_b$, were in excellent agreement with data acquired by the fast "pinhole" Faraday cup. Experiments involving an approximate $L_d \sim 2.4$ m drift length revealed a compression ratio of 60 with $t_{fwhm} \sim 4.5$ ns, corresponding to an overall current density compression factor of 240. The presence of the background neutralizing plasma was vital, notably for transverse confinement and compression.

Chapter 3

Theoretical Frameworks

Charged particle beam physics [Davidson and Qin, 2001] has a wide range of applications in modern scientific research, such as nuclear physics, particle physics, coherent radiation generation by intense electron beams, neutron sources, advanced accelerator concepts, pulsed power technology, high-voltage diodes, and inertial fusion energy. Space-charge-dominated beams are characterized by strong electric self-fields and, in the high-current case, strong magnetic self-fields. In particular, the nonlinear effects of intense self-fields produced by space-charge and current play a significant role in the equilibrium, stability, and transport dynamics of a charge bunch. A charged particle beam can exhibit a wide range of collective phenomena such as plasma waves and instabilities, and is a one-component, collisionless nonneutral plasma [Davidson, 2001] when considered in the beam frame. Therefore, much of the literature on laboratory-confined nonneutral plasmas is directly relevant to the study of intense charged particle beam propagation.

In order better understand laboratory observations and measurements, and to predict or explain new phenomena, theory, simulation, and experiment should be

coupled and complement one another. Therefore, theory and numerical simulation support offer insight into present experimental efforts in the Neutralized Drift Compression Experiment, as well as provide guidance for future experiments. The challenge for theoretical models is to realistically and tractably describe the important physics in associated experiments. Substantial progress has been made surrounding the theory of longitudinal bunch compression, including the development of a $3D$ kinetic formalism for neutralized drift compression and transverse focusing based on the Vlasov equation [Davidson and Qin, 2005], as well as macroscopic fluid models [Davidson and Qin, 2001] for pulse shaping [Qin and Davidson, 2002a] and final focusing [Qin and Davidson, 2002b, Qin *et al.*, 2004] within the context of unneutralized drift compression. However, much of the theoretical work on intense beam propagation relied on many idealized assumptions about the uniformity and symmetry of the ion beam and its dynamics. Therefore, in order to increase the sophistication of models for comparison with measurements, a number of experimental conditions need to be integrated into theoretical descriptions of neutralized drift compression, such as the effects of non-ideal voltage waveforms, finite acceleration gap size, finite beam temperature, partial beam neutralization by the background plasma, and plasma temperature. Each of these effects give rise to unwanted consequences, such as increased pulse lengths at focus, focal plane smearing, and reduced compression factors (both in the transverse and longitudinal directions).

The technique of particle-in-cell (PIC) simulation has been the primary computational tool for self-consistently including all of the aforementioned realistic effects into one model for comparison to neutralized drift compression experiments. A PIC code [Birdsall and Langdon, 1985] simulates the evolution of the full distribution

functions of all simulated species for given boundary and initial conditions, and is an invaluable resource for computational plasma physicists. However, such simulations are generally noisy and require large amounts of computation time in order to accurately model the physics on large-space scales (few m, or more) and long-time scales (few μs, or more). In addition, large plasma densities and magnetic fields can lead to prohibitively small time steps in traditional explicit PIC simulations because of the need to resolve fast phenomena occurring at the electron plasma frequency ω_{pe} and the electron cyclotron frequency ω_{ce}, which can both exceed 10^{12} rad s^{-1} (implying sub-ps time steps) in some parameter regimes of interest. Implicit techniques typically allow the under-resolution of one of the frequencies, but not both simultaneously. Therefore, even modest magnetic field values can hinder the use of a larger time step which would allow implicit PIC simulations to compete with other reduced numerical models in terms of required computational resources.

In describing beam compression experiments, previous theoretical models of intense charge bunch propagation are expanded upon by accounting for some of the non-ideal experimental parameters. Specifically, the ion beam has nonuniform and asymmetric density and axial flow velocity profiles, and propagates through a background plasma which incompletely ($< 100\%$) neutralizes the beam charge and current. Reduced theoretical models of experimental results provide valuable insights into the physical and technological limitations of neutralized drift compression, and provide guidance for future experiments. However, PIC simulations are also employed, not only for comparison to the reduced models, but to contribute to the forefront of ion beam compression research in regimes that require the advanced kinetic description.

This Chapter provides descriptions of the underlying theoretical frameworks for

the models which are employed in the next Chapter to investigate a number of realistic conditions found in neutralized drift compression experiments. Kinetic theory is used in Sec. 3.1 to derive the Klimontovich equation, plasma kinetic equation, and the Vlasov equation. In Sec. 3.2, moments of the Vlasov equation are evaluated and a macroscopic warm-fluid description is derived for the self-consistent evolution of charged particle beam parameters. An introduction to the basic methods and algorithms used in the LSP code for numerical PIC simulations is given in Sec. 3.3. A brief summary and discussion of the numerical models is provided in Sec. 3.4.

3.1 Kinetic theory

Kinetic theory attempts to take into account the motion of all the constituent particles involved. An exact kinetic description of a plasma consists of either the Klimontovich or Liouville equations, together with Maxwell's equations and the Lorentz force equations for the individual particle motion. The models incorporate both discrete particle effects and collective interactions, providing a complete classical description of the system. Such formalisms contain all of the exact six-dimensional orbits of each individual particle, insofar as the positions and velocities of all particles can be known exactly at one time, and therefore are far more complicated than needed. However, in order to extract useful information from generally intractable equations, the derivation of reduced statistical descriptions using appropriate approximations is desired [Nicholson, 1983]. In such an approach, the exact motion of all the particles in a plasma is replaced by ascertaining the evolution of average statistical properties.

Consider the particle orbits $\mathbf{X}(t)$ and $\mathbf{V}(t)$ in three-dimensional configuration space $\mathbf{x}$ and three-dimensional velocity space $\mathbf{v}$, respectively, the combination of which

represents the six-dimensional phase space occupied by a point particle with charge and mass at successive times t. The $\mathbf{x}$ and $\mathbf{v}$ are the Eulerian coordinates of the phase space, whereas $\mathbf{X}(t)$ and $\mathbf{V}(t)$ are the Lagrangian coordinates of the particle. The microscopic phase space density of species j is

$$N_j(\mathbf{x}, \mathbf{v}, t) = \sum_{i=1}^{N_0} \delta[\mathbf{x} - \mathbf{X}_i(t)] \, \delta[\mathbf{v} - \mathbf{V}_i(t)] \, , \tag{3.1}$$

where δ is the Dirac delta function, and N_0 is the total number of particles for species j. The total system density is a sum over the phase space density for each species.

The exact classical particle orbits can be determined for all later times, if given the exact classical positions and velocities of each particle at one particular time, according to the equations

$$\frac{d}{dt}\mathbf{X}_i(t) = \mathbf{V}_i(t) \tag{3.2}$$

$$m_j \, \frac{d}{dt}\mathbf{V}_i(t) = q_j \, \mathbf{E}^m[\mathbf{X}_i(t), t] + \frac{q_j}{c} \, \mathbf{V}_i(t) \times \mathbf{B}^m[\mathbf{X}_i(t), t] \, , \tag{3.3}$$

where q_j and m_j are the charge and mass of particle species j, and $\mathbf{E}^m$ and $\mathbf{B}^m$ are the self-consistent microscopic electric and magnetic fields resulting from the charge and current of all the other point particles (excluding particle i) along with any externally applied fields. The microscopic electromagnetic fields in Eq. (3.3) must satisfy Maxwell's relations [Griffiths, 1998]

$$\nabla \cdot \mathbf{E}^m(\mathbf{x}, t) = 4\pi\rho^m(\mathbf{x}, t) + 4\pi\rho_{ext}(\mathbf{x}, t) \tag{3.4}$$

$$\nabla \cdot \mathbf{B}^m(\mathbf{x}, t) = 0 \tag{3.5}$$

$$\nabla \times \mathbf{E}^m(\mathbf{x}, t) = -\frac{1}{c} \frac{\partial B^m(\mathbf{x}, t)}{\partial t} \tag{3.6}$$

$$\nabla \times \mathbf{B}^m(\mathbf{x}, t) = \frac{4\pi}{c} \mathbf{J}^m(\mathbf{x}, t) + \frac{4\pi}{c} \mathbf{J}_{ext}(\mathbf{x}, t) + \frac{1}{c} \frac{\partial \mathbf{E}^m(\mathbf{x}, t)}{\partial t} \,, \tag{3.7}$$

where the microscopic charge density and current (summed over species) are

$$\rho^m(\mathbf{x}, t) = \sum_j q_j \int d\mathbf{v} \; N_j(\mathbf{x}, \mathbf{v}, t) \tag{3.8}$$

$$\mathbf{J}^m(\mathbf{x}, t) = \sum_j q_j \int d\mathbf{v} \; \mathbf{v} \; N_j(\mathbf{x}, \mathbf{v}, t) \,, \tag{3.9}$$

and $\rho_{ext}(\mathbf{x}, t)$ and $\mathbf{J}_{ext}(\mathbf{x}, t)$ are the external charge and current densities, respectively. The closed set of Eqs. (3.2) through (3.9) yield the exact particle orbits and fields in terms of one another. Therefore, if the positions and velocities of all particles and fields are exactly known (in the classical sense) at one particular time, they can be completely and self-consistently determined for all later times.

The evolution of the plasma is evaluated by taking the time derivative of the phase space density $N_j(\mathbf{x}, \mathbf{v}, t)$ in Eq. (3.1) and using Eqs. (3.2) and (3.3) in order

to eliminate $d\mathbf{X}_i(t)/dt$ and $d\mathbf{V}_i(t)/dt$, resulting in [NICHOLSON, 1983]

$$\frac{\partial N_j(\mathbf{x},\mathbf{v},t)}{\partial t} = -\sum_{i=1}^{N_0} \mathbf{V}_i(t)\cdot\nabla_x\,\delta[\mathbf{x}-\mathbf{X}_i(t)]\,\delta[\mathbf{v}-\mathbf{V}_i(t)] - \sum_{i=1}^{N_0}\left\{\frac{q_j}{m_j}\,\mathbf{E}^m[\mathbf{X}_i(t),t] + \frac{q_j}{m_j c}\,\mathbf{V}_i(t)\times\mathbf{B}^m[\mathbf{X}_i(t),t]\right\} \cdot\nabla_v\,\delta[\mathbf{x}-\mathbf{X}_i(t)]\,\delta[\mathbf{v}-\mathbf{V}_i(t)]\,, \tag{3.10}$$

where $\nabla_x \equiv (\delta_x, \delta_y, \delta_z)$ and $\nabla_v \equiv (\delta_{v_x}, \delta_{v_y}, \delta_{v_z})$. Using the Dirac delta function identity $a\,\delta(a-b) = b\,\delta(a-b)$ and Eq. (3.1) again enables the recovery of the Klimontovich equation [KLIMONTOVICH, 1967]

$$\left\{\frac{\partial}{\partial t} + \mathbf{v}\cdot\nabla_x + \frac{q_j}{m_j}\,\left[\mathbf{E}^m(\mathbf{x},t) + \frac{\mathbf{v}}{c}\times\mathbf{B}^m(\mathbf{x},t)\right]\cdot\nabla_v\right\}\,N_j(\mathbf{x},\mathbf{v},t) = 0\,, \tag{3.11}$$

and, with Maxwell's equations [Eqs. (3.4) through (3.7)], constitutes the exact *Klimontovich-Maxwell* description of a plasma. The convective derivative of any quantity along an orbit in phase space includes the time variation of the quantity as well as that produced by the changing position in phase space according to

$$\frac{D}{Dt} \equiv \frac{\partial}{\partial t} + \frac{d\mathbf{x}}{dt}\cdot\nabla_{\mathbf{x}} + \frac{d\mathbf{v}}{dt}\cdot\nabla_{\mathbf{v}}\,, \tag{3.12}$$

where $d\mathbf{x}/dt$ and $d\mathbf{v}/dt$ refer to the change in position and velocity of a hypothetical test particle. Equations analogous to Eqs. (3.2) and (3.3) with $\mathbf{X}_i(t)$ and $\mathbf{V}_i(t)$ replaced by $\mathbf{x}$ and $\mathbf{v}$, respectively, allow the Klimontovich equation to be rewritten

$$\frac{D}{Dt}N_j(\mathbf{x},\mathbf{v},t) = 0\,. \tag{3.13}$$

The conclusion from Eq. (3.13) is simple: the microscopic phase space density of all particles composed of species j is conserved in time, as measured along their orbits. Equation (3.13) is a continuity equation for $N_j(\mathbf{x}, \mathbf{v}, t)$, which expresses the incompressibility of it in phase space, such that it is neither created nor destroyed.

In reality, complete determination of the charged particle dynamics using the aforementioned procedure is too arduous for even the most advanced numerical methods at this time. Average values of the plasma properties over many interparticle spacings, rather than accumulation of the exact single particle orbits for all species, are very useful however, and so the Klimontovich equation is a starting point for deriving other approximations to describe kinetic behavior. Rather than dealing with the discrete function $N_j(\mathbf{x}, \mathbf{v}, t)$, a function representing a probability density function, or smooth *distribution function*, of particles of species j within a unit volume $\Delta\mathbf{x}\ \Delta\mathbf{v}$ of phase space can be written as

$$f_j(\mathbf{x}, \mathbf{v}, t) \equiv \langle N_j(\mathbf{x}, \mathbf{v}, t) \rangle \ , \tag{3.14}$$

where the $\langle\ \rangle$ stands for a statistical ensemble averaging procedure [Reif, 1965].

By ensemble averaging, the time rate of change of the distribution function $f_j(\mathbf{x}, \mathbf{v}, t)$ can be determined from the Klimontovich equation, after defining fluctuations in the phase space density and fields according to [Davidson and Qin, 2001]

$$N_j(\mathbf{x}, \mathbf{v}, t) = f_j(\mathbf{x}, \mathbf{v}, t) + \delta N_j(\mathbf{x}, \mathbf{v}, t) \tag{3.15}$$

$$\mathbf{E}^m(\mathbf{x}, t) = \mathbf{E}(\mathbf{x}, t) + \delta\mathbf{E}(\mathbf{x}, t) \tag{3.16}$$

$$\mathbf{B}^m(\mathbf{x}, t) = \mathbf{B}(\mathbf{x}, t) + \delta\mathbf{B}(\mathbf{x}, t) \ , \tag{3.17}$$

where $\mathbf{E}(\mathbf{x},t) \equiv \langle \mathbf{E}^m(\mathbf{x},t) \rangle$ and $\mathbf{B}(\mathbf{x},t) \equiv \langle \mathbf{B}^m(\mathbf{x},t) \rangle$, since the ensemble-averaged relative fluctuations vanish $[\langle \delta N_j(\mathbf{x},\mathbf{v},t) \rangle = \langle \delta \mathbf{E}(\mathbf{x},t) \rangle = \langle \delta \mathbf{B}(\mathbf{x},t) \rangle = 0]$. The insertion of Eqs. (3.15) through (3.17) into Eq. (3.11), and subsequent ensemble averaging of the result, derives the exact form of the plasma kinetic equation

$$\left\{ \frac{\partial}{\partial t} + \mathbf{v} \cdot \nabla_{\mathbf{x}} + \frac{q_j}{m_j} \left[\mathbf{E}(\mathbf{x},t) + \frac{\mathbf{v}}{c} \times \mathbf{B}(\mathbf{x},t) \right] \cdot \nabla_{\mathbf{v}} \right\} f_j(\mathbf{x},\mathbf{v},t) = \\ -\frac{q_j}{m_j} \left\langle \left[\delta \mathbf{E}(\mathbf{x},t) + \frac{\mathbf{v}}{c} \times \delta \mathbf{B}(\mathbf{x},t) \right] \cdot \nabla_{\mathbf{v}} \, \delta N_j(\mathbf{x},\mathbf{v},t) \right\rangle . \tag{3.18}$$

The left side of Eq. (3.18), which varies smoothly in phase space as a function of $\mathbf{x}$ and $\mathbf{v}$, is not sensitive to discrete plasma particle effects, and represents the importance of collective effects. On the other hand, the right side of Eq. (3.18) is the ensemble average, is sensitive to discrete plasma particle effects, and represents the importance of collisional effects. In many instances, collisional effects can be neglected, resulting in the important equation in plasma physics known as the collisionless Boltzmann equation, or as the nonlinear Vlasov equation [Vlasov, 1945]

$$\left\{ \frac{\partial}{\partial t} + \mathbf{v} \cdot \nabla_{\mathbf{x}} + \frac{q_j}{m_j} \left[\mathbf{E}(\mathbf{x},t) + \frac{\mathbf{v}}{c} \times \mathbf{B}(\mathbf{x},t) \right] \cdot \nabla_{\mathbf{v}} \right\} f_j(\mathbf{x},\mathbf{v},t) = 0 . \tag{3.19}$$

Here, the average fields satisfy the corresponding versions of Maxwell's equations

$$\nabla \cdot \mathbf{E}(\mathbf{x},t) = 4\pi \rho(\mathbf{x},t) + 4\pi \rho_{ext}(\mathbf{x},t) \tag{3.20}$$

$$\nabla \cdot \mathbf{B}(\mathbf{x},t) = 0 \tag{3.21}$$

$$\nabla \times \mathbf{E}(\mathbf{x},t) = -\frac{1}{c}\,\frac{\partial \mathbf{B}(\mathbf{x},t)}{\partial t} \tag{3.22}$$

$$\nabla \times \mathbf{B}(\mathbf{x},t) = \frac{4\pi}{c}\,\mathbf{J}(\mathbf{x},t) + \frac{4\pi}{c}\,\mathbf{J}_{ext}(\mathbf{x},t) + \frac{1}{c}\,\frac{\partial \mathbf{E}(\mathbf{x},t)}{\partial t}\,, \tag{3.23}$$

and the ensemble-averaged charge density and current (summed over species) are

$$\rho(\mathbf{x},t) \equiv \langle \rho^m \rangle = \sum_j q_j \int d\mathbf{v}\; f_j(\mathbf{x},\mathbf{v},t) \tag{3.24}$$

$$\mathbf{J}(\mathbf{x},t) \equiv \langle \mathbf{J}^m \rangle = \sum_j q_j \int d\mathbf{v}\; \mathbf{v}\; f_j(\mathbf{x},\mathbf{v},t). \tag{3.25}$$

The system of Eqs. (3.19) through (3.25) are collectively referred to as the *Vlasov-Maxwell description* of a plasma, which retains the effects of collective interactions in low-collisionality plasmas, and is analytically tractable. The Vlasov equation strictly only applies to an ensemble average of many plasmas, but yields valid predictions for a single plasma in practice because fluctuations are usually small, due to the large number of particles comprising an individual system [Nicholson, 1983].

The primary difference between the Vlasov-Maxwell and Klimontovich-Maxwell equations is that the distribution function $f_j(\mathbf{x},\mathbf{v},t)$ is a smooth probability density in phase space, whereas the microscopic phase space density $N_j(\mathbf{x},\mathbf{v},t)$ is a singular function. Evaluation of the latter requires the determination of all of the particle orbits $\mathbf{X}_i(t)$ and $\mathbf{V}_i(t)$ in the presence of the self-consistently calculated electric and magnetic fields. The fields in the former framework correspond to the average electric and magnetic fields due to collective interactions. As mentioned earlier, the two

descriptions are intimately related via a statistical averaging procedure, denoted by $f_j(\mathbf{x}, \mathbf{v}, t) = \langle N_j(\mathbf{x}, \mathbf{v}, t) \rangle$. In much the same way as the Klimontovich equation can be rewritten into the form of Eq. (3.13), so can the Vlasov equation be rewritten as

$$\frac{D}{Dt} f_j(\mathbf{x}, \mathbf{v}, t) = 0, \tag{3.26}$$

which implies the conservation of the probability density function, and also that any f_j constructed out of functions that are constants of the motion of the individual particle orbits are solutions to the Vlasov equation [Nicholson, 1983].

The Vlasov-Maxwell description of a plasma is a reduced statistical description of the Klimontovich-Maxwell equations and is widely used to study the equilibrium and stability properties of intense charged particle beams, as well as other plasma systems in the collisionless regime. Indeed, the Vlasov-Maxwell equations self-consistently evolve the smooth probability density function of a plasma under the influence of its self-generated long-range electric and magnetic fields resulting from the average charge and current densities, respectively, as well as any externally applied fields. Therefore, the main contribution to the interparticle interaction in low-collisionality plasmas is present in the Vlasov-Maxwell description, which provides a realistic and tractable model of a collisionless plasma [Goldston and Rutherford, 1995]. In addition, global (spatially-averaged) conservation relations for number, momentum, and energy can be derived from the Vlasov-Maxwell equations for the nonneutral charged particle system when collisions, recombination, ionization, and particle losses from the system are neglected, and assuming that the system is isolated from physical contact with the surrounding enclosure [Davidson and Qin, 2001].

3.2 Macroscopic warm-fluid model

Use of the Vlasov kinetic theory to perform analytical studies of charged particle motion is a valuable tool, however, it becomes quite complex under even idealized conditions. The macroscopic warm-fluid description for charged particle beam dynamics is a continuum approximation, derived by evaluating velocity moments of the nonlinear Vlasov equation [Lund and Davidson, 1998]. Closure of the system of equations in the present analysis is achieved by assuming that heat flow is negligible between the beam and its surroundings and by ignoring the higher-order moments. The resulting approximate equations form a closed description of the nonrelativistic bulk fluid properties, the dynamics of which are reversible as well as isentropic; the extension to a relativistic framework is straightforward.

The advantage of the fluid approach, which averages over velocity space contributions to the kinetic distribution function and reduces the phase space to three spatial dimensions, is its simplicity compared to the Vlasov theory. By taking velocity moments of the nonlinear Vlasov equation [Eq. (3.19)], an infinite hierarchy of fluid equations describing the self-consistent evolution of local macroscopic variables can be derived [Davidson, 2001]. Since each fluid equation depends on the equation of immediately higher order, some kind of truncation, or closure, of the infinite system of equations is required in order to obtain a fluid theory. The closure may take many forms, each of which has associated implications on the characteristics of the fluid flow. The model is more approximate than the kinetic theory, since velocity-dependent effects (*e.g.* Landau damping) are clearly lost in the fluid framework.

As derived in Sec. 3.1, the nonlinear Vlasov equation is [Vlasov, 1945]

$$\left\{ \frac{\partial}{\partial t} + \mathbf{v} \cdot \nabla_{\mathbf{x}} + \frac{q_j}{m_j} \left[\mathbf{E}(\mathbf{x},t) + \frac{\mathbf{v}}{c} \times \mathbf{B}(\mathbf{x},t) \right] \cdot \nabla_{\mathbf{v}} \right\} f_j(\mathbf{x},\mathbf{v},t) = 0 \, , \tag{3.27}$$

and the electromagnetic fields are the macroscopic, ensemble-averaged fields. For simplicity, the present approach invokes the nonrelativistic and electrostatic approximations, and inductive electric fields and magnetic self-fields are ignored; the electric self-fields satisfy $\mathbf{E}_j^s(\mathbf{x},t) = -\nabla_{\mathbf{x}} \, \phi_j^s(\mathbf{x},t)$, where $\phi_j^s(\mathbf{x},t)$ is the electrostatic self-field potential. In such a case, $\phi_j^s(\mathbf{x},t)$ needs to be self-consistently determined from the distribution function according to Poisson's equation

$$\nabla_{\mathbf{x}}^2 \phi_j^s(\mathbf{x},t) = -4\pi q_j \int d\mathbf{v} \; f_j(\mathbf{x},\mathbf{v},t). \tag{3.28}$$

Therefore, the distribution function in Eq. (3.27) interacts with the total electric field

$$\nabla \cdot \mathbf{E}(\mathbf{x},t) = -\sum_j \nabla_{\mathbf{x}}^2 \, \phi_j^s(\mathbf{x},t) + 4\pi \rho_{ext}(\mathbf{x},t) \, , \tag{3.29}$$

along with any externally applied magnetic field

$$\nabla \times \mathbf{B}(\mathbf{x},t) = \frac{4\pi}{c} \, \mathbf{J}_{ext}(\mathbf{x},t). \tag{3.30}$$

The integral of the distribution function over all of velocity space (the zeroth-order velocity moment) defines the particle number density of species j

$$n_j(\mathbf{x},t) \equiv \int d\mathbf{v} \; f_j(\mathbf{x},\mathbf{v},t). \tag{3.31}$$

In addition, the mean fluid velocity of species j is determined by the first-order velocity moment of the nonlinear Vlasov equation

$$\mathbf{v}_j(\mathbf{x},t) \equiv \frac{1}{n_j(\mathbf{x},t)} \int d\mathbf{v}\ \mathbf{v}\ f_j(\mathbf{x},\mathbf{v},t). \tag{3.32}$$

Operating on the Vlasov equation with $\int d\mathbf{v}$ yields the continuity equation

$$\frac{\partial}{\partial t} n_j(\mathbf{x},t) + \nabla_{\mathbf{x}} \cdot [n_j(\mathbf{x},t)\ \mathbf{v}_j(\mathbf{x},t)] = 0. \tag{3.33}$$

Equation (3.30) expresses that fluid elements are neither created nor destroyed, such that the density can only increase or decrease at one particular location if a net amount of fluid enters or leaves the elemental spatial volume including that location. Operating on the Vlasov equation with $\int d\mathbf{v}\ \mathbf{v}$ yields the momentum balance equation

$$\begin{aligned} m_j\ n_j(\mathbf{x},t) \left[\frac{\partial}{\partial t} + \mathbf{v}_j(\mathbf{x},t) \cdot \nabla_{\mathbf{x}} \right] \mathbf{v}_j(\mathbf{x},t) + \nabla_{\mathbf{x}} \cdot \mathbf{P}_j(\mathbf{x},t) = \\ q_j\ n_j(\mathbf{x},t) \left[\mathbf{E}(\mathbf{x},t) + \frac{\mathbf{v}_j(\mathbf{x},t)}{c} \times \mathbf{B}(\mathbf{x},t) \right], \end{aligned} \tag{3.34}$$

where use has been made of the definition for the pressure tensor of species j

$$\mathbf{P}_j(\mathbf{x},t) \equiv n_j(\mathbf{x},t)\ \mathbf{T}_j(\mathbf{x},t) = m_j \int d\mathbf{v}\ [\mathbf{v} - \mathbf{v}_j(\mathbf{x},t)][\mathbf{v} - \mathbf{v}_j(\mathbf{x},t)]\ f_j(\mathbf{x},\mathbf{v},t). \tag{3.35}$$

The momentum balance equation is simply Newton's second law of motion for the forces applied to a fluid element. The continuity and momentum balance equations are the first two equations of the macroscopic warm-fluid model, resulting from evaluation of the zeroth- and first-order velocity moments of the nonlinear Vlasov equation.

For a macroscopic cold-fluid description of charged particle systems, the pressure-gradient term in neglected, or $\nabla_{\mathbf{x}} \cdot \mathbf{P}_j(\mathbf{x},t) \approx 0$ in the momentum balance equation [Eq. (3.34)], and the system of equations to this point is complete. However, if the inclusion of finite beam temperature (emittance) effects are desired, then the term needs to be retained and the second-order velocity moment of the nonlinear Vlasov equation has to be evaluated [Davidson, 2001]. Indeed, there are few cases in the literature where thermal effects are included in a self-consistent manner. Operating on the Vlasov equation with $\int d\mathbf{v}\,\mathbf{v}\,\mathbf{v}$ yields the energy balance equation

$$\begin{aligned}\frac{\partial}{\partial t}\mathbf{P}_j(\mathbf{x},t) + \nabla_{\mathbf{x}} \cdot [\mathbf{v}_j(\mathbf{x},t)\,\mathbf{P}_j(\mathbf{x},t)] + \mathbf{P}_j(\mathbf{x},t) \cdot [\nabla_{\mathbf{x}}\,\mathbf{v}_j(\mathbf{x},t)] \\ +[\nabla_{\mathbf{x}}\,\mathbf{v}_j(\mathbf{x},t)]^T \cdot \mathbf{P}_j(\mathbf{x},t) + \nabla_{\mathbf{x}} \cdot \mathbf{Q}_j(\mathbf{x},t) = \\ \frac{q_j}{m_j c}\left[\mathbf{P}_j(\mathbf{x},t) \times \mathbf{B}(\mathbf{x},t) - \mathbf{B}(\mathbf{x},t) \times \mathbf{P}_j(\mathbf{x},t)\right], \end{aligned} \tag{3.36}$$

where $[\ ]^T$ denotes dyadic transpose and use has been made of the definition for the heat flow tensor of species j

$$\mathbf{Q}_j(\mathbf{x},t) \equiv m_j \int d\mathbf{v}\,[\mathbf{v} - \mathbf{v}_j(\mathbf{x},t)][\mathbf{v} - \mathbf{v}_j(\mathbf{x},t)][\mathbf{v} - \mathbf{v}_j(\mathbf{x},t)]\,f_j(\mathbf{x},\mathbf{v},t). \tag{3.37}$$

Note that the continuity equation [Eq. (3.33)] is coupled through the flow velocity to the momentum balance equation [Eq. (3.34)], which is itself coupled through the pressure tensor to the energy balance equation [Eq. (3.36)].

The hierarchy of equations is truncated when an approximation is made in order to decouple the last equation from further equations. The chain of moment equations is closed at this point by making an assumption regarding the form of the heat flow tensor $\mathbf{Q}_j(\mathbf{x},t)$. To avoid dealing with the heat flow tensor explicitly, it is ignored

as negligibly small. Average thermal effects are incorporated into the model via the pressure tensor, which self-consistently evolves according to the energy balance equation [Eq. (3.36)] in the absence of heat flow, or $\nabla_{\mathbf{x}} \cdot \mathbf{Q}_j(\mathbf{x}, t) \approx 0$, described by

$$\begin{aligned} &\frac{\partial}{\partial t}\mathbf{P}_j(\mathbf{x}, t) + \nabla_{\mathbf{x}} \cdot [\mathbf{v}_j(\mathbf{x}, t)\, \mathbf{P}_j(\mathbf{x}, t)] \\ &+\mathbf{P}_j(\mathbf{x}, t) \cdot [\nabla_{\mathbf{x}}\, \mathbf{v}_j(\mathbf{x}, t)] + [\nabla_{\mathbf{x}}\, \mathbf{v}_j(\mathbf{x}, t)]^T \cdot \mathbf{P}_j(\mathbf{x}, t) = \\ &\frac{q_j}{m_j c}\, [\mathbf{P}_j(\mathbf{x}, t) \times \mathbf{B}(\mathbf{x}, t) - \mathbf{B}(\mathbf{x}, t) \times \mathbf{P}_j(\mathbf{x}, t)]. \end{aligned} \tag{3.38}$$

Note that $\nabla_{\mathbf{x}} \cdot \mathbf{Q}_j(\mathbf{x}, t) \approx 0$ is strictly justified when $f_j(\mathbf{x}, \mathbf{v}, t)$ is an even function of $[\mathbf{v} - \mathbf{v}_j(\mathbf{x}, t)]$.

The continuity equation [Eq. (3.33)], momentum balance equation [Eq. (3.34), also known as the equation of motion], energy balance equation [Eq. (3.38), also known as the equation of state], Poisson's equation [Eq. (3.28)], and the appropriate boundary and initial conditions form a closed system of macroscopic equations that describe the self-consistent evolution of the particle density, average flow velocity, average pressure tensor, and electrostatic potential, respectively. The energy balance equation can be simplified in the strong-focusing approximation by assuming that $[\mathbf{P}_j(\mathbf{x}, t) \times \mathbf{B}(\mathbf{x}, t) \approx \mathbf{B}(\mathbf{x}, t) \times \mathbf{P}_j(\mathbf{x}, t)]$ to the lowest order, which is the case when the external magnetic pressure is larger in magnitude than the internal pressure of the charged particle system. The assumption implies that the pressure tensor $\mathbf{P}_j(\mathbf{x}, t)$ is of the diagonal form [Davidson, 2001]

$$\mathbf{P}_j(\mathbf{x}, t) = P_{j\perp}(\mathbf{x}, t)(\mathbf{I} - \hat{\mathbf{b}}\hat{\mathbf{b}}) + P_{j\parallel}(\mathbf{x}, t)\hat{\mathbf{b}}\hat{\mathbf{b}}\,, \tag{3.39}$$

where $\mathbf{I}$ is the unit dyadic and $\hat{\mathbf{b}} = \mathbf{B}(\mathbf{x}, t)/|\mathbf{B}(\mathbf{x}, t)|$ is the unit vector along the

magnetic field. Equation (3.38) then reduces to two equations of state for the perpendicular ($P_{j\perp}$) and parallel ($P_{j\parallel}$) pressures [LUND and DAVIDSON, 1998]

$$\left[\frac{\partial}{\partial t} + \mathbf{v}_j(\mathbf{x},t)\cdot\nabla_{\mathbf{x}}\right] P_{j\perp}(\mathbf{x},t) + 2\,P_{j\perp}(\mathbf{x},t)\,\nabla_{\mathbf{x}}\cdot\mathbf{v}_j(\mathbf{x},t) - P_{j\perp}(\mathbf{x},t)\,\nabla_{\mathbf{x}}^{\hat{\mathbf{b}}}\left[\hat{\mathbf{b}}\cdot\mathbf{v}_j(\mathbf{x},t)\right] = 0 \tag{3.40}$$

$$\left[\frac{\partial}{\partial t} + \mathbf{v}_j(\mathbf{x},t)\cdot\nabla_{\mathbf{x}}\right] P_{j\parallel}(\mathbf{x},t) + P_{j\parallel}(\mathbf{x},t)\,\nabla_{\mathbf{x}}\cdot\mathbf{v}_j(\mathbf{x},t) + 2\,P_{j\parallel}(\mathbf{x},t)\,\nabla_{\mathbf{x}}^{\hat{\mathbf{b}}}\left[\hat{\mathbf{b}}\cdot\mathbf{v}_j(\mathbf{x},t)\right] = 0\,, \tag{3.41}$$

where $\nabla_{\mathbf{x}}^{\hat{\mathbf{b}}}$ is the gradient component along the magnetic field and $\hat{\mathbf{b}}\cdot\mathbf{v}_j(\mathbf{x},t)$ is the flow velocity component along the magnetic field. The equations of state Eqs. (3.40) and (3.41) can be derived without the strong-focusing approximation because the assumption that the pressure tensor is of diagonal form and isotropic in the plane perpendicular to the magnetic field can also be invoked in an *ad hoc* manner. It should also be noted that the right-hand side of the energy balance equation is zero in the absence of any externally applied magnetic fields (assuming the magnetic self-fields are still ignored), and the equations of state for the perpendicular and parallel pressure are recovered if the *ad hoc* assumption about the pressure tensor is made.

The warm-fluid model forms a coupled, nonlinear partial differential equation system that can be solved without the use of macroparticles. Its adoption for certain problems can yield numerical results which are less noisy, provide more stability, are computationally efficient, and can conserve energy to pre-determined levels of precision that are not generally accessible in second-order particle-pushing routines commonly used in PIC codes. However, PIC codes are also very useful, especially in

situations where the relevant dynamics cannot be addressed by fluid theory or other reduced analytical models alone.

3.3 Particle-in-cell (PIC) numerical simulation

In general, a numerical particle-in-cell (PIC) algorithm is a kinetic description of a plasma that seeks to model complicated charged particle behavior in the presence of collective self-electromagnetic fields, as well as any externally applied fields [Birdsall and Langdon, 1985]. Both Vlasov and PIC codes offer kinetic simulations of particle interactions through electromagnetic fields for studying the long-time behavior of collisionless plasma. However, the difference is that the former actually numerically solves the Vlasov-Maxwell equations for the evolution of $f_j(\mathbf{x}, \mathbf{v}, t)$, whereas the latter computes the discrete motions of individual charged particles which interact with self and externally applied electromagnetic fields. Both types of codes can be modified to include collisional effects in certain regimes.

As discussed in Sec. 3.1, if the positions and velocities of all the point particles in a plasma are classically known at a given time, they can be determined self-consistently for all later times according to the Klimontovich-Maxwell (discrete and collisional) or Vlasov-Maxwell (continuum and collisionless) descriptions. The PIC method attempts to simulate the evolution of the distribution function for each species in time by tracking the complex orbits of individual point particles in the six-dimensional phase space of the Lagrangian coordinates $\mathbf{X}(t)$ and $\mathbf{V}(t)$ under the influence of self-consistent electromagnetic forces.

Essentially, the fundamental nature of the numerical particle-in-cell method is to compute the trajectories of many charged particles within (and across the cells of) a

user-specified spatial grid, on which the self- and externally applied electromagnetic fields are self-consistently calculated. The grid is nonphysical, though, in that it does not resolve any spatial fluctuations smaller than a grid cell size and can also be a source of mathematical inaccuracy and instability. The particles of each species within an individual cell of the spatial grid approximate part of the distribution function $f_j(\mathbf{x}, \mathbf{v}, t)$ for that species in that cell.

Given the positions and velocities of all the discrete charged particles within a certain cell, the charge density ρ and current density $\mathbf{J}$ are calculated at the nearby indices of the mathematical grid surrounding the particles according to a particular interpolation scheme. The process of assigning charge and current to the nearby grid points of a charged particle according to its position within that grid cell is called *weighting*. A numerical field solver integrates Maxwell's equations, using the continuously varying (in space) instantaneous macroscopic ρ and $\mathbf{J}$ (as well as any external charge or current) as known quantities on the grid, in order to calculate the resultant average $\mathbf{E}$ and $\mathbf{B}$ fields. Therefore, both the moments of the distribution function (densities and currents) and the fields themselves are only known at the discrete Eulerian spatial indices of the mathematical grid.

Once the PIC algorithm calculates the fields on the grid, the electric and magnetic forces are interpolated back to the locations of the particles according to another weighting process. The momenta of all the particles within each grid cell are advanced after the explicit integration of the differential equations of motion,

$$m \frac{d}{dt}\mathbf{v} = \mathbf{F} \tag{3.42}$$

$$\frac{d}{dt}\mathbf{x} = \mathbf{v} \,, \tag{3.43}$$

using finite-difference techniques. The weighted forces on the right-hand side of Eq. (3.42) are then known at the locations of the discrete particles within each cell, and thereby act on those particles by updating their momenta from one time step to the next according to [Birdsall and Langdon, 1985]

$$m\,\frac{\mathbf{v}^{n+1} - \mathbf{v}^{n}}{t^{n+1} - t^{n}} = q\,\mathbf{E}^{n} + \frac{q}{c}\,\mathbf{v}^{n} \times \mathbf{B}^{n} \,, \tag{3.44}$$

where $\Delta t \equiv t^{n+1} - t^{n}$ is the ascribed, discrete time step of the simulation and the superscript denotes the temporal index. Analogous to the spatial grid, the user-specified discrete time interval for the advancement of the simulation smooths out any faster temporal fluctuations, and may also lead to numerical inaccuracy and instability if chosen improperly. Then, each of the particles is moved (or "pushed") in coordinate space, over small distances $\Delta\mathbf{x} \equiv \mathbf{x}^{n+1} - \mathbf{x}^{n}$ in the amount of time Δt, according to

$$\frac{\mathbf{x}^{n+1} - \mathbf{x}^{n}}{t^{n+1} - t^{n}} = \mathbf{v}^{n+1} \,, \tag{3.45}$$

using the newly determined velocity $\mathbf{v}^{n+1}$ for each particle from Eq. (3.45). Since the old and new $\mathbf{x}$ and $\mathbf{v}$ are not known at the same time in the cycle (the $\mathbf{v}^{n+1}$ must be known before calculating $\mathbf{x}^{n+1}$), this explicit integration method is known as the *leap-frog method* [Birdsall and Langdon, 1985]. Once all of the individual particles have been pushed through some unique $\Delta\mathbf{x}$ in the common amount of time Δt, the macroscopic charge and current densities are recalculated on the grid according to the

new coordinate positions ($\mathbf{x}^{n+1}$) and momenta ($\mathbf{p}^{n+1} = m\,\mathbf{v}^{n+1}$) of all the particles, and the process begins anew. The cycle is executed in a loop over many time steps in order to allow the ensemble of particles to evolve. The discrete temporal step and spatial grid sizes always impart some inaccuracy to the numerical simulation, however, through judicious choice of the time step and grid size based on the physical parameters under consideration, their effects can be made small.

As particles move in and out of a given cell within the spatial grid, they effectively cause the charge and current densities, and therefore the electric and magnetic fields, on the nearby grid indices to jump up or down by discrete amounts. The result is temporal and spatial *particle noise*, for which PIC codes are infamous. Two steps can be taken to reduce particle noise, both of which increase the required amount of computational effort. First, the number of particles per cell can be increased and, second, higher-order weighting schemes can be employed to smooth out the effects of the *finite-size* particles (from the grid's perspective). Higher-order weighting schemes (linear, quadratic, cubic, etc.) interpolate charge and current densities to adjacent cells beyond the nearest grid indices from particle positions within the cell, as well as interpolate electric and magnetic forces back to the particles from adjacent cells beyond the nearest grid indices. The charged particles are then finite-size rigid *clouds* which may pass through each other and contribute density to the grid more smoothly; therefore, higher-order interpolation methods are said to be within the cloud-in-cell (CIC) interpretation. The CIC model can reduce noise in the density, field, and force calculations because the field equations and equations of motion are integrated over more cells, but at the expense of more computational effort.

In addition to the fact that particle-in-cell simulations are generally noisy, they

can also require a large amount of computational time in order to accurately model the important details on large-space scales (few m, or more) and long-time scales (few μs, or more), due to the need to resolve fast temporal processes. Explicit methods only require a knowledge of the desired quantities at the preceding time step, and at adjacent grid points, in order to advance those quantities by one time step. However, the Courant condition for stable explicit electromagnetic field solvers requires that the time step and grid spacing Δg must satisfy $c < \Delta g/\Delta t$, where c is the speed of light, implying that an electromagnetic wave should not be allowed to cross an entire cell in one time step. Similarly, the particle Courant condition for stable explicit particle-pushing requires that the time step and spatial grid size must satisfy $\mathbf{v} < \Delta g/\Delta t$, where $\mathbf{v}$ is approximately the maximum particle velocity in the simulation, implying that a particle should not be allowed to cross an entire cell in one time step. Large densities and magnetic fields can lead to prohibitively small time steps in explicit PIC simulations because of the resolution requirement for fast phenomena occurring at the plasma frequency ($\omega_p \, \Delta t < 1$) and cyclotron frequency ($\omega_c \, \Delta t < 1$) for every species, which can become quite cumbersome when electrons are present. In practice, the Courant condition for electromagnetic waves is the most stringent requirement placed on the size of the time step, however, the particle Courant condition can also become important, especially for energetic electrons. Depending on the problem, the grid aspect ratio restriction for explicit electromagnetic field solving can also increase the required computational resources: in $2D$ and $3D$ problems, the aspect ratio of the grid spacing between indices compared to the other direction(s) must be between 1/4 and 4 for numerical stability.

Although explicit methods for solving the field equations and equations of motion

are the fastest available to PIC simulation because of their simplicity, *implicit* methods have been developed for field solvers [Welch *et al.*, 2004] and particle-pushing [Friedman, 1990] in order to alleviate some of the restrictions on the choice of time step. The main difference between explicit and implicit schemes for solving systems of differential equations is found in the domain dependence of the problem. In contrast to explicit methods, implicit methods solve for all the quantities simultaneously and require knowledge of those quantities at all grid positions at the preceding time step in order to proceed (rather than only those at adjacent grid points and the preceding time step); the field and particle equations to be integrated form a large system of coupled nonlinear equations. The domain of dependence for an implicit method is larger than the domain of known quantities at the preceding time step; the boundary conditions are the extra sources of information. Therefore, all the unknown points at the next time step fall within the domain of uniqueness established by the characteristic trajectories beginning from the boundary points. The result is significant: there is no restriction on the computational time step. Thus, implicit methods do not enforce the stringent Courant condition for electromagnetic waves, which usually sets the maximum size of the time step in explicit electromagnetic simulations (the particle Courant condition must still be met). Also, the grid aspect ratio requirement for stability in explicit methods is relaxed substantially for implicit methods.

The most significant advantage of implicit methods is the extension of simulation techniques to kinetic phenomena on slower time scales, so that simulations can take larger time steps. Implicit time integration allows the code to model long-time scale behavior by altering the governing equations in order to eliminate uninteresting

high frequency modes. Implicit techniques typically allow the under-resolution of either ω_p or ω_c (whichever is greatest), but not both simultaneously. Therefore, even modest magnetic field values can hinder the use of a larger time step, which would otherwise allow implicit PIC simulations to compete with other reduced numerical models in terms of required computational resources. However, it is acceptable to solve the fields implicitly while pushing the particles with an explicit integration of the equations of motion, as described earlier [Birdsall and Langdon, 1985]. The time step in such simulations may then be increased from the electromagnetic wave Courant condition to the particle Courant condition, so long as ω_p and ω_c for each species are still resolved, and the result may be an increase in time step by as much as a factor of 10 to 100, depending on the simulation parameters; this method is an attractive alternative to the entirely explicit method, and was used almost exclusively in simulations presented in the other Chapters.

Energy conservation is challenging to maintain in particle-in-cell codes, and keeping the total nonphysical "unaccounted for" energy accumulation or loss to less than $\pm 20\%$ over the duration of the simulation is usually considered adequate. Particle-pushing algorithms can only conserve momentum or energy, but not both at the same time. Energy is not instantaneously conserved microscopically in momentum-conserving algorithms because the field energy is either under- or over-emphasized at short wavelengths due to the spatial discreteness of the mathematical grid. Even so, the observed macroscopic total energy may change only by small amounts compared to other energies of importance in the simulation, which would suggest that most of the energy exchange between fields and particles takes place at long wavelengths (which also happens to be the regime where the PIC model most accurately simulates

a plasma) [Birdsall and Langdon, 1985]. Spurious plasma heating can occur if the Debye length λ_D for a given species is not resolved by the grid, such that the so-called Debye length numerical instability can heat the species until λ_D equals the grid cell size Δg. Fortunately, an energy-conserving push that is not susceptible to the Debye length instability can be invoked and the simulation can maintain numerical stability even for grid sizes larger than the plasma skin depth. This option is exclusively used in simulations presented in other Chapters, so that λ_D can be under-resolved by the grid while maintaining good energy conservation.

At present, vastly fewer particles are used in a particle-in-cell code than are present in real plasmas, but such a simulation of "superparticles" (each of which represents many particles) can still be accurate and useful. The PIC simulator is responsible for assigning well-posed initial simulation conditions such as setting boundary conditions, creating objects and defining materials' properties in the simulation space, choosing appropriate cell sizes for the nonphysical grid, choosing an appropriate discrete time step, and implementing diagnostics so that physical insight can be obtained. The output of a particle-in-cell simulation takes on many forms, such as the temporal and spatial dependence of the number densities of the various species, overall charge and current densities, the average electric and magnetic fields, and energy distributions of the various species in phase space, to name a few. Simulations must always be checked for numerical stability, accuracy, and convergence, as well as conservation of energy and momentum.

The LSP code [LSP, 1999, Hughes *et al.*, 1999] is an advanced $3D$ electromagnetic particle-in-cell code designed for complex, large-scale plasma simulations on parallel and serial platforms; the numerical code supports cartesian, cylindrical, and

spherical coordinate systems and can also be used in $1D$ and $2D$ geometries. Particle-in-cell simulation is a powerful computational tool for self-consistently incorporating many effects of beam propagation through a background plasma. The LSP code is used in this thesis in order to predict the evolution of the ion beam, as it acquires an axial velocity tilt and drifts through the plasma, to the focal plane under a a variety of circumstances. The reader is encouraged to refer to Appendix B for a more detailed description concerning the process of charge and current density assignment to the grid, field solvers, interpolation of the field values back to the particles within the grid, particle-pushing, and other options available in the LSP code.

3.4 Summary and discussion

This chapter provided derivations of the underlying theoretical frameworks for the models which are employed in subsequent Chapters to investigate a number of realistic conditions found in neutralized drift compression experiments. Kinetic theory was used to derive an exact description of a plasma, called the Klimontovich-Maxwell equations (Sec. 3.1). However, a complete determination of the charged particle dynamics by calculating the exact classical orbits and fields for all particles in the system was far too difficult. Therefore, a statistical ensemble averaging procedure was used, averaging over the discrete microscopic phase space density $N_j(\mathbf{x}, \mathbf{v}, t)$ in order to acquire a description of the evolution of the smooth probability density function $f_j(\mathbf{x}, \mathbf{v}, t)$.

When collective effects were important, and not collisional discrete particle effects, the plasma kinetic equation reduced to the collisionless Boltzmann equation,

which is also called the nonlinear Vlasov equation. The Vlasov equation, in conjunction with the ensemble-averaged Maxwell's equations, retained the main effects of collective interactions in low-collisionality plasmas. The Vlasov-Maxwell equations self-consistently evolved the smooth probability density function of a plasma under the influence of its own long-range electric and magnetic fields, as well as any externally applied fields. However, this complete description of collective processes in plasma required a knowledge of the six-dimensional distribution function as an initial condition prior to carrying out kinetic analytical studies or numerical simulations. Often, the Vlasov-Maxwell equations become complex and cumbersome even under idealized assumptions.

An alternative, reduced theoretical model called the macroscopic warm-fluid description has been derived for studying charged particle dynamics by taking successive velocity space moments of the Vlasov equation, and closing the hierarchy of equations by assuming the forms of the pressure and heat flow tensors (Sec. 3.2). The resulting approximate equations for the evolution of the charged particle system formed a closed description of the bulk fluid properties in the collisionless regime. In addition, numerical implementations of the warm-fluid model were generally more stable and computationally efficient, as well as less noisy, compared to particle-in-cell codes.

The technique of particle-in-cell simulation has been the primary computational tool for studying, in the most self-consistent way, many of the dynamics of charged particle beam transport through plasma (Sec. 3.3). A particle-in-cell code evolves the full distribution functions of all simulated species for given boundary and initial conditions by computing the discrete motions of individual charged particles,

which interact with self- and externally applied electromagnetic fields. The numerical method tracks "superparticles" across a nonphysical mathematical grid, which is used at discrete intervals in space, in order to (1) evaluate moments of the distribution function $f(\mathbf{x}, \mathbf{v}, t)$, (2) calculate the macroscopic electromagnetic fields associated with the charge and current densities of the charged particles within each of the grid cells, and (3) subsequently push the particles to new positions in the grid using the calculated electromagnetic forces. Such an ensemble of particles can be tracked numerically throughout time and space, while maintaining good accuracy, stability, and energy conservation. Therefore, the method was shown to be an invaluable resource for computational plasma physicists.

All of the particle-in-cell simulations presented throughout this thesis were performed using the LSP code. Unless otherwise mentioned, each LSP simulation solved the electromagnetic field equations, treated all particle species as explicit and kinetic, resolved ω_{pe} and Ω_{ce} (the electron plasma and cyclotron frequencies, respectively), used the cloud-in-cell model, was not susceptible to the so-called numerical Debye length instability, and conserved energy to good accuracy levels.

Chapter 4

Longitudinal Compression

The challenge for theoretical models is to realistically and tractably describe the important physics in associated experiments. The modeling of results obtained in the Neutralized Drift Compression Experiment provide valuable insights into the physical and technological limitations of longitudinal charge bunch compression. Theoretical techniques used to investigate the dynamical evolution of a compressing charge bunch propagating through background plasma include a warm-fluid model [Qin *et al.*, 2005], a kinetic formalism [Davidson and Qin, 2005], a hybrid combination of the fluid and Vlasov models [Sefkow and Davidson, 2006], and particle-in-cell numerical simulations [Welch *et al.*, 2005, Sefkow *et al.*, 2005b]. The numerical implementations of the models show very good agreement with experimental data and provide physical insights into non-ideal effects such as voltage waveform inaccuracy, consequences of finite acceleration gap size, beam temperature effects, and partial beam neutralization and residual space-charge effects, all of which give rise to decreased compression factors and increased pulse lengths at focus.

Reduced theoretical models and particle-in-cell simulations are used in this Chapter in order to accurately describe the propagation of an intense charge bunch in longitudinal compression experiments [Sefkow and Davidson, 2006]. The derivation of the equation for the induction module voltage waveform which imposes an ideal velocity tilt on a charge bunch is presented in Sec. 4.1. In Sec. 4.2, a numerical implementation of the warm-fluid model is presented as a tractable computational tool for investigating the non-ideal effects associated with the experimental acceleration gap geometry and voltage waveform of the induction module, which act to pulse-shape both the velocity and line density profiles of the beam (the induction module is shown in Figs. 1.7 and $A.1$, and discussed in Appendix A). In Sec. 4.3, a kinetic formalism based on the Vlasov equation is numerically employed in order to study the experimental current profiles of a longitudinally compressing intense ion beam, and explain the origin of the central peak in current at the focal plane (refer to Fig. 2.8). A hybrid fluid-Vlasov model that retains the advantages of both the fluid and kinetic approaches is implemented in Sec. 4.4 to describe the formation of pedestals in the current profiles around the main compressed pulse, which contribute to ion beam pre-heating of targets. Particle-in-cell numerical simulations are used in Sec. 4.5 to discuss various characteristics of the current and axial energy profiles upstream and downstream of the focal plane. As shown in Sec. 4.6, the comparison between experimental measurements and the various theoretical models, including particle-in-cell simulation, is excellent. The detailed physics of acceleration gap effects and aberration on longitudinal compression, and their dependence on various system parameters, is reviewed in Sec. 4.7. A brief summary and discussion of the results from the various numerical models concludes the Chapter in Sec. 4.8.

4.1 Ideal induction module voltage waveform

There exists an ideal induction module voltage waveform that results in the imposition of a perfect velocity tilt on an ion beam with zero temperature across an infinitely thin acceleration gap for achieving maximal longitudinal compression at a desired focal plane [Henestroza, 2006, Welch *et al.*, 2005, Barnard, 2006]. In the classical limit of point particles, there is no upper bound on the longitudinal current compression (or lower bound on the pulse length) under the assumptions mentioned, since an ideal velocity tilt will cause all of the beam particles to arrive at the longitudinal focal plane at the exact same time. In reality, not only does the beam have temperature and the acceleration gap have finite-size, but the ion beam particles also have finite extent (classically or quantum-mechanically), implying that the current density compression cannot be infinite, even in theory. In addition, as the beam density increases, so must the density of the background plasma provided for adequate neutralization of the beam's space-charge and current (since $n_p > n_b$ is required and $n_p >> n_b$ is desired), or else the intense self-fields would stagnate the otherwise compressing beam. Of course, once the requisite plasma density increases to the range of solids, more complicated physics becomes important and the beam will deposit its directed kinetic energy via collisions and other energy exchanging processes. The main point is that finite upper limits, even under highly idealized assumptions, do exist for longitudinal compression of intense ion beams. The theory of an ideally compressed beam is a mathematical exercise that can only be sought, but not realized, in experiments. Laboratory constraints and other physical realities ultimately limit the achievable compression factors and pulse lengths.

The derivation of the ideal velocity tilt, and the induction module voltage waveform that produces it, for an ion beam with zero temperature encountering an infinitely thin acceleration gap is as follows. Let v_h be the velocity of the head of the beam after it exits the gap at time $t = 0$; this antecedent portion of the beam has been decelerated relative to its initial velocity v_0 from the injector and transport sections. The focal plane lies at the end of the drift length L_d, and the arrival of the head at that location will occur at a time

$$t_h^{foc} = \frac{L_d}{v_h} \,. \tag{4.1}$$

In order for all the beam particles to coincidentally arrive at the same focal plane, the central and tail portions of the charge bunch are required to travel a greater distance than the head portion in the same amount of time, and so must be accelerated accordingly as they pass the gap. Therefore, the velocity of the particles that reach the gap at time t after the head of the beam must exit the gap with a time dependent velocity $v_b(t)$ according to

$$t_h^{foc} - t = \frac{L_d}{v_b(t)} \,, \tag{4.2}$$

which implies that

$$v_b(t) = \frac{L_d}{\frac{L_d}{v_h} - t} = \frac{v_h}{1 - \frac{v_h\, t}{L_d}} \,, \tag{4.3}$$

where t is evaluated from $t = 0$ to $t = t_p$ and t_p is the initial pulse length of the beam,

which is usually written as

$$t_p = \frac{L_b}{v_0} \,, \tag{4.4}$$

where L_b and v_0 are the initial length and velocity of the charge bunch before entering the acceleration gap.

The nonrelativistic energy of the beam is determined from $E_b(t) = \frac{1}{2} m_b v_b^2(t)$, where m_b is the mass of the beam particles, giving

$$E_b(t) = \frac{1}{2} m_b v_h^2 \left(\frac{1}{1 - \frac{v_h \, t}{L_d}} \right)^2 \tag{4.5}$$

for the time dependence of the beam energy exiting the gap, where t is again evaluated from $t = 0$ to $t = t_p$. The corresponding voltage waveform $V(t)$ for the induction module that produces the desired energy profile as the beam particles exit the acceleration gap is

$$V(t) = \frac{1}{q_b} [E_b(t) - E_0(t)] \,, \tag{4.6}$$

where q_b is the charge of the beam particles and $E_0(t)$ is the initial energy of the beam (usually a constant) entering the gap.

The velocity tilt is approximately linear for most parameters of interest. Using

$$\sum_{n=0}^{\infty} x^n = \frac{1}{1 - x} \tag{4.7}$$

for $|x| < 1$, Eq. (4.3) can be rewritten

$$v_b(t) = v_h \left[1 + \frac{v_h\, t}{L_d} + \left(\frac{v_h\, t}{L_d} \right)^2 + \left(\frac{v_h\, t}{L_d} \right)^3 + \ ... \right], \tag{4.8}$$

for $t = 0$ to $t = t_p$ and implies an approximately linear dependence on t when $v_h\, t/L_d << 1$. Certainly, this equality holds at least at early times. However, the ideal velocity tilt may deviate from linear dependence on t for late times, depending on the drift length L_d and initial pulse length t_p. At $t = t_p$, the entire charge bunch has emerged from the infinitely thin acceleration gap and, using Eq. (4.4),

$$\frac{v_h\, t_p}{L_d} = \frac{v_h}{L_d} \frac{L_b}{v_0}\,. \tag{4.9}$$

Since $v_h < v_0$ for longitudinal compression, and head particles are not allowed to pass the intended focal plane before tail particles exit the acceleration gap,

$$\frac{v_h}{v_0} < \frac{L_d}{L_b} \tag{4.10}$$

sets a minimum on the drift length L_d, given the other parameters, and assures that at least $v_h\, t/L_d < 1$ (if not $<< 1$) for $t \leq t_p$. Therefore, the expansion in Eq. (4.8) is justified. Equation (4.5) for the time dependence of the energy can be expanded in a series similar to Eq. (4.8) using

$$\sum_{n=1}^{\infty} n\, x^{n-1} = \left(\frac{1}{1-x} \right)^2 \tag{4.11}$$

for $|x| < 1$, which is justified for the same reasons just mentioned.

Recall from Eq. (4.1) that the longitudinal focal plane is found a distance

$$L_d = v_h \, t_h^{foc} \tag{4.12}$$

downstream of the acceleration gap. For maximum longitudinal compression, the tail of the charge bunch arrives at the focal plane at the same time as the head of the charge bunch. Let v_t be the velocity of the tail of the beam after it exits the gap at time $t = t_p$; this subsequent portion of the beam has been accelerated relative to its initial velocity v_0 from the injector and transport sections. Then, in order to solve for the time and drift length required to reach maximal compression, the initial pulse length t_p is related to the time when maximal compression occurs t_h^{foc} according to

$$v_t \, (t_h^{foc} - t_p) = v_h \, t_h^{foc}, \tag{4.13}$$

which rearranges to

$$t_h^{foc} = \frac{v_t}{v_t - v_h} \, t_p \tag{4.14}$$

and the drift length to the longitudinal focal plane, Eq. (4.12), becomes

$$L_d = \frac{v_h \, v_t}{v_t - v_h} \, t_p. \tag{4.15}$$

Making the assumptions that the initial energy $E_0(t)$ entering the acceleration gap is constant in time, and equal amounts of head and tail have been decelerated and

accelerated, respectively, allows the head and tail velocities to be defined as

$$v_h \equiv v_0 \left(1 - \frac{f}{2}\right) \tag{4.16}$$

$$v_t \equiv v_0 \left(1 + \frac{f}{2}\right) , \tag{4.17}$$

respectively, where the fractional velocity tilt f is defined as

$$f \equiv \frac{\Delta v_b}{v_0} = \frac{v_t - v_h}{v_0} . \tag{4.18}$$

Upon substitution of the head and tail velocity definitions, Eqs. (4.14) and (4.15) become

$$t_h^{foc} = \left(\frac{1}{f} + \frac{1}{2}\right) t_p \tag{4.19}$$

$$L_d = v_0 \frac{\left(1 - \frac{f}{2}\right)\left(1 + \frac{f}{2}\right)}{f} t_p = v_0 \left(\frac{1}{f} - \frac{f}{4}\right) t_p , \tag{4.20}$$

and give the time and drift length to the longitudinal focal plane in terms of the initial beam velocity, initial pulse length, and desired fractional velocity tilt. For the same initial beam energy, greater fractional tilts f give shorter drift lengths than smaller fractional tilts, and longer initial pulse lengths t_p give longer drift lengths than shorter initial pulse lengths. Substitution of Eqs. (4.16) and (4.20) into Eq. (4.3) yields the

time dependence of the velocity as the tilted beam exits the acceleration gap

$$v_b(t) = v_0 \, \frac{\left(1 - \frac{f}{2}\right)}{\left[1 - \left(\frac{f}{1+\frac{f}{2}}\right)\left(\frac{t}{t_p}\right)\right]} \, , \tag{4.21}$$

in terms of the initial beam velocity, initial pulse length, and desired fractional tilt, where t is evaluated from $t = 0$ to $t = t_p$.

The nonrelativistic energy of the charge bunch is time-dependently altered across the infinitely thin acceleration gap, and the required ideal voltage waveform $V(t)$ can now be determined from $E_b(t) = \frac{1}{2} m_b v_b^2(t)$, using Eqs. (4.6) and (4.21), to be [Henestroza, 2006]

$$V(t) = \frac{1}{2\,q_b} \, m_b \, v_0^2 \, \left(\left\{ \frac{\left(1 - \frac{f}{2}\right)}{\left[1 - \left(\frac{f}{1+\frac{f}{2}}\right)\left(\frac{t}{t_p}\right)\right]} \right\}^2 \, - \, 1 \right) \, , \tag{4.22}$$

and is given in terms of the initial beam energy, initial pulse length, and desired fractional velocity tilt, where the entire coefficient

$$\frac{E_0}{q_b} = \frac{1}{2\,q_b} \, m_b \, v_0^2 \tag{4.23}$$

is the initial beam energy per unit charge, but is often itself referred to as the "beam energy," in units of eV rather than J.

In experiments, the induction module is programmed to attempt the application of as near an ideal voltage waveform [Eq. (4.22)] as possible. The electric field induced across the acceleration gap is a result of the changing magnetic flux in the induction cores. Multiple induction cores are driven at once and each core contributes some field

to the specific $\mathbf{E}(r, z, t)$ across the finite-size acceleration gap, thereby modifying the axial flow velocity of the beam. The reader is encouraged to refer to Appendix A for more details concerning the operation of a single-gap linear induction accelerator. The effects of an imposed non-ideal voltage waveform on a beam with finite temperature across an acceleration gap of finite length are discussed in the theoretical work in the following Sections. In reality, the induced electric field encountered by the beam has significant extent in the spatial and temporal dimensions, relative to the size and pulse length of the beam, rather than modifying the beam energy over an infinitely thin slice at one axial location, and gives rise to a number of complications.

4.2 Macroscopic warm-fluid model

The macroscopic warm-fluid description for charged particle beam dynamics is a continuum approximation, derived by evaluating velocity moments of the Vlasov equation. Closure of the system of equations in the present analysis is achieved by assuming that heat flow is negligible between the beam and its surroundings, and by ignoring the higher-order moments. The resulting approximate equations form a closed description of the bulk fluid properties, the dynamics of which are reversible as well as isentropic.

The adoption of a warm-fluid model, which forms a coupled, nonlinear partial differential equation system without the use of macroparticles, can yield numerical results which are less noisy, provide more stability, are computationally efficient, and can conserve energy to pre-determined levels of precision that are not generally accessible in routines commonly used in particle-in-cell codes [Sefkow and Davidson, 2006].

In the beam frame, the nonrelativistic warm-fluid equations in the longitudinal direction for the line density $\lambda(z,t)$, flow velocity $u_z(z,t)$, and pressure $p_z(z,t)$ are given by [Qin and Davidson, 2002a, Qin *et al.*, 2005]

$$\frac{\partial}{\partial t}\lambda(z,t) + \frac{\partial}{\partial z}[\lambda(z,t)\, u_z(z,t)] = 0\,, \tag{4.24}$$

$$\begin{aligned} &\frac{\partial}{\partial t}u_z(z,t) + u_z(z,t)\,\frac{\partial}{\partial z}u_z(z,t) - \frac{q_b}{m_b}\,E_z^{tilt}(z,t) \\ &+f(z,t)\,\frac{q_b^2\, g}{4\pi\epsilon_0\, m_b}\,\frac{\partial}{\partial z}\lambda(z,t) + \frac{1}{\lambda(z,t)}\,\frac{r_b^2}{m_b}\,\frac{\partial}{\partial z}p_z(z,t) = 0\,, \end{aligned} \tag{4.25}$$

$$\frac{\partial}{\partial t}p_z(z,t) + u_z(z,t)\,\frac{\partial}{\partial z}p_z(z,t) + 3\,p_z\,\frac{\partial}{\partial z}u_z(z,t) = 0\,, \tag{4.26}$$

where $p_z(z,t) \equiv n(z,t)\,T_z(z,t)$, $T_z(z,t)$ is the effective longitudinal temperature, and zero heat flux ($q_z = 0$) is assumed. The above equations correspond to the continuity equation [Eq. (3.33)], momentum equation [Eq. (3.34)], and pressure equation [Eq. (3.41)], respectively, for a macroscopic fluid element of beam ions with charge q_b and mass m_b traveling in the axial direction in cylindrical coordinates. The beam ions experience an external field $E_z^{tilt}(z,t)$ in Eq. (4.25), which corresponds to the space- and time-dependent induced electric field the beam encounters in the acceleration gap in longitudinal compression experiments.

The perveance term is proportional to $\partial\lambda(z,t)/\partial z$ in Eq. (4.25), and is associated with the space-charge of the ion beam. The coefficient $f(z,t)$ of that term is a function describing the degree of charge neutralization by the background plasma, where $f = 0$ and $f = 1$ correspond to fully neutralized and fully unneutralized

ion beam charge, respectively, and the g-factor occurring in that term is a model [Qin *et al.*, 2005, Davidson and Startsev, 2004] for the longitudinal self-electric field of the ion beam, with $g = 2\ \ln(r_w/r_b)$, where r_w and r_b are the wall radius and beam radius, respectively. Pressure effects are important to include near the focal plane of the compressed charge bunch because of the presence of chromatic abberation, a consequence of considering finite beam temperature effects. For an ideal velocity tilt, beam particles with small deviations from the mean axial velocity will be longitudinally focused to different focal planes, causing decreased compression factors and increased pulse durations. For example, beam ions with velocity $u_z + u_{th}$ travel too quickly for a given velocity tilt and will longitudinally focus later in time and farther in space than those moving with velocity u_z; the opposite is true for beam ions with velocity $u_z - u_{th}$. The degree to which this effect decreases the amount of longitudinal compression depends on the thermal distribution involved and the drift length to the focal plane. The topic of chromatic aberration will be addressed in more detail in Sec. 4.7.

The goal of using the warm-fluid equations as a numerical model for comparison to neutralized drift compression experiments is to employ the experimental voltage waveform used by the induction module, in order to apply a non-ideal velocity tilt to an ion beam which has nonzero longitudinal thermal spread and subsequently propagates through a partially-neutralizing background plasma, corresponding to a nonzero value of $f(z,t)$. A plentiful supply of electrons is desired in order to effectively neutralize the beam's space-charge and current, implying the beam density n_b should be much less than the plasma density n_p everywhere downstream of the applied tilt, thereby ensuring the propagation of the intense beam well above the space-charge

limit for unneutralized beams. However, the beam density can approach values of the plasma density depending on the particular experimental profiles provided for $n_p(\mathbf{r}, t)$, especially near the simultaneous transverse and longitudinal focal plane, where the beam's current density rises more rapidly due to the small spot size achieved by means of transverse compression. For this reason, it can be especially important to include the perveance and pressure terms in the numerical framework. However, longitudinal compression will be the topic of this Chapter, and simultaneous transverse and longitudinal compression will be discussed in Chapter 6.

There exist other reasons for implementing a fast and accurate numerical model based on the warm-fluid equations. First, such a model allows for the lifting of restrictions on uniformity, symmetry, and solution-type (*e.g.*, self-similar) which have often been assumed in earlier studies. Second, a fluid model allows the determination of whether the observed features of the beam variables such as velocity and current are due to kinetic effects. Third, a non-particle-based numerical method allows the efficient and noiseless study of how deviations from ideal voltage waveforms affect the evolution of the beam's line density, velocity, and pressure profiles.

The numerical method of lines [Schiesser, 1991, Quarteroni and Valli, 1994] is used in order to solve the nonlinear warm-fluid partial differential equation system, after the problem is well-posed with initial conditions and boundary values [Richtmeyer and Morton, 1994]. The method of lines is efficient and can take advantage of a wide range of numerical integration techniques [Lambert, 1987, Shampine, 1994]. There are two primary steps to the method of lines: first, the spatial dimension is discretized and, second, the semi-discrete temporal problem of

only one independent variable is integrated as a system of ordinary differential equations [Shampine and Gordon, 1975, Ascher and Petzold, 1998]. In the present analysis, the discretization is carried out to fourth order using centered finite differences [Mitchell and Griffiths, 1980], although finite element and finite volume methods can alternatively be employed. The ordinary differential equations are numerically integrated in time using a high-order predictor-corrector Adams method [Bashforth and Adams, 1883], based on the Maclaurin series with backward differences [Beyer, 1987]. In general, a predictor-corrector scheme [Arfken, 1985, Press *et al.*, 1992] extrapolates a polynomial fit to the derivative from one time step to the next, then interpolates the new derivative based on extrapolation. The Adams method is observed to be faster than the Runge-Kutta method [Kutta, 1901] for the same high level of accuracy and precision (10^{-8}) [Higham, 1996]. Based on Richardson's extrapolation [Jeffreys and Jeffreys, 1988], a routine for an adaptive step size is used. Finally, the method of lines finds solutions between the spatial discretization by interpolation.

In order to investigate the physics of longitudinal compression in the Neutralized Drift Compression Experiment (NDCX), a theoretical model needs to incorporate the actual spatial and temporal dependence of the induced electric field within the finite-size acceleration gap of the induction module. The gap begins at the wall radius of $r_w = 3.8$ cm, is 3 cm long in the axial direction, and is symmetric about the azimuth. The top image in Fig. 4.1 illustrates the connection between the effective voltage drop across the acceleration gap, which is located from $z = -22$ cm to $z = -19$ cm at radii larger than the wall radius, and the resultant induced electric field found at radii less than the wall radius (where the beam encounters the applied force). The bottom

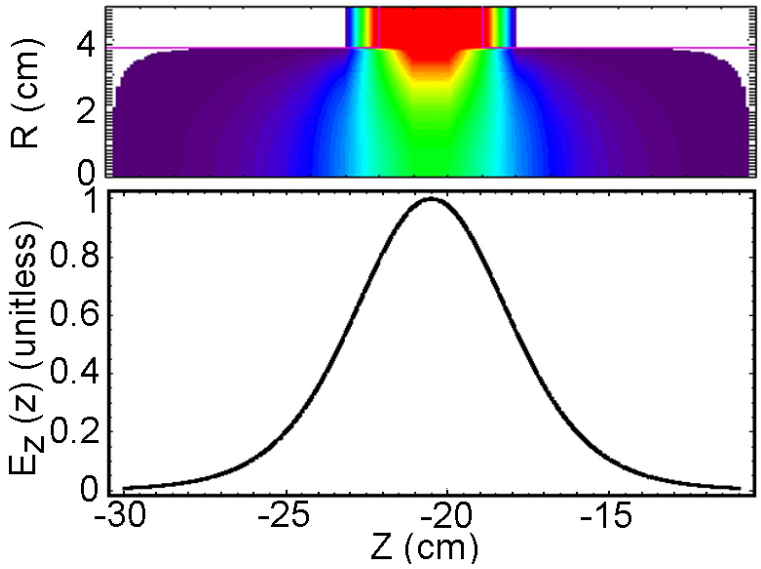

Figure 4.1: (Color) In models describing NDCX, the axial coordinate is measured in the laboratory frame from $z = -30$ cm to $z = +120$ cm. Snapshot (in time) of the $E_z^{tilt}(r, z)$ in the acceleration gap, calculated from the geometry of the currently existing induction module (top), and normalized slice of $E_z^{tilt}(r = 0, z)$ used in the fluid model to describe the axial spatial dependence of the electric field (bottom).

image in Fig. 4.1 shows the longitudinal spatial dependence of the axial electric field at the $r = 0$ axis, *i.e.*, the form of $E_z^{tilt}(z)$ used in the momentum equation of the warm-fluid model [Eq. (4.25)]. The axial coordinate used in the laboratory frame for NDCX models extends from $z = -30$ cm to $z = +120$ cm, and the background neutralizing plasma exists from $z = 0$ cm to $z = +120$ cm. The plasma drift length can be varied from $L_d \sim 1 - 2.5$ m in experiments, and can be similarly altered in the models by modifying the coordinate range as needed. Note from Fig. 4.1 that 95% of the $E_z^{tilt}(z)$ at $r = 0$ lies between approximately $z = -25.5$ cm and $z = -15.5$ cm. Therefore, the effective interaction range of this 3 cm-long gap is $\Delta z = 10$ cm.

Figure 4.2 highlights the difference between a typical experimental voltage waveform and an ideal waveform, which would result in the imposition of a perfect velocity

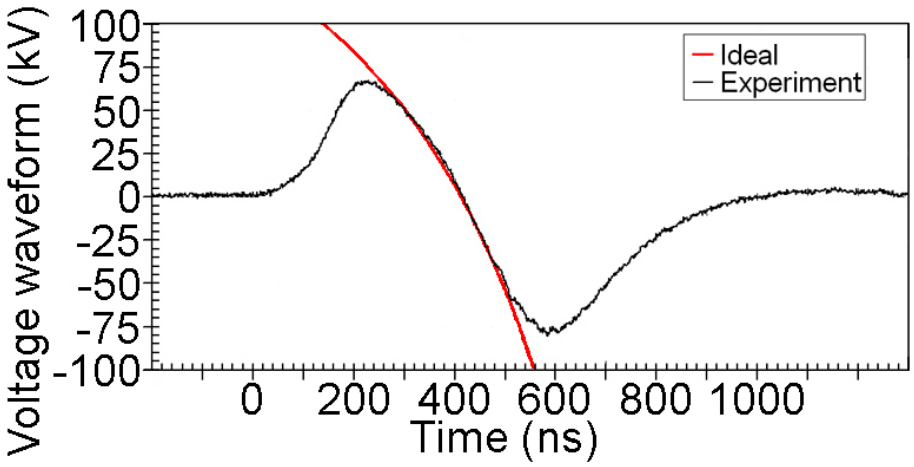

Figure 4.2: (Color) Comparison between the experimental (black) and ideal (red) voltage waveforms for application of the $E_z^{tilt}(t)$ in the gap. The ideal waveform imposes an ideal velocity tilt on the drifting beam (from $t \sim 100 - 600$ ns). The experimental waveform is used for $E_z^{tilt}(t)$ in the fluid model.

tilt on an ion beam with zero temperature across an infinitely thin gap. The experimental waveform plotted in Fig. 4.2 is employed to calculate the temporal dependence of the axial electric field $E_z^{tilt}(t)$ used in the momentum equation of the fluid model [Eq. (4.25)], and results in the application of an approximately 25% velocity tilt (defined as $\Delta u_z/u_0$) to the beam in the gap region. If the voltage waveform affects equal amounts of the beam's head and tail, the fractional tilt is also known as $f = 0.25$ (refer to Sec. 4.1).

The numerical implementation of the fluid model is utilized in order to realistically predict the evolution of the ion beam as it acquires a velocity tilt and drifts through the plasma towards its longitudinal focal plane of maximum beam current. In order to directly compare the fluid model to a particle-in-cell simulation, the LSP code [LSP, 1999, Hughes *et al.*, 1999] is used, as mentioned in earlier Chapters. The same initial parameters are used in both the $2D$ $\{r, z\}$ particle-in-cell simulation and

$1D$ warm-fluid code. In both numerical models, a 300 keV K^+ beam with initial radius $r_b = 2$ cm and current $I_0 = 25$ mA is injected into the geometry in the $+\hat{z}$ direction, approximately $\Delta z = -8$ cm upstream of the gap (at the $z = -30$ cm plane), with a $T_b = 0.4$ eV Maxwellian temperature in both the transverse and longitudinal directions. The corresponding normalized effective emittance [Eq. (1.1)] and perveance [Eq. (1.2)] for these beam parameters are 1.3×10^{-2} cm-mrad and 6.4×10^{-4}, respectively. The experimental voltage waveform shown in Fig. 4.2 is included in both models, resulting in an approximate 25% velocity tilt imposed on the beam, as mentioned earlier, before the beam drifts through a column filled with plasma of density $n_p = 5 \times 10^{10}$ cm^{-3} and temperature $T_p = 3$ eV, from $z = 0$ cm to $z = +120$ cm. The particle-in-cell simulation demonstrates that the plasma almost completely neutralizes the charge and current of the ion beam. A longitudinal compression factor of 50 (defined as I_b^{max}/I_0), with approximate full-width, half-maximum pulse duration of $t_{fwhm} \sim 3.2$ ns, is achieved for the given parameters by both codes. The focal plane occurs near $z = +110$ cm, approximately $L_d \sim 1.3$ m downstream of the gap, implying the effective initial pulse length t_p undergoing compression due to the experimental voltage waveform of Fig. 4.2 is approximately $t_p \sim 275$ ns, according to Eq. (4.20).

Many observed features in the beam current profiles from particle-in-cell simulation are recovered using the warm-fluid model. Since the experiments and simulations involve only longitudinal compression, and not simultaneous focusing of the beam in the transverse direction, the beam density remains at least an order-of-magnitude smaller than the plasma density ($n_p \sim 0.5 - 1 \times 10^{11}$ cm^{-3}) at all locations in the device. Also, LSP simulations show good ($> 95\%$) neutralization of

the beam's space-charge by the plasma, in agreement with theory when $n_p >> n_b$ [Kaganovich *et al.*, 2001, Rose *et al.*, 2001, Welch *et al.*, 2005]. Therefore, the $f(z,t)$ coefficient of the perveance term in the momentum equation of the warm-fluid model [Eq. (4.25)] is taken to be small (< 0.05) in the presence of plasma, from $z = 0$ cm to $z = +120$ cm. The $f(z,t)$ coefficient is set to unity in the region of the acceleration gap, where no plasma is present. When only longitudinal compression takes place (without simultaneous transverse focusing), the perveance term in the momentum equation is not dominant for these beam parameters, and little difference in the compression physics can be found between a completely neutralized beam ($f = 0$ in the plasma region) and an *almost* completely neutralized beam ($f < 0.05$ in the plasma region). However, as will be discussed in Chapter 6, when simultaneous transverse and longitudinal compression takes place and $n_p >> n_b$ is not strictly satisfied, the perveance becomes the critical term for determining the maximum achievable amount of charge bunch compression, due to the inverse-square dependence of the current density on the beam radius [$J_z(z,t) \sim r_b(z,t)^{-2}$], and substantial differences are found between the completely neutralized and *almost* completely neutralized cases.

The current is calculated in the warm-fluid model from the product $\lambda(z,t)\, u_z(z,t)$ and transformed to the laboratory frame in order to compare with particle-in-cell diagnostics, which measure the beam current at a specified plane in laboratory coordinates. The $I_0 = 25$ mA initial current is chosen by the initial line density (constant) for a given velocity (also constant). Since the current through a plane is the transverse integral of the current density through that plane, a direct comparison can be made between the $2D$ $\{r,z\}$ LSP simulations and the $1D$ warm-fluid model calculations in the longitudinal direction. Figure 4.3 illustrates the similarity between compression

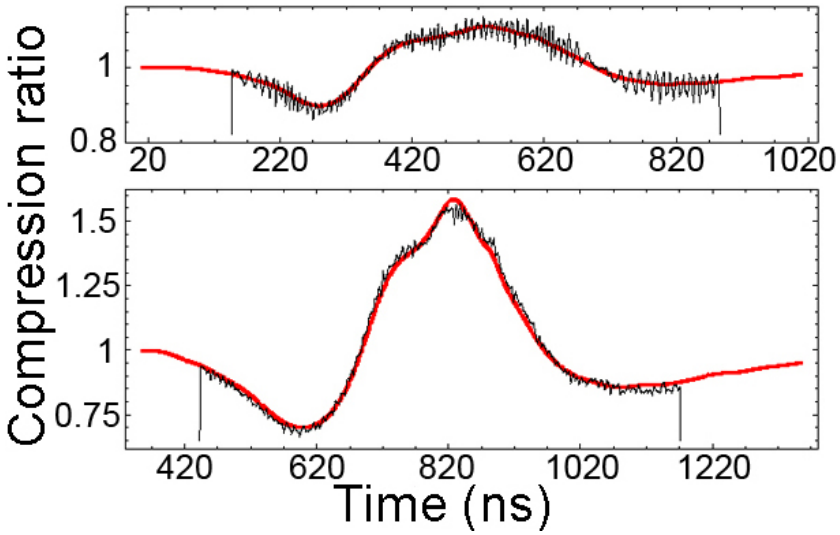

Figure 4.3: (Color) Longitudinal compression ratio $I_b(t)/I_0$ in the laboratory frame from particle-in-cell simulation (black) and the warm-fluid model (red) at $z = -8$ cm, just beyond the acceleration gap (top), and at $z = +29$ cm (bottom).

dynamics from the particle-in-cell simulations and the corresponding profiles calculated using the warm-fluid model (both in the laboratory frame). The definition of the compression ratio is $I_b(t)/I_0$ (the I_0 in experiments can vary between approximately 10 and 80 mA). Excellent agreement is shown between the two results, indicating that the various features (*e.g.*, asymmetric dips and bumps) in the current profiles of the longitudinally compressing ion beam are due to the non-ideal voltage waveform deviations from the ideal waveform in experiments using the actual acceleration gap. Such features cannot be observed in models which do not use the finite-size gap and experimental voltage waveform. Note that the particle-in-cell result, which requires $\sim$ 18 hours of computation time on 12 processors to push approximately 5×10^5 particles, is noisier than the reduced model warm-fluid result, which requires < 10 minutes on a single processor.

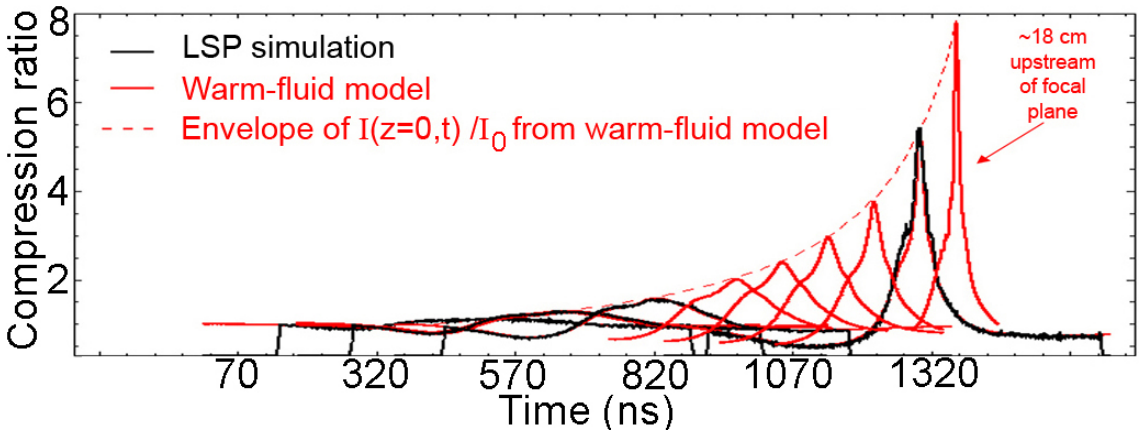

Figure 4.4: (Color) Longitudinal compression ratio $I_b(t)/I_0$ in the laboratory frame obtained from particle-in-cell simulation (black) and the warm-fluid model (red) at multiple axial locations from $z = -8$ cm to $z = +92$ cm.

A comparison of the longitudinal compression profiles calculated by the two models, at various axial locations in the beam frame from $z = -8$ cm to $z = +92$ cm, is shown in Fig. 4.4. The envelope of the compression ratio at $z = 0$ cm in the beam frame, which is the center of the charge bunch and where the decelerated "head" meets the accelerated "tail", is plotted as a dashed line. Such an envelope should ideally touch each individual current profile at the location of peak compression compared to the rest of the beam: the center of the beam, moving at the average beam velocity, would experience a build-up of density at that location as the beam compresses through background plasma. Evidently, the warm-fluid results in Fig. 4.4 are in very good quantitative agreement with the kinetic particle-in-cell treatment, since hardly any discrepancy is evident (especially early in time).

An interesting consequence of the experimental velocity-tilting process is that the $E_z^{tilt}(z,t)$ in the gap acts not only as a means for pulse-shaping the *velocity* of the ion beam, but it also pulse-shapes the *line density*. Specifically, the line density profile in the beam frame, which is initially constant (or a step function), is transformed by

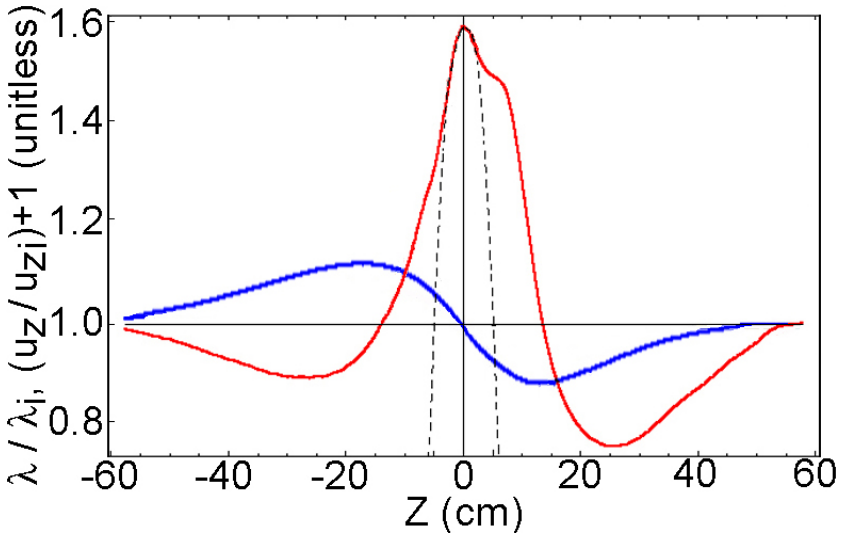

Figure 4.5: (Color) Normalized line density (red) and axial velocity (blue) in the beam frame after most of the velocity tilt has been applied ($t = 830$ ns) in the warm-fluid model. The center of the beam is located at $z = +29$ cm in the laboratory frame at this instant of time. The dashed line is the parabola $1.6\,(1 - z^2/36)$.

this particular tilt application process into a parabolic line density profile. Figure 4.5 depicts the line density and axial velocity profiles (calculated in the beam frame) from the warm-fluid model, after the tilt is applied to the beam and the pertinent portion of the voltage waveform passes ($t = 830$ ns, refer to Fig. 4.2). At $t = 830$ ns, the center of the beam in the laboratory frame is located at $z = +29$ cm, about $\Delta z = -81$ cm upstream from the longitudinal focal plane. The quantities are normalized to the initial line density and the initial beam frame axial velocity (an arbitrary shift of $+1$ is applied to the normalized velocity profile, since $v_0 = 0$ in the beam frame). Note that the velocity of the center of the tilted beam is unchanged, since the voltage waveform symmetrically changes polarity. The parabola $1.6\,(1 - z^2/36)$ is plotted as a dashed line in the center of the beam frame in order to exhibit the fact that the portion of the beam that is tilted very well (corresponding to the linear region in the velocity profile)

has its constant line density profile transformed into a parabolic line density profile. The pressure profile (not shown) is transformed, in the region of the linear velocity tilt, into a double-parabolic profile. Information on such transformations of the beam profiles is valuable, since a parabolic line density profile and double-parabolic pressure profile with a linear velocity tilt is a self-similar drift compression solution in the longitudinal direction of the warm-fluid model, as well as a particular solution to the corresponding $1D$ Vlasov equation, when complete neutralization of the beam is assumed. Drift compression solutions that satisfy a self-similar symmetry condition can be used in reduced models in order to transversely focus the entire beam pulse onto the same focal spot at the location of the target [Qin *et al.*, 2005]. Solutions obeying self-similarity are required for this procedure because, for each slice in a bunched beam, a drift compression and final focus lattice design can transversely focus all the different slices onto the same focal spot only if the current $[\lambda(z,t)\, u_z(z,t)]$ and emittance [related to $p_z(z,t)$] of all the slices depend on the longitudinal coordinate in the same manner.

The family of self-similar profiles under discussion is

$$\lambda(z,t) = \lambda_b(t)\, [1 - z^2/z_b(t)^2], \tag{4.27}$$

$$u_z(z,t) = -u_b(t)\, z/z_b(t), \tag{4.28}$$

$$p_z(z,t) = p_b(t)\, [1 - z^2/z_b(t)^2]^2, \tag{4.29}$$

where $z_b(t)$, $\lambda_b(t)$, $u_b(t)$, and $p_b(t)$ are time-dependent scale factors, measured relative to the center of the beam. Note that the length of the ion beam pulse, in the beam frame, that is affected by the linear velocity tilt is $L_b(t = 830 \text{ ns}) = 2\, z_b(t = 830$

ns) = 12 cm in Fig. 4.5, and corresponds to an approximate pulse length of 100 ns for the $300keV$ K^+ ion beam (at t = 830 ns). Following [Qin *et al.*, 2005], it can be shown that the functions of time $\lambda_b(t)$, $u_b(t)$, and $p_{z,b}(t)$ are invariants of the non-classical point symmetry group transformation. Substitution of the invariants into the warm-fluid equations would result in the loss of dependence on the axial coordinate z, and recovery of the longitudinal envelope equation for those invariants.

The potential inadequate treatment of the beam's distribution function $f_b(\mathbf{x}, \mathbf{v}, t)$ is a weak point in the fluid description of beams. A kinetic description spatially and temporally evolves a distribution function without many of the assumptions and constraints imposed by the warm-fluid model. Another significant drawback of a macroscopic one-fluid model in this particular case is its inability to support multiple-valued functions. For instance, the imposition of some waveforms will cause the $u_z(z)$ velocity dependence of the beam to become multiple-valued when faster accelerated particles attempt to overtake slower decelerated particles. For an ideal tilt, this occurs just downstream of the focal plane, but such a multiple-valued axial velocity function can occur anywhere from a few to dozens of cm upstream of the focus when a non-ideal waveform is used in experiments, especially when the waveform is above the ideal waveform early in time and below it late in time (refer to Fig. 4.2). Even when the applied waveform has an ideal shape, the one-fluid solution cannot propagate to longitudinal focus: the axial velocity profile becomes close to vertical in $\{z, u_z\}$ phase space as the beam reaches peak compression, and the focus will necessarily be composed of many fluid elements with different flow velocities but similar positions. However, formalisms based on the Vlasov equation can be used to investigate the propagation of a longitudinally compressed beam all the way to its focus.

4.3 Kinetic model

A $3D$ kinetic formalism based on the Vlasov equation has recently been developed for the simultaneous transverse and longitudinal focusing of a charge bunch in the presence of a plasma, which is assumed to completely charge and current neutralize the beam [Davidson and Qin, 2005]. Thus, the self-field forces of the ion beam are neglected in the model. Under such circumstances, the Vlasov equation can be solved for a wide range of initial beam distribution functions $f_b(\mathbf{r}, \mathbf{v}, 0)$ yielding exact dynamically compressing solutions [Davidson and Qin, 2005]. Neutralized drift compression of intense ion beams can be numerically investigated using the framework of this kinetic model, so that comparisons will be made to particle-in-cell simulations [Sefkow *et al.*, 2005a, Sefkow *et al.*, 2005b] and fast Faraday cup measurements [Sefkow *et al.*, 2006]. Although the original is a $3D$ formalism, azimuthal symmetry will be assumed here and the following kinetic model is treated in $2D$ $\{r, z\}$ coordinates.

Many choices of beam equilibria are possible for use in such a kinetic model of neutralized drift compression. It was shown in Sec. 4.2 that the acceleration gap and time-dependent voltage waveform can transform, in the beam frame, a constant line density profile into a parabolic line density profile in the region where a linear velocity tilt is imposed on the drifting ion beam. This observation is relevant to the task of simultaneous transverse and longitudinal focusing of an ion beam because the line density, axial velocity, and pressure profiles under discussion comprise a self-similar drift compression solution and can be used in models in order to transversely focus the entire beam pulse onto the same focal spot on the target [Qin *et al.*, 2005]. Therefore, for an ion beam which has already acquired a linear velocity tilt and whose

line density profile has been transformed into one with parabolic shape, we consider as an example the distribution function

$$f_b(W_\perp, W_z) = A\,\sqrt{(1 - W_z)}\,e^{-W_\perp}\,, \tag{4.30}$$

where A is a constant, and $0 \leq W_z < 1$. The constants of the motion, $W_\perp$ and W_z, are defined as

$$W_\perp = \frac{x^2 + y^2}{r_b^2(t)} + \frac{r_b^2(t)}{r_{b,0}^2\,v_{th,\perp}^2}\left[\left(v_x - \frac{x}{r_b(t)}\frac{dr_b(t)}{dt}\right)^2 + \left(v_y - \frac{y}{r_b(t)}\frac{dr_b(t)}{dt}\right)^2\right] \tag{4.31}$$

$$W_z = \frac{z^2}{z_b^2(t)} + \frac{z_b^2(t)}{z_{b,0}^2\,v_{th,z}^2}\left(v_z - \frac{z}{z_b(t)}\frac{dz_b(t)}{dt}\right)^2\,. \tag{4.32}$$

The quantities $r_b(t)$ and $z_b(t)$ are related to the rms transverse and axial dimensions of the charge bunch, and in the absence of an applied magnetic focusing field solve the effective envelope equations [Davidson and Qin, 2005]

$$\frac{d^2 r_b(t)}{dt^2} = \frac{r_{b,0}^2\,v_{th,\perp}^2}{r_b^3(t)} \tag{4.33}$$

$$\frac{d^2 z_b(t)}{dt^2} = \frac{z_{b,0}^2\,v_{th,z}^2}{z_b^3(t)}\,, \tag{4.34}$$

where the constants $r_{b,0}^2\,v_{th,\perp}^2$ and $z_{b,0}^2\,v_{th,z}^2$ are scaled transverse and longitudinal emittances. The constituent constants are the initial radius at the midplane, perpendicular thermal velocity, bunch length ($L_b = 2\,z_b$), and parallel thermal velocity of the beam ions. Then, the dynamical evolution of the number density of the charge bunch in

the beam frame is given by

$$n_b(r,z,t) = N_b \, \frac{\theta\{[z_b(t)+z][z_b(t)-z]\}}{\pi^{3/2} \, r_{b,0}^2 \, z_{b,0}} \left(\frac{r_{b,0}^2 \, z_{b,0}}{r_b^2(t) \, z_b(t)} \right) \times \left[1 - \left(\frac{z}{z_b(t)} \right)^2 \right] \, exp[-r^2/r_b^2(t)] \, , \tag{4.35}$$

where θ is the Heaviside step function, and $N_b = \int d\mathbf{r} \int d\mathbf{v} \; f_b(\mathbf{r},\mathbf{v},0)$ is a constant equal to the number of particles in the charge bunch. In this model, the number density is maximum at $(r,z,t) = (0,0,t)$, which is the center of the beam pulse in the beam frame. Note that, for this particular choice of $f_b(W_\perp, W_z)$, the line density profile is parabolic, the longitudinal pressure profile is double-parabolic, and the axial velocity profile is linearly dependent on z, *i.e.*,

$$v_z(z,t) = \frac{z}{z_b(t)} \frac{dz_b(t)}{dt} \, , \tag{4.36}$$

with an initial negative tilt, $[dz_b(t)/dt]_{t=0} < 0$, ensuring that the beam longitudinally compresses from its initial bunch length $L_{b,0} = 2 \, z_{b,0}$ at $t \equiv t_{kinetic} = 0$.

The kinetic model is solved numerically after choosing appropriate initial conditions, which closely represent the experimentally measured parameters. Since this model initializes a parabolic line density profile and already has an applied linear velocity tilt, the numerical solution of the beam's evolution begins with the center of the beam located at the center of the acceleration gap, at time $t_{kinetic} = 0$. However, a relative temporal offset is involved because the warm-fluid model and LSP simulations include the finite amount of time required to apply the E_z^{tilt} to the passing ion beam in the gap, which is responsible for the transformation of the line density from a

constant to parabolic profile. The 300 keV K^+ charge bunch is initialized with a 25% linear velocity tilt, Maxwellian temperature of $T_b = 0.4$ eV in both the transverse and longitudinal directions, constant radius $r_{b,0} = 2$ cm, and pulse half-length of $z_{b,0} = 9.6$ cm. The corresponding normalized effective emittance is 1.3×10^{-2} cm-mrad [Eq. (1.1)]. The full beam length of $L_b = 19.2$ cm corresponds to a pulse duration of $t_p = 160$ ns for the velocity involved here [Eq. (4.4)].

The transverse and axial dimensions of the charge bunch, $r_b(t)$ and $z_b(t)$, are both decreasing functions of time (until the focal plane is reached) for the initial conditions which specify compression in both directions:

$$r_b(t=0) = r_{b,0} \tag{4.37}$$

$$[dr_b(t)/dt]_{t=0} = -r_{b,0}/L_d \tag{4.38}$$

$$z_b(t=0) = z_{b,0} \tag{4.39}$$

$$[dz_b(t)/dt]_{t=0} = -z_{b,0}/L_d \,, \tag{4.40}$$

where L_d is the drift length to longitudinal focus ($L_d \sim 130$ cm, here). Once the effective envelope equations [Eqs. (4.33) and (4.34)] are solved for $r_b(t)$ and $z_b(t)$, the dynamical evolution of the number density of the charge bunch in the beam frame is solved according to Eq. (4.35). For the case where the ion beam's charge and current are completely neutralized, the calculation of the peak beam density expected at the focal plane gives insight into the density requirements for the neutralizing plasma near that location. As will be discussed in Chapter 6, beam compression will begin to stagnate due to defocusing space-charge forces when the beam density n_b surpasses the plasma density n_p, which can occur near a simultaneous focal plane even when

large plasma densities are employed, since n_b has inverse-square dependence on the beam radius r_b, as well as inverse linear dependence on pulse length L_b (or, z_b). However, the present Chapter is concerned with only longitudinal compression.

The kinetic model solutions considered here, which do not include the actual gap or experimental voltage waveform, can be directly compared to those from the other models beginning at axial and temporal locations sufficiently far removed from the region affected by the gap. For example, consider an axial location of $z = +29$ cm in the laboratory frame, since, by that location, the warm-fluid model and the particle-in-cell simulation clearly exhibit solutions (near the center of the beam) maintaining a parabolic line density profile with linear velocity tilt (refer to Fig. 4.5). The initialization described in Eqs. (4.37) through (4.40) assure that the kinetic solution coincides at the appropriate time with the parabolic line density profile (shown as a dashed line in Fig. 4.5) assembled downstream of the acceleration gap by the actual $E_z^{tilt}(z,t)$ used in the warm-fluid and LSP models. For the kinetic model, recall that the center of the charge bunch ($z = 0$ cm in the lab frame) is initialized at the location of the center of the gap with a linear velocity tilt already applied to it. The self-similar parabolic line density solution is then longitudinally compressed by the linear velocity tilt to a pulse length of $z_b(t) = 6$ cm, which corresponds to a duration of $t_p = 100$ ns, after an elapsed time of $t_{kinetic} = 410$ ns. The warm-fluid model assembles the same solution at the center of the beam (refer to Fig. 4.5) after an elapsed time of $t = 830$ ns. Both solutions coincide at the axial coordinate $z = +29$ cm in the laboratory frame. Evidently, the temporal offset between the two models for the mentioned parameters is $\Delta t = +420$ ns, which is also the location in time of the sign change in the voltage waveform (and polarity switch of the axial electric

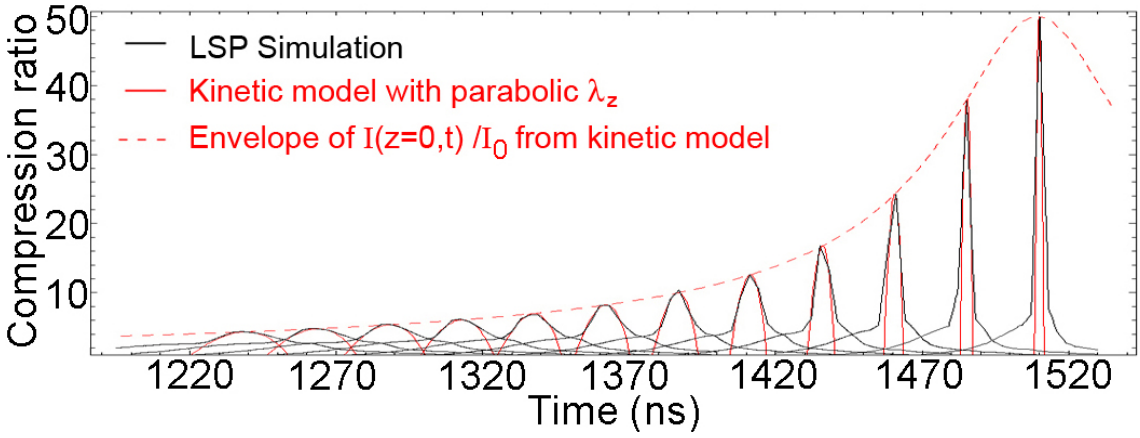

Figure 4.6: (Color) Longitudinal compression ratio $I_b(t)/I_0$ in the laboratory frame obtained from particle-in-cell simulation (black) and the kinetic model (red) at multiple axial locations near the focal plane from $z = +77$ cm to $z = +110$ cm.

field, refer to Fig. 4.2). This observation is true because the center of the beam is unaffected by the applied velocity tilt, and exits the acceleration gap traveling at the initial beam velocity, which is enforced by the kinetic model in the beam frame according to $v_z(z = 0, t) = 0$ for all time.

Figure 4.6 shows the comparison between the longitudinal compression ratios $I_b(t)/I_0$ predicted by the kinetic model and by particle-in-cell simulation for a number of axial locations throughout the drift region, including the longitudinal focal plane. The kinetic model results are transformed to the laboratory frame and calculated from

$$I(z,t) = 2\,\pi\,e_b \int dr\; r\; n_b(r,z,t)\; v_z(z,t)\;, \tag{4.41}$$

in order to compare to the laboratory frame current probes from the LSP code. The axial flow velocity in the kinetic model is defined in Eq. (4.36). A current compression ratio of 50, with pulse duration of $t_{fwhm} = 3.2$ ns, is predicted by both models. The

initial current of the K^+ beam is $I_0 = 25$ mA, and determined by the choice of constant N_b in Eq. (4.35). The peak ion beam density expected at the focal plane is a function of both $r_b(t)$ and $z_b(t)$. For a longitudinal current compression of 50 and focal spot radius of $r_b^{min} = 1$ cm, which corresponds to a current density compression factor of 200, the peak on-axis beam density achieved at the focal plane is approximately $n_b^{foc} \sim 2 \times 10^{10}$ cm^{-3} (and substantially lower away from the focal plane). This result indicates the kinetic model assumption (complete neutralization of the ion beam by the plasma) is reliable, since typical plasma densities in experiments are $5 - 10 \times 10^{10}$ cm^{-3}, and theory predicts adequate neutralization under these circumstances.

According to Fig. 4.6, the parabolic line density profile with a linear velocity tilt clearly accounts for the highly compressed region found near the center of the beam. Evidently, the parts of the beam which are not tilted well form a *pedestal* of current around the *peak* of current in each profile near the longitudinal focal plane. Figure 4.7 highlights the amount of deviation between the experimental and ideal voltage waveforms, which is the cause of pedestal formation. By charge conservation arguments, since the peaks in the current profiles near focus are due to the parts of the beam which participate in the region of linear velocity tilt, the formation of pedestals correspondingly reduce the total amount of current compression achievable at the beam's center. Therefore, pedestals around the current peaks are undesirable and should be minimized, especially those in front of the main pulse, since unwanted pre-heat of the target may occur.

It is important to note that the kinetic formalism, as used in this Section, only applies to the center of the beam which is tilted well, since the charge bunch is initialized with a linear velocity tilt and parabolic line density profile. In fact, Figs.

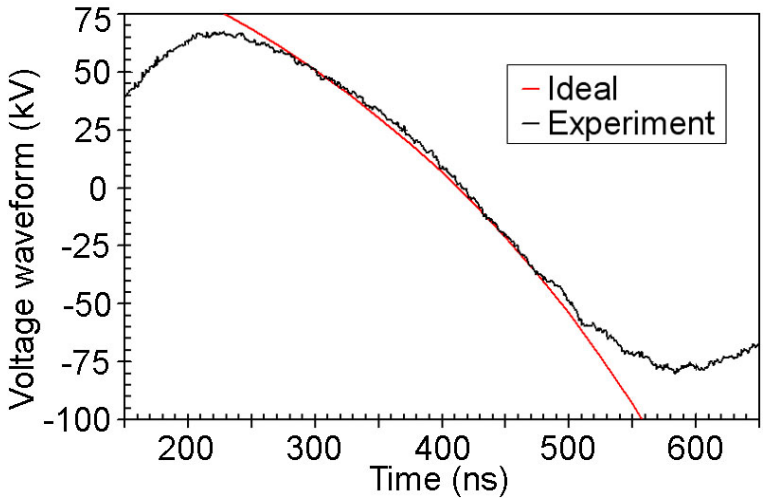

Figure 4.7: (Color) Comparison between the experimental voltage waveform (black) and ideal waveform (red) that would impose an ideal velocity tilt on the drifting beam. The axes have been reduced in scale relative to Fig. 4.2 in order to more clearly illustrate the differences between the two.

4.5 and 4.6 indicate that the majority of the beam affected by the experimental voltage waveform does not participate in neutralized drift compression within the region of the linear velocity tilt. Therefore, to understand the longitudinal dynamics of the parts of the beam that interact with the nonlinear part of the voltage waveform, and hence became part of the pedestal, the space- and time-dependent electric force found in the gap needs to be included in the model. Such an external force can be accounted for in the kinetic model as long as the self-forces of the beam can be neglected in the acceleration gap, and a dense plasma is provided in the drift region, since the model requires complete neutralization of the beam's charge and current. Provided an initial distribution function $f_b(\mathbf{r}, \mathbf{v}, 0)$, the kinetic model [Davidson and Qin, 2005] permits an exact determination of the beam's distribution function $f_b(\mathbf{r}, \mathbf{v}, t)$ for all later times, which can be used to investigate the detailed dynamic focusing of the charge bunch, in both the longitudinal and transverse directions, for the case of complete charge

and current neutralization. However, for peak experimental parameters ($E_0 = 400$ keV and $I_0 \sim 80$ mA), the perveance is approximately 1.3×10^{-3} [Eq. (4.2)] and well above the limit for unneutralized ballistic transport, indicating that the beam's self-field effects on the dynamics of the charge bunch cannot be ignored in regions without plasma, such as the transport section and acceleration gap.

4.4 Hybrid fluid-Vlasov model

The warm-fluid and kinetic models presented in the previous sections each have advantages and disadvantages. The main advantage (disadvantage) of the fluid (kinetic) model is its ability (inability) to correctly anticipate the non-ideal effects of an experimental voltage waveform's influence on the line density, axial velocity, and pressure profiles of the charge bunch as it undergoes neutralized drift compression. The main disadvantage (advantage) of the one-fluid (kinetic) code is its inability (ability) to propagate such a solution to the longitudinal focal plane when the flow velocity becomes multiple-valued. A hybrid combination of the two theoretical models is found to provide a satisfactory formalism for describing longitudinal drift compression in experiments from injection to focus [Sefkow and Davidson, 2006].

Given the fluid variables $\lambda(z,t)$, $u_z(z,t)$, and $p_z(z,t)$, a distribution function $f(z,v_z,t)$ can be constructed that allows the propagation, by means of the corresponding $1D$ Vlasov equation, of the compressing current profiles $I(z,t)$ of a charge bunch to the focal plane. Such a construction neglects the self-forces of the ion beam once the Vlasov solution propagates the fluid variables to focus, so the assumption in using the hybrid model is the complete neutralization of the ion beam by the

plasma near the focal plane region. This assumption holds true for recent experiments, which concentrate on longitudinal focusing without simultaneous transverse focusing to small spot size, where very good ($> 95\%$) charge neutralization is verified. Finally, the hybrid approach is most accurate in the regime where imperfections in the voltage waveform dominate the expected final compression ratios and minimum pulse durations. In the other limit, when voltage waveform control is nearly ideal, beam temperature effects give rise to chromatic abberation of the longitudinal focal plane, resulting in decreased compression factors and increased pulse lengths, as will be discussed in Section 4.7. Also, partial neutralization effects by the plasma (if present) give rise to defocusing self-forces (since the ion beam propagates beyond the traditional space-charge limit) as well as emittance growth, and will be discussed in Chapter 6. Both effects are expected to play a role in the determination of the upper limit of achievable current density compression when experimental voltage waveform imperfections do not dominate.

The $1D$ Vlasov equation (neglecting space-charge and external forces) in the longitudinal direction is [Eq. (3.19)]

$$\frac{\partial}{\partial t} f(z, v_z, t) + v_z \frac{\partial}{\partial z} f(z, v_z, t) = 0 \,, \tag{4.42}$$

and the general solution is a function of two variables, $\xi = z - v_z\,(t - t_0)$ and v_z,

$$f(z, v_z, t) = f[z - v_z\,(t - t_0), v_z, 0] \,, \tag{4.43}$$

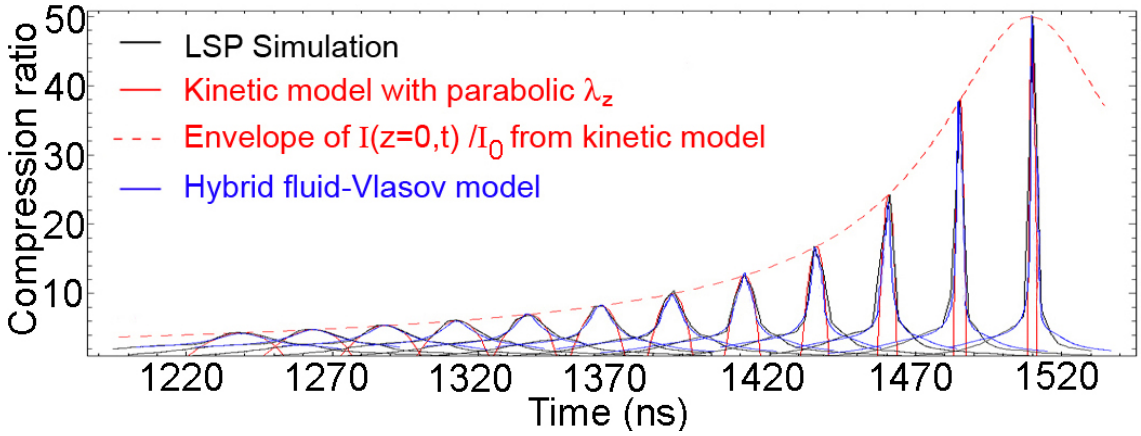

Figure 4.8: (Color) Longitudinal compression ratio $I_b(t)/I_0$ in the laboratory frame obtained from particle-in-cell simulation (black), the kinetic model (red), and the hybrid model (blue) at multiple axial locations near the focal plane from $z = +77$ cm to $z = +110$ cm.

where

$$\xi = z - v_z(\xi, t_0)\,(t - t_0)\,, \tag{4.44}$$

and

$$v_z = \frac{z - \xi}{t - t_0}\,. \tag{4.45}$$

Assuming an initial Maxwellian distribution with thermal velocity $v_{th,z}$, the current profile as a function of space and time for specified "initial" $\lambda(z,t)$ and $u_z(z,t)$ fluid variables is given by

$$I(z,t) = \frac{1}{(t-t_0)^2}\int \frac{d\xi}{\sqrt{2\pi}\,v_{th,z}}\,\lambda(\xi,t_0)\,(z-\xi) \times exp\left(-\frac{[z-\xi-v_z(\xi,t_0)\,(t-t_0)]^2}{2\,(t-t_0)^2\,v_{th,z}^2}\right)\,. \tag{4.46}$$

Here, $\lambda(z = \xi, t = t_0)$ and $v_z(\xi, t_0) = u_z(z = \xi, t = t_0)$ are evaluated as output from the warm-fluid model at a time $t = t_0$ *after* the voltage waveform has returned to zero ($t \sim 1\mu$s, here), corresponding to the required condition of no external forces. Effectively, the adoption of the hybrid model combines the advantages of the fluid and kinetic formalisms by propagating the warm-fluid solution to longitudinal focus as an initial condition to the $1D$ Vlasov equation.

The hybrid model solutions compared to those from the kinetic model and particle-in-cell simulation are shown in Fig. 4.8. Very good agreement is obtained between the full particle-in-cell simulation and the hybrid fluid-Vlasov treatment. Evidently, the formation of the pedestals in current due to beam interaction with the nonlinear part of the voltage waveform is described very well by the hybrid model.

4.5 PIC numerical simulation

As mentioned in earlier Sections in this Chapter, only kinetic treatments can properly compute the longitudinal compression factors of ion beams with finite temperature that have been velocity-tilted using a non-ideal voltage waveform imposed across a finite-size acceleration gap. Near the focal plane, the warm-fluid treatment will break down once the macroscopic variables attempt to take on multiple-values; sometimes this can happen significantly far upstream of the focal plane due to imperfections in the prescribed voltage waveform, if it over-decelerates or over-accelerates portions of the head or tail of the charge bunch, respectively, relative to the ideal voltage waveform. Whether the ion beam has been tilted ideally or not, faster tail particles will overtake slower head particles, and a framework that properly retains the velocity distribution information is therefore required to ascertain the current profiles in

the vicinity of the focal plane, as well as generally downstream of the focal plane. Knowledge of the complete set of simulated current profiles $I_b(z,t)$ of a charge bunch upstream and downstream of the focal plane is valuable when making comparisons to experimental data for a given set of system parameters, since the diagnostic is situated at one particular axial location for each measurement and not necessarily at the focal plane.

Consider the particle-in-cell simulation first discussed in Secs. 4.2 through 4.4. Figures 4.4, 4.6, and 4.8 do not include compression ratio profiles downstream of the focal plane. Longitudinal compression ratios from the particle-in-cell simulation at multiple axial locations, in steps of $\Delta z = 5$ cm, before and after the focal plane are presented at the top of Fig. 4.9. On the log scale, charge conservation is more apparent, in that significant portions of the head and tail of the charge bunch are decelerated or accelerated into the central peak portion, while the remainder of the surrounding beam, whose current is compressed into the central region, contributes long regions where $I_b(t)/I_0 < 1$; summing over the entire pulse yields the amount of charge present in the initial pulse length t_p.

Individual compression ratio profiles at the various fixed axial locations are not generally symmetric in time about their respective peak values in the laboratory frame when beam temperature effects are included. Even when the applied voltage waveform is itself symmetric in voltage and time (which this one is not, as shown in Fig. 4.2), the current profiles can only be symmetric in the beam frame, and therefore are not symmetric after transformation to the laboratory frame, where head and tail particles are moving relatively towards the center of the charge bunch but nevertheless have entirely $+\hat{z}$-directed momentum in the laboratory frame. As will be discussed

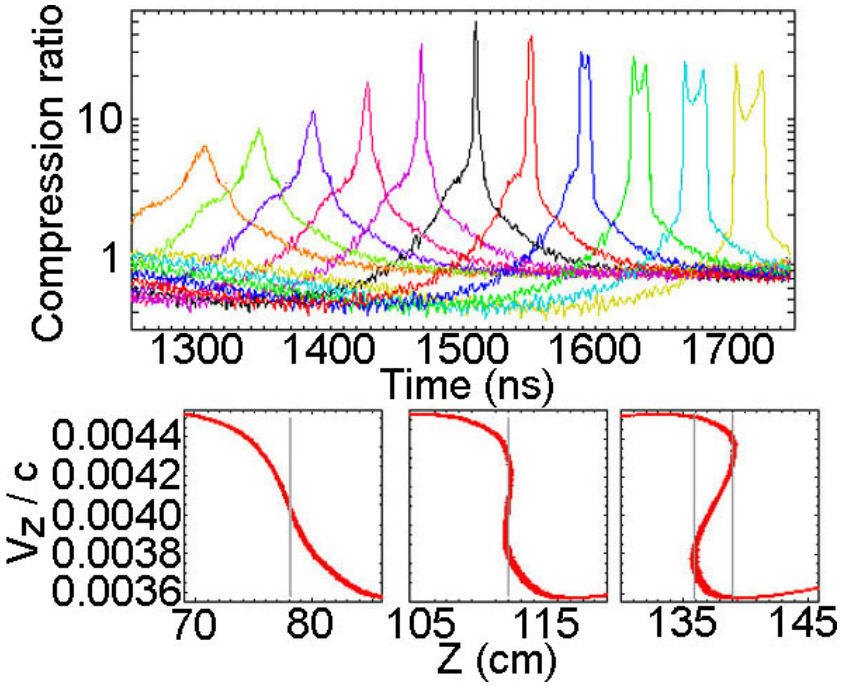

Figure 4.9: (Color) Longitudinal compression ratio $I_b(t)/I_0$ (Log scale) in the laboratory frame obtained from a particle-in-cell simulation at multiple axial locations before and after the focal plane, from $z = +85$ cm to $z = +135$ cm (top). The beam $\{z, v_z\}$ phase space in the laboratory frame before focus at $t = 1270$ ns (bottom left), near focus at $t = 1550$ ns (bottom center), and after focus at $t = 1760$ ns (bottom right).

in greater detail in Sec. 4.7, the slower head particles suffer more aberration due to longitudinal beam temperature during the focusing process because the thermal velocity is a greater fraction of the velocity of the head of the charge bunch compared to that of the tail. Therefore, temperature alone (even with an ideal waveform) results in asymmetric individual $I_b(t)/I_0$ profiles, and deviations from the ideal waveform only exacerbate the issue and lead to the formation of significant pedestals in current around the main compressed pulse, as discussed in Sec. 4.3. After transformation to the laboratory frame, slower head particles with increased aberration are sampled for relatively longer durations at one particular axial location (at the focal plane, or

upstream of it) before the arrival of the main pulse, and will therefore contribute more current to the pre-pulse for $t < t^{peak}$, whereas the opposite is true for the faster tail particles contributing to the post-pulse. After the focal plane passes, the situation reverses and the pre-pulse is reduced relative to the post-pulse, because the head particles are surpassed by the tail particles.

In addition, note from Fig. 4.9 that the profiles and the envelope of the peak current (from one profile to the next) are not generally symmetric about the focal plane itself. The reason is clear upon inspection of the ion beam $\{z, v_z\}$ particle phase space at the bottom of Fig 4.9, where three separate snapshots before, near, and after longitudinal focus are provided. Vertical gray lines in the bottom left and center particle phase space plots designate the location of the center of the beam and the peak current. Prior to longitudinal focus, this location is also usually near the inflection point where the curvature changes sign in the laboratory frame, caused by the particular non-ideal experimental voltage waveforms. For an ideal tilt, the plot of the $\{z, v_z\}$ phase space at longitudinal focus would be entirely vertical, however, significant deviation from that plane leading to decreased compression factors and increased pulse lengths can be caused by inaccurate application of the velocity tilt. The slower particles just in front of the main pulse and faster particles just behind it, resulting from the times when the voltage waveform begins and ends its approximation of the ideal waveform, contribute to the broadening of the pedestal current as well. In this particular case, the bottom center phase space plot shows that the misaligned head particles in front of the main pulse ($z = +112$ cm to $z = +114$ cm) have a slightly more vertical slope than the tail particles behind the main pulse ($z = +108$ cm to $z = +110$ cm), which implies another source of increased asymmetrical current in the

pre-pulse pedestal. After focus, the current profiles acquire *double-peak* and *plateau* characteristics, which directly result from tail beam current passing head beam current. The double-peaks originate in the backward S-shape of the $\{z, v_z\}$ phase space after the focal plane passes, as illustrated in the bottom right plot of Fig. 4.9. Two gray vertical lines in that plot draw attention to the turning-points associated with the double-peaks in the current profiles, where (constantly-evolving) portions of the beam maintain near-vertical configurations in $\{z, v_z\}$ space (and, hence, contribute peaks to the current profile) as the beam relatively decompresses. The intervening plateau region is a consequence of the extra current, relative to the profile upstream of the focal plane by the same amount, residing between the two gray lines, as evidenced by the fact that three distinct velocity spreads exist at one particular spatial coordinate in that region (as opposed to just one in the analogous upstream profile). Often, a measured double-peak and plateau signal can be used to infer the distance of the focal plane from the diagnostic in experiments. However, depending on the applied voltage waveform, double-peaks and plateaus can occur upstream of the focal plane, as well. Furthermore, double-peaks and plateaus are not formed in the current profiles when the initial beam pulse length is equal to (or less than) the prescribed pulse length t_p of the waveform [Eq. (4.21)]. In practice, creating an ion beam with sufficient uniformity in density and velocity space for pulse lengths of a few hundred ns is difficult, and is the subject of active research for short-pulse injector technology.

Profiles of the beam's average kinetic energy through various axial locations in the laboratory frame are given in Fig. 4.10. Early in time, less energetic beam particles arrive at a given location upstream of the focal plane, followed by a rapid increase in average kinetic energy due to the velocity tilt. Beyond the focal plane, after

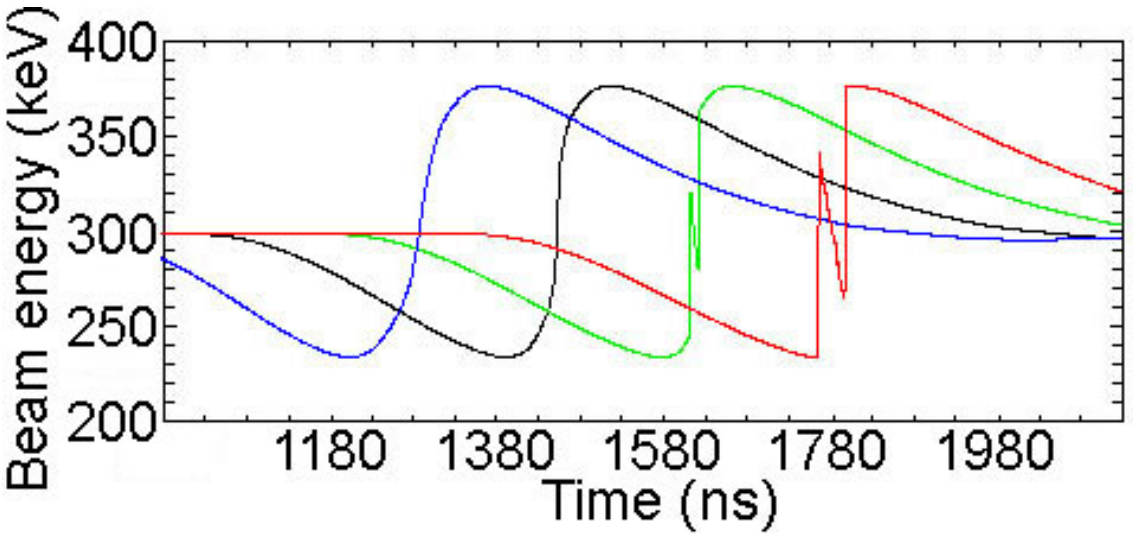

Figure 4.10: (Color) Profiles of average beam kinetic energy in the laboratory frame obtained from particle-in-cell simulation at $z = +80$ cm (blue), $z = +100$ cm (black), $z = +120$ cm (green), and $z = +140$ cm (red). The longitudinal focal plane occurs at $t = 1510$ ns at the axial location $z = +110$ cm.

significant portions of the charge bunch's faster tail pass the slower head, the average kinetic energy profiles first jump discontinuously after encountering the front portion of the backward S-shape in the $\{z, v_z\}$ phase space (corresponding to the first of the double-peaks, shown at the bottom right of Fig. 4.9), are subsequently followed by a decreasing section corresponding to the intervening plateau region, and are ultimately followed by another discontinuous jump after passing the rear portion of the backward S-shape (corresponding to the second of the double-peaks). The inability to propagate these discontinuities is the underlying reason behind the failure of fluid formalisms for longitudinal compression near the focal plane.

Generally, ion beam trajectories must be evaluated numerically by particle-in-cell techniques in order to take into account all the effects that ultimately determine the

quality of the focal plane. There is no universally valid analytic model for determining the expected current compression factor and pulse length, or even the current profile $I_b(t)$, at the focal plane because of the sensitive dependence on voltage waveform accuracy and finite-size gap geometry, most beam parameters, neutralization processes by the plasma, and other deleterious effects that decrease the compression results expected from an ideal situation. Many other effects of realistic beams with nonstationary density and velocity profiles require particle-in-cell simulations due to the general intractability of all the complex interactions possible, such as instabilities, collisions between beam particles or with plasma or neutral species, ionization of beam, plasma, or gas, nonlinear coupling between the longitudinal and transverse directions, and $3D$ effects. Three-dimensional effects can include such topics as beam off-centering, misalignment of focusing and/or accelerating elements, and beam-beam effects in the interaction regions of colliders or heavy ion fusion drivers. All of the aforementioned issues, and any other nonlinear forces, can give rise to emittance growth of the beam and therefore affect the longitudinal compression dynamics.

4.6 Comparison between theoretical models and experiment

In order to compress the ion beam in the longitudinal direction in experiments, the time-dependent voltage waveform imposes a velocity tilt on the passing ion beam. The beam drifts through a plasma column until a focal plane in current density is created between $L_d \sim 1 - 2.5$ m downstream of the gap (the length of the plasma column is a variable in experiments). The location of the focal plane of the beam is

determined by the slope of the pertinent part of the voltage waveform [$dV(t)/dt < 0$] and the beam energy. A high degree of space-charge neutralization by the plasma is required in order to compress intense ion beams to current densities of interest for high energy density physics and heavy ion fusion applications.

In recent experiments, the voltage waveform is timed to act upon the middle 1 μs of a $t_p \sim 6\,\mu$s beam. Future experiments seek to shorten the pulse length of the beam, ideally to the length of the compressing portion of the waveform, in order to minimize the amount of preheat impinging a target. As mentioned in Chapter 2, a fast "pinhole" Faraday cup measures the absolute beam current $I_b(t)$ in the presence of plasma, and is located at the far end of the plasma region such that the focal plane coincides with the collector plate [Sefkow *et al.*, 2006]. Experiments confirm that the collector only measures a signal proportional to I_b, without the negative influence of the other charged particle species in the system. The fast Faraday cup measurements are corroborated by optical measurements using a scintillator and fast phototube arrangement [Bieniosek *et al.*, 2005b]. However, only the fast Faraday cup diagnostic measures the actual ion beam current in the presence of plasma.

In order to compare measurements to numerical models and simulations, experiments are conducted in order to achieve large longitudinal compression ratios with short temporal pulse lengths. As in Sec. 2.5, an $E_0 = 320$ keV K^+ beam with initial radius $r_b = 2$ cm and current $I_0 = 19$ mA [corresponding to a perveance of 4.3×10^{-4}, according to Eq. (1.2)] is injected in the $+\hat{z}$ direction, and an approximate 15% velocity tilt is applied to the beam across the 3 cm gap, using the voltage waveform shown in Fig. 2.6. The beam drifts approximately $L_d \sim 2.4$ m through a plasma of density $n_p \sim 10^{10} - 10^{11}$ cm^{-3}. In order to simulate the experiment,

the measured experimental voltage waveform is used in both the hybrid fluid-Vlasov model and particle-in-cell simulation. This particular implementation of the kinetic model does not include a finite-size gap or non-ideal velocity tilt. In the models and particle-in-cell simulation, the ion beam is initialized $\Delta z = -8$ cm upstream of the gap (at $z = -30$ cm, as discussed in Sec. 4.2) with the same initial radius and current, and a $T_b = 0.2$ eV Maxwellian temperature in both the transverse and longitudinal directions [corresponding to a normalized effective emittance of 9.3×10^{-3} cm-mrad, according to Eq. (1.1)]. The plasma density and temperature are $n_p = 5 \times 10^{10}$ cm^{-3} and $T_p = 3$ eV, respectively. The kinetic model, fluid-Vlasov model, and LSP simulation all predict a current compression ratio of 60, with a full-width, half-maximum pulse length of approximately $t_{fwhm} \sim 4.5$ ns, at the focal plane located at $z = +219$ cm ($L_d \sim 2.4$ m), in excellent agreement with the fast Faraday cup measurement [Sefkow *et al.*, 2006]. In addition, the simulated beam reaches a peak on-axis density of approximately $n_b^{foc} \sim 1.8 \times 10^{10}$ cm^{-3} with final radius ($1/e$) $r_b^{foc} \sim 1$ cm at the focal plane, corresponding to a current density compression factor of 240.

Figure 4.11 plots the peak longitudinal compression factor measurement using the fast Faraday cup [Sefkow *et al.*, 2006] and provides a comparison to the corresponding results from particle-in-cell simulation, the kinetic model, and the hybrid fluid-Vlasov model [Sefkow and Davidson, 2006]. The experimental and particle-in-cell results are the same as those discussed in Sec. 2.5 and plotted in Fig. 2.8. The measurement is an average of the four best shots measured with the fast Faraday cup at the focal plane, which range in compression ratios from 55 to 65. The compressed ion beam signal is normalized to the initial beam current (without an applied tilt), and expanded around the location of peak compression in order to show the error

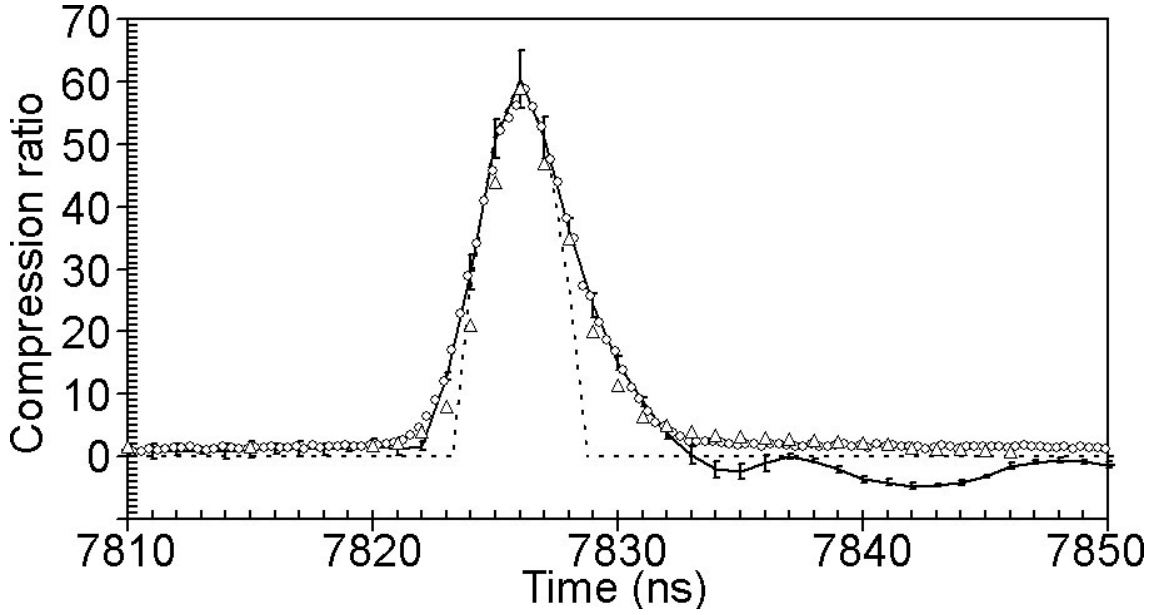

Figure 4.11: Comparison of longitudinal current compression $I_b(t)/I_0$ at the focal plane ($z = +219$ cm) between the experimental measurement using a fast Faraday cup (solid line with error bars), particle-in-cell simulation (open circles), kinetic model (dashed line), and hybrid model (open triangles) in the laboratory frame.

bars. The error bars plotted for the experiment are the 95% confidence intervals in the mean of the four shots. The measured ringing reflections in the experimental signal *after* the compressed beam pulse are due to impedance mismatch in the 50Ω circuit. The voltage waveforms used in these experiments are able to more closely approximate the ideal waveform over a wider interval of time and, therefore, compressed more of the ion beam pulse relative to the waveform shown in Figs. 2.2 and 2.7.

The hybrid model and the PIC simulation very accurately reproduce the measured amount of longitudinal compression, as well as the pulse duration. The kinetic model accurately reproduces the region of peak compression in the central portion of the beam but does not include the formation of the current pedestal due to the

imperfectly tilted beam, as discussed earlier. The shortest achievable pulse durations of the compressed ion beams in recent experiments are limited by the accuracy of experimental voltage waveform. As mentioned, waveform inaccuracy dominates the compression dynamics when significant nonlinear deviations from the ideal waveform are present, giving rise to current pedestal formation at the cost of reduced compression and longer pulse durations. If the beam had an ideal slope to its velocity tilt, chromatic aberration due to longitudinal temperature effects (discussed in Sec. 4.7) and partial neutralization effects (discussed in Sec. 6.2) are expected to dominate the minimum achievable pulse duration, as mentioned in Section 4.4.

4.7 Acceleration gap effects and aberration

In Sec. 4.1, the derivation of the equation describing an ideal velocity tilt [Eq. (4.21)], and the voltage waveform that produces it [Eq. (4.22)], assumed the beam encountered the imposed ideal time-dependent potential across an infinitely thin acceleration gap, had no thermal velocity distribution, and was entirely monoenergetic entering the gap. Realistically, an ion beam created in the laboratory must encounter a finite-size acceleration gap, always has some small but finite longitudinal temperature, and might not be entirely monoenergetic entering the gap (or have the appropriate energy for the imparted voltage waveform). On the first point, practical engineering considerations such as voltage hold-off and the Volt-second capability of the induction module's magnetic flux must be taken into account, which limit the strength and time rate of change of the induced electric field responsible for the application of the velocity tilt onto the ion beam. Also, voltage waveform accuracy and reproduction fidelity of the ideal waveform is an experimental concern. In order to make

better comparison to experimental data and provide detailed insight into the limiting physics of neutralized drift compression in the laboratory, a theoretical model needs to incorporate the actual spatial and temporal dependence of the induced electric field found in the finite-size gap, as discussed earlier in Sec. 4.2. In this Section, sets of $2D$ $\{r, z\}$ LSP simulations are executed in order to quantitatively assess and classify the origin of different sources of longitudinal focal plane degradation involving the acceleration gap. In order to isolate the effects of space-charge and plasma neutralization processes on the longitudinal dynamics from those arising strictly from the gap and initial beam parameters, the perveance and self-fields of the charge bunch are neglected by assuming perfect neutralization of the beam by the plasma in the particle-in-cell simulations presented in this Section, which is a valid assumption in the limit $n_p >> n_b$ everywhere in the drift region (including the focal plane).

4.7.1 Dependence on gap size and voltage waveform

In order to ascertain the effects of the actual 3 cm long acceleration gap in experiment on the longitudinal beam dynamics, two types of gap and voltage waveform for modifying the velocity distribution of an $E_0 = 400$ keV K^+ ion beam are studied. As in the numerical models of Sections 4.2 through 4.5, the axial coordinate in the laboratory frame extends from $z = -30$ cm to $z = +120$ cm. The plasma drift length can be varied from $1 - 2.5$ m in experiment, and can be similarly altered in the models by modifying the coordinate range as needed. In order to approximate an "infinitely thin" acceleration gap in $2D$ $\{r, z\}$ particle-in-cell simulations, which use a finite-size mathematical grid, either the beam would be directly injected from a chosen plane with the prescribed ideal velocity tilt [Eq. (4.21)] as a time-dependent

initial condition, or an axial electric field [Eq. (4.22)] can be strictly imposed over two adjacent grids. In the latter case, the shape of the longitudinal electric field in the axial coordinate would be triangular over the three nodes of the two grids, due to interpolation of the field to the grid nodes (refer to Sec. 3.3), and equals the same total energy as if all the field were located within one grid instance (two grid nodes). Depending on the size of the grid, which needs to be very small compared to the initial bunch length L_b, the time step is chosen so the energy of each of the beam particles is only modified by the electric field in a duration of a few time steps, in order to satisfy the particle Courant condition (refer to Sec. 3.3); such is the lower limit for approximating an "infinitely thin" gap in particle-in-cell simulation, whose numerics rely on finite differencing methods with underlying mathematical grids, without prescribing the velocity tilt as an initial condition. The other gap modeled in simulations is the actual finite-size gap in experiment. As mentioned in Sec. 4.2, the gap begins at the wall radius of $r_w = 3.8$ cm, is 3 cm long in the axial direction, is symmetric about the azimuth, and extends from $z = -22$ cm to $z = -19$ cm (refer to Fig. 4.1). All beam simulations involving the actual 3 cm long gap use an initial beam radius of $r_b = 2$ cm and convergence angle $\Delta\theta_r = -20$ mrad at the injection plane $z = -30$ cm, the reason for which will be discussed shortly.

Two types of voltage waveform are employed for application of the velocity tilt over the two different types of gap. They are referred to as the "sharp" and "smooth" waveforms, and are representatively plotted in Fig. 4.12. The $V(t)$ shown [refer to Eq. (4.22)] corresponds to an ideal waveform for an $E_0 = 400$ keV K^+ beam intending to apply a fractional tilt $f = 0.5$ over the initial pulse length $t_p = 300$ ns, from $t = 200$

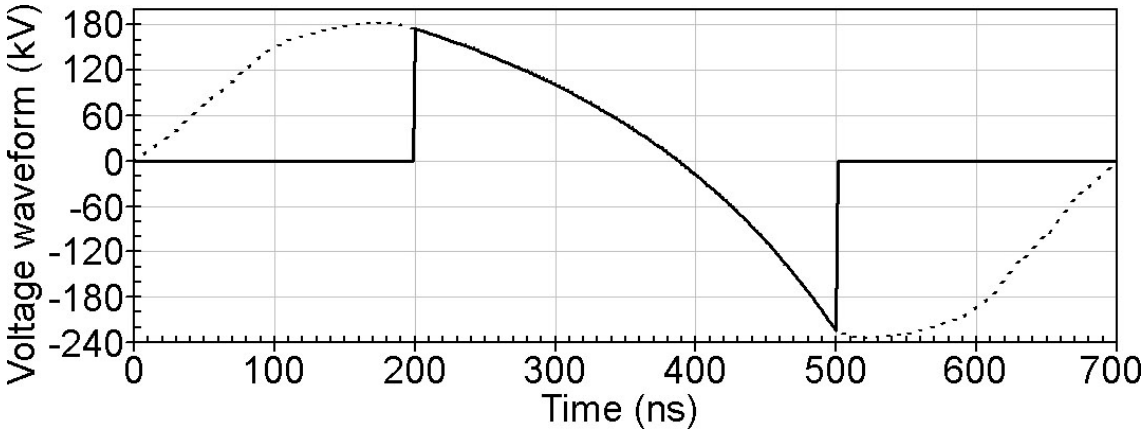

Figure 4.12: Representative "sharp" (solid line) and "smooth" (dashed line) voltage waveforms used in particle-in-cell simulations. The $V(t)$ shown [refer to Eq. (4.22)] corresponds to an ideal waveform for an $E_0 = 400$ keV K^+ beam with fractional tilt $f = 0.5$ and initial pulse length $t_p = 300$ ns, from $t = 200$ ns to $t = 500$ ns.

ns to $t = 500$ ns. The drift length to the longitudinal focal plane for these parameters is predicted by Eq. (4.20) to be $L_d = 78.7$ cm, or at a location of approximately $z = +58.2$ cm in the coordinate system here. Also, note that the resulting ideal velocity tilt [Eq. (4.21)] deviates from linearity later in the pulse. The "sharp" waveform ensures that only the ideal waveform is applied for the duration of the beam's initial pulse length. In experiments, the voltage waveform is produced by 12 independent modulator-driven magnetic cores, so the induction module can be programmed to provide a wide range of possible waveforms. The experimental waveform necessarily requires time for *ramping-up* to the peak positive voltage and for *ramping-down* to zero voltage, after the conclusion of the pertinent portion $[dV(t)/dt < 0]$ of the waveform for longitudinal compression, and results in a waveform akin to the "smooth" one shown in Fig. 4.12. Therefore, the "sharp" waveform might be considered an ideal case and the "smooth" waveform considered a more realistically achievable case. $2D$ $\{r, z\}$ particle-in-cell simulations comparing both voltage waveforms shed insight

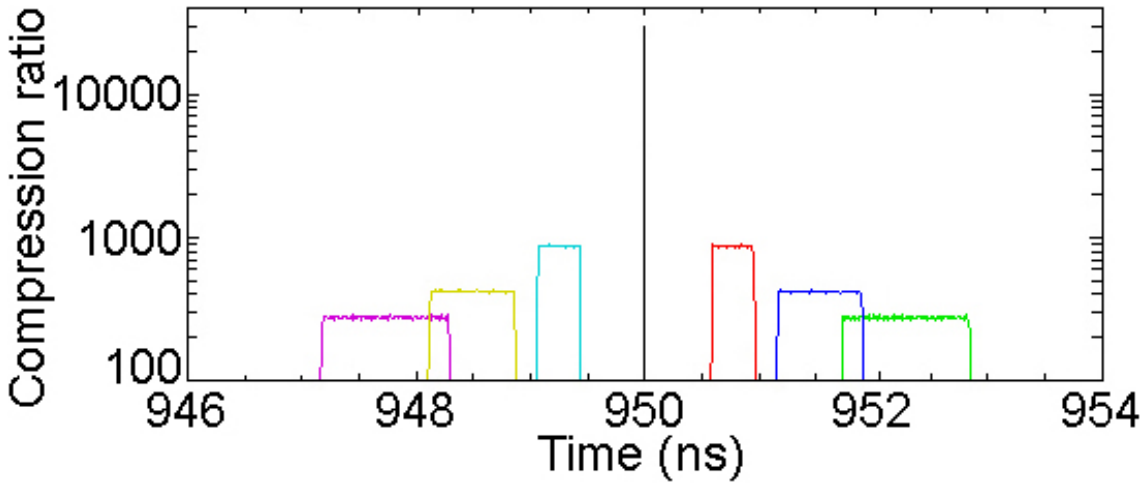

Figure 4.13: (Color) Longitudinal compression ratio $I_b(t)/I_0$ (Log scale) in the laboratory frame obtained from particle-in-cell simulation at multiple axial locations near the focal plane ($z = +58.25$ cm), in steps of $\Delta z = 0.1$ cm. The beam is initialized with $T_b = 0$ eV and ideally velocity-tilted using the "sharp" voltage waveform across an infinitely thin gap.

into the contribution to the longitudinal focusing dynamics from the suspected non-ideal extra voltage present in the "smooth" waveform (from $t = 0 - 200$ ns and $t = 500 - 700$ ns in Fig. 4.12).

A beam with an ideal velocity tilt results from applying the "sharp" voltage waveform from Fig. 4.12 over an infinitely thin acceleration gap in particle-in-cell simulation located at $z = -20.5$ cm, which coincides with the center of the 3 cm long actual gap. The initial cold K^+ beam parameters are $E_0 = 400$ keV, $t_p = 300$ ns, and $T_b = 0$ eV (corresponding to no emittance). As manifest in the current profiles of Fig. 4.13, the perfectly velocity-tilted beam with zero temperature achieves maximal longitudinal compression at the focal plane $z = +58.25$ cm. Since particle-in-cell codes evolve point particles, there should be no upper bound on the longitudinal current compression (or lower bound on the pulse length), as mentioned in Sec. 4.1, except for the temporal constraint of the finite time step. The ideal velocity tilt causes all of

the beam particles to arrive at the longitudinal focal plane at the exact same time, and results in a compression ratio of $30,000$ and pulse length of 0.01 ns, which are the expected classical limiting values given the initial pulse length $t_p = 300$ ns and discrete time step $\Delta t = 0.01$ ns. Since the initial pulse length is exactly equal to the intended pulse length to be compressed by the voltage waveform, the entire beam undergoes longitudinal compression and double-peaks and plateaus in the current profiles are not formed, as mentioned in Sec. 4.5. Since the initial current density is constant, the initial beam temperature is zero, the acceleration gap is infinitely thin, and an ideal velocity tilt is perfectly imparted, the axial beam number density profiles vary as $v_z^{-1}(z,t)$ and the resulting current profiles in the laboratory frame at fixed axial locations are constant in time (square-shaped, as in Fig. 4.13). Furthermore, the individual current profiles are symmetric about the center of the charge bunch in space and time, as well generally about the focal plane. Lastly, the beam focuses at time $t = 950$ ns, corresponding to $t_t^{foc} = L_d/v_t = 450$ ns [the tail analog of Eq. (4.1)] after the end of the "sharp" voltage waveform (refer to Fig. 4.12). No difference in compression is observed when the "smooth" waveform is used instead, even in the presence of excess beam (more than t_p), because the extra voltage cannot act across an infinitely thin gap to cause the velocity of the excess beam to lie along the ideal tilt slope, and thereby alter the current profile of the resulting main pulse.

The simulation just described is run again, except the infinitely thin gap is replaced with the finite-size 3 cm long gap. In this case, the induced electric field varies as a function of space according to Fig. 4.1 and as a function of time according to the "sharp" waveform in Fig. 4.12. As revealed in Fig. 4.14, the cold beam suffers longitudinal focus degradation compared to the case using an infinitely thin gap.

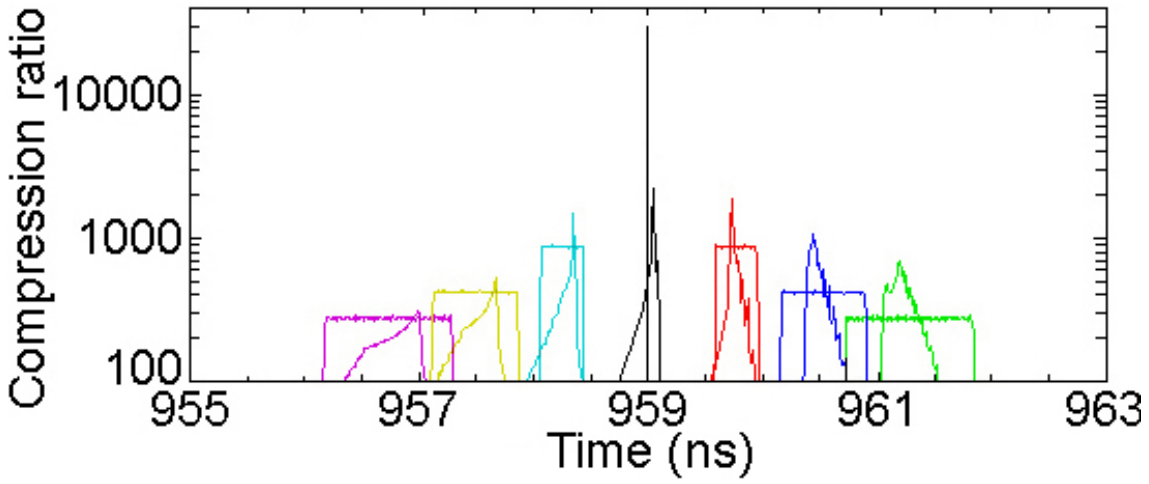

Figure 4.14: (Color) Longitudinal compression ratio $I_b(t)/I_0$ (Log scale) in the laboratory frame obtained from particle-in-cell simulation at multiple axial locations near the focal plane ($z = +59.5$ cm), in steps of $\Delta z = 0.1$ cm. The beam is initialized with $T_b = 0$ eV and encounters the "sharp" voltage waveform across a 3 cm long gap. The results for the infinitely thin gap case (including the spatial and temporal offset) from Fig. 4.13 are provided for comparison (constant current profiles).

The compression factor at the focal plane reduces to 2200, and the full-width, half-maximum pulse length increases to 0.03 ns, as a sole result of the finite-size gap. Also, the beam focuses at the axial location $z = +59.5$ cm at $t = 959$ ns, approximately 1.25 cm downstream of the focal plane associated with an infinitely thin gap located at the center of the 3 cm long gap. The additional 9 ns corresponds to the transit time required by the beam particles for the extra 1.25 cm, traveling at the average (initial) velocity v_0. Evidently, the spatial extent of the acceleration gap affects the drift length to the focal plane in a more complicated way than just adding the half-length of the finite-size gap to the original (ideal) calculation; the spatial and temporal offset compared to the infinitely thin gap case is related to the initial bunch length L_b and pulse length t_p compared to the effective length of the gap and transit time across the gap required by the beam particles, respectively, and will be discussed later in

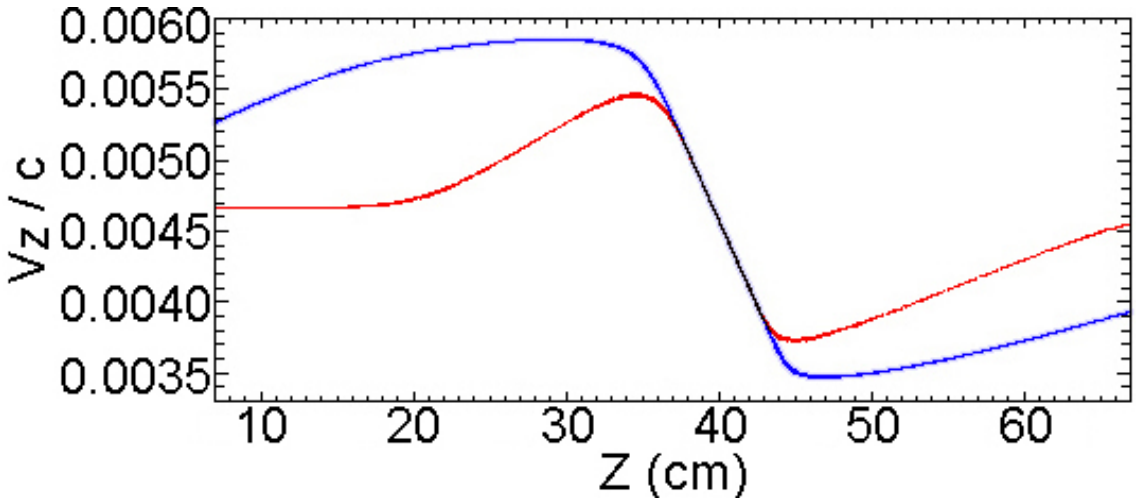

Figure 4.15: (Color) $\{z, v_z\}$ phase space at $t = 820$ ns for the $T_b = 0$ eV beam after application of the "sharp" voltage waveform (red) and "smooth" voltage waveform (blue) across the finite-size acceleration gap.

this Section. For comparison, the original simulation results from Fig. 4.13 using an infinitely thin gap are also provided in Fig. 4.14, with the spatial and temporal offset included for clarity. More discussion on the results of Fig. 4.14 will follow after the introduction of another simulation.

Another simulation of the finite-size acceleration gap case is executed, except the "sharp" voltage waveform is exchanged with the more realistic "smooth" waveform from Fig. 4.12. Figure 4.15 presents the significant difference witnessed in the $\{z, v_z\}$ phase space of the beam in the two waveform cases involving the finite-size gap. In both simulations, the initial beam pulse length is much longer than the amount intended for longitudinal compression ($t_p = 300$ ns), so that the extra voltage acts on the charge bunch. The longitudinally compressing portion of the beam at this particular time ($t = 820$ ns) is located in the region of negative slope, from approximately $z = +36$ cm to $z = +44$ cm. Decompressing portions of the charge bunch (regions of positive slope) precede and follow the compressing region. Note the differences in

shape due to the presence or absence of the extra voltage from the finite rise and fall time of the "smooth" waveform across the finite-size gap.

The transit time of the beam particles across the finite-size gap is an important consideration, since it causes the particles to sample a significant temporal range of the voltage waveform. Here, particles moving at v_0 require approximately 75 ns, which is about 25% of the intended t_p for longitudinal compression, to cross the roughly 10 cm of on-axis axial distance affected by the induced electric field near the gap (refer to Fig. 4.1). The durations of the head (tail) particles intended for deceleration (acceleration) by the time-dependent electric field within the gap are increased (decreased). In both waveform cases, particles at the entrance of the gap at $t = 200$ ns (refer to Fig. 4.12) begin to experience the correct amount of decelerating electric force, but do not encounter the requisite integrated amount of it because their transit time across the gap is so large. Since the voltage waveform changes appreciably in the time taken by the particles to cross the gap, the integrated force over that distance and time is less than the intended amount to achieve the desired fractional tilt. In addition, particles within the finite-size gap around the times when the longitudinally compressing part of the waveform begin ($t = 200$ ns, here) and end ($t = 500$ ns, here) do not receive the entire electric force required to participate in the intended velocity tilt, and so only contribute to the longitudinally *decompressing* head and tail portions of the beam before and after the main compressing pulse, respectively, as mentioned earlier. Since those portions are decompressing, their spatial extents later in time (as shown in Fig. 4.15) grow significantly compared to the original separation, due to the relative expansion away from the main compressing pulse. It should be apparent that the temporal and spatial "shapes" of the electric field in the gap (from the voltage

waveform and boundary conditions of the physical gap) impress themselves upon the phase space of the resulting beam.

The result in Fig. 4.15 clearly demonstrates that the "sharp" voltage waveform, which intends to ideally compress exactly 300 ns of beam pulse, actually compresses less of the beam than the "smooth" waveform. The important difference between the "sharp" and "smooth" waveforms is that the extra voltage present in the "smooth" waveform acts on the excess beam involved to re-populate the low and high velocity space regions of the intended fractional tilt, which are left more unpopulated in the "sharp" waveform case (the range of the intended velocity tilt is approximately $v_z/c = \{0.0035, 0.0058\}$). Therefore, the suspected non-ideal extra voltage from the ramp-up and ramp-down of the "smooth" waveform is actually *advantageous* because it provides extra integrated force to populate the lower- and higher-energy velocity space of the charge bunch's head and tail, respectively, with the excess surrounding beam. It effectively recovers some of the fractional tilt normally lost in the "sharp" waveform case due to the finite-size gap. In the case of the infinitely thin gap, it is clear that the same does not occur because the integrated force cannot be increased without the added spatial extent of the finite-size gap, and explains why a difference between the "sharp" and "smooth" waveforms is not seen in that case. The "sharp" and "smooth" waveforms, applied across the finite-size gap, result in approximate effective fractional tilts of $f = 0.3$ and $f = 0.4$, respectively, rather than the intended $f = 0.5$ [however, the drift length L_d does *not* change according to Eqs. (4.15) or (4.20) due to the change in v_h, v_t, and f]. In other words, the actual 3 cm long gap effectively reduces the amount of imparted fractional tilt because of its inability to realize the maximum expected charge bunch head deceleration and tail acceleration,

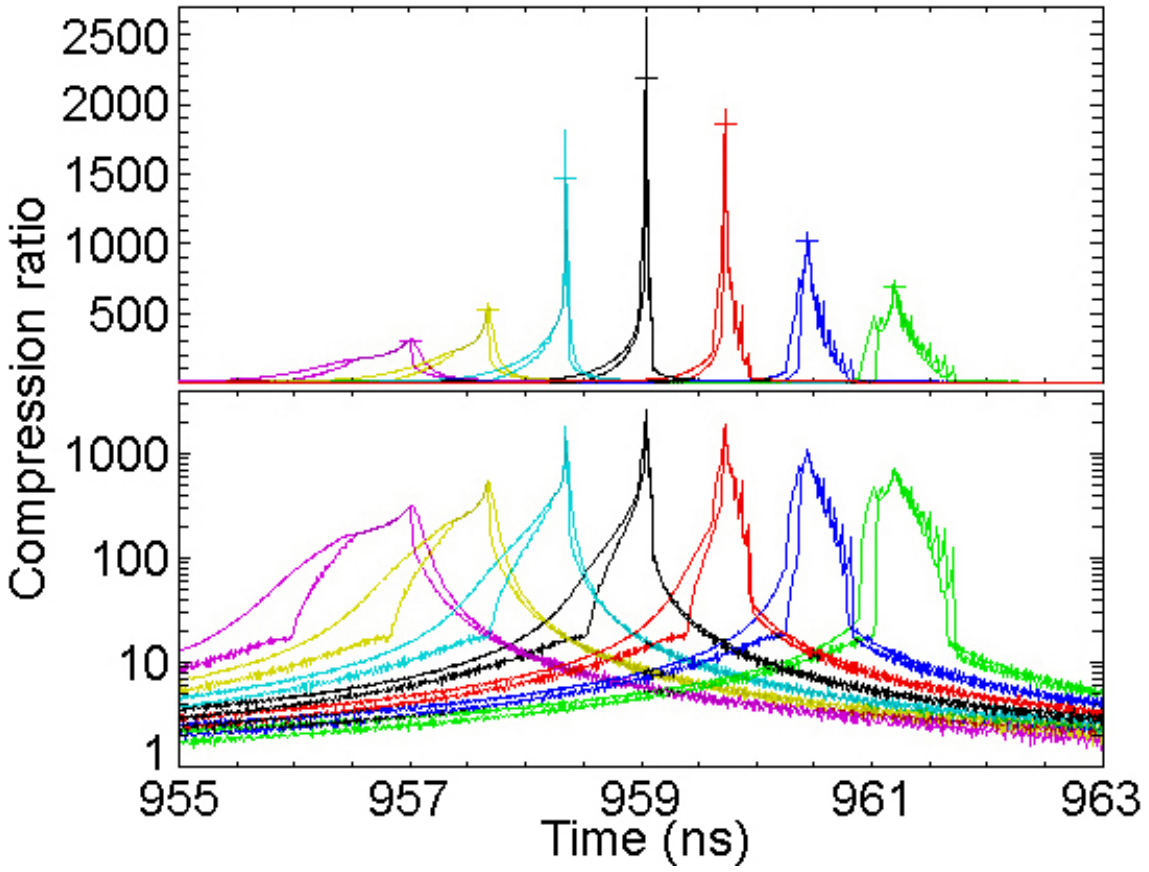

Figure 4.16: (Color) Longitudinal compression ratio $I_b(t)/I_0$ comparison between "smooth" (top profiles in both plots) and "sharp" (bottom profiles in both plots) voltage waveforms on linear (top) and Log (bottom) scales in the laboratory frame obtained from particle-in-cell simulation, at multiple axial locations near the focal plane ($z = +59.5$ cm), in steps of $\Delta z = 0.1$ cm. The beams are initialized with $T_b = 0$ eV and are velocity-tilted across a 3 cm long gap. Nonphysical horizontal bars are added on the linear scale plot to clearly demarcate the peak compression obtained by the "sharp" waveform, which does not compress the ion beam as well as the "smooth" waveform. The Log scale plot is provided to more clearly show the increased amount of current in the pre-pulse pedestals of the profiles due to the "smooth" voltage waveform.

due to the associated transit time of the beam particles, which temporally sample more of the voltage waveform than intended.

The longitudinal compression results from the "sharp" and "smooth" voltage waveform cases for a beam with zero temperature interacting with a finite-size acceleration gap are shown in Fig. 4.16. In the linear plot, the difference in compression and pulse length is clearly seen for the various current profiles at equally-spaced axial locations. The maximum current compression at the focal plane increases from 2200 to 2650 due to the larger effective fractional tilt f provided by the extra voltage present in the "smooth" waveform. However, more current contribution to the prepulse pedestals also occurs due to the extra voltage, as more clearly seen on the Log plot of Fig. 4.16, and the full-width, half-maximum pulse length at the focal plane increases by approximately 17% to 0.035 ns.

Figure 4.17 plots the beam $\{z, v_z\}$ phase space, for an initially cold ($T_b = 0$ eV) beam, at the longitudinal focal plane for the case imposing the "sharp" voltage waveform across an infinitely thin acceleration gap, and compares it to the same for the cases imparting the "smooth" and "sharp" waveforms across the experimental finite-size gap. As described earlier, the ideal velocity tilt of a beam without temperature across an infinitely thin gap results in a perfect longitudinal compression at a desired focal plane that is mathematically infinite (with a vanishing pulse length) in the point particle limit, as discussed in Sec. 4.1 and shown on the left of Fig. 4.17, where all of the beam particles arrived at the longitudinal focal plane ($z = +58.25$ cm) at the exact same time ($t = 950$ ns). The corresponding compression "result" of $30,000$ (instead of ∞) is limited by the finite discrete time interval used in the numerical simulation. The center and right frames of Fig. 4.17 illustrate the effects

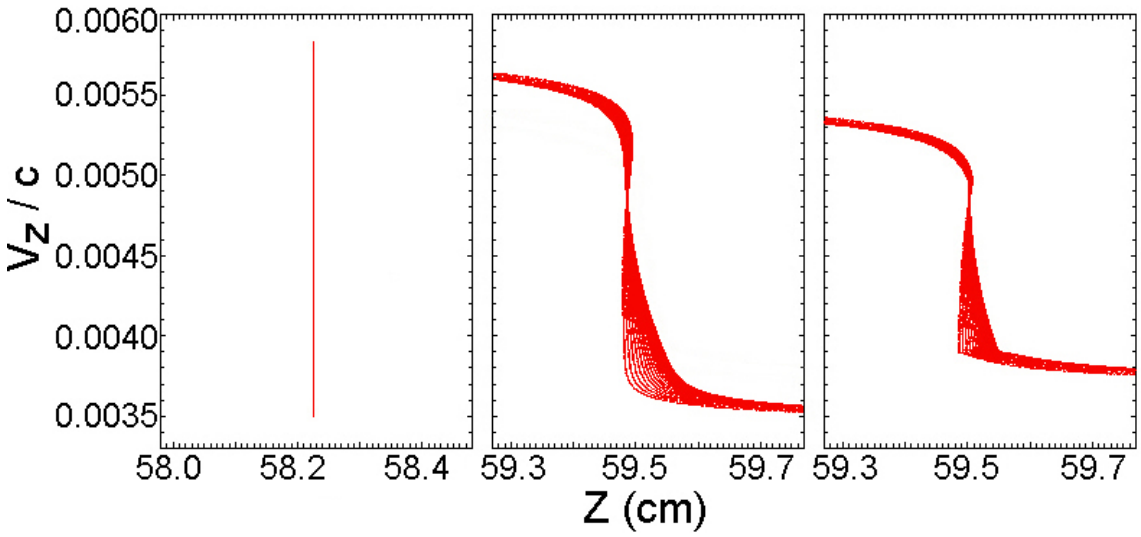

Figure 4.17: (Color) $\{z, v_z\}$ phase space at the focal plane for the $T_b = 0$ eV beam using the "sharp" voltage waveform across an infinitely thin gap (left), and "smooth" (center) and "sharp" (right) voltage waveforms across the finite-size gap. Longitudinal focus occurs at $z = +58.25$ cm and $t = 950$ ns for the infinitely thin gap case and at $z = +59.5$ cm and $t = 959$ ns for the finite-size gap cases.

of a finite-size acceleration gap and the application of "smooth" and "sharp" voltage waveforms, respectively, on an initially cold beam.

Two important conclusions can be drawn from the center and right plots of Fig. 4.17. First, the imposition of the time-dependent voltage waveform $V(t)$ across a finite-size gap imparts velocity spread akin to an effective longitudinal temperature on an otherwise initially cold beam with no space-charge. Therefore, it sets a finite upper bound on the maximum longitudinal compression factor and minimum pulse length, due to chromatic aberration of the focal plane, as opposed to the artificial case of an infinitely thin gap. The origin of this $2D$ effect is found in the coupling of the transverse and longitudinal phase space of the beam as it traverses the finite-size gap. The equations and boundary conditions describing the electric field in the gap necessitate the existence of radial components wherever $\partial E_z(r, z)/\partial z \neq 0$, as

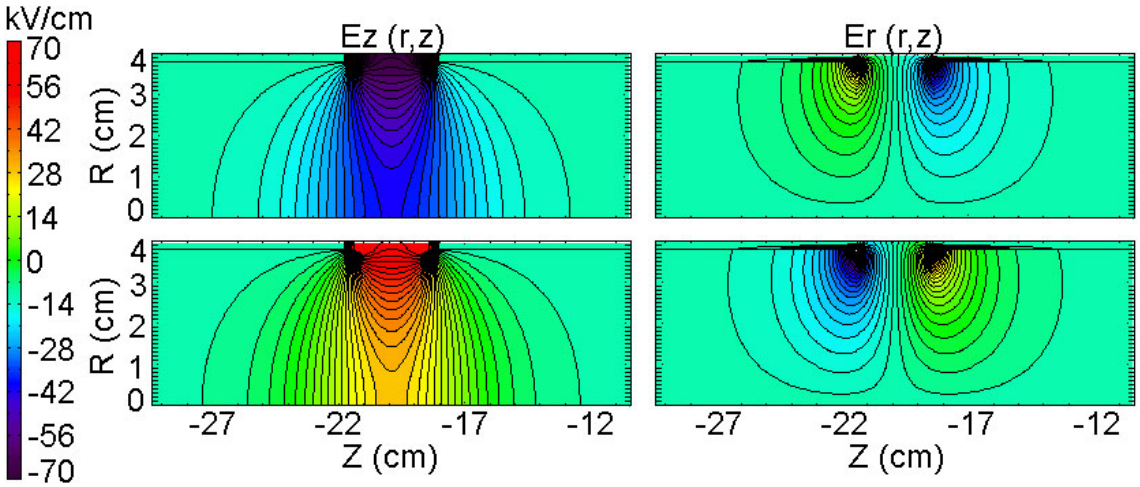

Figure 4.18: (Color) $\{r, z\}$ isocontour plots of $E_z(r, z)$ at $t = 200$ ns (top left) and $t = 500$ ns (bottom left) and $E_r(r, z)$ at $t = 200$ ns (top right) and $t = 500$ ns (bottom right) near the 3 cm acceleration gap. All plots are on the same linear scale.

illustrated in Fig. 4.18. The time-dependent nature of the voltage waveform and the transit time across the gap imply an imbalance of integrated $E_r(r, z, t)$ felt by each particle. The time-dependent radial electric fields modify the v_r distribution of the beam non-uniformly, just as the axial electric fields modify the v_z distribution of the beam in order to apply a longitudinally compressing tilt. As a result, particles initially at different radii entering the gap sample unequal amounts of integrated $E_z(r, z, t)$ across the gap, instead of the same radially-independent integrated amount. During the compressing part of the voltage waveform $[dV(t)/dt < 0]$, beam particles at larger radii encounter a stronger imbalance of E_r fields, acquire more time-dependent changes to v_r, and are subsequently decelerated [for times when $V(t) > 0$ and $E_z(t) < 0$] or accelerated [for times when $V(t) < 0$ and $E_z(t) > 0$] in the axial direction *more* than particles initially closer to the $r = 0$ axis. When the switch from more axial deceleration to acceleration for particles farther off-axis occurs, it causes the X-shaped spread in the longitudinal velocity, apparent in the center and right plots of Fig. 4.17.

Therefore, due to the transverse movement of the particle trajectories within the gap, the beam acquires a longitudinal (in addition to transverse) velocity spread similar to temperature (and emittance), and chromatic aberration of the focal plane arises.

The effective longitudinal temperature increase acquired by the beam, due to the coupling of the transverse and longitudinal dynamics in the finite-size gap, is dependent upon the gap geometry, voltage waveform, and beam parameters, such as axial velocity, radius, convergence angle, and emittance, and will be quantitatively determined in Sec. 4.7.2 for the beam parameters considered here. It is important to note that the reduced fractional axial velocity tilt f a beam suffers crossing a finite-size gap, as discussed earlier and shown in Figs. 4.15 and 4.17, should also be interpreted as an increase in effective longitudinal temperature, since the drift length L_d to the focal plane does not change with the reduced f value according to Eq. (4.20). As will be shown in upcoming simulations, the presence of additional beam temperature in the gap decreases the compression ratio and increases the pulse length at focus without changing the axial location of the focal plane.

Since the coupling effect that gives rise to an increase in effective longitudinal beam temperature in the finite-size gap is related to both the transverse and longitudinal dynamics of the beam, it is also dependent upon the transverse convergence or divergence of the beam as it enters the gap, in addition to its radius. Intense beams generally have significant radially-converging angles, which are almost always much larger than the transverse velocity spread, as they exit the transport section and enter the gap, for transverse confinement as well as focusing. As will be discussed in Sec. 6.1, the radial electric field imbalance across the gap provides an average time-dependent radial defocusing force to both the head *and* tail of the beam as the

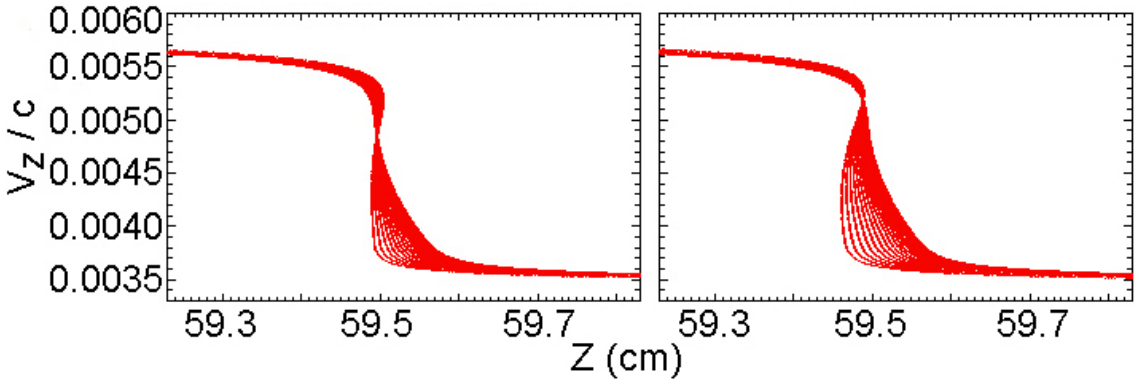

Figure 4.19: (Color) $\{z, v_z\}$ phase space at the focal plane for the $T_b = 0$ eV, $r_b = 2$ cm beam with a -20 mr convergence angle at $z = -30$ cm (left) [from Fig. 4.17] and no convergence angle (right) using the "smooth" voltage waveform across the finite-size gap. The approximate maximum compression ratios and minimum full-width, half-maximum pulse lengths are 2650 and 0.035 ns compared to 1500 and 0.065 ns.

charge bunch traverses the gap during the longitudinally compressing $[dV(t)/dt < 0]$ part of the waveform. However, radial motion is the reason why particles at different radii sample unequal amounts of $E_z(r, z, t)$ across the gap and acquire effective longitudinal temperature. Therefore, a beam entering the gap with a trajectory that is converging radially, due to the focusing force applied by the last set of quadrupoles or solenoids in the transport section, will have some of its initial convergence offset by the time-dependent radial defocusing force, and thereby sample less integrated imbalance of $E_z(r, z, t)$ across the gap, and acquire less effective longitudinal temperature, compared to the case of an incoming beam without an applied radial angle. In other words, the necessary convergence angle of the beam (quoted as $\Delta\theta_r$ in radians as the beam radius r_b over the transverse focusing length L_r) as it enters the gap helps reduce the amount of extra effective longitudinal temperature acquired and therefore increases the achievable maximum compression ratio. The effect is shown in Fig. 4.19 for the beam parameters under previous consideration, with $r_b = 2$ cm

and a convergence angle of $\Delta\theta_r = -20$ mrad. The v_r of the beam particles varies radially as $-v_r(r) = -v_z^0\,(r/r_b)(r_b/L_r)$ for $r = 0$ to $r = r_b$. The case without a convergence angle suffered more gap-induced effective temperature increase, and focal plane aberration, due to more disparate radial movement within the gap compared to the case with an -20 mrad angle applied to the $r_b = 2$ cm beam at the plane of injection $z = -30$ cm. The $r_b = 2$ cm, $\Delta\theta_r = -20$ mrad case is approximately the optimum radial initial condition for the average off-setting of the time-dependent defocusing force for the voltage waveforms of Fig. 4.12. It minimizes the sampled $E_z(r, z, t)$ imbalance felt by the beam particles, and is used in all of the previous and following simulations involving the finite-size gap. Further discussion on the role of the radial electric field components in the gap on longitudinal compression dynamics will be provided in Chapter 6.

The second conclusion drawn from Fig. 4.17 is that the effective reduction of the intended fractional tilt, as mentioned earlier, by the "smooth" and "sharp" waveforms acting across the finite-size gap, affects the faster tail particle velocities more than the slower head particle velocities. From the left frame of Fig. 4.17, the expected minimum head and maximum tail velocities after application of the tilt are approximately $v_z^h/c = 0.00350$ and $v_z^t/c = 0.00583$, respectively. From the center and right frames of Fig. 4.17, the maximum realized tail velocities in the finite-size gap cases are substantially reduced compared to the ideal result from the infinitely thin gap case, more so than the relative difference between the minimum head velocities compared to the ideal result. This effect occurs because accelerated tail particles have reduced transit times relative to the decelerated head particles, and therefore the integrated energy gain by the tail particles is not equal and opposite to the integrated energy

loss by the head particles, since the energy modulation from the voltage waveform is not imparted instantaneously and particles necessarily sample more waveform (in time) than intended.

In reality, not only does the acceleration gap have finite-size, but an experimentally-realizable charge bunch always has non-zero initial longitudinal temperature, implying that the longitudinal compression factors and temporal pulse lengths at focus will be further reduced and increased, respectively, due to larger amounts of chromatic aberration relative to the cold beam cases. Also, non-zero temperature and emittance affect transverse compression, as well. For example, in transverse compression experiments, a factor of 3 change in emittance, whether brought about by an increase in beam radius, temperature, or various nonlinear forces, resulted in an increase of 30% in minimum spot size. In order to quantify how non-zero beam temperature further reduces the previously established finite upper limits on longitudinal compression of a cold beam with NDCX-relevant parameters, additional simulations including the non-zero temperature and emittance of an ion beam are carried out.

4.7.2 Dependence on emittance

In a similar simulation to the first one presented in Section 4.7.1, the "sharp" voltage waveform is employed over an infinitely thin acceleration gap and causes a fractional tilt of $f = 0.5$ on a beam whose initial parameters are $E_0 = 400$ keV and $t_p = 300$ ns, with a $T_b = 0.2$ eV Maxwellian distribution in both the transverse and longitudinal directions [corresponding to a normalized effective emittance of 9.3×10^{-3} cm-mrad, according to Eq. (1.1)]. The chosen beam temperature is consistent with measurements and longitudinal compression results from experiments, as previously discussed

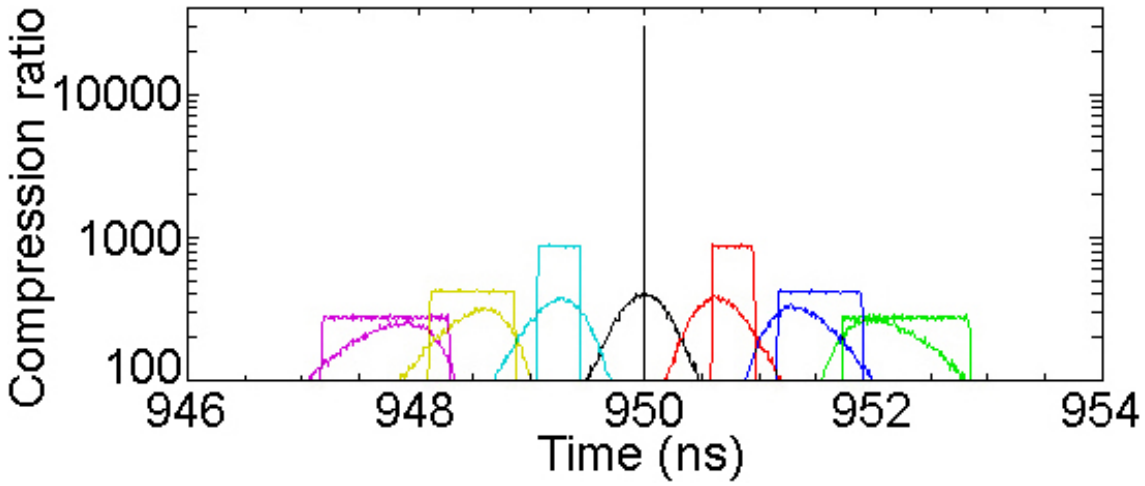

Figure 4.20: (Color) Longitudinal compression ratio $I_b(t)/I_0$ (Log scale) comparison in the laboratory frame obtained from simulation, at multiple axial locations near the focal plane ($z = +58.25$ cm), in steps of $\Delta z = 0.1$ cm, for beams initialized with $T_b = 0$ eV (constant current profiles) and $T_b = 0.2$ eV (varying current profiles), both of which are ideally tilted using the "sharp" waveform across an infinitely thin gap.

in Sections 2.5 and 4.6. The current compression results near the focal plane in the laboratory frame are given in Fig. 4.20, alongside the reproduced results from Fig. 4.13 involving the same simulation with no initial emittance. The maximum current compression ratio at the focal plane is 400 with a full-width, half-maximum pulse length of approximately $t_{fwhm} \sim 0.60$ ns.

The results in Fig. 4.20 show that the overall longitudinal compression is significantly affected by chromatic aberration effects, which causes a smearing of the longitudinal focal plane because of the spread in axial velocities involved. A positive effect of the aberration is an increased level of axial tolerance for aligning a diagnostic or target with the focal plane: increased levels of beam temperature cause the peak current compression to not vary as sensitively as a function of axial coordinate compared to colder beam cases. As similarly discussed in Section 4.5, the individual compression ratio profiles at the various fixed axial locations around the focal

plane are not generally symmetric in time about their respective peak values in the laboratory frame, due to the inclusion of beam temperature effects. As mentioned earlier, the presence of temperature alone (even with an ideal voltage waveform applied across an infinitely thin gap) results in asymmetric individual $I_b(t)/I_0$ profiles away from the focal plane, and experimental deviations from the ideal voltage waveform only exacerbate the issue and lead to the formation of significant pedestals in current around the main compressed pulse. Slower head particles suffer increased levels of chromatic aberration (to be discussed shortly) and are sampled for longer durations at one particular axial location (at the focal plane, or upstream of it) in the laboratory frame before the arrival of the main pulse. They therefore contribute more current to the pre-pulse for $t < t^{peak}$, whereas the opposite is true for the faster tail particles contributing to the post-pulse. After the focal plane has passed, the situation reverses and the pre-pulse is reduced relative to the post-pulse because the head particles are surpassed by the tail particles. Although, since the exact amount of initial beam pulse $t_p = 300$ ns is perfectly tilted by the voltage waveform in the simulation shown in Fig. 4.20, double-peaks and plateaus in the current profiles are not created. In addition, the current profiles and the envelope of the peak current (from one profile to the next) are symmetric about the focal plane itself.

Returning to the results presented in Figs. 4.14 and 4.16 in Sec. 4.7.1, it is clear that the current profiles in those plots are asymmetric due to the effective non-uniform longitudinal temperature imparted to an initially cold beam by the finite-size acceleration gap. Likewise, the individual current profiles and the envelope of the peak current (from one profile to the next) are not generally symmetric about the focal plane itself because more than the prescribed initial pulse length $t_p = 300$ ns of beam

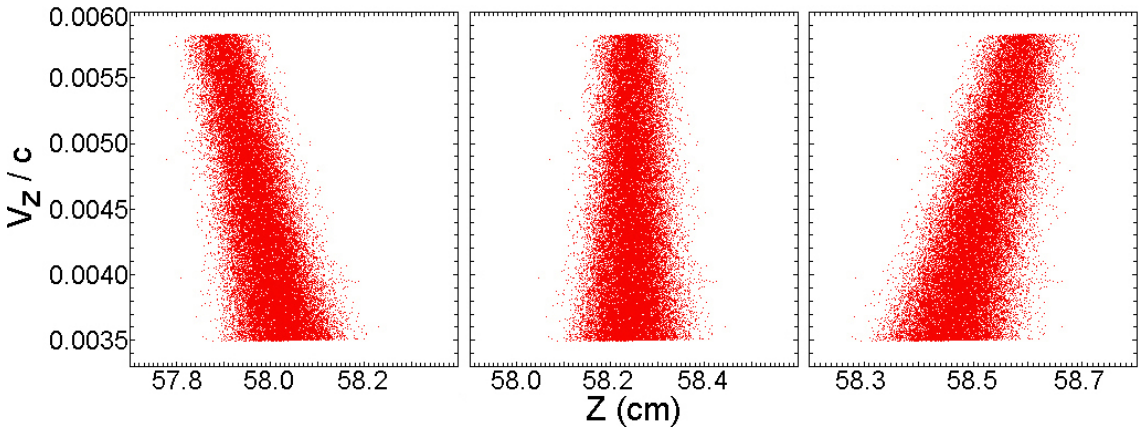

Figure 4.21: (Color) $\{z, v_z\}$ phase space for the $T_b = 0.2$ eV beam, using the "sharp" voltage waveform across an infinitely thin gap, 2 ns before arrival at the focal plane (left), at the focal plane (center), and 2 ns after passing the focal plane (right). Longitudinal focus occurs at $z = +58.25$ cm and $t = 950$ ns.

is used in those simulations, causing the formation of double-peaks and plateaus in the current profiles downstream of the focal plane, as discussed in Sec. 4.5.

In order to quantify the amount of chromatic aberration caused by longitudinal temperature alone, the $\{z, v_z\}$ phase space 2 ns upstream of the focal plane, at the focal plane, and 2 ns downstream of the focal plane for the $T_b = 0.2$ eV beam using the "sharp" waveform across an infinitely thin gap are presented in Fig. 4.21. The distance traveled in 2 ns by the beam in this case corresponds to approximately 0.2 cm, and so the yellow, black, and blue varying current profiles of the $T_b = 0.2$ eV case in Fig. 4.20 are directly related to the left, center, and right frames of Fig. 4.21, respectively. Inspection of the two figures immediately highlights the contribution of the axial thermal velocity distribution (Maxwellian, here) from an ideally tilted beam to the shape of the current profile at a fixed location in the laboratory frame. Additional simulations regarding the role of the type of thermal distribution on the longitudinal current compression will be discussed in Sec. 4.7.4.

A significant effect apparent in Fig. 4.21 is that slower head particles suffer more aberration due to beam temperature during the longitudinal focusing process, a result of the fact that the thermal velocity of a charge bunch with non-zero temperature is always a greater fraction of the velocity of the head compared to that of the tail, as mentioned earlier. The contribution of chromatic aberration for an ion beam with finite emittance, which has been ideally velocity-tilted across an infinitely thin gap, to the temporal smearing of the longitudinal focal plane can be calculated as follows.

Consider an ion beam with a non-zero Waterbag axial velocity distribution with thermal velocity $v_{th} << v_0$, where the so-called Waterbag distribution is uniformly populated with velocities between $v_0 - v_{th}$ and $v_0 + v_{th}$ (the density is also uniform). The effective drift length to the longitudinal focal plane of the slower head particles can be calculated from Eq. (4.15) to be

$$L_d^{h+} = \frac{(v_h + v_{th})\, v_t}{v_t - (v_h + v_{th})}\, t_p \,, \tag{4.47}$$

for the head particles moving with the slightly faster velocity $v_h + v_{th}$ and

$$L_d^{h-} = \frac{(v_h - v_{th})\, v_t}{v_t - (v_h - v_{th})}\, t_p \,, \tag{4.48}$$

for the head particles moving with the slightly slower velocity $v_h - v_{th}$. The definitions for the head velocity v_h, tail velocity v_t, and initial pulse length t_p are given in Eqs. (4.16), (4.17), and (4.4), respectively. Then, the intended focal plane is no longer infinitely thin at one axial location L_d downstream of the acceleration gap, but takes on a range of values around that location, due to the beam's temperature, whose

width about L_d for the head of the charge bunch is

$$w^h \equiv L_d^{h+} - L_d^{h-} = 2\,\frac{v_t^2}{(v_t - v_h)^2 - v_{th}^2}\,v_{th}\,t_p\,. \tag{4.49}$$

Similarly, the intended focal plane takes on a range of values whose width about L_d for the tail of the charge bunch is

$$w^t = 2\,\frac{v_h^2}{(v_t - v_h)^2 - v_{th}^2}\,v_{th}\,t_p\,. \tag{4.50}$$

The increased amount of aberration suffered by the slower head particles compared to the faster tail particles is then

$$w^h - w^t = 2\,\frac{v_t^2 - v_h^2}{(v_t - v_h)^2 - v_{th}^2}\,v_{th}\,t_p\,, \tag{4.51}$$

and can be rewritten in terms of the initial beam velocity v_0 and the fractional velocity tilt f, using Eqs. (4.16) and (4.17) and their associated assumptions, as

$$w^h - w^t = \frac{4}{f}\;\frac{1}{1 - (\frac{v_{th}}{f\,v_0})^2}\,v_{th}\,t_p\,. \tag{4.52}$$

The effective longitudinal temperature of a Waterbag distribution is defined as

$$T_W \;\equiv\; m_b \int_{-v_{th}}^{+v_{th}} \frac{d\mathbf{v}}{2\,v_{th}}\,\mathbf{v}^2 = \frac{1}{3} m_b v_{th}^2\,, \tag{4.53}$$

where m_b and v_{th} are the mass and thermal velocity of the beam particles, respectively,

whereas the temperature of a Maxwellian distribution is defined as

$$T_M \equiv m_b \int_{-\infty}^{+\infty} \frac{d\mathbf{v}}{\sqrt{2\pi}\, v_{th}} \mathbf{v}^2 \, exp\left(-\frac{\mathbf{v}^2}{2\, v_{th}^2}\right) = m_b v_{th}^2 \,, \tag{4.54}$$

and $T_M = 3\, T_W$ for the same v_{th} involved. Therefore, to analyze the PIC simulations involving beams with Maxwellian thermal distributions, the extra factor of $\sqrt{3}$ in v_{th} ($v_{th}^M = v_{th}^W/\sqrt{3}$) should be taken into account in Eqs. (4.47) to (4.52).

For the parameters of the simulations presented in Figs. 4.20 and 4.21, the widths about L_d for the slower head and faster tail of the charge bunch are calculated to be $w^h = 0.151$ cm and $w^t = 0.054$ cm, respectively, and agree well with the result in the center frame of Fig. 4.21, which quantitatively shows those widths and the same factor of 2.8 difference in spread between the slowest head particles and fastest tail particles (w^h/w^t). The full-width, half-maximum temporal pulse length of the ideally-tilted beam at the axial location of peak longitudinal focus, due to the chromatic aberration of the non-zero temperature beam, should be approximately equal to the weighted average

$$t_{fwhm} = \frac{1}{2} \left[\frac{\left(\frac{w^h}{v_h}\right) w^h + \left(\frac{w^t}{v^t}\right) w^t}{w^h + w^t} \right] \,, \tag{4.55}$$

which is $t_{fwhm} = 0.58$ ns for the parameters here, in close agreement with the full-width, half-maximum temporal pulse length of approximately $t_{fwhm} \sim 0.60$ ns plotted in the black current profile from simulation in Fig. 4.20 for the $T_b = 0.2$ eV case. Equation (4.55) is not equal to the analytical formula for the minimum achievable pulse length of an ideally-tilted beam reported elsewhere [Roy *et al.*, 2005b,

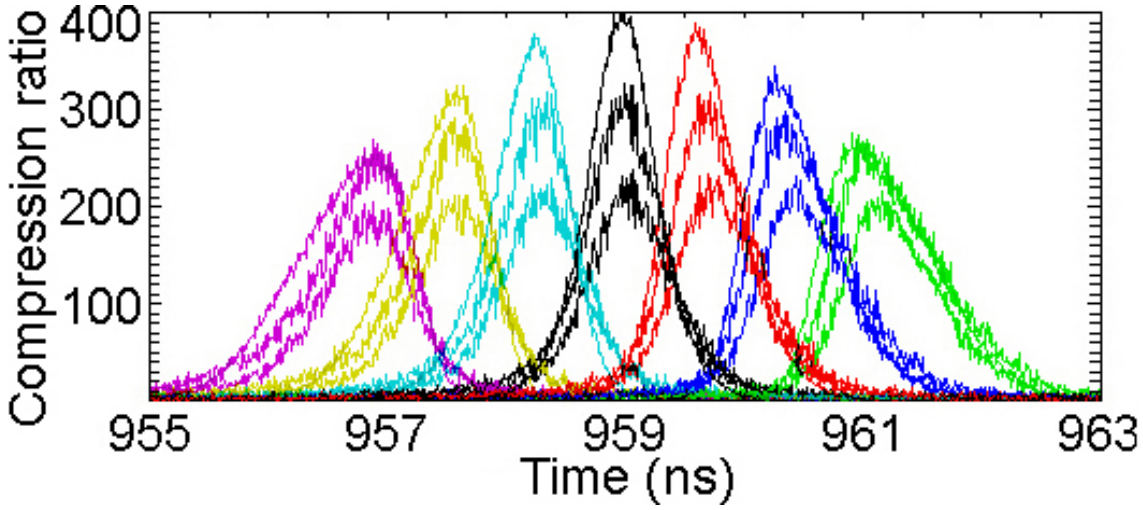

Figure 4.22: (Color) Longitudinal compression ratio $I_b(t)/I_0$ comparison between "smooth" (middle profiles) and "sharp" (bottom profiles) voltage waveforms in the laboratory frame obtained from particle-in-cell simulation at multiple axial locations near the focal plane ($z = +59.5$ cm), in steps of $\Delta z = 0.1$ cm. The beams are initialized with $T_b = 0.2$ eV and are velocity-tilted across a 3 cm long gap. The results for the infinitely thin gap case (including the spatial and temporal offset) from Fig. 4.20 are provided for comparison (top profiles).

Welch *et al.*, 2007], which does not include the relative increase in chromatic aberration experienced by the head of the charge bunch compared to that of the tail.

Next, two additional beam simulations, using the same beam parameters including the 0.2 eV Maxwellian temperature distribution, are executed in order to compare the effectiveness of the longitudinal compression using the "sharp" and "smooth" voltage waveforms (refer to Fig. 4.12) imposed over the finite-size gap to the simulation discussed earlier involving the "sharp" waveform over an infinitely thin gap. The current compression profiles near the focal plane using the two waveforms applied to the $T_b = 0.2$ eV beam over the finite-size gap are shown in Fig. 4.22 on a linear scale, should be compared to the complimentary $T_b = 0$ eV case results in Fig. 4.16, and are accompanied by the infinitely thin gap compression results of the same $T_b = 0.2$

eV beam previously plotted on a Log scale in Fig. 4.20. The aforementioned spatial and temporal offset between the two gaps is included for clarity. As before, the "smooth" waveform effectively compresses more beam than the "sharp" waveform acting over the finite-size gap. The maximum longitudinal compression factor and full-width, half-maximum pulse length for the infinitely thin gap case are 400 and $t_{fwhm} \sim 0.6$ ns, respectively. The corresponding "sharp" waveform results compared to those from the "smooth" waveform, both of which are employed over the finite-size gap, are approximately 235 compared to 320 (+36% increase) and 0.65 ns compared to 0.70 ns (+8% increase), respectively. The reduction in compression and increase in pulse lengths for the finite-size gap cases relative to the infinitely thin gap case are due to the decreased effective fractional tilts (acting as effective longitudinal temperature increases), compared to the intended $f = 0.5$, and increased levels of chromatic aberration. The positive effect of reduced compression factors and increased pulse lengths is the additional axial tolerance afforded to the experimenter in the alignment of the longitudinal focal plane with the plane of the diagnostic or target. The axial compression ratios do not vary as quickly as a function of space for the cases involving increased levels of aberration.

The $\{z, v_z\}$ phase space for the three cases just mentioned at the longitudinal focal plane are provided in Fig. 4.23, and should be compared to the complimentary $T_b = 0$ eV case results in Fig. 4.17. As discussed previously in Section 4.7.1, the two main effects of the finite-size acceleration gap are evident again in these $T_b = 0.2$ eV Maxwellian beam temperature simulations, except for the increased axial velocity spread present at initialization. The slower head particles experience more aberration relative to the faster tail particles, and the decrease in maximum tail velocities from

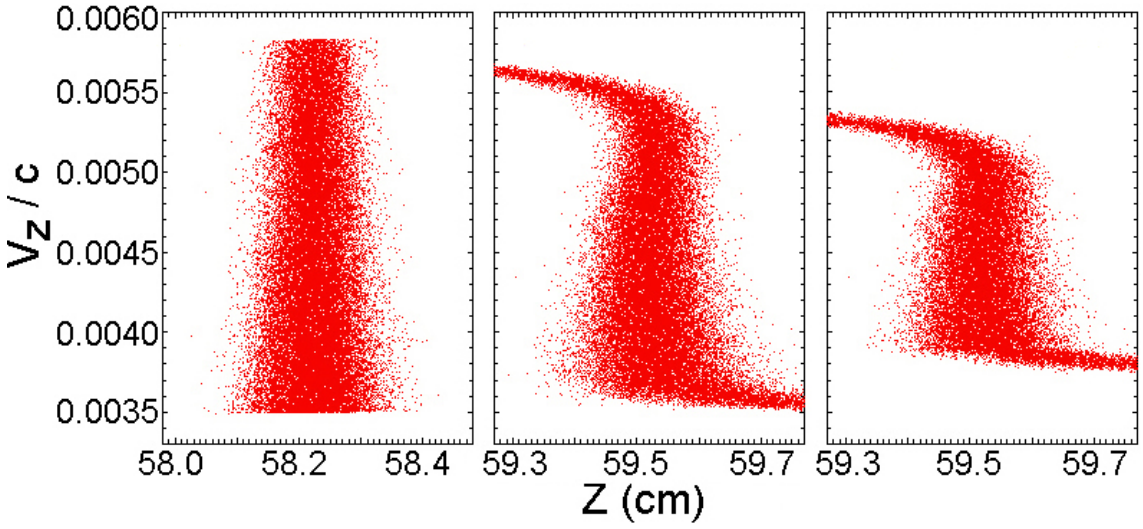

Figure 4.23: (Color) $\{z, v_z\}$ phase space at the focal plane for the $T_b = 0.2$ eV beam using the "sharp" voltage waveform across an infinitely thin gap (left), and "smooth" (center) and "sharp" (right) voltage waveforms across the finite-size gap. Longitudinal focus occurs at $z = +58.25$ cm and $t = 950$ ns for the infinitely thin gap case and at $z = +59.5$ cm and $t = 959$ ns for the finite-size gap cases.

the ideal case is relatively larger than the corresponding increase in minimum head velocities from the ideal case. Evidently, the fractional tilt is again reduced from the intended $f = 0.5$ to approximately $f = 0.4$ and $f = 0.3$ for the "smooth" and "sharp" waveform cases, respectively, across the finite-size gap. Due to the beam initialization increase from the idealized $T_b = 0$ eV beam temperature to the realistic $T_b = 0.2$ eV Maxwellian beam temperature, the compression factors for the "sharp" and "smooth" waveforms across the finite-size gap precipitously drop from 2200 to 235 and 2650 to 320, respectively, and the full-width, half-maximum pulse lengths increase from 0.03 ns to 0.65 ns and 0.035 to 0.70 ns, respectively. The reduction in f causes the apparent increase in effective longitudinal temperature, and is independent of the beam's initial convergence angle here, due to the fact that the actual longitudinal temperature increase from transverse coupling in the gap is small compared to the

initialized temperature.

A suite of numerical simulations involving a range of initialized Maxwellian longitudinal temperatures, for the case of the "smooth" voltage waveform across the finite-size gap, is carried out in order to investigate the dependence of the current compression ratio on the emittance of the charge bunch for parameters relevant to experiments. The initialized temperatures are T_b = 0.1 eV, 0.2 eV, 0.4 eV, 0.8 eV, and 1.6 eV. The peak compression ratios achieved at the focal plane and the corresponding full-width, half-maximum pulse lengths are presented in the first three columns of Table 4.1. The data in Table 4.1 correspond to the peak current compression profiles for those cases plotted together in Fig. 4.24 for simultaneous comparison at longitudinal focus. The $T_b = 0$ eV case discussed earlier is included in Table 4.1 and Fig. 4.24 for reference.

From Table 4.1, the compression factor decreases and the minimum pulse length increases with an approximate square root dependence on the initial beam temperature ($T_b^{-0.48}$ and $T_b^{0.5}$, respectively) as expected, since $t_{fwhm} \sim v_{th} \sim \sqrt{T_z}$ according to Eq. (4.55) for $v_{th} << v_h, v_t$. For the $T_b = 0$ case, the beam gains effective longitudinal temperature from the finite-size gap, and does not result in an infinite compression

Table 4.1: Longitudinal compression dependence on initial emittance for E_0 = 400 keV, t_p = 300 ns, and f = 0.5. The $T_b = 0$ eV case is included for reference.

T_b (PIC)	I_b^{max}/I_0 (PIC)	t_{fwhm} (PIC)	t_{fwhm} [Eq. (4.55)]	T_b^{inf} [Eq. (4.55)]
0 eV	2650	0.035 ns	0 ns	7.5×10^{-4} eV
0.1 eV	430	0.51 ns	0.41 ns	0.16 eV
0.2 eV	320	0.70 ns	0.58 ns	0.30 eV
0.4 eV	230	1.01 ns	0.81 ns	0.62 eV
0.8 eV	160	1.40 ns	1.15 ns	1.19 eV
1.6 eV	115	2.05 ns	1.63 ns	2.55 eV

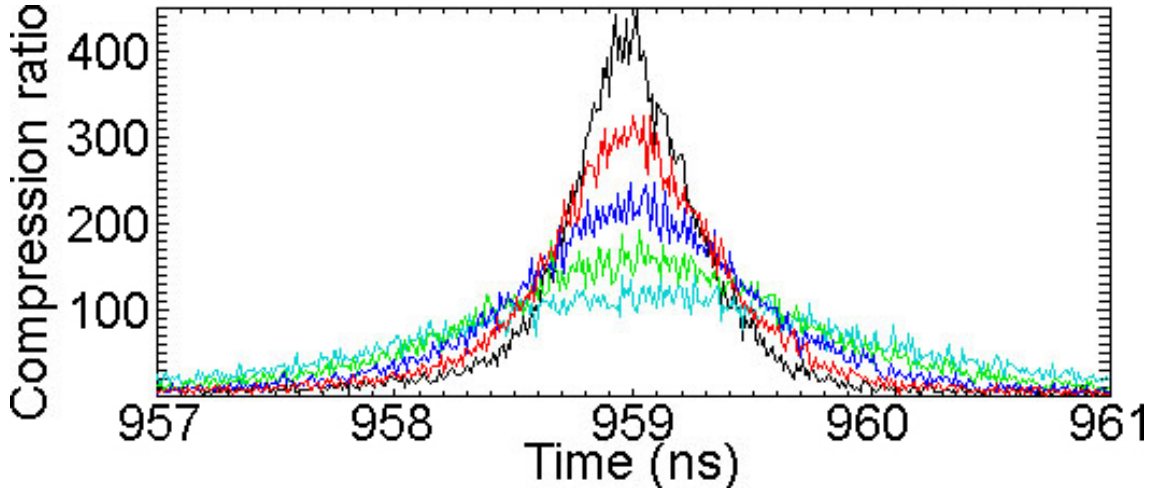

Figure 4.24: (Color) Longitudinal compression ratio $I_b(t)/I_0$ comparison using the "smooth" voltage waveform across the finite-size gap in the laboratory frame obtained from simulation at the focal plane ($z = +59.5$ cm) for initialized beam temperatures of $T_b = 0.1$ eV (black), 0.2 eV (red), 0.4 eV (dark blue), 0.8 eV (green), and 1.6 eV (light blue).

factor with vanishing pulse length. The minimum full-width, half-maximum pulse length of a beam with finite temperature, which acquires an ideal velocity tilt across an infinitely thin gap and is perfectly neutralized in the drift length, will be limited by the initial longitudinal beam temperature (emittance) according to Eq. (4.55). The predicted t_{fwhm} from that equation is shown in the fourth column of Table 4.1. Although Eq. (4.55) includes the linearly-weighted average effect of the chromatic aberration experienced by all the beam particles, the equation does not include the finite-size gap or "smooth" waveform effects on the minimum pulse width (both of which increase the beam's effective longitudinal temperature), as shown by the discrepancy between the third and fourth columns of Table 4.1. Note that the difference between those columns also increases approximately with the square root of the initial beam temperature.

The inferred initial beam temperatures T_b^{inf} required to produce the t_{fwhm} from the particle-in-cell simulations using Eq. (4.55), as if the extra temperature is included in the initial beam and given an ideal velocity tilt over an infinitely thin gap, are presented in the fifth column of Table 4.1. The inferred effective temperatures are $55\% \pm 5\%$ higher on average than the initial T_b used in simulations involving the 3 cm gap. The elevated inferred temperatures indicate the required presence of an additional geometrical constant ($\sqrt{1.55}$, here) in v_{th} [Eqs. (4.50) and (4.51)] to raise the effective temperature, and thereby take into account the particular combined effects of the finite-size gap and "smooth" waveform for the set of beam parameters considered here, which actually reduces the achieved f but is manifest as additional effective longitudinal temperature. Recall that, for $T_b = 0.2$ eV, the infinitely thin gap case results in a $t_{fwhm} = 0.6$ ns and the finite-size gap with a "smooth" waveform case results in a $t_{fwhm} = 0.7$ ns, whereas Eq. (4.55) predicts $t_{fwhm} = 0.58$ ns. Therefore, 17% of the temperature discrepancy is due to error in the equation (the averaging procedure linearly weights the velocities from v_h to v_t, but the tilt deviates from linear later in the pulse, in this case) and 83% of the temperature discrepancy is due to the actual increased effective temperature from the finite-size gap and "smooth" waveform. Additional simulations involving halved and doubled gap sizes have been carried out, but only support a weak dependency on the length of the acceleration gap. However, the gap and transit time of the particles should be considerably smaller than the initial bunch length L_b and pulse length t_p, respectively, for effectively imparting an intended fractional tilt f.

The amount of effective temperature imparted to an $E_0 = 400$ keV beam as it encounters the "smooth" waveform for $t_p = 300$ ns and $f = 0.5$ across a finite-size

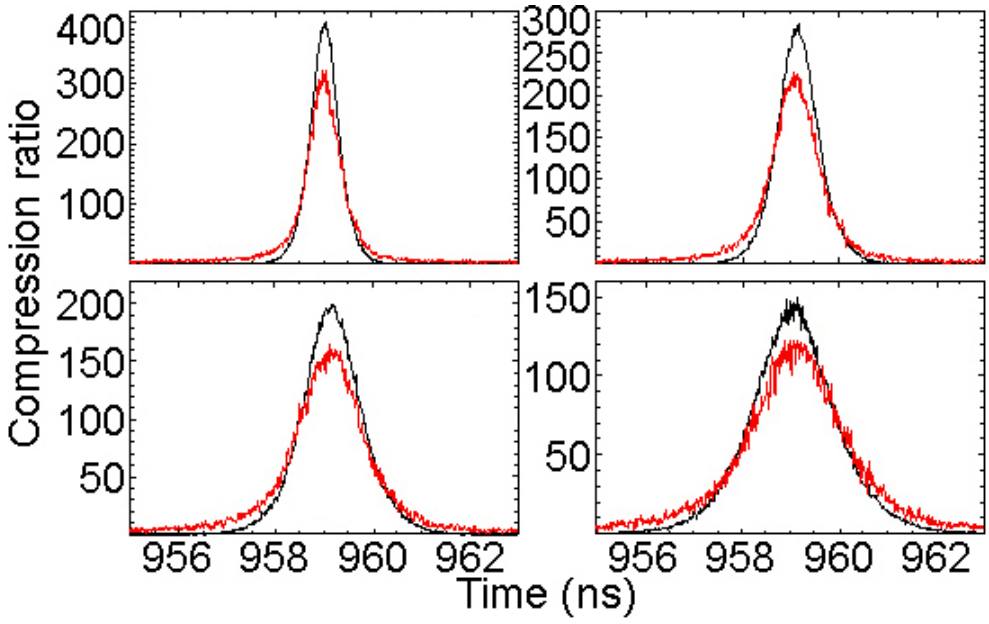

Figure 4.25: (Color) Longitudinal compression ratio $I_b(t)/I_0$ comparison between the "sharp" waveform across the infinitely thin gap (black) and "smooth" waveform across the finite-size gap (red) in the laboratory frame obtained from particle-in-cell simulation at the focal plane (including the temporal and spatial offset) for the initialized beam temperatures of $T_b = 0.2$ eV (top left), $T_b = 0.4$ eV (top right), $T_b = 0.8$ eV (bottom left) and $T_b = 1.6$ eV (bottom right).

gap can be determined by comparing such simulations to cases involving infinitely thin gaps acting on beams of the same initial finite temperature. Alternatively, two separate temperatures can be used (an increased amount for the infinitely thin gap case) in order to determine the temperature for which the maximum compression ratio and full-width, half-maximum pulse length are equal. As shown in Fig. 4.25, four cases of initial beam temperature are compared between the finite-size gap employing the "smooth" waveform to the infinitely thin gap employing the "sharp" waveform (the "smooth" and "sharp" waveforms produce identical results across an infinitely thin gap, as mentioned earlier). Simulations initialized with beam temperatures of $T_b = 0.2$ eV, $T_b = 0.4$ eV, $T_b = 0.8$ eV, and $T_b = 1.6$ eV each result in an approximate

20% relative decrease in maximum compression ratio and increase in full-width, half-maximum pulse length for the finite-size gap and "smooth" waveform case compared to the infinitely thin gap case, as plotted in Fig. 4.25 (the $T_b = 0.2$ eV result is also plotted in Fig. 4.22). Therefore, the effective longitudinal temperature difference between the two cases, due to the reduced f from finite-size acceleration gap and "smooth" waveform effects, is approximately 45% and in very good agreement with the previous results, which state that the compression factor decreases with the square root of increasing beam temperature. As in the previous paragraph, the inferred effective temperatures are $\sim$ 55% higher on average in Table 4.1, and $\sim$ 83% of that discrepancy ($\sim$ 45%) is due to the effects of the finite-size gap and "smooth" waveform. As a check, simulations comparing $T_b = 0.1$ eV in the finite-size gap case to $T_b = 0.145$ eV in the infinitely thin gap case confirm the same longitudinal compression result. In summary, the 3 cm gap and "smooth" voltage waveform together add the equivalent of approximately 45% of the beam's initial emittance, for the parameters considered here, to the resulting effective longitudinal emittance as the beam acquires its velocity tilt, by reducing the achieved f relative to the intended f and coupling the transverse and longitudinal phase space of the beam as it traverses the gap, as discussed in Sec. 4.7.1.

The general derivation of the geometrical constant that takes into account the additional effective longitudinal temperature imparted on the beam by the finite-size acceleration gap is not provided here. Note that the amount of effective longitudinal temperature imparted to the beam by coupling of transverse motion in the gap depends on the gap geometry, voltage waveform, and beam parameters entering the gap, such as axial velocity, radius, transverse and longitudinal emittance, and any

convergence angle of the beam, which is usually much larger than any contributing transverse temperature effects, as discussed earlier. The effective longitudinal temperature of the beam exiting the gap is intimately linked to the minimum achievable pulse length when a nearly ideal voltage waveform is employed, with smaller temperatures associated with higher compression ratios and shorter pulse lengths. Deviations from the ideal slope by the experimental voltage waveform also increase the effective temperature inferred by the measured temporal pulse length at the focal plane. When such errors in the voltage waveform dominate the chromatic aberration due to initial beam temperature, the minimum pulse length is said to be waveform-dominated, instead of emittance-dominated. In reality, Eq. (4.55) is of limited value because the minimum achievable pulse length is actually a complex function of the aforementioned experimental considerations, in addition to partial neutralization effects and some other deleterious issues affecting longitudinal compression factors and pulse lengths, as mentioned earlier.

4.7.3 Dependence on pulse length and fractional tilt

Since the voltage waveform of the induction module imparts the axial velocity tilt to the beam, it is inextricably linked to the amount of current compression achieved at the focal plane. Assume that the ideal waveform $V(t)$ [Eq. (4.22)] can be accurately reproduced over the duration of the intended pulse length t_p, as in the "smooth" waveform of Fig. 4.12. The two induction module $V(t)$ waveform parameters that can be adjusted by the experimenter for longitudinal compression are the intended pulse length t_p and the amount of desired fractional tilt f.

First, consider changes in the waveform $V(t)$ due to t_p while holding $E_0 = 400$ keV

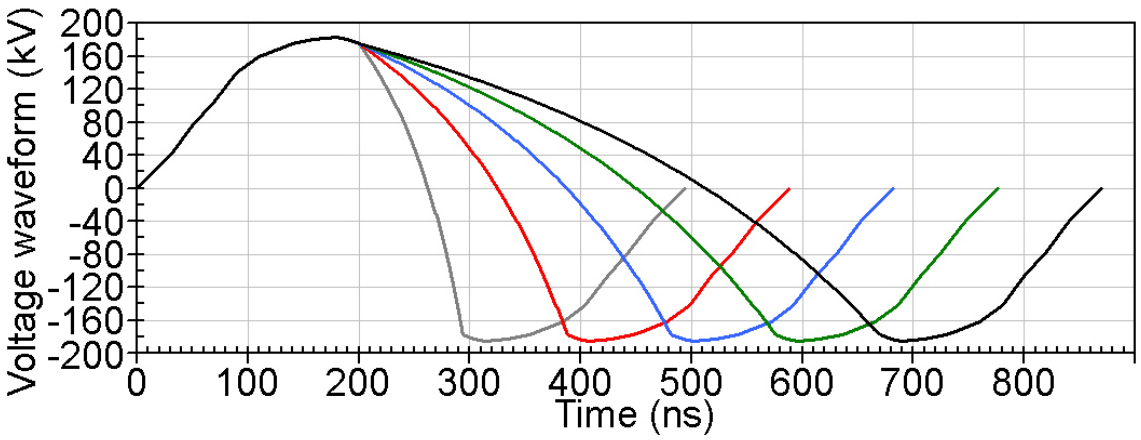

Figure 4.26: (Color) "Smooth" voltage waveforms $V(t)$ for $E_0 = 400$ keV, $f = 0.5$, and $t_p = 100$ ns (gray), $t_p = 200$ ns (red), $t_p = 300$ ns (blue), $t_p = 400$ ns (green), and $t_p = 500$ ns (black).

and $f = 0.5$ constant. The "smooth" voltage waveforms for $t_p = 100$ ns to 500 ns, in steps of 100 ns, are displayed in Fig. 4.26. All of the waveforms considered here are ± 180 kV symmetric, as opposed to the waveform in Fig. 4.12, whose range is $\{+180$ kV, -225 kV$\}$. The reason for the change is that, in reality, a peak experimental voltage exists due to voltage hold-off requirements, and a plus-minus symmetric waveform takes the most advantage of the available voltage for a given limit. The drift length to the longitudinal focal plane increases linearly with t_p for constant E_0 and f [according to Eq. (4.20)], as does the amount of chromatic aberration [according to Eqs. (4.49) and (4.50)] and the minimum achievable pulse length [according to Eq. (4.55)]. The competing positive effect is the increasing amount of total longitudinal compression, since the compression of longer lengths of initial beam pulses results in larger amounts of total current at the focal plane, assuming charge conservation [$I^f/I_0 = (q^f/t_p^f)\,(q_0/t_p^0)^{-1} = t_p^0/t_p^f$ for $q^f = q_0$]. However, the strength of the effect plateaus due to increased aberration associated with longer drift lengths. Therefore,

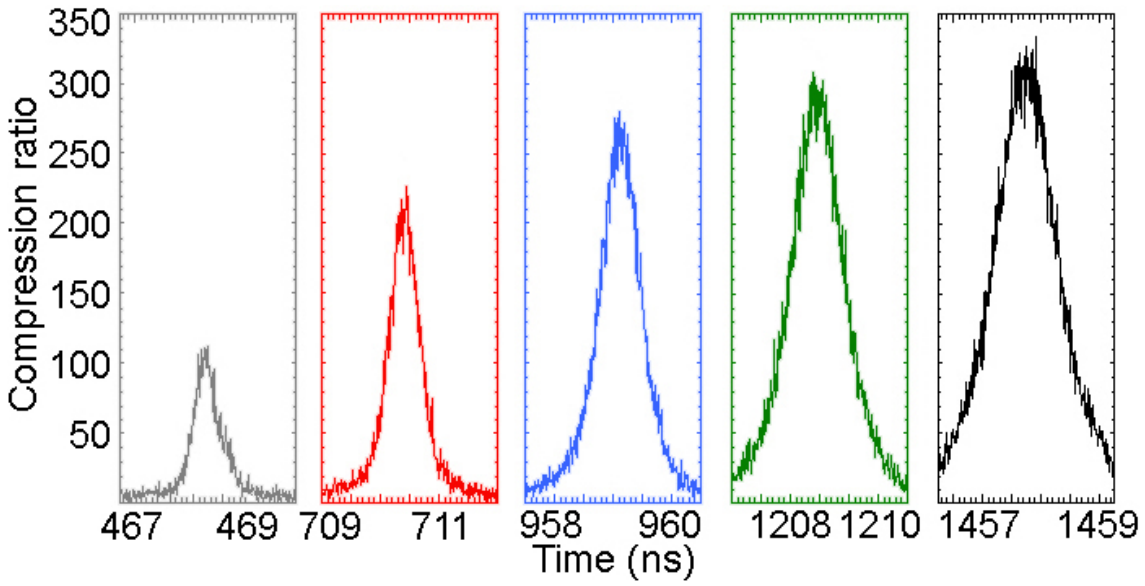

Figure 4.27: (Color) Longitudinal compression ratio $I_b(t)/I_0$ comparison using the "smooth" waveforms of Fig. 4.26 across the finite-size gap in the laboratory frame obtained from simulation at the focal planes for $T_b = 0.2$ eV, $f = 0.5$, and $t_p = 100$ ns (gray), $t_p = 200$ ns (red), $t_p = 300$ ns (blue), $t_p = 400$ ns (green), and $t_p = 500$ ns (black). The plots are color-coded to the waveforms in Fig. 4.26.

careful assessment between the desired amount of longitudinal compression compared to the desired pulse length and available plasma drift length for experiments is required.

The particle-in-cell simulation results for longitudinal compression of an $E_0 = 400$ keV and $T_b = 0.2$ eV K^+ ion beam across the 3 cm acceleration gap, using the "smooth" waveforms in Fig. 4.26, are shown in Fig. 4.27. The actual initial pulse lengths are longer than the prescribed t_p pulse lengths intended to undergo longitudinal compression. As mentioned earlier, the extra voltage in the "smooth" waveform acts on the extra initial pulse length to increase the compression ratio, fractional tilt, and t_{fwhm} (slightly) achieved at the focal plane compared to the "sharp" waveform case. The five plots of the current profiles are color-coded to match the

Table 4.2: Longitudinal compression dependence on initial pulse length t_p for $E_0 =$ 400 keV, $T_b = 0.2$ eV, and an intended $f = 0.5$.

t_p	I_b^{max}/I_0	t_{fwhm}	L_d [Eq. (4.20)]	t^{foc} (PIC)	z^{foc} (PIC)	ΔL_d
100 ns	120	0.5 ns	26.2 cm	468.3 ns	+8.4 cm	+2.65 cm
200 ns	220	0.6 ns	52.5 cm	710.5 ns	+33.5 cm	+1.45 cm
300 ns	280	0.7 ns	78.7 cm	959.0 ns	+59.5 cm	+1.25 cm
400 ns	310	0.9 ns	104.9 cm	1208.5 ns	+85.6 cm	+1.15 cm
500 ns	325	1.2 ns	131.2 cm	1457.5 ns	+111.7 cm	+0.95 cm

waveforms in the previous figure. The compression dependence on initial pulse length t_p is provided in Table 4.2 in terms of the approximate maximum compression factor at focus, full-width, half-maximum pulse length at focus, drift length and total time to focus, the location of the focal plane in the PIC axial coordinates, and the spatial offset between the focal lengths for the finite-size and infinitely thin gaps (ΔL_d). The data in Table 4.2 correspond to the results in Fig. 4.27.

Recall from Sec. 4.1 that, for the same initial beam energy, greater fractional tilts f give shorter drift lengths L_d than smaller fractional tilts, and longer initial pulse lengths t_p give longer drift lengths than shorter initial pulse lengths. From Fig. 4.27 and Table 4.2, the longitudinal compression ratio increases almost linearly with t_p for short initial pulse lengths ($\sim t_p^{0.8}$), but slower than the square root of t_p for longer initial pulse lengths ($\sim t_p^{0.3}$). The minimum t_{fwhm} at focus increases more slowly than the square root of t_p for shorter initial pulse lengths ($\sim t_p^{0.3}$), but slightly faster than linearly with t_p for longer initial pulse lengths ($\sim t_p^{1.05}$), in agreement with the linear dependence of Eq. (4.55) on t_p. Also, the t_{fwhm} from Eq. (4.55) underestimates the pulse length at focus by an approximately constant 20% for $t_p \geq 300$ ns, due to the 45% extra effective longitudinal temperature given to the beam by the gap effects, as

discussed at the end of Sec. 4.7.2. Although, as t_p decreases to 200 ns and 100 ns, the underestimation of t_{fwhm} by Eq. (4.55) increases to 36% and 62%, respectively, since the initial bunch length L_b and pulse length t_p each become comparable to the effective gap length and transit time, respectively. The failure of Eq. (4.55) for short pulse lengths is expected, since its derivation assumed an infinitely thin gap relative to the initial beam pulse length. Essentially, if the gap is not thin enough compared to the bunch length intended to undergo longitudinal compression, beam particles sample very large amounts of the $V(t)$ waveform, resulting in a drastically reduced effective fractional tilt f. In other words, the actual v_h is larger than the intended v_h, and the actual v_t is smaller than the intended v_t, resulting in a reduced f from the intended value, and the change is not constant as a function of t_p. None of the simulations in Table 4.2 achieve the intended $f = 0.5$ due to the finite-size acceleration gap effects. However, longer initial pulse lengths achieve greater fractional tilts f, but at the cost of experiencing more longitudinal aberration from beam temperature over the greater drift lengths. Figure 4.28 illustrates both phenomena graphically; the figure also shows that v_t decreases more than v_h increases, as discussed earlier. The actual fractional tilts achieved for $t_p = 100$ ns and $t_p = 500$ ns are approximately $f = 0.25$ and $f = 0.43$, respectively. The $t_p = 300$ ns case is similar to one of the simulations presented earlier in this Section, however the compression ratio is reduced from 320 to 280, corresponding to the same percentage reduction in waveform voltage late in time (-225 kV to -180 kV).

According to the fifth and sixth columns of Table 4.2, the time required and the actual drift length to the longitudinal focal plane increase approximately with linear dependence on t_p ($\sim t_p^{0.96}$ and $\sim t_p^{0.95}$, respectively), in agreement with Eqs.

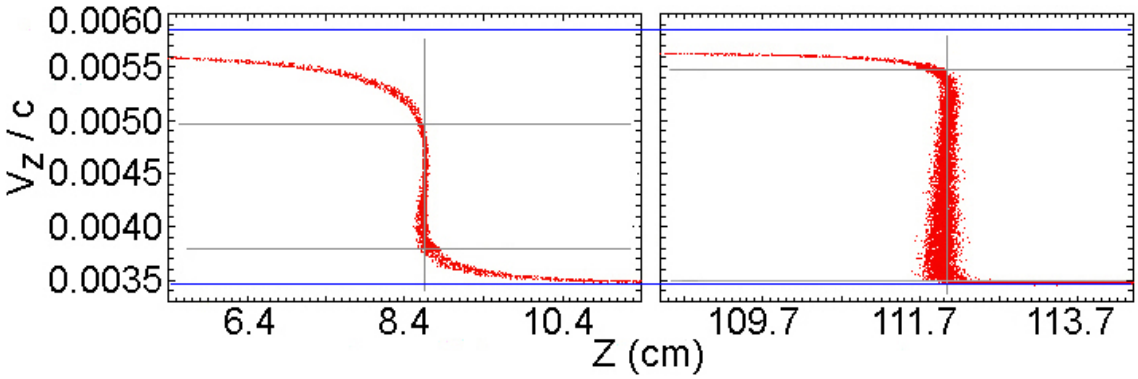

Figure 4.28: (Color) $\{z, v_z\}$ phase space near the focal planes for the $t_p = 100$ ns (left) and $t_p = 500$ ns (right) cases shown in Fig. 4.27 and Table 4.2. Blue horizontal lines demarcate the v_h and v_t expected for an $f = 0.5$ velocity tilt, and the gray horizontal lines show the approximate v_h and v_t achieved by the beam in each case.

(4.19) and (4.20) for the parameters considered here (recall that an extra $t = 200$ ns needs to be subtracted from t^{foc} because of the ramp-up times, and an extra $z = 20.5$ cm needs to be added to z^{foc} to calculate the total drift length in these coordinates). The slightly less than linear dependence is probably caused by the fact that, although the longer initial pulse lengths are associated with linearly increased drift lengths, greater achieved fractional tilts shorten the drift lengths. In addition, the seventh column of Table 4.2 demonstrates the fact that, as the initial bunch and pulse lengths increase relative to the effective gap length and transit time across the gap, respectively, the spatial (and also temporal) offset between the focal lengths for the finite-size and infinitely thin gaps (ΔL_d) decreases ($\sim t_p^{-0.6}$). Therefore, the origin of the offset between the two gap cases mentioned throughout this Section lies in the quantitative ratios of L_b and t_p to the effective gap length and transit time, respectively. Another interpretation could be that the finite-size acceleration gap effects change the resulting fractional tilt f while decreasing the v_t more than increasing the v_h, as discussed earlier, and therefore L_d [refer to Eq. (4.15)] becomes

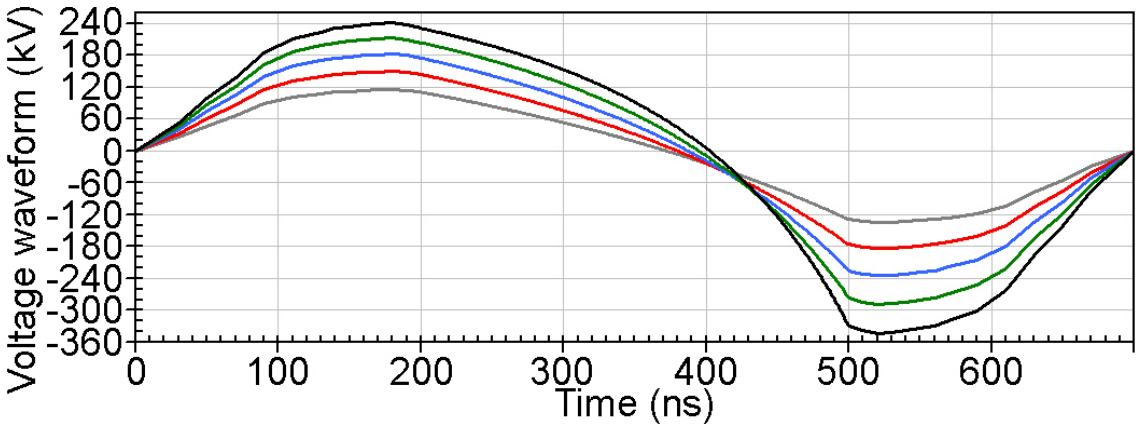

Figure 4.29: (Color) "Smooth" voltage waveforms $V(t)$ for $E_0 = 400$ keV, $t_p = 300$ ns, and $f = 0.3$ (gray), $f = 0.4$ (red), $f = 0.5$ (blue), $f = 0.6$ (green), and $f = 0.7$ (black).

larger compared to the case where the velocities are changed by the same amount.

Analytical neutralized drift compression equations exist [Davidson and Qin, 2005] for calculating the expected compression ratio and minimum pulse length for the case of an ideal velocity-tilted beam with arbitrary distribution passing through a perfectly neutralizing plasma. However, such emittance-dominated solutions do not include the finite-size acceleration gap effects either, such as the reduction in fractional tilt f, effective longitudinal temperature increase due to the gap, or increased chromatic aberration experienced by the head particles compared to the tail particles.

Second, consider changes in the waveform $V(t)$ due to the intended fractional tilt f while holding $E_0 = 400$ keV and $t_p = 300$ ns constant. The "smooth" voltage waveforms for $f = 0.3$ to $f = 0.7$, in steps of $f = 0.1$, are displayed in Fig. 4.29. This time, none of the waveforms are $\pm V^{max}$ kV symmetric, in order to capture the full voltage range for each of the various intended fractional tilts f. The required time and drift length to the longitudinal focal plane decrease as $\frac{1}{f} + \frac{1}{2}$ and $\frac{1}{f} - \frac{f}{4}$, respectively, with increasing f for constant E_0 and t_p [Eqs. (4.19) and (4.20)]. The amount

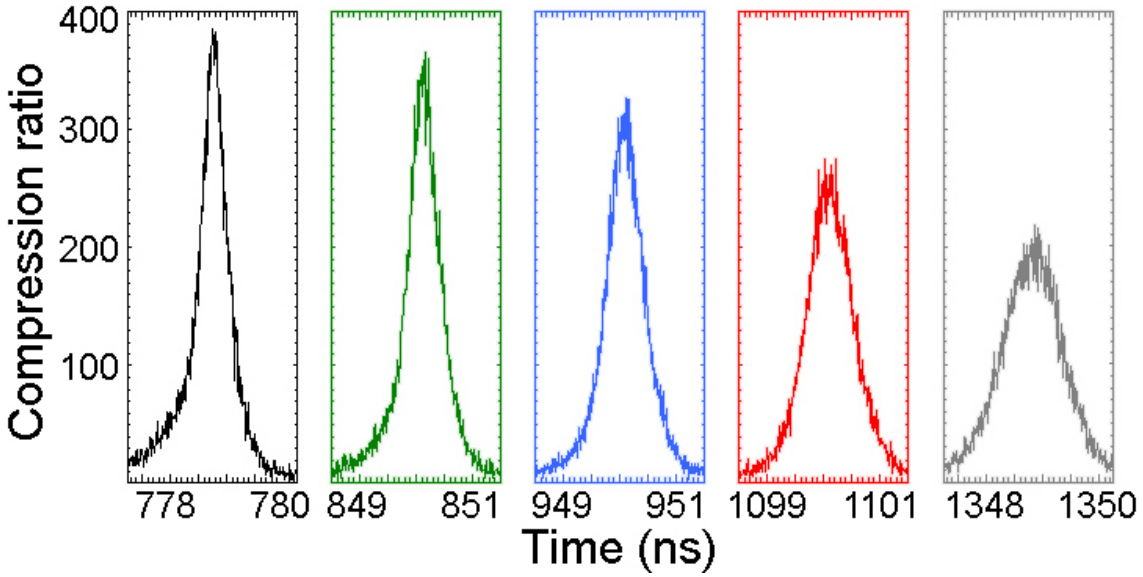

Figure 4.30: (Color) Longitudinal compression ratio $I_b(t)/I_0$ comparison using the "smooth" waveforms of Fig. 4.29 across the finite-size gap in the laboratory frame obtained from simulation at the focal planes for $T_b = 0.2$ eV, $t_p = 300$ ns, and $f = 0.3$ (gray), $f = 0.4$ (red), $f = 0.5$ (blue), $f = 0.6$ (green), and $f = 0.7$ (black). The plots are color-coded to the waveforms of the same color in Fig. 4.29.

of chromatic aberration [Eqs. (4.49) and (4.50)] and the minimum achievable pulse length [Eq. (4.55)] decrease with increasing f, as well. Therefore, larger fractional tilts are generally desired for increased levels of longitudinal compression and shorter pulse lengths at focus. However, a careful assessment of the desired amount of longitudinal compression compared to the increased transverse focusing aberration, associated with the velocity tilt during simultaneous transverse compression to a coincident focal plane, is required.

The particle-in-cell simulation results for longitudinal compression of an $E_0 = 400$ keV and $T_b = 0.2$ eV K^+ ion beam across the finite-size gap, using the "smooth" waveforms in Fig. 4.29, are shown in Fig. 4.30. The actual initial pulse lengths are longer than the prescribed $t_p = 300$ ns pulse length intended to undergo longitudinal

Table 4.3: Longitudinal compression dependence on intended fractional tilt f for $E_0 = 400$ keV, $T_b = 0.2$ eV, and $t_p = 300$ ns.

f	I_b^{max}/I_0	t_{fwhm}	L_d [Eq. (4.20)]	t^{foc} (PIC)	z^{foc} (PIC)	ΔL_d
0.3	210	1.4 ns	136.8 cm	1359.8 ns	+117.3 cm	+1.00 cm
0.4	260	1.0 ns	100.7 cm	1109.0 ns	+81.5 cm	+1.25 cm
0.5	320	0.7 ns	78.7 cm	959.0 ns	+59.5 cm	+1.25 cm
0.6	360	0.6 ns	63.7 cm	859.1 ns	+44.5 cm	+1.25 cm
0.7	380	0.5 ns	52.6 cm	787.8 ns	+33.5 cm	+1.35 cm

compression. As mentioned earlier, the extra voltage in the "smooth" waveform acts on the extra initial pulse length to increase the compression ratio, fractional tilt, and t_{fwhm} (slightly) achieved at the focal plane compared to the "sharp" waveform case. The five plots of the current profiles are color-coded to match the waveforms in the previous figure. The compression dependence on intended fractional tilt f is provided in Table 4.3 in terms of the approximate maximum compression factor at focus, full-width, half-maximum pulse length at focus, drift length and total time to focus, the location of the focal plane in the axial coordinates, and the spatial offset between the focal lengths for the finite-size and infinitely thin gap cases (ΔL_d). The data in Table 4.3 correspond to the results in Fig. 4.30.

Recall again that, for the same initial beam energy, greater fractional tilts f give shorter drift lengths L_d than smaller fractional tilts. From Fig. 4.30 and Table 4.3, the maximum longitudinal compression ratio increases almost linearly with f ($\sim f^{0.82}$) for smaller intended fractional tilts ($0.3 \leq f < 0.5$), but slows to approximately the square root of f ($\sim f^{0.51}$) for larger intended fractional tilts ($0.5 \leq f < 0.7$). The minimum t_{fwhm} at focus decreases faster than linearly with increasing f ($\sim f^{-1.23}$), in agreement with Eq. (4.55) for the parameters considered here ($\sim f^{-1.25}$). Although,

the t_{fwhm} from Eq. (4.55) maintains its approximately 20% underestimation of the pulse length at focus as a function of f, since the ratios of the initial bunch length L_b and pulse length t_p for compression to the effective gap length and transit time, respectively, remain constant. The constant offset to the prediction provided by Eq. (4.55) offers validation that the discrepancy is solely due to the relative size of the finite-gap and transit time compared to the initial beam bunch length L_b and pulse length t_p, respectively, and not the intended fractional tilt f. The intended fractional tilt is not achieved in any of the cases presented in Table 4.3 due to the finite-size gap reduction of the maximum v_t and increase in minimum v_h, which is relatively larger in the case of the former compared to the latter, as mentioned earlier. The resulting relative decrease in f is approximately 20% for $t_p = 300$ ns and approximately independent of the value of the intended fractional tilt, for the parameters considered here. Recall from Sec. 4.7.2 that the maximum compression ratio reduction and full-width, half-maximum pulse length increase due to the finite-size gap are also approximately 20%. Again, smaller fractional tilts f suffer more longitudinal aberration from beam temperature due to the greater drift lengths required. The $t_p = 300$ ns case is the same as the simulation presented earlier in this Section.

As displayed in the fifth and sixth columns of Table 4.3, the required time and the actual drift length to the longitudinal focal plane decrease approximately with $\sim f^{-0.81}$ and $\sim f^{-1.12}$ dependence, respectively, in agreement with Eqs. (4.19) and (4.20) for the parameters considered here (recall that an extra $t = 200$ ns needs to be subtracted from t^{foc} because of the ramp-up times, and an extra $z = 20.5$ cm needs to be added to z^{foc} to calculate the total drift length in these coordinates). In addition, the seventh column of Table 4.3 demonstrates the fact that the spatial

(and also temporal) offset between the focal lengths for the finite-size and infinitely thin gap cases (ΔL_d) is weakly dependent on, or approximately constant with, f for the range considered here, since the initial bunch and pulse lengths relative to the effective gap length and transit time across the gap, respectively, are approximately constant.

The results presented in this subsection indicate that an optimum drift length exists, for a given set of beam parameters, that balances the larger maximum compression ratios achieved by longer initial pulse lengths t_p and larger intended fractional tilts f with the increased t_{fwhm} values of the former and decreased t_{fwhm} values of the latter. Longer initial pulse lengths are shown to increase the drift length to focus, as well as increase chromatic aberration, and shorter initial pulse lengths are shown to achieve smaller fractional tilts due to the finite-size gap. Also, larger tilts are shown to decrease the drift length to focus and longitudinal chromatic aberration, but will adversely affect the transverse aberration during final focus. The amount of tilt achieved in the laboratory is limited by the available magnetic flux of the induction module and voltage hold-off considerations in the gap.

4.7.4 Dependence on energy and thermal distribution

The last topic that will be covered in this Section is the dependency of longitudinal compression on the longitudinal ion beam kinetic energy and distribution. The derivation of the ideal voltage waveform $V(t)$ [Eq. (4.22)] for imparting the velocity tilt on the passing ion beam assumed a particular incoming beam energy, and that the incoming beam energy is constant. Therefore, the particular slope of the $V(t)$ is only ideal for one particular beam energy, and slight differences in directed beam

energy cause the beam to longitudinally focus to different axial locations, with lower compression ratios and longer pulse lengths. Also, the role of the longitudinal distribution on the shape of the current profiles was suggested earlier, since aberration of the thermal velocity spread causes beam particles to arrive at any particular axial location with a range of times. The resulting current profile, then, is a direct consequence of the distribution of particle energies and both the average directed energy and the distribution play a role in its temporal shape in the laboratory frame. Various pulse shapes may therefore be realized at the target.

In the laboratory, the accuracy of the beam energy is known to approximately $\pm 5\%$. In order to maximize the reliability of the longitudinal focusing capability, the shot-to-shot variation in directed beam energy and imposed voltage waveform must be minimized. Also, the beam's initial axial energy over the microseconds of its long initial pulse length might generally not be uniform, since it depends on the high-power diode technology used to create the space-charge-dominated beam. In practice, the ion beam energy may statistically fluctuate on fast time scales (contributing to additional longitudinal emittance), as well as gradually drift its mean energy by as much as $\pm 10\%$ over the course of a $t_p = 6-10\mu$s pulse, or as much as $\pm 1-2\%$ over the course of an approximate window of 300 ns. In order to quantify the effects of these two types of energy variations from an ideal situation for longitudinal compression, a set of simulations similar to the ones outlined earlier in this Section are carried out. Active research is underway to control energy variations in beam injectors, as well as to uniformly create shorter pulses than is possible with current technology, in order to maximize compression capability and reduce the beam pre-pulse.

First, recall the simulation of an $E_0 = 400$ keV K^+ beam with an initialized

Maxwellian temperature of $T_b = 0.2$ eV that is velocity-tilted across the finite-size acceleration gap using the "smooth" waveform of Fig. 4.12. The results are reported in Fig. 4.22 of Section 4.7.2; the ideal waveform used is for the parameters $E_0 = 400$ keV, $t_p = 300$ ns, and $f = 0.5$. The actual initial pulse lengths are longer than the prescribed $t_p = 300$ ns pulse length intended to undergo longitudinal compression. As mentioned earlier, the extra voltage in the "smooth" waveform acts on the extra initial pulse length to increase the compression ratio, fractional tilt, and t_{fwhm} (slightly) achieved at the focal plane compared to the "sharp" waveform case. The simulation is repeated four times, except the constant initial beam energy is altered to $E_0 = 380$ keV (-5%), 390 keV (-2.5%), 410 keV ($+2.5\%$), and 420 keV ($+5\%$), in order to represent the approximately $\pm 5\%$ accuracy of the beam energy in experiments.

The focal plane of the original $E_0 = 400$ keV simulation is located at $z = +59.5$ cm and $t = 959$ ns. The current compression profiles through the same plane for the four other beam energy cases are shown in Fig. 4.31. Of course, the more energetic beams arrive at the focal plane first, followed by the less energetic beams, in order. The two cases simulating charge bunches with faster average velocities do not come to their respective focal planes at this axial location, because their drift lengths are longer due to their higher initial velocities. The opposite is true for the charge bunches with slower average velocities, and those two cases are already beyond their respective focal planes at this axial location, as can be inferred from their double-peak and plateau signatures in Fig. 4.31.

In order to directly compare the amount of longitudinal compression achieved by the different beam energies using the voltage waveform intended for a beam with $E_0 = 400$ keV, the current profiles through their respective focal planes at separate

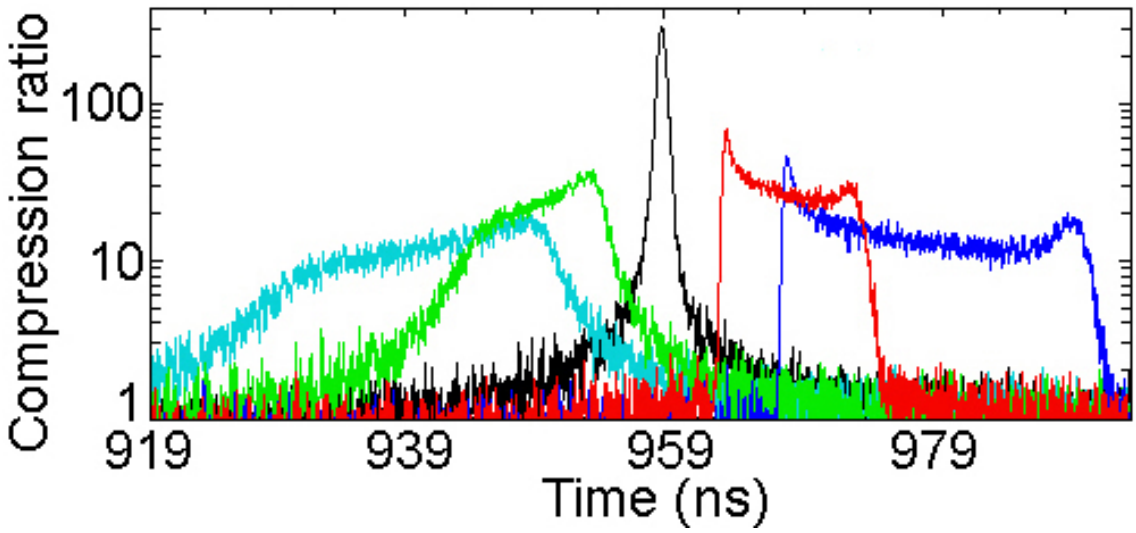

Figure 4.31: (Color) Longitudinal compression ratio $I_b(t)/I_0$ (Log scale) comparison of $\pm 5\%$ constant kinetic energy variations obtained from simulations using the "smooth" waveform across the finite-size gap and $T_b = 0.2$ eV beams at $z = +59.5$ cm in the laboratory frame for $E_0 = 420$ keV (light blue), $E_0 = 410$ keV (green), $E_0 = 400$ keV (black), $E_0 = 390$ keV (red), and $E_0 = 380$ keV (dark blue).

axial locations are plotted as a function of absolute time on a linear scale in Fig. 4.32. The five plots of the current profiles are color-coded to match those in Fig. 4.31. The compression dependence on initial E_0 variation over the $\pm 5\%$ accuracy range is provided in Table 4.4 in terms of the approximate maximum compression factor at focus, full-width, half-maximum pulse length at focus, total time to focus, and the location of the focal plane in the axial coordinates. The data in Table 4.4 correspond to the results in Fig. 4.32.

As evident in Fig. 4.32 and Table 4.4, small $\pm 2.5-5\%$ discrepancies in initial beam energy from the intended beam energy for the particular voltage waveform result in a range of approximately $20 - 40\%$ relative decrease, respectively, in the amount of longitudinal compression measured at the focal plane. Higher beam energies achieve shorter t_{fwhm} at longer axial focal planes z^{foc} and later in time. Although, the t_{fwhm}

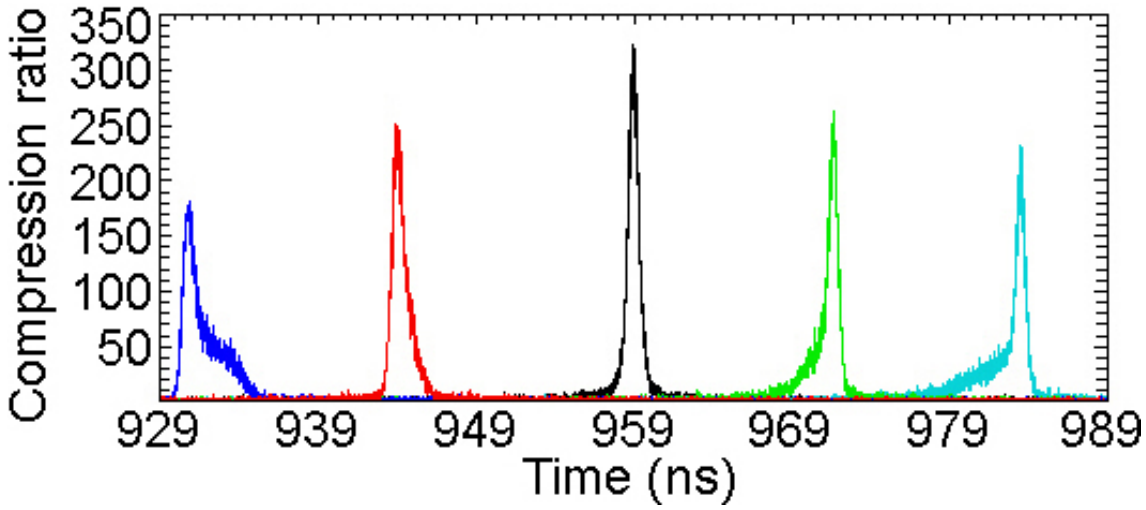

Figure 4.32: (Color) Longitudinal compression ratio $I_b(t)/I_0$ comparison of ±5% constant kinetic energy variations, using the "smooth" waveform across the finite-size gap, in the laboratory frame obtained from simulation of $T_b = 0.2$ eV beams for $E_0 = 420$ keV (light blue) at $z = +65.0$ cm, $E_0 = 410$ keV (green) at $z = +62.3$ cm, $E_0 = 400$ keV (black) at $z = +59.5$ cm, $E_0 = 390$ keV (red) at $z = +56.4$ cm, and $E_0 = 380$ keV (dark blue) at $z = +53.6$ cm. The plots are color-coded to the profiles of the same color in Fig. 4.31.

value does not reflect the significant pedestals in current formed by the beam energy inaccuracy, which are particularly virulent for the ±5% cases in Fig. 4.32. Changes in beam energy by ±10 keV (±2.5%) result in an average change of approximately ±2.8 cm in the axial focal plane location.

As demonstrated here, a particular voltage waveform's slope only results in optimum longitudinal compression for a particular beam energy E_0 at a particular axial location. Experimental beam energy scans to align the plane of the diagnostic with a peak compression result, while holding the voltage waveform fixed, may not necessarily find the true optimum compression achievable for the waveform under consideration, as quantitatively shown in Fig. 4.32 and Table 4.4. Instead, discernment of the actual optimum longitudinal compression due to a particular voltage waveform is

Table 4.4: Longitudinal compression dependence on initial E_0 inaccuracy over a $\pm 5\%$ range with $T_b = 0.2$ eV for $E_0 = 400$ keV, $t_p = 300$ ns, and $f = 0.5$.

E_0	I_b^{max}/I_0	t_{fwhm}	t^{foc} (PIC)	z^{foc} (PIC)
380 keV	180	0.9 ns	930.9 ns	+53.6 cm
390 keV	250	0.8 ns	944.1 ns	+56.4 cm
400 keV	320	0.7 ns	959.0 ns	+59.5 cm
410 keV	260	0.7 ns	971.8 ns	+62.3 cm
420 keV	230	0.6 ns	983.7 ns	+65.0 cm

possible by first fixing both the beam energy E_0 and $V(t)$ waveform and conducting an axial scan of the resulting current profiles with a movable diagnostic. Once a set of longitudinal compression ratios $I_b(t)/I_0$ in the laboratory frame at multiple axial locations before and after the focal plane is measured for a given E_0 and $V(t)$, such as many of those presented throughout this Chapter, the repetition of such a set of measurements for various E_0 with $V(t)$ fixed will result in the conclusive determination of the optimum compression ratio achievable by the given $V(t)$. The maximum current compression profiles from each individual set of measurements for various E_0 will look similar to Fig. 4.32 when plotted together. An energy scan alone without additional information from a movable diagnostic is not sufficient to uniquely determine the maximum achievable compression ratio for a given $V(t)$, especially given the experimental uncertainty and inaccuracy involved in creating the E_0 and $V(t)$. For example, without an axial scan of the diagnostic for a range of beam energies, any of the measured maximum compression ratios portrayed in Fig. 4.32 may be mistaken for the "optimum" compression ratio when, in fact, only one of them may be so called (the black one). If the temporal shape of the "optimum" current profile measured in

the laboratory without an axial scan of the diagnostic resembles any of the asymmetric non-black profiles in Fig. 4.32, it is likely (but not definitive) that the measured maximum is not actually the optimum for the given $V(t)$ (because deviations by the experimental voltage waveform from the ideal can also create asymmetry in the actual optimum current profile, as discussed earlier). Also, note that the experimental current compression result discussed in Sections 2.5 and 4.6 is symmetric in time, but is dominated by waveform deviations from the ideal (refer to Fig. 4.7).

Second, return again to the original simulation of an $E_0 = 400$ keV K^+ beam with an initialized Maxwellian temperature of $T_b = 0.2$ eV that is ideally velocity-tilted across the finite-size gap using the "smooth" waveform of Fig. 4.12, the initialization and results of which are reiterated as introduction for the previous set of simulations. As mentioned earlier, the beam's initial axial energy might generally not be uniform. In practice, the ion beam energy in experiment may statistically fluctuate on fast time scales (contributing to additional longitudinal emittance), as well as gradually drift its mean energy by as much as $\pm 1 - 2\%$ over the course of an approximate window of 300 ns. In order to quantify the effects of such an average energy drift as the beam enters the acceleration gap, compared to an ideal situation for longitudinal compression, two additional PIC simulations are carried out. The first allows the kinetic energy of the initial $E_0 = 400$ keV beam to rise linearly with time over the pertinent $t_p = 300$ ns to $E_0 = 408$ keV ($+2\%$); the second allows the kinetic energy of the initial $E_0 = 400$ keV beam to sink linearly with time over the pertinent $t_p = 300$ ns to $E_0 = 392$ keV (-2%).

The focal plane of the original $E_0 = 400$ keV simulation is located at $z = +59.5$ cm and $t = 959$ ns. In order to directly compare the amount of longitudinal compression

achieved by the different beams with increasing and decreasing energy profiles using the voltage waveform intended for a beam with constant $E_0 = 400$ keV, the current profiles through their respective focal planes at separate axial locations are plotted as a function of absolute time on a linear scale in Fig. 4.33. As opposed to the last set of simulations, the slightly more energetic beam arrives at its focal plane first in time, followed by the nominal and slightly less energetic beams, in order. The compression dependence on initial E_0 with linear increase or decrease by $\pm 2\%$ over the $t_p = 300$ ns window intended to undergo longitudinal compression is provided in Table 4.5 in terms of the approximate maximum compression factor at focus, full-width, half-maximum pulse length at focus, total time to focus, and the location of the focal plane in the axial coordinates. The data in Table 4.5 correspond to the results in Fig. 4.33.

As evident in Fig. 4.33 and Table 4.5, small $\pm 2\%$ increases or decreases in initial beam energy from the intended beam energy over the $t_p = 300$ ns pulse length for the particular voltage waveform result in an approximate 22% relative decrease in the amount of longitudinal compression measured at the respective focal planes. Both of the types of initial temporal energy change achieve longer t_{fwhm} at a focal plane upstream of the nominal case, for the parameters considered here; although, the t_{fwhm} do not reflect the significant pedestals formed by the beam energy drifts, which are particularly prevalent in both of those cases in Fig. 4.33. Contrary to intuition, both types of temporal change in initial axial beam energy result in the formation of a focal plane at the same axial location, approximately 0.2 cm upstream of the nominal location, for the parameters considered here. The beam with slightly less average initial kinetic energy over its pulse length would be expected to exhibit a shorter drift

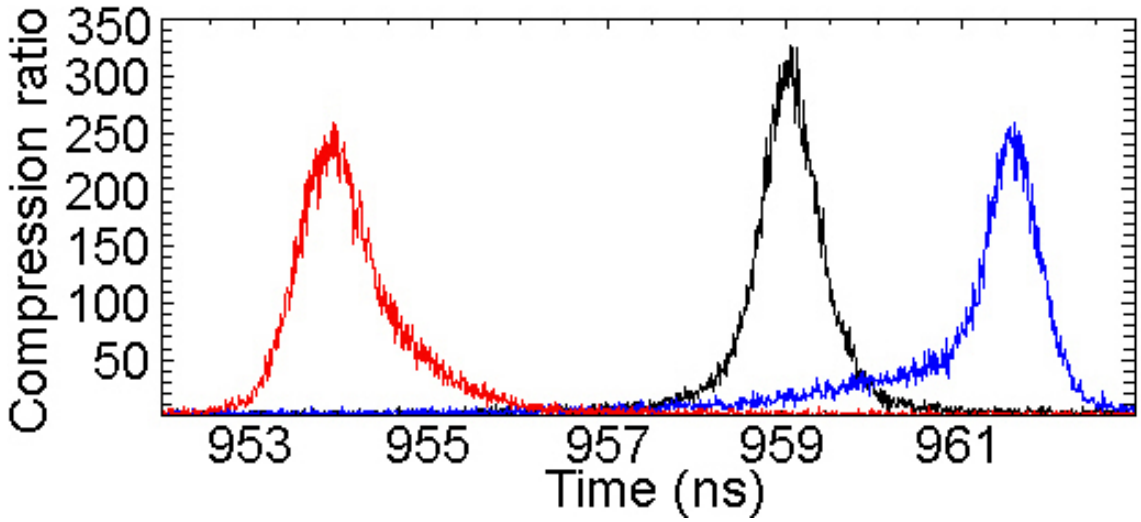

Figure 4.33: (Color) Longitudinal compression ratio $I_b(t)/I_0$ comparison of initial E_0 with linear increase or decrease by $\pm 2\%$ over the pertinent $t_b = 300$ ns, using the "smooth" waveform across the finite-size gap, in the laboratory frame obtained from simulation of $T_b = 0.2$ eV beams for rising $E_0 = 400 - 408$ keV (red) at $z = +59.3$ cm, constant $E_0 = 400$ keV (black) at $z = +59.5$ cm, and sinking $E_0 = 400 - 392$ keV (dark blue) at $z = +59.3$ cm.

length and time to focus, and the opposite for the beam with slightly higher average initial kinetic energy. The reason for the departure from the expected, such as the shorter drift length and time to focus for the faster beam and the longer drift length and time to focus for the slower beam, is that the initial linear temporal decrease and increase in axial beam energies are effectively decompressing and compressing initial velocity tilts, respectively. Therefore, the beam whose energy decreases as a function of time entering the gap acquires a slightly smaller total tilt than nominal (since the initial decompressing tilt had to be negated by the imposed waveform). Conversely, the beam whose energy increases as a function of time entering the gap acquires a slightly larger total tilt than nominal. Consequently, the relative drift length of the former is slightly longer than intended and that of the latter is slightly shorter than

Table 4.5: Longitudinal compression dependence on initial linear increase or decrease in $E_0(t)$ by $\pm 2\%$ with $T_b = 0.2$ eV for $E_0 = 400$ keV, $t_p = 300$ ns, and $f = 0.5$.

E_0	I_b^{max}/I_0	t_{fwhm}	t^{foc} (PIC)	z^{foc} (PIC)
$400 - 392$ keV	250	0.8 ns	961.5 ns	+59.3 cm
400 keV	320	0.7 ns	959.0 ns	+59.5 cm
$400 - 408$ keV	250	0.8 ns	953.9 ns	+59.3 cm

intended. In both cases, the maximum longitudinal compression ratio achieved at the focal plane is relatively decreased compared to that achieved by the beam with the intended energy for the particular $V(t)$.

As demonstrated here and discussed in Sec. 4.1, a particular voltage waveform's slope only results in optimum longitudinal compression for a particular constant beam energy E_0 at a particular axial location. Unintentional experimental beam energy increases or decreases, whether constant in time or not, due to injector technology will not reach the optimum compression achievable, compared to the constant beam energy case for the specific waveform under consideration. This fact is quantitatively illustrated in Figs. 4.32 and 4.33 and Tables 4.4 and 4.5. In summary, if the beam enters the acceleration gap when its energy is too high or low by a few percent, or increases or decreases in time by a few percent, one of the suboptimal "maximum" compression ratios portrayed in Figs. 4.32 or 4.33 may be measured in the laboratory and mistaken for the actual optimum compression ratio. A beam with constant energy a few percent larger than the intended energy of the waveform, or with an energy profile that rises by a few percent over the pulse length, results in the deformation of the vertical $\{z, v_z\}$ phase space at focus into one that is slightly curved forward (instead of entirely vertical). Conversely, a beam with constant energy a few percent

smaller than the intended energy of the waveform, or with an energy profile that decreases by a few percent over the pulse length, results in the deformation of the vertical $\{z, v_z\}$ phase space at focus into one that is slightly curved backward. Both types of change reduce the compression by smearing the focal plane in a manner similar to chromatic aberration.

Finally, the type of intense ion beam distribution that characterizes the longitudinal temperature affects the temporal shape of the current profiles in the laboratory frame, and therefore the associated compression ratios and pulse lengths. The original $E_0 = 400$ keV, $t_p = 300$ ns, $f = 0.5$ simulation (presented and analyzed earlier), using the "smooth" waveform across the finite-size gap, is revisited one more time in order to discern the effect on longitudinal focus, located at $z = +59.5$ cm and $t = 959$ ns, when the $T_b = 0.2$ eV Maxwellian distribution is changed to a $T_b = 0.6$ eV Waterbag distribution. Recall from Sec. 4.7.2 that the Waterbag thermal distribution is a uniform-density velocity distribution between $v_0 - v_{th}$ and $v_0 + v_{th}$, and $T_M = 3\,T_W$ for the same v_{th} involved, according to Eqs. (4.53) and (4.54). Therefore, for $T_M = T_W$, the thermal velocities of the two distributions satisfy $v_{th}^W = \sqrt{3}\,v_{th}^M$. However, in order to directly compare the effect of the shape of the two distributions equally in particle-in-cell simulation, the Waterbag distribution width must be equal to the full $3\,v_{th}^M$ ($3\,\sigma = 99.73\%$) Maxwellian distribution, so $v_{th}^W = 3\,v_{th}^M$ and $T_W = 3\,T_M$ are employed.

The current profiles for the Maxwellian and Waterbag distributions at axial locations near the shared focal plane ($z = +59.5$ cm) are plotted as a function of absolute time on a linear scale in Fig. 4.34. At $t = 959$ ns, the Maxwellian current profile peaks at a compression ratio of 320 (refer also to Fig. 4.22), whereas the Waterbag

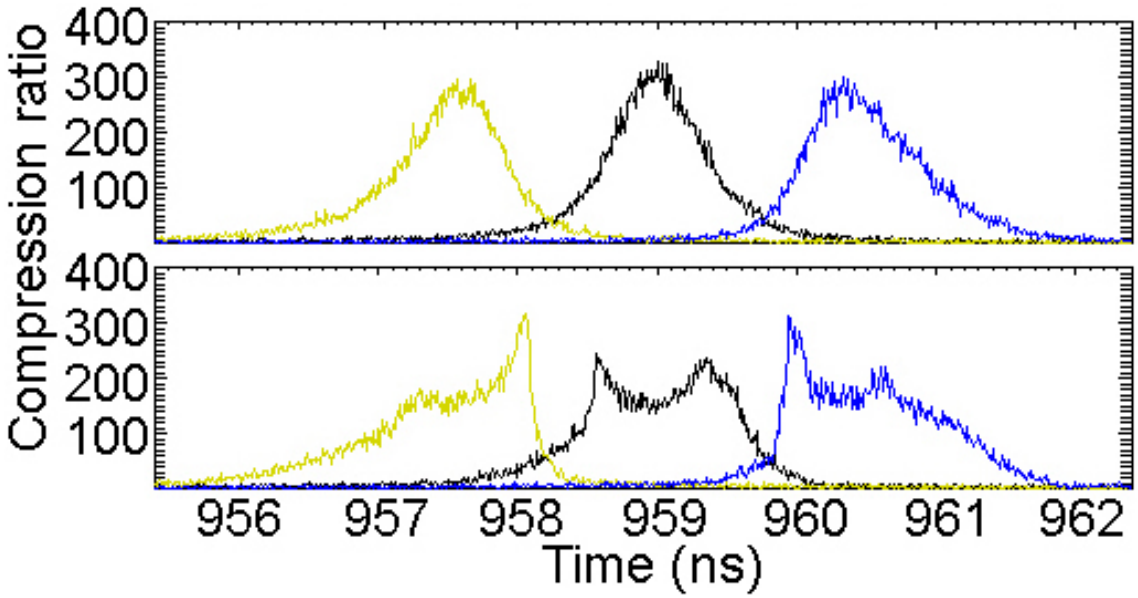

Figure 4.34: (Color) Longitudinal compression ratio $I_b(t)/I_0$ comparison for the "smooth" waveform across the finite-size gap in the laboratory frame obtained from simulation at $z = +59.3$ cm (yellow), at the focal plane $z = +59.5$ cm (black), and at $z = +59.7$ cm (blue) for beams initialized with a $T_b = 0.2$ eV Maxwellian (top profiles) [from Fig. 4.22] and $T_b = 0.6$ eV Waterbag distribution (bottom profiles).

current profile is near a local minimum compression ratio of 150. Compression ratios closer to the Maxwellian maximum for the Waterbag case $(300 - 320)$ are found just upstream and downstream from the intended focal plane at later and earlier times, respectively, within the individual profiles. The approximate t_{fwhm} at the various locations are similar for both cases, but the Maxwellian case maintains higher peak compression ratios near the center of each of the profiles due to the increased velocity space population densities near the desired v_z values for the particular waveform compared to the Waterbag case, whose velocity space population densities are equidistant about the same desired v_z values. Consequently, the bell-shaped normal distribution in the Maxwellian case achieves more compression and therefore shorter t_{fwhm} times, with similar pedestals in current due to the finite-size gap and chromatic aberration.

The bell shapes found in the profiles of the Maxwellian case are replaced with shapes approximating squares in the Waterbag case, as one might anticipate. The sharp peaks in current late in time for individual profiles upstream of the intended focus, and those early in time for individual profiles downstream, are due to the sharp velocity space boundaries of the Waterbag distribution; the Maxwellian case does not have the same features because of its diffuse shape. Specifically, the sharp velocity space boundaries for the faster particles in the tail of the beam contribute to relatively larger peaks in current because of the decreased levels of chromatic aberration suffered by the tail compared to the head. Therefore, the relatively increased current peaks arrive later in time for profiles upstream of focus, and earlier in time for those downstream, where the beam tail particles pass the head particles.

In practice, intense ion beam longitudinal distributions are closer to Maxwellian in the Neutralized Drift Compression Experiment because of their creation from an emitter within the diode maintained at a certain temperature. However, the blue Waterbag profile in Fig. 4.34 suggests that, if an ion beam with a Waterbag distribution could be used for experiments requiring longitudinal compression, pre-heat of targets could be substantially reduced because the pre-pulse current pedestal for that case is significantly lower compared to the Maxwellian distribution, and the elapsed time required by the blue Waterbag profile to increase from low to peak current is significantly shorter than the same required by the Maxwellian distribution.

4.8 Summary and conclusions

The derivation of the ideal velocity tilt, and the voltage waveform that produces it, for an ion beam with zero temperature encountering an infinitely thin acceleration

gap was presented (Sec. 4.1). However, the theory of an ideally compressed beam is a mathematical exercise that can only be sought, but not realized, in experiments. The deleterious effects of an imposed non-ideal voltage waveform on a beam with finite temperature across an acceleration gap of finite length were included in the theoretical and simulation work in this Chapter. Ultimately, laboratory constraints and other physical realities limit the achievable compression factors and pulse lengths.

Reduced theoretical models have been used in order to realistically describe the longitudinal compression and propagation through neutralizing background plasma of an intense charge bunch in the NDCX device. A numerical implementation of the warm-fluid model was presented as a tractable computational tool for investigating the non-ideal effects associated with the experimental acceleration gap geometry and voltage waveform of the induction module, which act as a means to pulse-shape both the velocity and line density profiles in the beam frame (Sec. 4.2). The main observed features in the beam profiles were recovered with the fluid model, indicating that they do not require kinetic explanations and their origin lies in the finite nature of the gap. Pulse-shaped self-similar drift compression solutions can be realized in order to transversely focus the entire charge bunch to the same focal plane in upcoming simultaneous transverse and longitudinal focusing experiments.

A kinetic formalism based on the Vlasov equation has been employed in order to understand the physics of the central portion of the beam which acquired a linear velocity tilt with a parabolic line density profile (Sec. 4.3). The model was used to show that the peaks in the experimental current profiles were a result of the fact that only the central portion of the beam which was tilted well contributed effectively to the main compressed pulse. Significant portions of the charge bunch resided in

the nonlinearly compressing part of the ion beam because of deviations between the experimental and ideal waveforms. Those regions formed a pedestal of current around the central peak, thereby decreasing the total amount of achievable compression and increasing the pulse durations achieved at the focal plane.

A hybrid fluid-Vlasov model which retained the advantages of both the fluid and kinetic approaches was implemented to describe the formation of pedestals in the current profiles by taking into account the finite-size gap effects but ignoring partial neutralization effects near focus (Sec. 4.4). Whether the ion beam has been tilted ideally or not, faster tail particles will overtake slower head particles and a framework that properly retains the velocity distribution information is therefore required to ascertain the current profiles in the vicinity of the focal plane (Sec. 4.5). Knowledge of the complete set of simulated current profiles $I_b(z,t)$ is valuable when making comparisons to experimental data. Generally, ion beam trajectories must be evaluated numerically using a particle-in-cell code in order to take into account all the effects that ultimately determine the quality of the focal plane, since general solutions without assumptions become intractable due to all the complex interactions possible. However, for experiments involving only longitudinal focusing, the comparison between measurements and the various models was excellent (Sec. 4.6).

Simulations ascertained the implications of achieving longitudinal compression in the laboratory, as compared to an ideal waveform acting on a cold beam across an infinitely thin gap (Sec. 4.7). In reality, the electric field encountered by the beam has extent in space and time, relative to the size and pulse length of the beam, and gives rise to a number of complications. Quantitative examples explored the dependency of the physical limits of longitudinal compression on various parameters, such as the

finite-size gap, realistic "smooth" voltage waveforms, initial beam emittance, initial pulse length, intended fractional tilt, initial beam kinetic energy, and distribution. For example, the finite-size gap imparts an effective longitudinal temperature to the beam due to the coupling of transverse and longitudinal dynamics within it (Sec. 4.7.1). It was shown that emittance, whether present in the initial beam or imparted by the gap, contributes to aberration of the longitudinal focal plane (Sec. 4.7.2). Theory and simulation revealed that slower head particles suffer from the problem more than faster tail particles. In addition, the finite-size gap reduces the intended fractional tilt as a function of the initial pulse length, also resulting in effective longitudinal temperature increase (Sec. 4.7.3). An optimum drift length was argued to exist, for a given set of beam parameters, that balances the competing effects that determine the compression ratios and pulse lengths at focus. Finally, beam energy variations in experiments due to injector technology limitations, whether constant in time or not, were shown to result in sub-optimal compression (Sec. 4.7.4).

In summary, no universally valid analytic model exists for determining the expected current compression ratio and pulse length at focus because of the intractability of including its dependence on many parameters, such as voltage waveform and finite-size gap geometry, beam parameters, partial neutralization by the plasma, and other effects that decrease the compression results. Therefore, particle-in-cell simulations were employed to investigate most of the major "realistic" effects contributing to the physical limits of longitudinal compression.

Chapter 5

Large-Space Scale and Long-Time Scale Plasma Flow

In order to satisfy $n_p >> n_b$ in the Neutralized Drift Compression Experiment and provide excellent neutralization for intense charge bunch compression, numerical simulations [Welch *et al.*, 2001, Kaganovich *et al.*, 2001] suggest plasma densities $10 - 100$ times the local ion beam density throughout the drift chamber are required, thereby allowing quiescent beam propagation above the traditional space-charge limit as the beam focuses [Welch *et al.*, 2003a]. Plasmas are currently created in two different ways for use in ongoing beam transport and compression experiments. The types of plasma sources used to provide the $1 - 2.5$ m of background plasma column (refer to Fig. 1.7) are the filtered cathodic-arc plasma source and the barium titanate ($BaTiO_3$) ferroelectric plasma source.

In Chapter 4, it was assumed that the full length of the drift chamber was entirely filled with a prescribed amount of uniform and stationary high-density background plasma. Plasma details such its formation, dynamical flow to fill the drift region, and

spatially- and temporally-dependent variations were ignored. The plasma parameters largely control the degree of neutralization of the beam space-charge and current; the effectiveness of the neutralization is dependent upon the density and temperature profiles of the plasma, in particular, and will be discussed in Chapter 6. The upper limit of achievable ion beam current density compression increases as the available plasma density increases, especially near the focal plane, and will also be investigated further in Chapter 6. In order to increase the understanding of techniques for creating plasma columns in beam compression experiments, assess the temporal evolution of the spatial plasma density profiles, and provide comparisons with measurements, both types of sources are modeled in large-space scale and long-time scale particle-in-cell simulations. All of the $2D$ and $3D$ plasma flow simulations presented in this Chapter are performed using the LSP code, solve the electromagnetic field equations, treat all particle species as explicit and kinetic, resolve ω_{pe} and Ω_{ce}, use the cloud-in-cell model, are not susceptible to the so-called numerical Debye length instability, and conserve energy to good accuracy levels.

Three-dimensional simulations of the filtered cathodic-arc plasma source used in experiments to create and inject highly ionized, supersonic plasma jets into the system, in the presence of a complex magnetic topology, are presented in Sec. 5.1, and the coupling efficiency of the plasma flow from source to drift region is discussed. Three-dimensional particle-in-cell simulations of plasma flow from the $BaTiO_3$ ferroelectric source in a variety of symmetric and asymmetric circumstances are reported in Sec. 5.2, and comparison to on-axis plasma density measurements is provided. In order to transversely focus an intense beam with an axial velocity tilt to a sub-mm radius coincident with the longitudinal focal plane, a strong final-focus solenoid

filled with high-density plasma will be used in future experiments. In Sec. 5.3, two-dimensional large-space scale and long-time scale simulations are carried out in order to assess the feasibility of supersonically injecting high-density plasma into a final-focus solenoid from the low-field region for beam neutralization experiments. Experiments are planned to measure whether such an injected plasma can fill the high-field region of a strong solenoid, and provide quantitative comparison to the predictions made by simulations.

5.1 Filtered cathodic-arc plasma source

A pair of pulsed, cathodic-arc plasma sources were initially designed and fabricated at the Lawrence Berkeley National Laboratory for experiments on the Neutralized Transport Experiment (refer to Sec. 1.4) [Henestroza *et al.*, 2004]. The filtered cathodic-arc plasma source (FCAPS), also known as the metal vapor vacuum arc (MEVVA) source, produces highly ionized aluminum plasma with supersonic ion velocities, over a density range of $n_p \sim 10^8 - 10^{12}$ cm^{-3} and in pulse durations of $1 - 1000$ μs, by adjusting the arc current and discharge voltage of its pulse-forming network. The cathodic-arc plasma source is of the gun variety and consists of a replaceable cathode rod surrounded by a ceramic insulator and a grounded anode [MacGill *et al.*, 1998]; it is coupled to a solenoidal coil, which can be curved up to $\pm\pi/2$ radians, serving as a macroparticle debris and neutral atom filter [Anders, 1999]. The macroparticle filter contributes to the externally applied magnetic field configuration responsible for manipulating the plasma parameters achieved in the experiment, such as the ion kinetic energy [Anders and Yushkov, 1999]. In general, the lack of macroparticles and neutral species is attractive for beam experiments because of the concern over

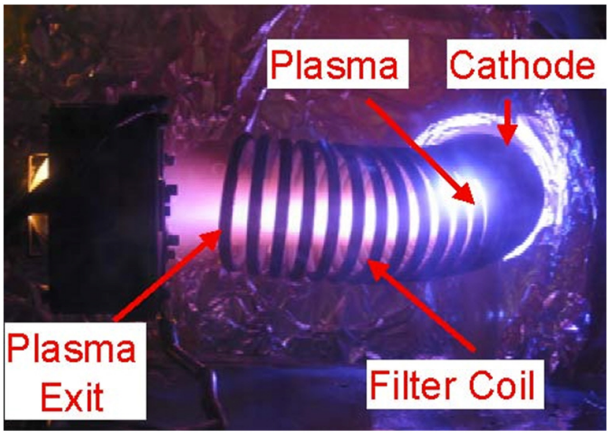

Figure 5.1: (Color) Photograph of the filtered cathodic-arc plasma source in operation on a test stand, before installation on the NDCX device [ATI, 2006].

charge-exchange and scattering processes involving the beam. Therefore, the high-current cathodic-arc source is a good choice for providing neutralizing plasma in beam compression experiments because a negligible fraction of neutral atoms and molecules exist in the plasma. Also, such sources are easy to construct, reliable, and have long lifetimes (approximately 10^5 shots). A photograph of the filtered cathodic-arc plasma source in operation on a test stand, before installation for beam compression experiments, is provided in Fig. 5.1 [ATI, 2006].

Longitudinal compression experiments require plasma densities in the $n_p \sim 10^{10} - 10^{11}$ cm^{-3} range, due to predictions of maximum beam density provided by theory and simulations, whereas simultaneous transverse and longitudinal compression experiments are expected to require plasma densities in the range of $n_p \sim 10^{12} - 10^{14}$ cm^{-3} or higher, depending on the strength of the applied focusing elements involved [Sefkow *et al.*, 2007]. The filtered cathodic-arc source is able to produce peak densities around $n_p \sim 10^{12}$ cm^{-3} near the exit of the macroparticle filter region. Therefore,

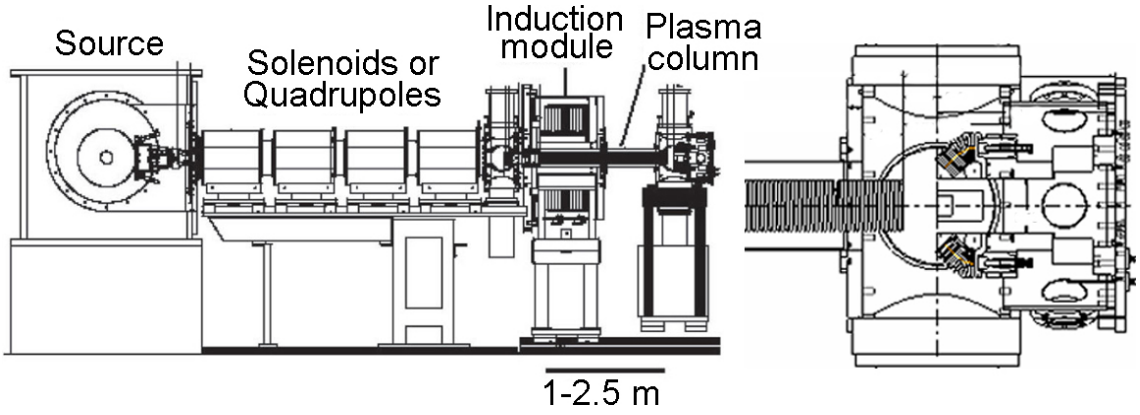

Figure 5.2: Schematic of the NDCX device (left) and close-up drawing of the end of the plasma column and diagnostic box region (right). As shown, the two cathodic-arc source filter coils are angled at $\theta = \pm\pi/4$ radians relative to the axis of the long guide solenoid, which is aligned along the plasma column region. The drift tube and guide solenoid can be modified to extend from $1 - 2.5$ m.

the plasma source may be able to provide just enough plasma density for initial simultaneous transverse and longitudinal focusing experiment goals involving beam radii $r_b < 0.5$ cm. However, plasma sources capable of providing densities $n_p > 10^{12}$ cm^{-3} are under investigation (both modified existing sources and additional sources) for future experiments, which will seek to greatly increase the achievable amount of compression in ion beam current density and provide sub-mm spot sizes.

Figure 5.2 illustrates the location of the filtered cathodic-arc plasma source for neutralized drift compression experiments; the schematic on the left of the figure is a reproduction of Fig. 1.7 and the drawing on the right is a close-up of the end of the plasma column and diagnostic box region. Two source and filter pairs are installed on opposite off-axis sides in the diagnostic box at the downstream end of the experiment and positioned to face the upstream direction. The pairs need to be placed out of the line-of-sight of the beamline in order to avoid interacting with the beam, as well as to accommodate beam diagnostics. High-density plasma is created at vacuum arc

cathode spots [JUTTNER, 1987] on the surfaces of the *Al* sources. However, virtually any metal can be used as the cathode material. Magnetic fields provided by the two curved filter coils assist in the upstream injection of plasma by guiding it into the beamline from the two off-axis locations downstream of the drift chamber. The curved magnetic fields of the bent filter coils cause only ionized metal plasma to symmetrically reach the neutralization region. The filter coils are placed at angles of $\pm\pi/4$ radians relative to a long axial guide solenoid used throughout the main drift region. In order to fill the variable $1 - 2.5$ m high-density plasma column in the beamline, a solenoidal magnetic field of the same length is required in the drift region in order to act as a guide for the plasma flow. The filter coils and guide solenoid are situated close enough to each other in order to provide some magnetic field coupling of fringe fields between them, and facilitate the transfer of plasma from the sources to the neutralized drift region. The guide solenoid provides confinement of the cathodic-arc plasma throughout the drift region by magnetizing the electrons. In fact, the presence of the background magnetic field slightly influences ion beam particle trajectories, as well as neutralization physics, by constraining the electron motion. Finally, an important point to mention regarding filtered cathodic-arc plasma sources is that plasma streams into the beamline at supersonic ion velocities: the ion species can attain tens to a few hundred eV in directed energy, depending on the mass, with a typical range of ion drift velocities around $0.5-3\times10^4$ m/s [ANDERS and YUSHKOV, 1999]. A one-dimensional model of a single cathode spot and the resulting plasma jet ascribe the acceleration of the ions to the electron pressure gradient acting through electron-ion friction [WIECKERT, 1987].

The main drawback to the previously described method of providing a high-volume

plasma in the drift region is the injection method. Both an electrostatic trap (biased negatively to a few kV) and a permanent magnetic dipole are found experimentally to be necessary to reduce the supersonic upstream movement of the flowing plasma to lower density levels. The additional trap and dipole use valuable axial real estate in the experiment and increase both the required length of unneutralized transport (a concern for beams with large perveance) as well as the focal distance. Of greater consequence is whether electrons from the plasma are nevertheless allowed to penetrate up the beamline, into the acceleration gap, and farther upstream into the magnetic transport region. If the electrostatic trap and permanent magnetic dipole insufficiently stop the upstream plasma motion, the ion charge bunch dynamics can be greatly affected by the presence of electrons in regions originally intended for unneutralized transport. The beam's emittance can deleteriously increase due to the nonlinear space-charge forces and partial neutralization effects from the electron presence, possibly resulting in a significant degradation in focal spot and pulse length. Preliminary research suggests that some cathodic-arc plasma can penetrate the trap and dipole with associated densities a few orders-of-magnitude lower than the bulk plasma densities, which may affect beam transport. Other sources of secondary electrons and electron clouds, such as halo beam ion impact on the chamber walls [Covo *et al.*, 2006b] in the transport section and aperture region, are under active investigation, in order to understand and mitigate their impact on ion beam compression experiments [Covo *et al.*, 2006a].

Guidance for designing the filtered cathodic-arc plasma sources in order to achieve desired plasma density in the drift region, as well as to understand plasma flows in complex magnetic geometries, can be provided with large-space scale and long-time

scale plasma flow particle-in-cell simulations. Parameters that affect the coupling efficiency of the plasma from sources to the drift region include the arc voltage and cathode material, the angle θ of the filter coils relative to the guide solenoid, the horizontal separation distance d between the end of the guide solenoid and midplane exit of the filter coils, the offset h of the midplane exit of the filter coils from the beamline axis, the absolute amounts of magnetic field provided by the filter coil and guide solenoid currents, and the relative ratio r of the peak magnetic field strengths between the guide solenoid and filter coils.

The calculations in Fig. 5.3 employ an analytical model [Gilson, 2006] to determine the $3D$ magnetic field topologies in the intermittent region between the field coils and guide solenoid (slices through the midplane are shown). Both the analytical model and the numerical particle-in-cell model consider the full $3D$ problem due to the lack of symmetry in any coordinate ($\{r, z\}$ or $\{x, z\}$ coordinate systems alone would not describe the magnetic field topology properly). The filter coils are treated as straight finite-length solenoids placed at an angle relative to the guide solenoid, and therefore the model only approximates the correct field topology (the filter coils are actually curved). The inner radii of the filter coils and guide solenoid are $r_f = 2.5$ cm and $r_g = 3$ cm, respectively; the offset $h = \pm 6$ cm and the angle $\theta = \pm\pi/4$ for the filter coils in all of the illustrative cases in Fig. 5.3. It is obvious that shorter separation distances d result in higher intermittent field regions because of the increased overlap of fringe fields between the solenoids. Reduced filter coil angles can also help improve the plasma flow line-of-sight to the guide solenoid, but at the cost of reducing the offset height and decreasing the levels of clearance for the beam and its diagnostics. Experiments show that stronger magnetic fields in cathodic-arc sources

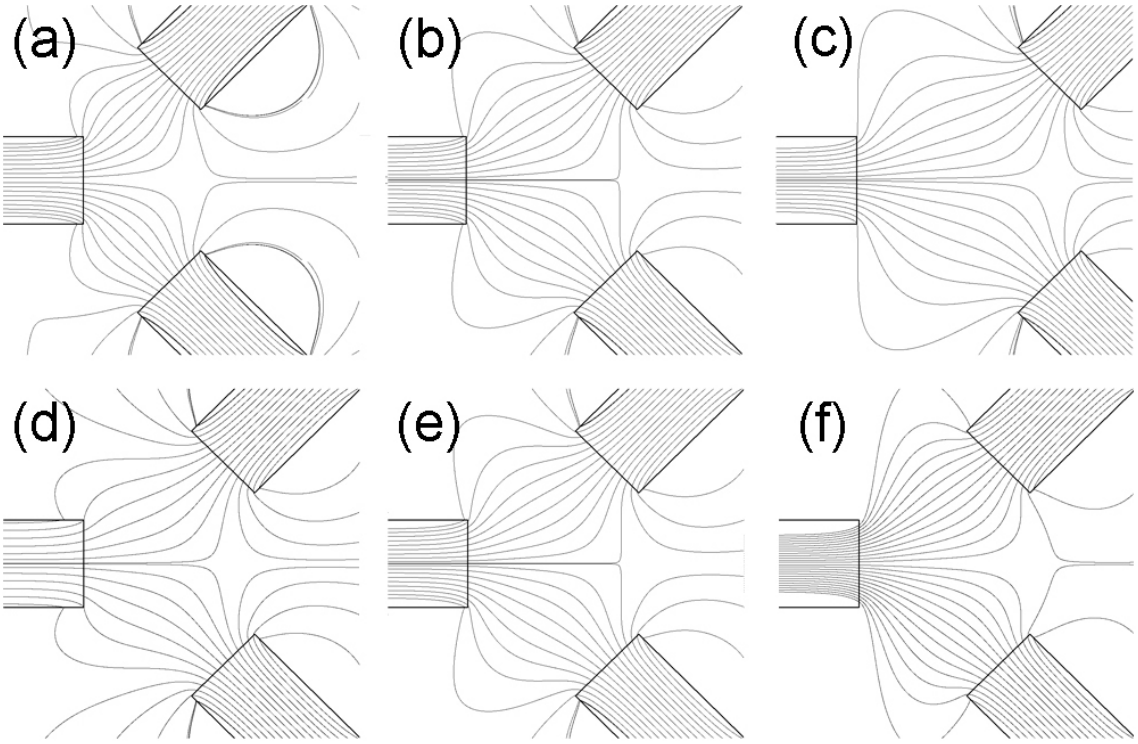

Figure 5.3: Analytical calculation of magnetic field lines [Gilson, 2006] from three straight finite-length solenoids, approximately corresponding to possible geometrical configurations for cathodic-arc plasma injection into the NDCX beamline. Slices through the midplane of the $3D$ topology are shown. The inner radii of the filter coils and guide solenoid are $r_f = 2.5$ cm and $r_g = 3$ cm, respectively; the offset $h = \pm 6$ cm and the angle $\theta = \pm\pi/4$ for the filter coils in all of the cases. In the top row, the peak magnetic fields from the filter coils and guide solenoid are of equal strength (2 kG) but the separation distance is $d = 5$ cm (a), $d = 8$ cm (b), and $d = 11$ cm (c). In the bottom row, the separation distance is constant ($d = 8$ cm) but the relative ratio of peak magnetic field strengths between the guide solenoid and filter coils is $r = 0.25$ (d), $r = 1$ (e), and $r = 4$ (f). Cases (b) and (e) are identical. The beam would travel from left to right in this coordinate system, as in Fig. 5.2.

can increase plasma temperatures and reduce density gradients compared to free expansion [Anders and Yushkov, 1999]; also, different magnetic field geometries may increase or decrease the kinetic energy of the plasma ions, depending on the configuration. The absolute values and relative ratio of peak magnetic field strengths in the guide solenoid and filter coils are important to consider in terms of plasma steering and flow because of the effects of ∇B and curvature drifts, as well as the role of magnetic mirroring [Goldston and Rutherford, 1995], especially as it relates to the exchange of parallel and perpendicular energies.

Optimization of the plasma density and uniformity throughout the drift length involves the proper placement and orientation of the sources and filter coils relative to the long guide solenoid in the drift region, finding the appropriate combination of filter coil and guide solenoid magnetic field strengths, and ensuring an adequate amount of both axial and radial plasma-fill in the guide solenoid. In addition, the plasma ion kinetic energies of cathodic-arc plasmas can be directly manipulated by judicious choice of magnetic field configurations [Anders and Yushkov, 1999]. Planned filtered cathodic-arc source experiments will provide plasma density measurements as a function of space and time for the aforementioned parameters. The magnetic field topology created by the two curved filter coils and the longer guide solenoid can be numerically calculated for various geometries in order to determine the optimum relative positioning of the components. The plasma flow profiles for the different scenarios can be assessed using LSP simulations and, in conjunction with experimental measurements, provide insight into the coupling efficiency of the off-axis plasma sources to the axial neutralization section; particle-in-cell simulations offer an increased understanding of plasma flow in complicated magnetic field topologies, where

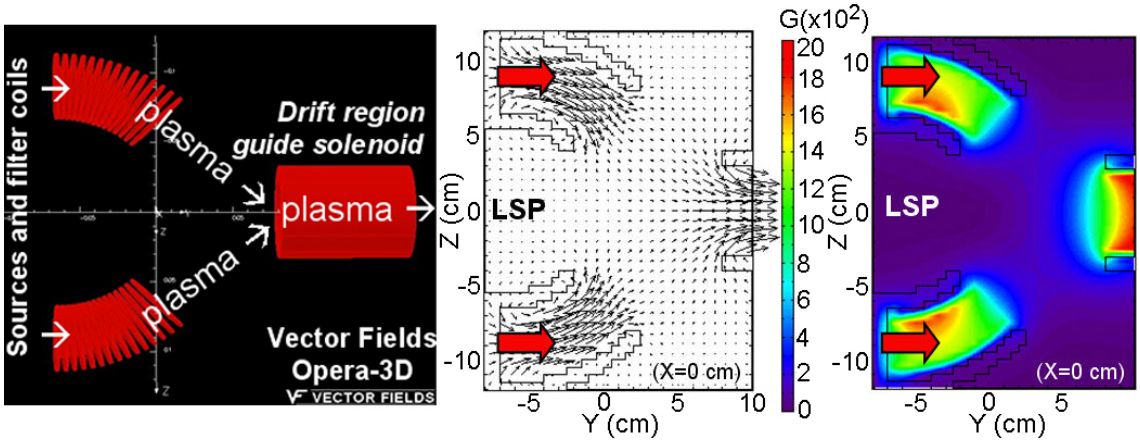

Figure 5.4: (Color) Schematic and magnetic field topology from the cathodic-arc plasma flow simulation (slices through the $x = 0$ cm midplane are shown). Magnetic fields corresponding to case (b) in Fig. 5.3 (with curved filter coils) are calculated by Vector Fields Opera-3D from the solenoid arrangement (left), and the resulting vector field (middle) and isocontours of total field magnitude (right) are initialized into the LSP code. White and red arrows show the intended plasma flow and location of the sources, respectively. The beam would travel in the $-\hat{y}$ direction in this coordinate system, aligned on the $z = 0$ axis. The intended focal plane is near $y = 0$.

other theories and methods may be inadequate or intractable.

Large-space scale and long-time scale 3D particle-in-cell simulations are carried out in order to study the evolution of the plasma flow provided by the filtered cathodic-arc source. The goal is to study the coupling efficiency of the plasma flow from creation, through the curved filter coils, and into the drift region guide solenoid, where beam neutralization occurs. A diagram of the simulation set-up, which closely resembles the configuration used by the filter coils and guide solenoid for initial longitudinal compression experiments in the NDCX device, is shown in Fig. 5.4. 3D Cartesian coordinates are employed for $x = \{-5 \text{ cm}, +5 \text{ cm}\}$, $y = \{-8 \text{ cm}, +10 \text{ cm}\}$, and $z = \{-12 \text{ cm}, +12 \text{ cm}\}$ (note that 2D slices through planes will be shown for clarity reasons). The 3D magnetic fields from static current flow through the configuration

of filter coils and drift region guide solenoid corresponding to case (b) in Fig. 5.3 are calculated [JUNG, 2006] using the finite-element code Vector Fields Opera-3D [VFO-3D, 2005]. The geometry includes the offset $h = \pm 6$ cm, angle $\theta = \pm\pi/4$, and separation distance $d = 8$ cm. The relative ratio of peak magnetic field strengths between the guide solenoid and filter coils is $r = 1$, with an absolute peak magnitude of $B_z = 2$ kG within them. The magnetic topology is then conformed to the discrete grid used in the simulation space. Figure 5.4 also presents the resulting vector field and isocontours of total field magnitude (as slices through the $x = 0$ midplane) initialized in the code.

Since the simulation is conducted in three dimensions, and the associated computation time increases with the total number of nodes on the simulation grid, the spatial resolution in each direction is limited to 0.5 cm (approximately 3.8×10^4 total nodes). The beam would travel in the $-\hat{y}$ direction in this coordinate system, aligned on the $z = 0$ axis. Also, recall that the plasma injection occurs at the downstream end of the experiment and the intended focal plane lies in the $y = 0$ region. Conducting boundary conditions are imposed at the walls of the filter coils, guide solenoid, and diagnostic box. An open boundary is modeled inside the guide solenoid of radius $r_g = 3$ cm, which is where confined plasma flows upstream for $1 - 2.5$ m to form the plasma column, at $y = +10$ cm and $z = 0$ in the LSP plots of Fig. 5.4.

Plasma is continually injected into this configuration until steady state flow is observed; the red arrows in Fig. 5.4 indicate the locations of injection. The ion species modeled is Al^+, as in the experiment, since aluminum is inexpensive, easily arced, and does not introduce foreign elements into the beamline. The simulated ions are injected from the base of the two bent filter coils of radius $r_f = 2.5$ cm at

$y = -7$ cm and $z = \pm 9$ cm, with a supersonic drift velocity in the $+\hat{y}$ direction of 1.44 cm μs^{-1} ($E_i \sim 29$ eV of directed energy for Al^+), in agreement with experimental measurements [Anders and Yushkov, 1999, ATI, 2006]. At the two plasma jet injection locations, the supersonic ion directed energy is parallel to the background magnetic field, where the unit vector pointing in the direction of the magnetic field is $\hat{\mathbf{b}} = \mathbf{B}/B$. The peak ion current density is approximately $J_{pi} \sim 40$ mA cm^{-2}, although an equal amount of electron current density is also injected, corresponding to a peak plasma density estimate of $n_p \sim 2 \times 10^{11}$ cm^{-3} near the sources within the filter coils. Gaussian distributions with temperatures $T_i = 1$ eV and $T_e = 5$ eV are imposed on the injected ion and electron populations, respectively. The injected ion Mach number, defined as the ratio of directed ion velocity to ion sound speed (including the T_i correction), is approximately 2.7. Scattering effects are included by using internally-computed Spitzer rates for Coulomb collisions between charged particles. The simulation is executed out to $t = 40$ μs with a time step satisfying the constraints of $\omega_{pe}^{peak}\Delta t < 0.75$ and $\omega_{ce}^{peak}\Delta t < 1$ (about 1.33×10^6 total steps), where ω_{pe}^{peak} and ω_{ce}^{peak} are the peak expected electron plasma and cyclotron frequencies, respectively. During steady state plasma flow, more than 5×10^5 particles are explicitly pushed on the simulation grid at each time step. It should be noted that the plasma injection described in this simulation is only an approximate model, since the actual plasma creation mechanism itself is not included.

The plasma jets originate within a high-field region ($B_z = 2$ kG) and the $\theta = \pm\pi/4$ bends in the filter coils are intended to direct plasma towards the $z = 0$ axis. Generally, the complex magnetic topology throughout the entire region significantly affects the plasma flow profiles, including near the source, where it influences the

discharge and plasma properties. Not only does the relative strength of the filter coils and guide solenoid play a role, but the intervening gradients modify the phase space of the plasma particles. In the configuration considered here, the ions are unmagnetized with gyro-radii ($\rho_L = v_\perp/\omega_c$) on the same scale as system dimensions (cm), whereas the electrons are magnetized with gyro-radii on the μm scale. Therefore, the electrons mostly follow field lines and ambipolar forces greatly influence ion movement. It should be noted the plasma beta is very small, *i.e.*, the ratio of plasma pressure to magnetic pressure throughout the simulation space is much less than unity.

Figure 5.5 illustrates plasma electron densities obtained from particle-in-cell simulation at various times in the form of $2D$ $\{y, z\}$ and $\{x, z\}$ isocontours through different planes. The faster ions of the explosively-created supersonic Al^+ plasma, some of which are accelerated by an electron sheath in the $+\hat{y}$ direction during the initial expansion, do not couple well to the guide solenoid because of their high average energies, and instead strike the diagnostic box at $x^2 + z^2 > 9$ cm^2 at $y = +10$ cm. Subsequent ions are not accelerated and the simulation space fills with plasma. As plasma ions exit the top (bottom) filter coil near the $y = 0$ cm plane, they begin to turn with the magnetic field and gain average directed energies in the $-\hat{z}$ $(+\hat{z})$ and $-\hat{x}$ $(+\hat{x})$ directions of approximately $E_i \sim 5$ eV and $E_i \sim 3.5$ eV, respectively, at the expense of 8.5 eV from the initial $E_i \sim 29$ eV injected in the $+\hat{y}$ direction. Electrostatic sheaths are quickly established near the conducting boundaries of the filter coils to increase the incident ion flux due to preferential electron loss near those boundaries. After the exit from the filter coils, the plasma expands into an intermediate region of decreased magnetic field strength (refer to Fig. 5.4) between the filter coils and guide solenoid, before encountering an increased field strength region near

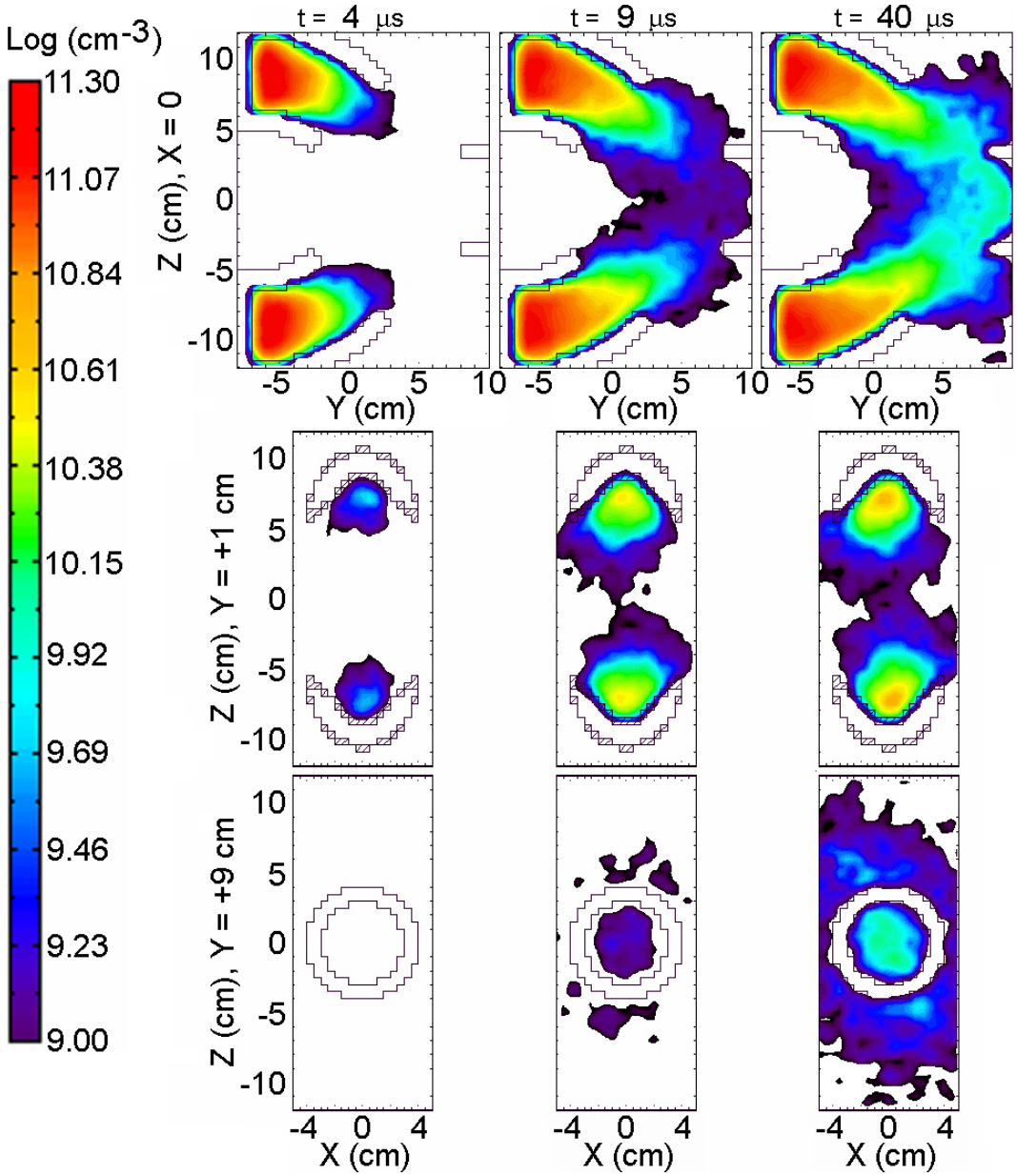

Figure 5.5: (Color) Filtered cathodic-arc plasma electron density isocontours from LSP simulation at $t = 4$ μs (left column), $t = 9$ μs (center column), and $t = 40$ μs (right column). Results are presented as (y, z) slices at $x = 0$ (first row), (x, z) slices at $y = +1$ cm (second row), and (x, z) slices at $y = +9$ cm (third row). The role of electron guiding-center drifts in the non-uniform magnetic field is evident. All plots are on the same Log scale.

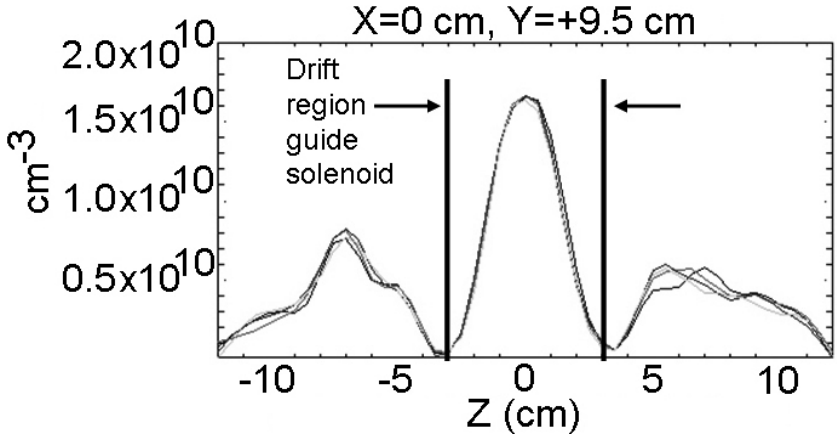

Figure 5.6: Plasma density axial slices at late times ($t = 35 - 40\mu$s) across the guide solenoid region at $x = 0$ and $y = +9.5$ cm. Steady state plasma flow profiles are reached by about $t \sim 15$ μs. Of the plasma that reaches the $y = +9.5$ cm plane, approximately 50% of it has been coupled into the drift region guide solenoid.

the guide solenoid (also $B_z = 2$ kG) at $y = +8$ cm. Apparently, the plasma density drops the most near the exit of the filter coil due to the expansion into the low-field region. By $t = 8$ μs, plasma densities in excess of 10^9 cm^{-3} begin to fill the $z = 0$ axis region within the guide solenoid, with average $+\hat{y}$-directed and $\pm\hat{z}$-directed (towards the $z = 0$ axis) ion energies of approximately $E_i \sim 75$ eV and $E_i \sim 10$ eV, respectively.

The initial expansion of the plasma into the simulation space ceases around $t = 15$ μs, when steady state plasma flow conditions begin. The plasma density in the center of the guide solenoid is shown to exceed $n_p = 1.5\times10^{10}$ cm^{-3} in steady state conditions (the initial density in the filter coils is $n_p \sim 2 \times 10^{11}$ cm^{-3}). As shown in Fig. 5.6, approximately 50% of the plasma that reaches the $y = +9.5$ cm plane is coupled into the drift region guide solenoid. Also, both plasma jets from the two filter coils overlap near the $y = +9.5$ cm plane, and nearly equal populations of particles moving in the transverse $\pm\hat{x}$ and $\pm\hat{z}$ directions exist there.

After steady state plasma flow is reached, the $+\hat{y}$-directed average ion energy into the guide solenoid remains around the approximate value of $E_i \sim 19$ eV. The 10 eV difference compared to the initial injection energy is coupled through the magnetic field configuration into directed motion in the other two directions, as well as additional spread in all directions. Obviously, at least some of this energy transfer is necessary in order to divert the plasma created off-axis onto the $z = 0$ axis for coupling into the guide solenoid. However, some directed ion energy is also diverted away via ambipolar forces, as well as perpendicular and parallel ∇B field gradients and curvature effects, all of which give rise to electron guiding-center drifts.

It is evident in Fig. 5.4 that magnetic field gradients, both perpendicular and parallel to $\hat{\mathbf{b}}$, and curved magnetic fields are present in the filtered cathodic-arc plasma injection configuration; guiding-center drifts (gyro-averaged particle motion) across the magnetic field, as well as acceleration and deceleration along the magnetic field, are expected for the electrons (since they are the only magnetized species), and ambipolar forces will play a significant role in the dynamics. Plasma drifts arising from magnetic field gradients and curvature are important in this scenario, since they affect the coupling efficiency (50%, here) of plasma into the drift region guide solenoid.

Since they are the only magnetized species, the electrons acquire perpendicular (to $\hat{\mathbf{b}}$) guiding-center drift velocities from the non-uniform magnetic fields according to [Goldston and Rutherford, 1995]

$$\mathbf{v}_d = -\frac{W_\perp}{e_c}\frac{\mathbf{B}\times\nabla B}{B^3} - \frac{2W_\parallel}{e_c}\frac{\mathbf{B}\times(\hat{\mathbf{b}}\cdot\nabla)\hat{\mathbf{b}}}{B^2}\,, \tag{5.1}$$

where e_c is the electron charge, and $W_\perp$ and $W_\parallel$ are the average perpendicular and

parallel particle energies relative to the applied magnetic field, respectively. An important point is that this formula is only valid for non-uniform fields whose gradient scale lengths are much greater than the gyro-radii involved (the electrons, in this case). The ∇B and curvature drifts affect the first-order particle motion and arise from consideration of only perpendicular gradients in B and curvature of locally-constant B. In addition, particles traveling in a curved magnetic field experience an outward centrifugal "pseudo-force", $\mathbf{F}_{cf} = mv_{\parallel}^2\mathbf{R}_c/R_c^2$, where R_c is the radius of curvature vector from the local center-of-curvature to the magnetic field line [Goldston and Rutherford, 1995]. Figure 5.5 convincingly shows electron guiding-center drifts in the $-\hat{x}$ ($+\hat{x}$) direction, as well as centrifugal "pseudo-forces", affecting plasma injected from the top (bottom) filter coil. Although, the radius of curvature of the local magnetic field changes polarity as a particle moves away from its filter coil of origin and closer to the guide solenoid (refer to Fig. 5.4), and some of the drift motion is offset as a result. However, the non-uniform magnetic topology considered here complicates matters further: the fields of the filter coils are curved relative to the field of the guide solenoid, and changes in perpendicular and parallel velocity relative to the local $\hat{\mathbf{b}}$ ($v_{\perp}$ and $v_{\parallel}$, respectively) due to electron guiding-center drifts are only measured relative to local fields. Indeed, due to the orientation of the three solenoids, some $v_{\perp}$ is actually $v_{\parallel}$ relative to the guide solenoid and vice versa. Regardless, competing effects like the reduction of density gradients and variation in ∇B and curvature drifts imply that the ion velocity, which responds to ambipolar forces as a function of absolute and relative field strengths of the three solenoidal coils, will exhibit non-monotonic behavior. Experimental evidence affirming this conjecture and additional related details are provided in [Anders and Yushkov, 1999].

Due to the spacing between the filter coils and guide solenoid, as well as the relative magnetic field strength between the two, gradients in magnetic field strength parallel to $\hat{\mathbf{b}}$ unavoidably and significantly alter the zeroth-order parallel velocity dynamics of any magnetized species because of forces arising in the direction opposite to the field gradients. The magnetic moment of a charged particle, $\mu = mv_{\perp}^2/2B$, is an adiabatic invariant in the limit of no collisions. The conservation of μ in the presence of a magnetic field whose strength varies in the direction of $\hat{\mathbf{b}}$ leads to a well-known result called the magnetic mirror effect [Chen, 1984]. Conservation of kinetic energy implies that the velocity component of a charged particle parallel to the magnetic field will increase or decrease if the field strength decreases or increases along the field line. In the absence of electric fields and collisions, two constants of the motion, W (total kinetic energy) and μ, ensure that parallel velocity must change as a function of field strength according to $mv_{\parallel}^2/2 = W - \mu B$; in other words, for constant W and μ, when the local magnetic field changes, so must the particle's $v_{\perp}$ at the expense of the particle's $v_{\parallel}$.

Due to the magnetic mirroring effect, plasma electrons streaming out of the filter coil (from high magnetic field to low) are expected to accelerate, and electrons streaming into the guide solenoid (from low magnetic field to high) are expected to decelerate, in general, due to the force arising in the direction opposite to the field gradient, $\mathbf{F}_{\parallel} = -\mu\nabla B$. However, this effect is relatively minor in this particular application because of the supersonic nature of the injected ions, relative ratio $r = 1$ of peak magnetic field strengths, and separation distance $d = 8$ cm between the filter coils and guide solenoid. Figure 5.5 demonstrates that only a small fraction of the plasma is reflected away from the magnetic field surrounding the guide solenoid, and

the substantial majority of electrons are able to penetrate the high-field region of the guide solenoid. If the guide solenoid were much stronger than the filter coils and the ions weren't supersonic, the mirroring effect would greatly reduce the amount of plasma that would be able to penetrate into the high-field region of the solenoid.

The presence of the magnetic field and ambipolar forces increases the temperature relative to expansion without a field, but decreases the corresponding density gradient. For this reason, the specifics of the dynamics are configuration-dependent for complicated magnetic geometries, such as those considered here. As the plasma expands along field lines and the density decreases, the electron and ion temperatures become increasingly decoupled. An electron temperature drop from $T_e = 5$ eV to $T_e = 1 - 2$ eV is typically observed in cathodic-arc plasma source experiments and theoretical models including magnetic fields [Anders and Yushkov, 1999], and a decrease from $T_e = 5$ eV to $T_e = 2 - 3$ eV in electron temperature is observed in the present particle-in-cell simulation from the source to the guide solenoid. Due to anisotropic energy distributions, ion temperatures are not well defined. Figure 5.7 shows the electron temperature distribution in the $x = 0$ plane from the previously discussed simulation. Comparison to a simulation initialized with $T_e = 10$ eV is provided, and clearly resembles the original simulation when the factor of 2 difference in scales is taken into account. In addition, three further simulations considering injected ion and electron temperature pairs of $T_i = 1$ eV, 3 eV, and 10 eV with $T_e = 5$ eV, 10 eV, and 20 eV, respectively, result in small differences ($< 20\%$) between density profiles and coupling efficiencies. The corresponding ion Mach numbers are approximately 2.65, 1.72, and 1.06, respectively, where slightly higher coupling efficiencies and densities are associated with larger Mach numbers and lower temperatures, but

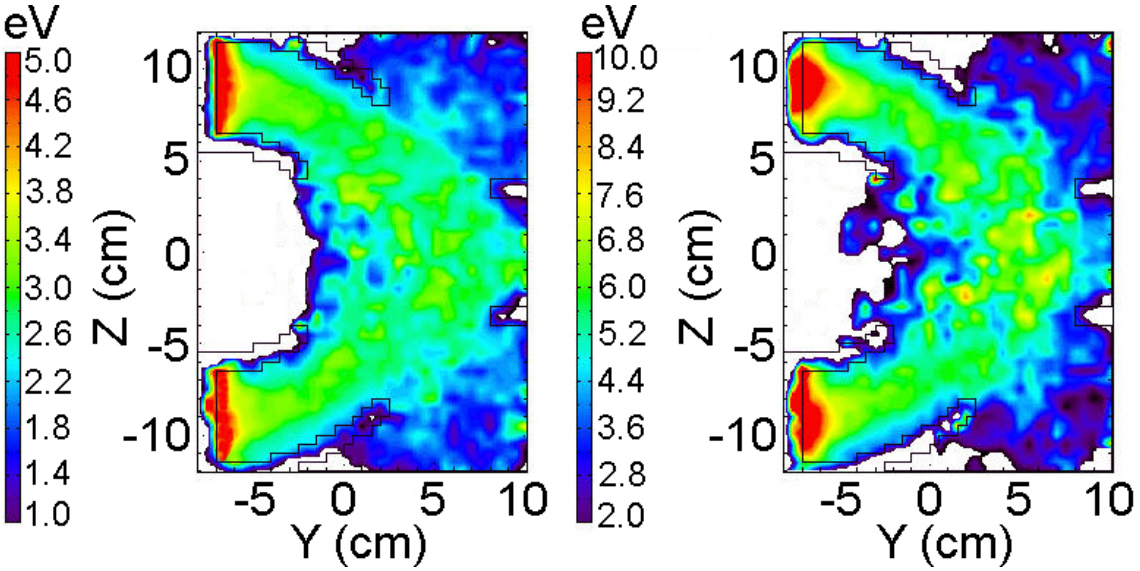

Figure 5.7: (Color) Cathodic-arc plasma electron temperature isocontours from particle-in-cell simulation during steady state plasma flow, presented as (y, z) slices at $x = 0$. The electron temperature decreases by a factor of 2 from inside the filter coils to the guide solenoid in the cases of initial $T_e = 5$ eV (left) and $T_e = 10$ eV (right). The linear scales take into account the factor of 2.

further research on this topic is required.

An important effect has been neglected in the present simulations. Filtered cathodic-arc plasma sources typically create a range of ion charge states. However, this more complex effect is not included in the simulations outlined here. Recent velocity measurements [Yushkov *et al.*, 2000] demonstrate that the ion velocity is virtually independent of the charge state, implying that the simulation of the singly-ionized Al^+ case presented here is generally valid. Consequently, since the directed ion energy is practically independent of charge state, the ion acceleration mechanism near the source itself is assumed to be hydrodynamic in nature and not associated with an electric field from a change in potential. The presence of the macroparticle filter's magnetic field is also known to directly increase the ion charge state of the

cathodic-arc source, as measured in [Anders and Yushkov, 1999].

The plasma densities used in the filtered cathodic-arc plasma injection simulation are estimated to be a factor of $5-10$ lower than the expected peak values achievable by the pair of sources in the experiment ($n_p \sim 10^{12}$ cm^{-3}), due to the desire to relax the numerical time step requirement of resolving processes on the plasma frequency time scale. However, the normal operating regime of the cathodic-arc source for initial longitudinal compression experiments is approximately the same (plasma densities in the low $n_p \sim 10^{10}$ cm^{-3} range, with temperatures around $T_p \sim 3$ eV).

The simulations provide evidence for significant plasma density loss in the filter coils due to a combination of electron curvature drifts, electrostatic sheath acceleration near the coils to increase incident ion flux, the centrifugal "pseudo-force", and acceleration of plasma electrons away from the high-field region due to the force arising in the direction opposite to the field gradient. Reducing the macroparticle filter angle $\theta = \pm\pi/4$ has the effect of increasing the density of the transported plasma to the $z = 0$ axis, but may also increase the neutral and macroparticle debris population if reduced too much. Plasma densities can be further increased for neutralization experiments by increasing the arc current and discharge voltage, increasing the number of filtered cathodic-arc sources beyond two, and moving the filter coils closer to the end of the guide solenoid. A wide range of electron densities can be chosen for beam experiments by judicious choice of the parameters involved in the plasma injection, including the timing of the beam arrival in the drift length. Further optimization of the coupling efficiency from plasma source to the guide solenoid in the neutralized drift region is possible using the numerical simulation technique outlined here.

The particle-in-cell simulations discussed in Sec. 5.1 lend increased confidence that

sufficiently high plasma density can be provided by the filtered cathodic-arc plasma source throughout the drift region for beam compression experiments. The goals of the $3D$ numerical simulations of the FCAPS have been achieved and discussed: to study, as realistically as possible, the coupling efficiency of the plasma flow from creation, through the curved filter coils, and into the drift region guide solenoid, where beam neutralization occurs. Finally, the various limitations and advantages of this particular choice of plasma injection configuration have been explained, and suggestions for additional simulations and optimization have been provided.

5.2 Ferroelectric plasma source

An additional source of large-volume plasma, which provides unbound electrons for beam neutralization experiments, involves a design based upon the use of ferroelectric ceramics [Rosenman *et al.*, 2000]. Recent research indicates the potential for ferroelectric materials to be used as large-surface-area electron emitters, capable of producing high current densities [Dunaevsky *et al.*, 2001b, Dunaevsky and Fisch, 2004]. The principle of operation of a plasma source made of ferroelectric material is centered around the fact that materials with large dielectric constants can greatly amplify local surface electric fields relative to a normal conductor. Ferroelectric materials in common use as plasma sources typically have dielectric constants anywhere from $\epsilon_r \sim 1000 - 6000$; barium titanate ($BaTiO_3$, $\epsilon_r \sim 1000 - 3000$) was selected for development into a plasma source for the Neutralized Drift Compression Experiment due to its durability and cost. Earlier plasma source research

[Efthimion *et al.*, 2005a, Efthimion *et al.*, 2005b] for beam neutralization experiments developed a ferroelectric plasma source (FEPS) constructed from lead zirconium titanate [$Pb(Zr,Ti)O_3$, $\epsilon_r \sim 3000 - 6000$]. However, a shift to $BaTiO_3$ ferroelectric material was made due to its increased robustness, as well as lack of creating lead-containing dust (a safety issue) [Efthimion *et al.*, 2007].

In order to exploit the ferroelectric effect and develop a large-volume and high-density source of plasma, a ferroelectric material is placed between a rear continuous electrode and a front wire electrode; the dielectric is in contact with the rear electrode, whereas a "microgap" spacing exists between the dielectric surface and the front electrode. An applied bias ($4 - 7$ kV) pulsed into the rear electrode produces a large electric field normal to the dielectric material, creating an electron avalanche and surface plasma in the microgap comprised of the ferroelectric ceramic itself [Dunaevsky *et al.*, 2001a]. Point-like explosions of metallic plasma are expelled from the ceramic and accelerated past the front electrode.

To make an arbitrarily long plasma source that is useful for beam neutralization experiments, the aforementioned ferroelectric material is formed into a ring with an inner diameter of $D_r = 7.62$ cm [Efthimion *et al.*, 2007]. Each ring is approximately $z_r = 3.7$ cm long and the source design allows for a number of rings to be stacked together, forming a cylindrical ferroelectric plasma source. The rear (outer) electrode receives the high-voltage bias and is formed by a solid wrapping of copper; the front (inner) electrode is created with a metallic mesh. Additional wiring secures the placement of the mesh and ensures that the entire inner surface is grounded. Such a plasma source, about $L = 85$ cm in length, has been developed at the Princeton

Plasma Physics Laboratory for application in neutralized drift compression experiments [Gilson, 2006]. Four evenly-spaced axial ports, consisting of $z_p = 5$ cm-long delrin rings with two diametrically opposite holes cut into them of $D_p = 2.54$ cm diameter, are included for transverse diagnostic access; plasma is not created in these "gap" regions, which divide the ferroelectric source into modular sub-segments of approximately $15 - 18$ cm in length. After the high-voltage and high-current (~ 1.2 kA peak) pulse has passed into the device, the chamber of the 85 cm-long tube is then filled, over the course of $3 - 9$ μs, with plasma composed of the dielectric's material. The firing of the plasma source relative to the intense ion beam is timed in experiments on the NDCX device such that the plasma is present at peak density when the beam passes through the drift section ($E_0 \sim 300$ keV K^+ ion beams require $t \sim 0.7$ μs to traverse the 85 cm distance). Plasma conditions can also be controlled by adjusting the parameters of the applied high-voltage pulse.

The ferroelectric plasma source has been designed, assembled, tested, and characterized at the Princeton Plasma Physics Laboratory before integration into the NDCX device for beam compression experiments. In order to sufficiently neutralize beams for compression experiments, numerical simulations of the longitudinal compression experiments demonstrate the need to provide plasma densities of approximately $n_p \sim 10^{10}$ cm^{-3} (refer to Chapters 2 and 4). Figure 5.8 contains two photographs of the plasma source [Gilson, 2006]. The $BaTiO_3$ ferroelectric source was originally envisioned to replace the axially-injected filtered cathodic-arc source in the main drift region, due to a number of advantages. However, initial simultaneous transverse and longitudinal focusing experiments planned for NDCX, which will be discussed in Chapter 6, are expected to require plasma densities of at least $n_p \sim 10^{12}$

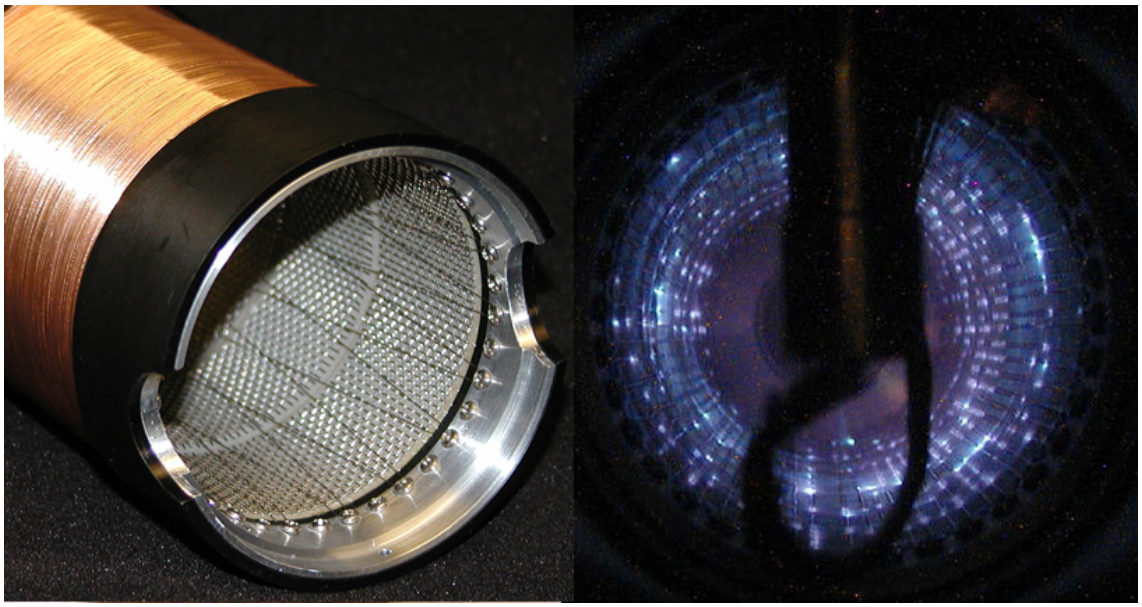

Figure 5.8: (Color) Photograph of the constructed $BaTiO_3$ ferroelectric plasma source (left) and open-shutter exposure of the source in operation (right) [GILSON, 2006]. Plasma is created near the points where the front (inner) mesh electrode is near the surface of dielectric material.

cm^{-3} near the focal plane. Therefore, experimenters will utilize both plasma sources in tandem: the ferroelectric source can provide sufficient plasma density throughout 85 cm of the main drift region because it provides plasma densities $n_p < 10^{11}$ cm^{-3}, whereas the cathodic-arc source can be employed near the focal plane in order to provide additional plasma for neutralization of the large beam densities n_b expected during simultaneous transverse and longitudinal focusing experiments. Further discussion on this topic will be provided in Chapter 6.

The main advantage of the ferroelectric source over the cathodic-arc source in forming a plasma column is found in the method by which plasma fills the drift length. In contrast to the cathodic-arc source plasma injection method, the cylindrical ferroelectric plasma source does not require an external magnetic field to act as a

guide for axially flowing plasma; the source radially fills the chamber with high-density plasma, which is created at the wall radius, and flows inward towards $r = 0$ in order to fill the drift region. Therefore, a long guide solenoid for plasma confinement, that also affects beam trajectories and neutralization processes, is unnecessary. In addition, the electrostatic trap and magnetic dipole in the NDCX device, mentioned in Sec. 5.1, can be removed since simulations and measurements show that the electrons from the ferroelectric plasma source do not move significantly upstream from the source region (discussed later in Sec. 5.2). Finally, compared to other types of plasma sources, the ferroelectric source consumes less power per discharge and also operates at low neutral pressures ($p_n \sim 10^{-5} - 10^{-6}$ Torr), helping to prevent charge-exchange processes or the stripping of beam ions to higher charge states by neutrals.

The ferroelectric plasma source is modeled in large-space scale and long-time scale particle-in-cell simulations. The goals of the numerical simulations are to investigate: (1) how the volume fills with high-density plasma; (2) how the plasma profiles evolve with time inside of the source; and (3) whether non-uniform plasma creation affects the plasma production (both azimuthal and axial asymmetry in creation conditions). In order to study asymmetric plasma creation and flow, the $BaTiO_3$ source simulations are carried out in $3D$. Azimuthally-asymmetric plasma formation was observed experimentally by noting that plasma light was not uniform along each segment's walls; axially-asymmetric plasma formation also occurs due to the presence of transverse diagnostic access ports, which do not create plasma.

Figure 5.9 provides a schematic of the simulation space set-up in the LSP code. Cylindrical coordinates are employed, and periodic boundary conditions are imposed in both the θ and z directions. Conducting boundaries are assumed at $r_{wall} = 3.8$

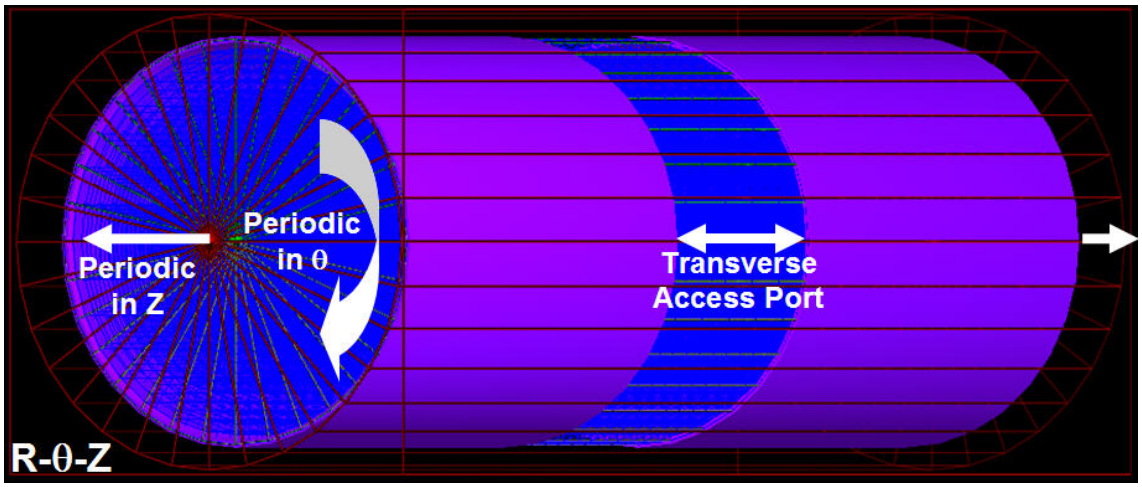

Figure 5.9: (Color) Simulation space set-up of the $3D$ ferroelectric source in the LSP code. The regions where plasma is produced are indicated by purple cylindrical shells.

cm (in order to simulate the grounded front/inner electrode), and a transverse access port of $\Delta z = 5$ cm is included in between two $z = 10$ cm-long regions of plasma formation (purple cylindrical shells in Fig. 5.9). The actual plasma source basically consists of four such units in series with four transverse access ports. Due to the periodic axial boundary conditions, the two ends of the actual ferroelectric source are not modeled in this particular simulation.

It should be noted that the exact composition of the ferroelectric ceramic (from which the plasma forms) is not known, due to the manufacturer's nondisclosure of material development methods. Laboratory tests to identify the elements present in dust left over after operation of the plasma source revealed many different elements [Gilson, 2006], and so the plasma ions are most likely a mix of several species and molecules. In order to determine the unknown effective mass of the plasma's ion population, several particle-in-cell simulations are executed in order to determine the best comparison with experiments. As will be discussed later, an effective ion mass

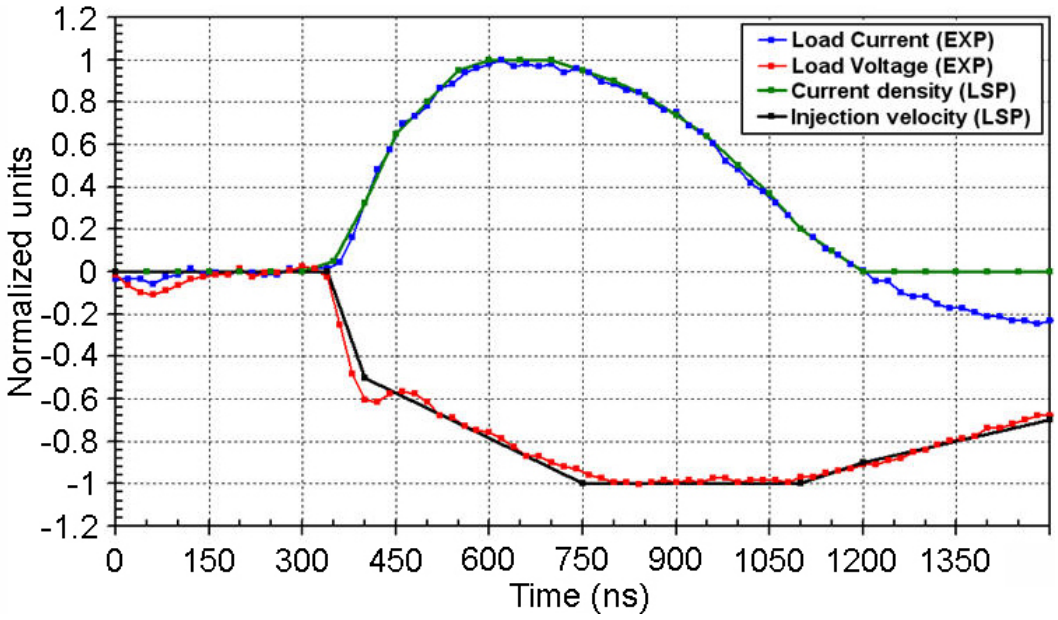

Figure 5.10: (Color) Input parameters used in particle-in-cell simulation for the injected ion species in the ferroelectric source. The peak current density is $J_r^i = -10$ mA cm^{-2}, and the peak radial injection velocity is $v_r^i = -0.375$ cm μs^{-1}.

corresponding to $m_i^{eff} = 3 \times Ba$, which is heavier than the mass of $BaTiO_3$, is observed to agree well with experimental measurements of the on-axis plasma density as a function of time.

Langmuir probe density measurements [Efthimion *et al.*, 2005b] of the ferroelectric source indicate that the source discharge current is proportional to the plasma density. For this reason, the assumption is made that the temporal current density of the injected ions in the simulations is proportional to the measured load current of the plasma source, as shown in Fig. 5.10. When the current density returns to zero, no more particles are created. The second assumption used in initialization is that the temporal injection velocity of the ions is proportional to the load voltage, as shown in Fig 5.10, since the load voltage determines the electric field in the dielectric and near the microgap. The explosively-produced ions and electrons are injected into the LSP

simulations in the $-\hat{r}$ direction (from the two $\Delta z = 10$ cm regions of plasma creation at $r_{wall} = 3.8$ cm) over the full $\Delta\theta = 2\pi$ azimuth of the ferroelectric rings (refer to Fig. 5.9), and with an isothermal temperature of $T_p = 20$ eV. The average electron temperature in the ferroelectric source is measured to be approximately $T_e \sim 20$ eV at the time of peak plasma density, and good comparison is found between the simulations and experiments when the ions are initialized with the same temperature. For the ions, the peak injected ion current density is $J_r^i = -10$ mA cm^{-2} and the peak radial injection velocity is $v_r^i = -0.375$ cm μs^{-1}, which corresponds to approximately $E_i \sim 30$ eV of directed ion energy. Neutrals and collisions of any kind are not included. It should be noted that the plasma injection in this simulation is only a model since the details of the plasma creation mechanism are not included.

The simulation presented here is executed out to $t = 20$ μs with a time step of $\omega_{pe}^{peak}\Delta t < 0.2$ (about 8×10^5 total steps). Early in time ($t < 3.5$ μs), an electron sheath accelerates most of the heavy subsonic plasma ions, and facilitates plasma expansion towards $r = 0$, with the fast ions of the initial expansion causing large average kinetic energies (up to $E_i \sim 500$ eV) to arrive at $r = 0$ first (with associated low plasma densities). Figure 5.11 shows the plasma densities obtained in the simulation at various times in the form of radial slices through $\theta = \pi$ and $2D$ $\{r, \theta\}$ isocontours through the midplane of one of the two plasma-creating ferroelectric ceramic segments. The plasma density in the core is shown in the simulation to exceed $n_p \sim 10^{10}$ cm^{-3} by $t = 4.7$ μs, and it peaks on axis at $n_p \sim 2.5 \times 10^{10}$ cm^{-3} around $t = 6$ μs. At that time, nearly equal populations of ions moving in the $+\hat{r}$ and $-\hat{r}$ directions exist near $r = 0$, with an average kinetic energy of $E_i \sim 30$ eV ($E_i^{peak} = 150$ eV). The ferroelectric source plasma persists in the chamber above the $n_p \sim 10^{10}$ cm^{-3} density

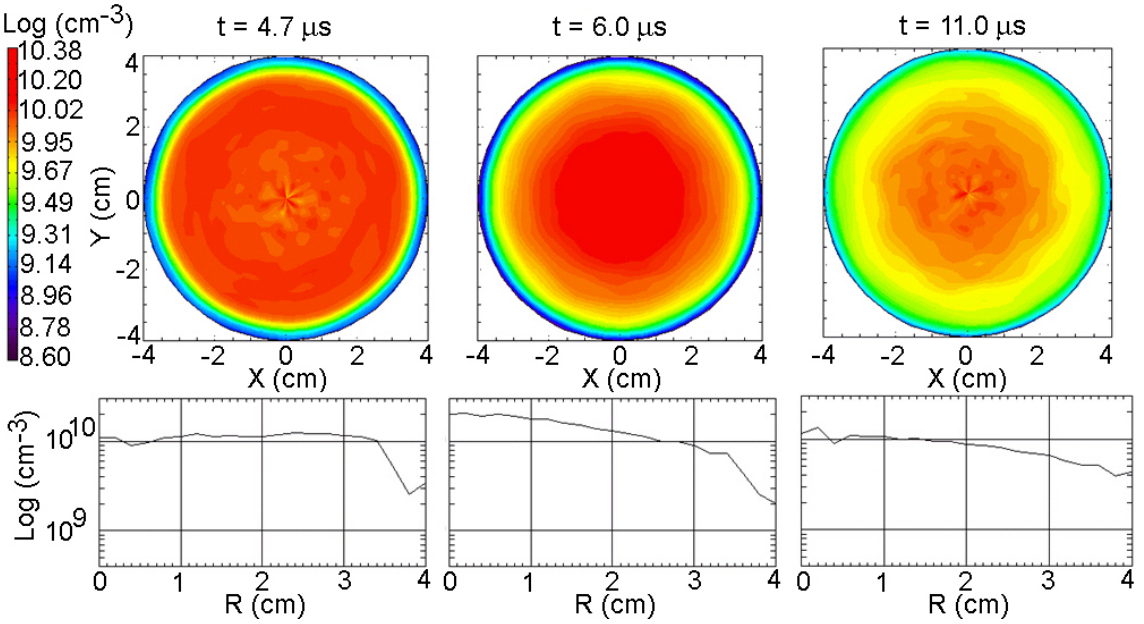

Figure 5.11: (Color) Plasma electron density radial slices at $\theta = \pi$ (bottom) and $\{r, \theta\}$ isocontours (top) through the midplane of a ferroelectric ceramic segment in the particle-in-cell simulation at $t = 4.7$ μs (left), $t = 6$ μs (center), and $t = 11$ μs (right). All plots are on the same Log scale.

level until $t = 11$ μs. Azimuthal symmetry in plasma density and temperature is maintained throughout the simulation, as shown in Fig. 5.11.

Of importance for beam neutralization experiments is whether the $\Delta z = 5$ cm "gaps" associated with the transverse access ports, which do not create plasma, would become filled with sufficient density plasma on the time scale of interest (around the time of peak density in the center of plasma-creating regions) in order to maintain very good charge neutralization of the beam as it propagates and compresses. Figure 5.12 shows the plasma densities obtained at various times in the simulations, in the form of axial slices through the $r = 0$ axis, and $2D$ $\{r, z\}$ isocontours through $\theta = \pi$. The plasma density in the axial "gap" created by the transverse access port is shown to exceed $n_p \sim 10^9$ cm^{-3} by $t = 5$ μs; it peaks in the middle of the "gap" at

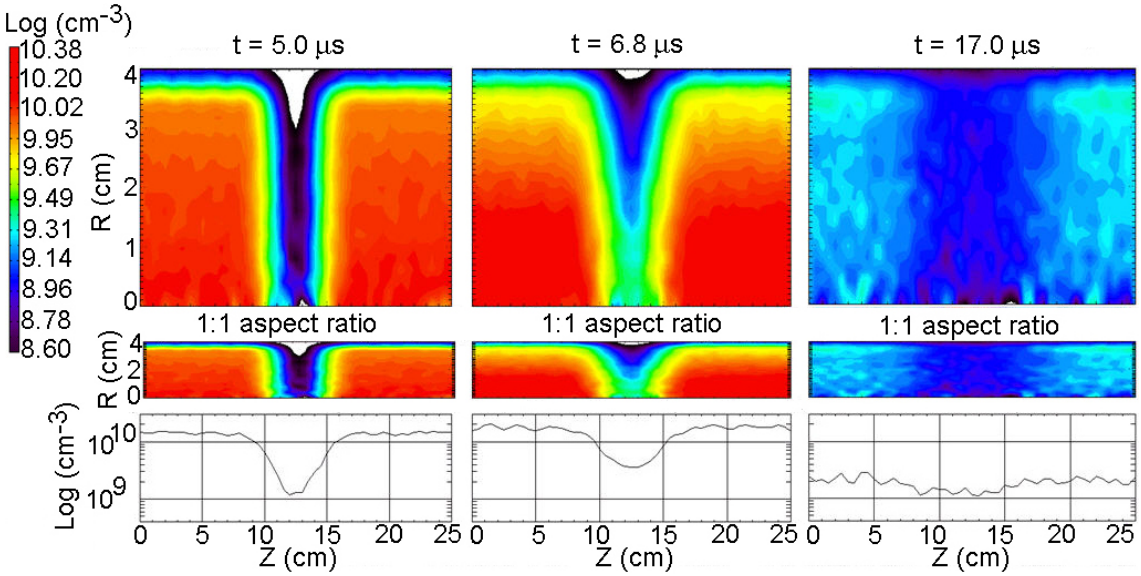

Figure 5.12: (Color) Plasma electron density axial slices at $r = 0$ (bottom) and $\{r, z\}$ isocontours through $\theta = \pi$ (top) in the particle-in-cell simulation at $t = 5$ μs (left), $t = 6.8$ μs (center), and $t = 17$ μs (right). For perspective, $1:1$ aspect ratio $\{r, z\}$ contour plots are included. All plots are on the same Log scale.

$n_p \sim 4.0 \times 10^9$ cm^{-3} around $t = 6.8$ μs, about $\Delta t \sim +0.8$ μs after the peak density is achieved in the center of the plasma-forming regions. Therefore, the axial regions initially vacant of plasma become filled with a somewhat lower-density plasma within $\Delta t = +1$ μs after the time of global peak plasma density, accompanied by a relative decrease of approximately 5 at the center of the "gap". The significant thermal energy is responsible for the maintenance of plasma densities above $n_p \sim 10^9$ cm^{-3} in the "gap" until $t = 17$ μs.

The comparison between LSP particle-in-cell simulations and the on-axis plasma electron density measurements [Gilson, 2006] at the midplane of the ferroelectric ceramic segment is provided in Fig. 5.13 as a function of time. The experimental results are qualitatively similar in magnitude and duration to the numerical simulation for the chosen initial condition, $T_i = T_e = 20$ eV (at injection). The initialized ion

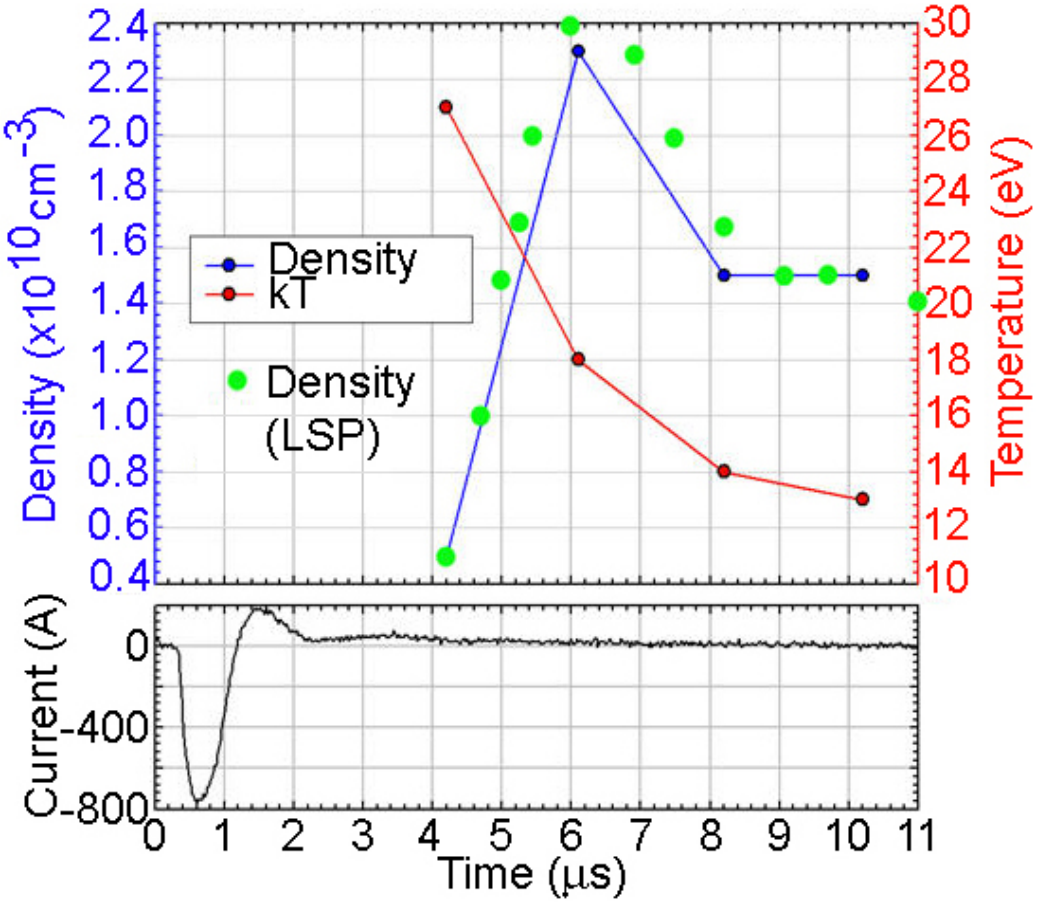

Figure 5.13: (Color) On-axis plasma electron density (top, blue) and temperature (top, red) measurements at the midplane of the ferroelectric ceramic segment, with discharge current shown (bottom). Comparison to plasma electron density from the LSP simulation (top, green) is provided for the initial conditions $T_i = T_e = 20$ eV.

injection velocity and current density profiles, shown in Fig. 5.10, cause the plasma flow to coincide with the appropriate arrival time and magnitude of the peak on-axis density as measured in the source ($t \sim 6$ μs), as well as the accurate reproduction of the decay in the observed values at later times.

Presently, the comparison between the simulations and experiments is only qualitative, for a number of reasons. First, the initialized ion injection velocity and current

density temporal profiles of Fig. 5.10 are assumed, although based on realistic physical arguments. Second, as shown in Fig 5.13, the on-axis electron temperature drops monotonically in the measurements, possibly due to complex phenomena (*e.g.*, recombination) which are not included in the simulations. A constant electron temperature of $T_e = 20$ eV is therefore chosen as the initial condition (and the value persists throughout the simulation), in order to match the approximate average in the experimental data. Third, the choice of effective plasma ion mass is somewhat arbitrary, since different elements and molecules may contribute to the ion constituency, as mentioned earlier. For the assumed electron temperature, ion mass choices other than $m_i^{eff} = 3 \times Ba$ alter the on-axis plasma density time history of Fig. 5.13 because of the electron-driven acceleration of the ions into the central core; the use of lighter (heavier) ion species causes the arrival of on-axis peak plasma density to occur earlier (later) in time, and the density values to be less (greater) than the measured value, since the electron temperature largely determines the strength of the sheath, which accelerates the ions away from the ferroelectric ceramic surface during early times (for a constant force, a change in mass causes an equal but opposite change in the amount of associated acceleration). Fourth, a colder (hotter) initial ion temperature alters the on-axis plasma density time history of Fig. 5.13 because the reduced (additional) thermal energies increase (decrease) the peak on-axis value and the amount of time the plasma density persists in the source. Ion temperature measurements in the ferroelectric plasma source are not available at this time. Fifth, whether explosive-like ferroelectric-based plasmas are actually formed near thermal equilibrium near the point of creation is still under investigation. These insights indicate the possibility

that, without further experimental information, the problem may admit multiple solutions, or be far more complicated. Additional experimental determination of the aforementioned relevant quantities is an important topic for future work, as well as the inclusion in the PIC simulation of some of the neglected effects. Even though there are many unknowns, the application of reasonable assumptions, and the compelling comparison with experimental measurements suggests that this simple model, which uses an effective ion mass and ignores more sophisticated details and effects, still provides important insights into the plasma flow in such a device.

Another outstanding issue that was resolved with LSP simulations is whether non-uniform plasma creation in the azimuthal direction affects plasma profiles. The desire to study such situations has been stimulated by the observation during ferroelectric source testing that the plasma formation conditions at the wall are not always uniform in the azimuthal direction. During source operation, the light from the plasma emission (refer to Fig. 5.8) is sometimes not θ-symmetric. One might expect non-uniform emission from the ceramic rings if the geometry of the dielectric-microgap-mesh region is not the same throughout the device, especially if the degree to which the front electrodes are secured varies (either during source construction or extended operation). Significant regions are found to be absent of light in some instances, prompting reassembly of the device to ensure taut (and hopefully constant) front electrode conditions [Gilson, 2006]. Therefore, the question arises as to whether asymmetric plasma emission conditions severely modify the resulting plasma density profiles achieved in the plasma source.

Simulations indicate that asymmetric plasma creation conditions at the source walls nevertheless result in azimuthally-symmetric profiles at the time of peak on-axis

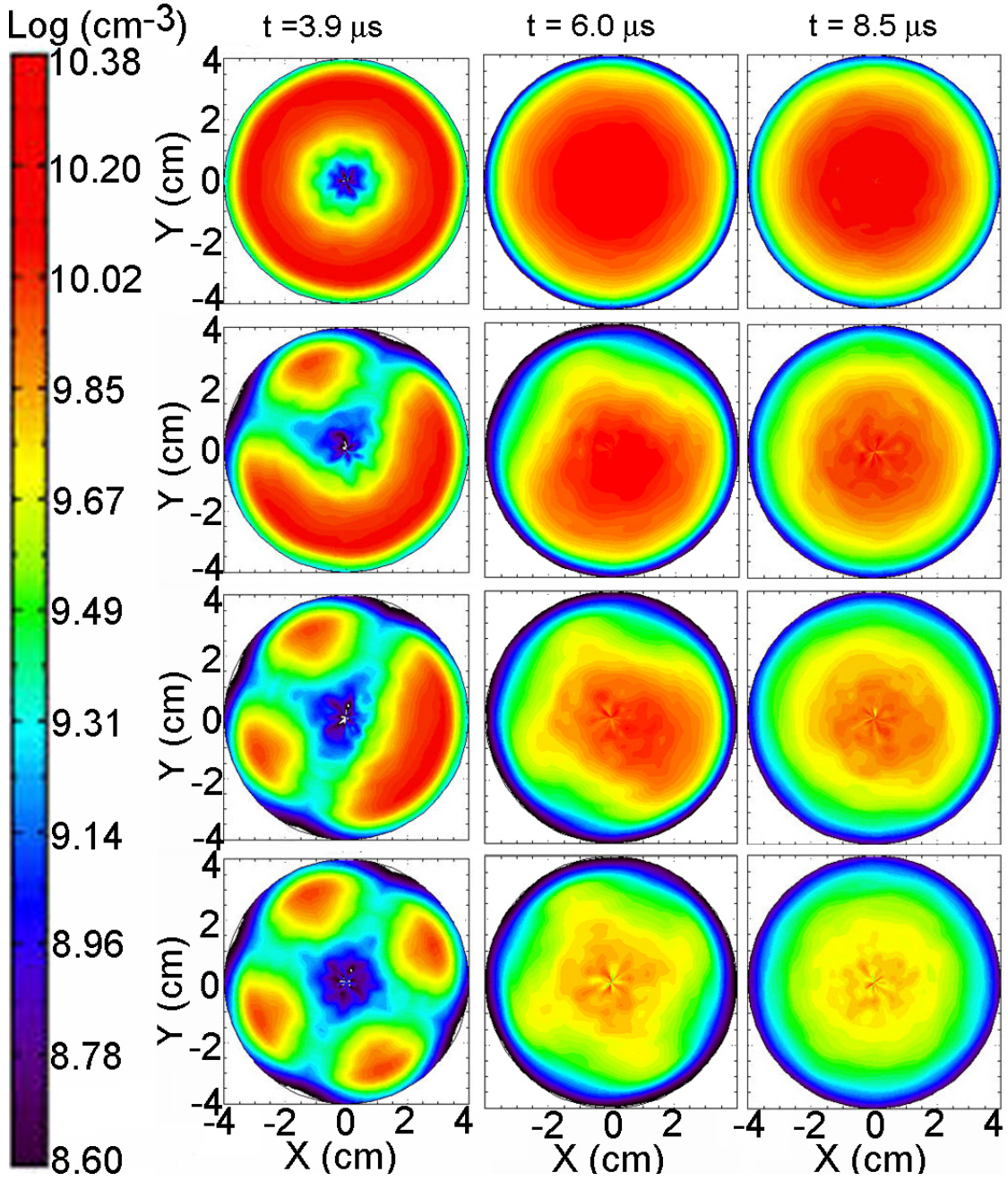

Figure 5.14: (Color) Plasma electron density $\{r, \theta\}$ isocontours through the midplane of a ferroelectric ceramic segment in LSP particle-in-cell simulation at $t = 3.9$ μs (left column), $t = 6$ μs (center column), and $t = 8.5$ μs (right column). Azimuthal "holes" of size $\Delta\theta = \pi/4$ approximate non-uniform emission effects from the source radius: uniform plasma creation (first row), two "holes" (second row), three "holes" (third row), and four "holes" (fourth row). All plots are on the same Log scale.

plasma density. Four additional simulations are executed with one to four "holes" of non-emitting regions, each of which is $\Delta\theta = \pi/4$ in azimuthal radians and extends the entire axial distance. Therefore, the size of the simulated "holes" exaggerates the effect observed in the ferroelectric source, but satisfactorily implies that non-uniform plasma creation conditions are manageable. Figure 5.14 highlights three of the four azimuthally-asymmetric simulations and provides the uniform, no-"hole" case for reference (the following discussion applies equally to the missing case, which is omitted only for reasons of size and clarity considerations). For early times ($t < 6$ μs), the plasma density profiles resulting from non-uniform emission take on myriad shapes, and reflect the emission conditions at the inner radius of the source. However, at the time of peak on-axis density in the ferroelectric source ($t = 6$ μs), non-uniformities mostly disappear and plasma symmetry is nearly established. By $t = 8.5$ μs, about $\Delta t \sim +2.5$ μs after peak density is realized in the source, the initial azimuthal asymmetry in plasma creation conditions is entirely absent. Evidently, the role of the plasma temperature is important in "washing out" non-uniform emission conditions. It should be noted that the peak on-axis value depends on the amount of plasma creation asymmetry at the source walls, since more locations that do not create plasma lead to lower total plasma densities in the source. Also, the peak density present in the device at late times varies as a function of the amount of non-emitting area, underlying the importance of using experimental measurements to gauge the magnitude and relative time of achieved peak plasma density, in order to appropriately trigger the injection of the ion beam in compression experiments.

As mentioned earlier, an important difference between the ferroelectric and cathodic-arc sources is found in the method by which plasma fills the drift region. In the case of

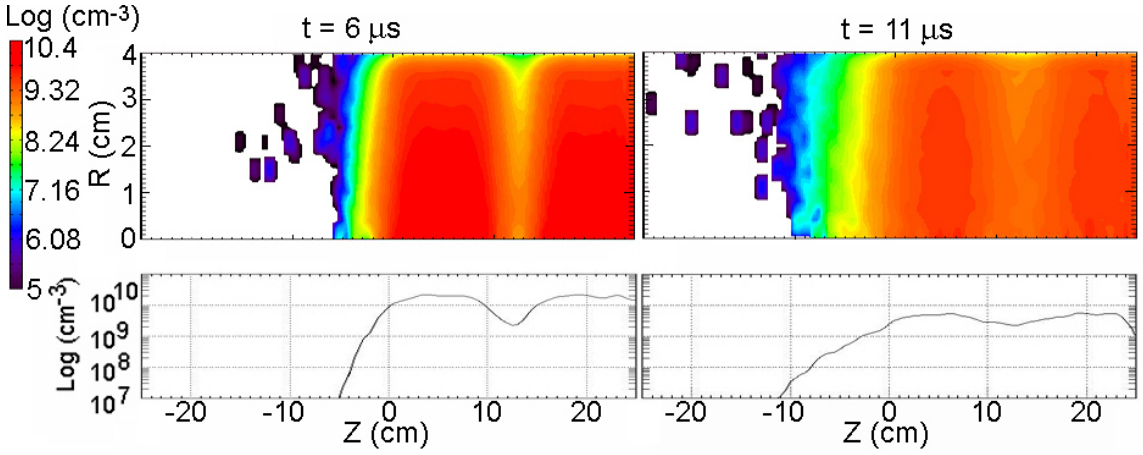

Figure 5.15: (Color) Plasma electron density axial slices at $r = 0$ (bottom) and $\{r, z\}$ isocontours through $\theta = \pi$ (top) in the particle-in-cell simulation at $t = 6$ μs (left) and $t = 11$ μs (right). Due to space-charge, the radially-directed injection velocities, and the lack of external solenoidal guide field, electron populations do not axially move a significant distance away from the plasma source. All plots are on Log scale.

the former, plasma is injected with supersonic ion drift velocity from the downstream end of the device towards the upstream end. Besides the fact that the additional guide solenoid, electrostatic trap, and dipole required by the cathodic-arc source take up valuable axial real estate in the experiment, the directed axial movement of the plasma is a concern if it allows electrons to penetrate into the upstream beamline; the ion charge bunch dynamics can greatly suffer from an electron presence in the regions originally intended for unneutralized beam transport. Therefore, in order to predict the amount of upstream electron penetration of the radially-injected ferroelectric plasma without the presence of a guide solenoid, electrostatic trap, and magnetic dipole, additional simulations of the source are carried out.

The difference between this ferroelectric source simulation and the previous cases is the removal of the axial periodic boundary conditions. Instead, extra vacuum chamber is modeled upstream of the ceramic rings (for axial values $z < 0$) and a

symmetry boundary condition is invoked at the downstream end of the geometry (at $z = +25$ cm). The result is presented in Fig. 5.15. Since the ferroelectric source injects the plasma towards the $r = 0$ axis with only transverse momentum, the axial motion of the plasma upstream of the device is solely a result of thermal expansion (the same mechanism by which the axial "gap" regions are filled). By the time of peak on-axis plasma density ($t = 6$ μs), the plasma has only penetrated approximately $\Delta z = -4$ cm into the upstream region, at density levels $n_p > 10^8$ cm^{-3}. By $t = 11$ μs, the plasma has only traveled an additional $\Delta z = -4$ cm upstream (a total of approximately $\Delta z = -8$ cm from the original axial location).

The numerical simulations described in Sec. 5.2 provide increased confidence that sufficiently high plasma density can be provided by the ferroelectric plasma source throughout the drift region for beam compression experiments on the NDCX device. The goals of the ferroelectric source simulations have been achieved and discussed. The volume of the plasma source is filled with azimuthally-symmetric plasma in cases of both uniform and non-uniform emission conditions at the inner wall; the axial "gap" regions created by the transverse diagnostic access ports become filled with plasma whose density is within a factor of 10 of the peak density; and the axial electron motion upstream due to thermal expansion of the radially-injected plasma is relatively small ($\Delta z \sim -8$ cm) on the time scales of interest for beam compression experiments ($t < 10$ μs). In addition, qualitative comparisons show good agreement with experimental measurements, various limitations of the PIC simulation model have been discussed, and suggestions for future research are provided.

5.3 Plasma injection into a strong solenoid

As discussed in Chapter 4, the process of imposing an axial velocity tilt onto an intense ion beam as it traverses the acceleration gap defocuses the otherwise radially converging trajectories of the ions in a time-dependent manner. One proposed method for achieving simultaneous transverse and longitudinal compression to a coincident focal plane involves the use of a strong final-focus solenoid mounted in the beamline, near the end of the drift region. The magnetic field of the solenoid leads to radial focusing of the defocused charge bunch according to the Lorentz force, $-F_r = +q[(-v_\theta) \times (+B_z)] = -m_i \ (\mathrm{d}\mathbf{v}/\mathrm{dt})_r$. The use of a final-focus solenoid for achieving simultaneous compression reduces the effective transverse focal length relative to the case without a final-focus solenoid. Therefore, less plasma for beam neutralization can be used throughout the drift region, since the beam density remains low until reaching the solenoid as a result of the relatively larger beam radius. Also, intense charge bunches can be transversely compressed to sub-mm spot sizes over the shorter transverse focal lengths, with smaller spots associated with stronger solenoids [Sefkow *et al.*, 2007]. Significant effort has been spent on this method as a means to achieve simultaneous focusing (and is the primary subject of Chapter 6).

The main challenge surrounding the use of a final-focus solenoid for simultaneous focusing experiments is how to penetrate the high-field region of the solenoid with sufficiently high plasma density, in order to ensure adequate neutralization of the ion beam near the focal plane. Solenoids with magnitudes in the range $B_z \sim 30 - 150$ kG are under consideration, because of the desired beam energies, transverse focal lengths, and final spot sizes involved. As mentioned earlier (also to be discussed in Chapter 6), simulations of simultaneous focusing using final-focus solenoids suggest

that plasma densities in the range of $n_p \sim 10^{12} - 10^{14}$ cm^{-3} or higher will be needed near the focal plane, depending on the strength of the applied focusing elements [Sefkow *et al.*, 2007]. One proposed method to fill a strong solenoid with plasma is to longitudinally inject supersonic cathodic-arc plasma (refer to Sec. 5.1) into it from the downstream end. The plasma may penetrate into the high-field region in a certain amount of time, and the compressing ion beam could be timed to enter the plasma-filled solenoid from the upstream end.

The attempt of plasma injection into a final-focus solenoid is similar in nature to the simulations of cathodic-arc plasma coupling from the source to the guide solenoid in Sec. 5.1, except for the considerable change in magnetic field strength from the guide solenoid ($B_z = 2$ kG) in the previous case to the necessary final-focus solenoid strength ($B_z \sim 30 - 150$ kG) in this case. Due to the spacing between the filter coils of the cathodic-arc sources and final-focus solenoid, injected plasma must cross from low magnetic field regions to a very high-field region. In fact, the ratio of magnetic fields is even greater when compared to the minimum magnetic field between the filter and final-focus solenoids. The large gradients in magnetic field strength parallel to $\hat{\mathbf{b}}$ will alter the zeroth-order parallel velocity dynamics of magnetized species, because of forces arising in the direction opposite to the field gradients, as mentioned in Sec. 5.1. Both species become magnetized as they approach the final-focus solenoid.

Recall from Sec. 5.1 that the conservation of a charged particle's magnetic moment μ in the presence of a magnetic field whose strength varies in the direction of $\hat{\mathbf{b}}$ leads to a well-known result called the magnetic mirror effect [Chen, 1984]. Conservation of total kinetic energy implies that the particle's velocity parallel to the magnetic field $v_\parallel$ will increase or decrease (at the expense of $v_\perp$) if the field strength decreases or

increases, respectively, along $\hat{\mathbf{b}}$. Magnetic mirroring decelerates the injected plasma as it flows towards the high-field region, and is expected to be the determining factor for whether plasma can fill a strong solenoid. Therefore, its evaluation plays a significant role in the design considerations involving this proposed method for achieving simultaneous charge bunch compression.

Generally, penetration into the high-field region only occurs for magnetized particles whose $v_\parallel/v_\perp$ ratio satisfies [Goldston and Rutherford, 1995]

$$v_\parallel / v_\perp \; > \; \sqrt{\frac{B_{max}}{B_{min}} - 1} \, , \tag{5.2}$$

in the B_{min} region. Particles with smaller initial $v_\perp$ experience smaller decelerating forces ($F_\parallel = -m\, v_\perp^2\, \nabla B/2\, B$, from Sec. 5.1) as they approach regions of larger magnetic field. Particles with larger supersonic ion drift velocities ($\sim v_\parallel$) and smaller $v_\perp$ are expected to penetrate the high-field region. Since the supersonically injected ions are more likely to have the necessary $v_\parallel/v_\perp$, they are more likely to allow greater electron penetration into the high-field region via ambipolar forces. Magnetized particles with velocity ratios satisfying Eq. (5.2) fall into a "loss cone" in velocity space, independent of charge and mass, and experience deceleration but are not completely reflected by the increasing magnetic field strength gradient parallel to $\hat{\mathbf{b}}$ (particles with $v_\parallel = v$ and $v_\perp = 0$ have no magnetic moment and feel no force). Large particle populations within the "loss cone" are desired in this application for plasma penetration into the high-field region. The result of the aforementioned dynamics is the formation of anisotropic plasmas in the vicinity of the strong solenoid.

The large-space scale and long-time scale $3D$ particle-in-cell simulations of cathodic-arc plasma injection into the complex magnetic topology [composed of two filter coils

($B_z = 2$ kG) and a guide solenoid ($B_z = 2$ kG)] from Sec. 5.1 are repeated in order to study the evolution of the plasma flow in the presence of a final-focus solenoid. The goal is to study the coupling efficiency of the plasma flow from creation, through the curved filter coils, and into the final-focus solenoid. The coordinate system is the same. However, the magnetic topology is significantly altered due to the relative magnetic field decrease in the filter coils to approximately $B_z = 0.45$ kG and increase in the final-focus solenoid to $B_z = 53$ kG. The same Cartesian geometry as in Sec. 5.1 includes the offset $h = \pm 6$ cm, angle $\theta = \pm\pi/4$, except two separation distance cases, $d = 8$ cm and $d = 16$ cm, are investigated. The relative ratio of peak magnetic field strengths between the three solenoids is much greater than unity, and significant fringe-fields from the final-focus solenoid are present within the filter coils.

Many parameters are retained from the original simulations in Sec. 5.1, including the spatial resolution in each direction (0.5 cm, yielding 3.8×10^4 and 5.5×10^4 total nodes for the $d = 8$ cm and $d = 16$ cm cases, respectively) and the supersonic injection velocity in the $+\hat{y}$ direction for the Al^+ ions (1.44 cm μs^{-1}) from the filter coils. However, the peak ion current density is increased to $J_{pi} \sim 2$ A cm^{-2} (from 0.04 A cm^{-2}), corresponding to a peak plasma density estimate of $n_p \sim 10^{13}$ cm^{-3} near the sources within the filter coils. Gaussian distributions with temperatures $T_i = 3$ eV and $T_e = 10$ eV are imposed on the injected ion and electron populations, respectively, corresponding to an injected ion Mach number of approximately 1.7. Scattering effects are included by using internally-computed Spitzer rates for Coulomb collisions between charged particles. The simulation is executed out to $t = 25$ μs with a time step satisfying the constraints of $\omega_{pe}^{peak}\Delta t < 0.2$ and $\omega_{ce}^{peak}\Delta t < 1$ (about 2.5×10^7 total steps). The significant decrease in temporal step size is due to the

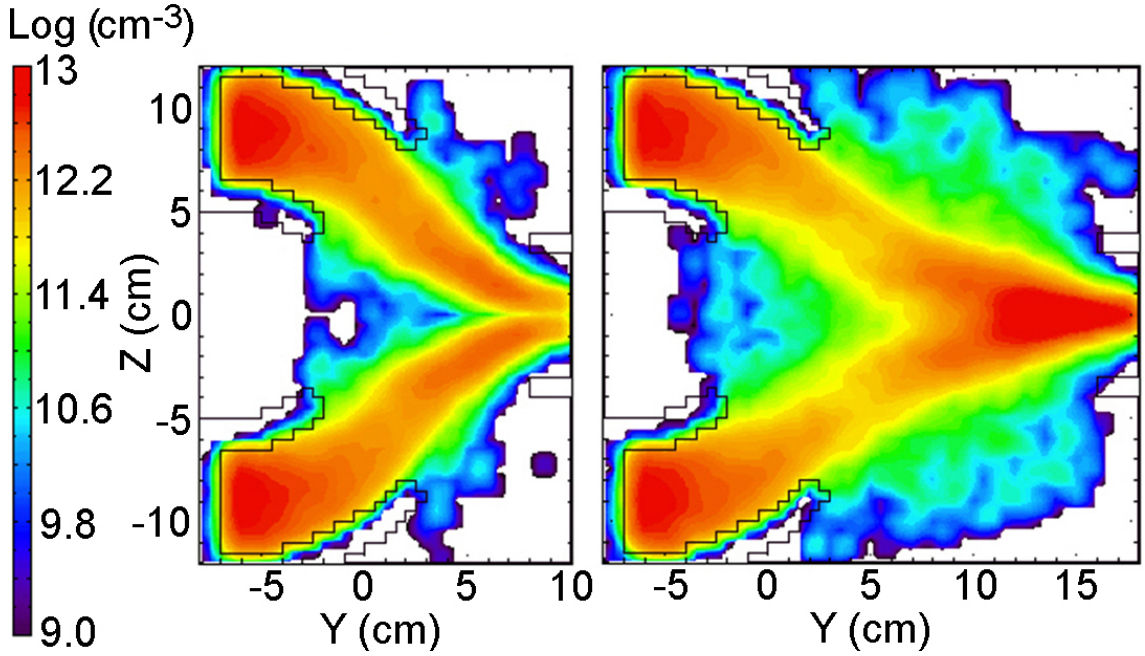

Figure 5.16: (Color) Plasma electron density $\{y, z\}$ isocontours (Log scale) through the $x = 0$ axis from the $3D$ particle-in-cell simulation of supersonic cathodic-arc plasma injection into a $B_z = 53$ kG final-focus solenoid, with a separation distance $d = 8$ cm (left) and $d = 16$ cm (right) from the filter coils. The $d = 16$ cm case is similar to the configuration planned for future experiments.

increase in peak magnetic field to $B_z \sim 53$ kG, resulting in a larger electron cyclotron frequency. During steady state plasma flow (starting around $t \sim 15$ μs), more than 5×10^5 particles are explicitly pushed on the simulation grid at each time step. In the configuration considered here, both species become magnetized as they exit the filter coils and travel towards the final-focus solenoid.

Results of the large-space scale and long-time scale simulations for the $d = 8$ cm and $d = 16$ cm cases, using a final-focus solenoid of strength $B_z = 53$ kG, are presented in Fig. 5.16 in the form of $\{y, z\}$ isocontours of plasma electron density n_{pe} (during steady state flow) through the $x = 0$ axis. The density profiles are directly comparable to the top right frame in Fig. 5.5, except for the relative increase in initial

current density by the factor of 50. Contrary to the simulations in Sec. 5.1, both species become magnetized in the region between the three solenoids, and largely follow field lines while executing guiding-center drift orbits (as discussed in Sec. 5.1). Significant levels of magnetic mirroring occur in both cases. The case with the shorter separation distance couples plasma to the final-focus solenoid, but the plasma density is lower at the $z = 0$ axis than off-axis, which is not desirable for beam compression experiments. Conversely, the $d = 16$ case illustrates plasma filling the final-focus solenoid with peak density located on-axis, as observed more clearly in Fig. 5.17.

The $\{x, z\}$ isocontours of plasma electron density n_{pe} (during steady state flow) at various y locations, shown in Fig. 5.17, demonstrate that the $d = 16$ cm separation distance case fills the final-focus solenoid with more relative uniformity in the $\{x, z\}$ planes (the θ direction) than the $d = 8$ cm case. Simplistically, the increased separation distance d gives the plasma more time and space to execute its complex $3D$ plasma motion. The $d = 8$ cm case evidently does not undergo enough electron guiding-center drift in the $\pm\hat{x}$ direction in order to symmetrically fill the solenoid with plasma in the $\{x, z\}$ plane, as manifest in the plasma profiles in Fig. 5.17. Therefore, the larger separation distance case is better for beam compression experiments, since the plasma density is more uniform and centered on the beam's axis of propagation ($z = 0$ in the $-\hat{y}$ direction). Apparently, the separation distance makes a significant difference on the dynamics of plasma flow in a strong solenoid, since it (and other parameters) affects the local magnetic topology experienced by the injected plasma.

Additional large-space scale and long-time scale $2D$ $\{r, z\}$ LSP simulations of plasma flow into a $B_z = 40$ kG final-focus solenoid are performed in order to further

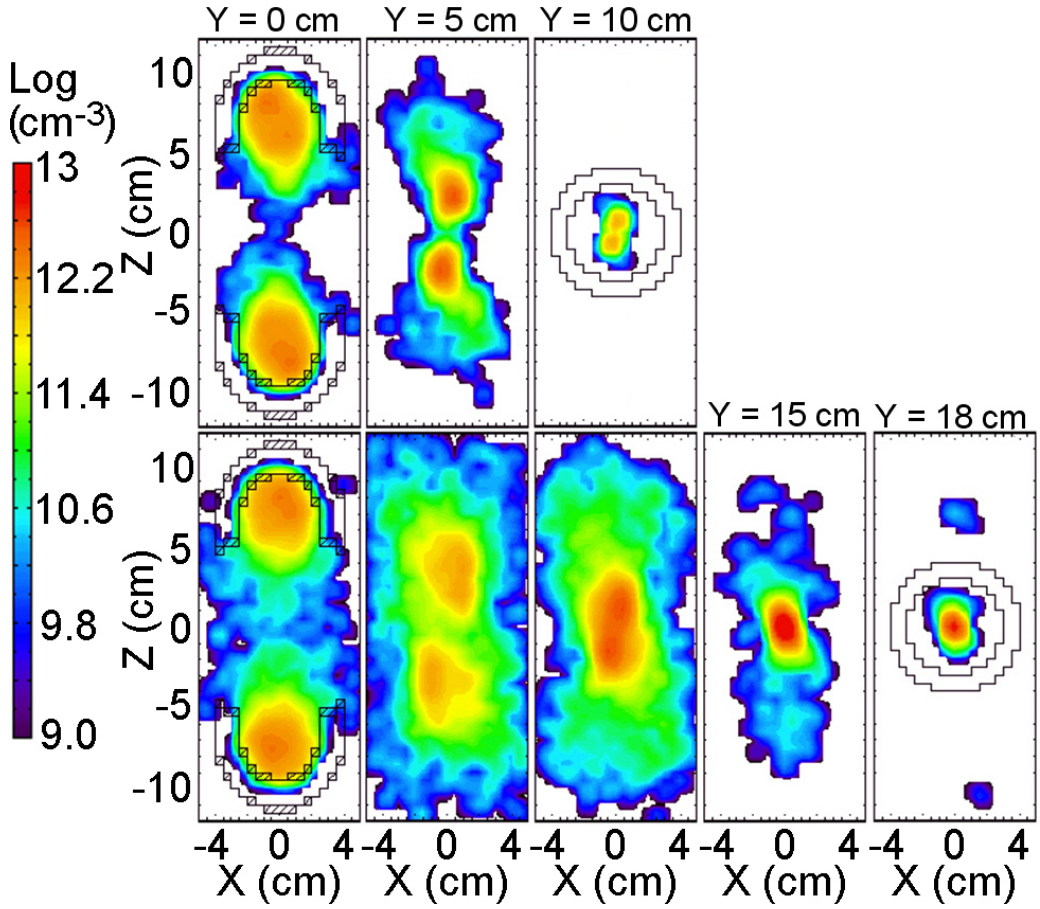

Figure 5.17: (Color) Plasma electron density $\{x, z\}$ isocontours (Log scale) through various y locations from the $3D$ particle-in-cell simulation of supersonic cathodic-arc plasma injection into a $B_z = 53$ kG final-focus solenoid, with a separation distance $d = 8$ cm (top) and $d = 16$ cm (bottom) from the filter coils.

investigate the feasibility of plasma-filling using a supersonically injected cathodic-arc plasma source. The simulations are carried out in reduced-dimensionality $2D$ $\{r, z\}$ cylindrical geometry in order to decrease the computational requirements, but increase the spatial resolution of the nonphysical particle-in-cell grid, since increased resolution is desired in the fringe-field and $r = 0$ regions. As discussed in Sec. 3.3, implicit methods for pushing electron particles in LSP [Friedman, 1990] can be used in order to under-resolve either the electron cyclotron or electron plasma frequency

ω_{pe}, but not both at the same time. Due to the large plasma densities under consideration ($n_p \sim 10^{12} - 10^{14}$ cm^{-3} or higher), the employment of more computationally-demanding implicit particle-pushing and field-solving methods is not cost-effective because ω_{ce} is within an order-of-magnitude of ω_{pe} (both are between $5 - 8 \times 10^{11}$ rad s^{-1} for $B_z \sim 40$ kG and $n_p \sim 10^{14}$ cm^{-3}).

The $\{r, z\}$ simulation grid extends from $r = 0$ to $r = 4$ cm and $z = -10$ cm to $z = +20$ cm, with a spatial resolution of $\Delta r = 0.05$ cm and $\Delta z = 0.2$ cm (approximately 1.4×10^4 total nodes). A 10 cm-long, $B_z = 40$ kG solenoid with inner radius $r^{sol} = 4$ cm is positioned between $z = -5$ cm and $z = +5$ cm. The solenoidal magnetic field in cylindrical geometry is calculated in LSP for off-axis values according to a sixth-order power series expansion (of the on-axis field and its derivatives) in the radial coordinate of an ideal finite-length solenoid [Thoma, 2002]. Cathodic-arc plasma injection occurs in the upstream direction from the downstream end, at the injection plane $z = +20$ cm in the low-field region. A conducting boundary at $r_{wall} = 3.8$ cm and open boundaries at the axial coordinates $z = -10$ cm and $z = +30$ cm are modeled. Since the intended simultaneous focal plane of the intense beam may lie within (or just beyond) the solenoid, depending on the choice of beam and solenoid parameters (further discussion on this will follow in Chapter 6), the plasma density profiles within and downstream of the final-focus solenoid are important to evaluate.

The magnetic field topology in the simulation is shown in Fig. 5.18. The beam would travel in the $+\hat{z}$ direction in this coordinate system, centered on the $r = 0$ axis. The filter coils and sources of the cathodic-arc plasma source are not modeled due to the reduction in dimensionality. Therefore, the assumption is made to continually inject a constant $\{r, \theta\}$ profile of the approximate maximum experimental plasma

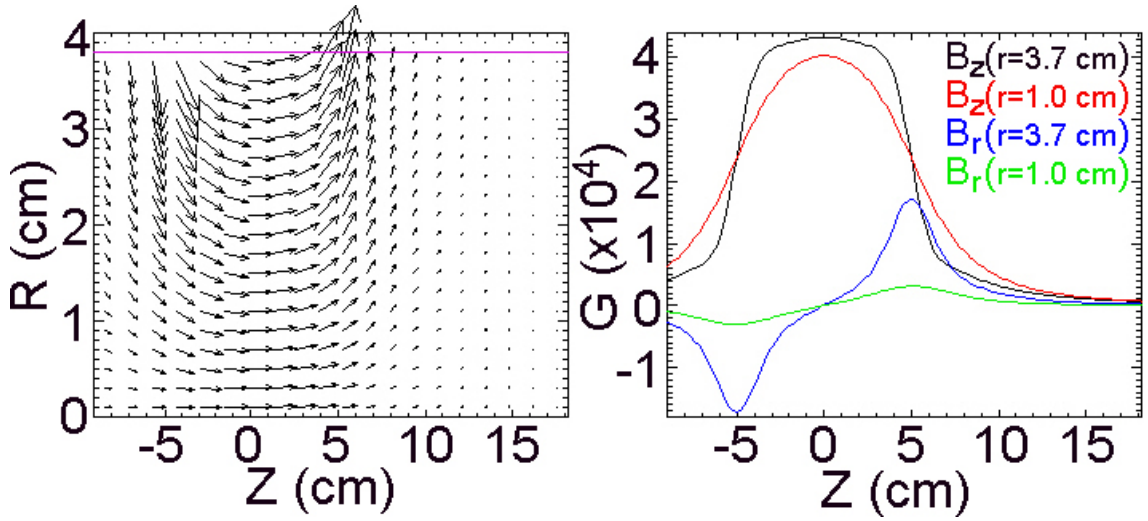

Figure 5.18: (Color) Magnetic field vector plot (left) and axial slices of the $B_r(z)$ and $B_z(z)$ magnetic field components at $r = 1$ and $r = 3.7$ cm (right). Constant plasma density $n_p \sim 10^{12}$ cm^{-3} with supersonic ion velocity is injected in the upstream direction, towards the downstream end of a $B_z = 40$ kG final-focus solenoid. The beam would travel in the $+\hat{z}$ direction in this coordinate system.

density $n_p \sim 10^{12}$ cm^{-3} (over the full $\theta = 2\pi$) at the injection plane in the low-field region, a location which would lie between the final-focus solenoid and filter coils (the latter not included). As in Sec. 5.1 and the previous simulation, the plasma ion species is Al^+, and the ions are injected from $r = 0$ to $r = 3.8$ cm. Gaussian distributions with temperatures $T_i = 1$ eV and $T_e = 5$ eV are imposed on the injected ion and electron populations, respectively. The plasma beta is very small in this simulation due to the large magnetic pressure associated with the $B_z = 40$ kG field. Scattering effects are included by using internally-computed Spitzer rates for Coulomb collisions between charged particles.

In order to determine the dependence on cathodic-arc injection velocity for filling the strong solenoid with plasma, four simulations are conducted using the initial supersonic ion injection velocities $v_z^i = -1.5$ cm μs^{-1}, -3 cm μs^{-1}, -6 cm μs^{-1},

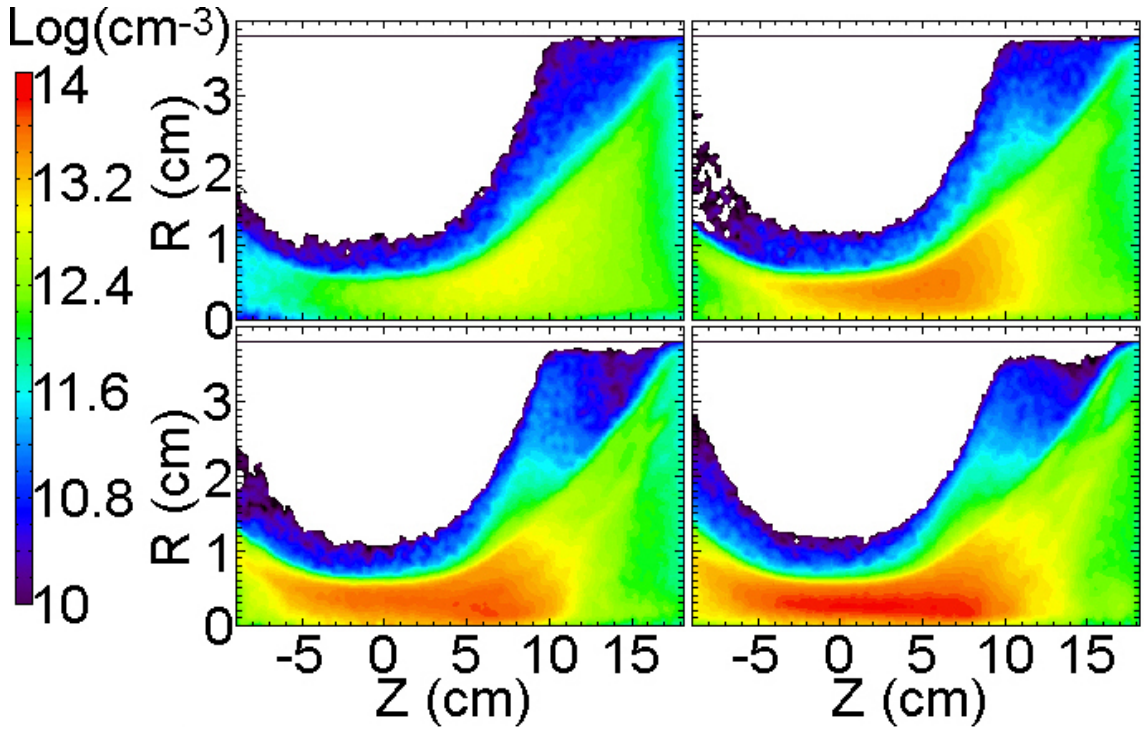

Figure 5.19: (Color) Plasma electron density isocontours (Log scale) from particle-in-cell simulation at $t = 30$ μs during steady state plasma flow into a $B_z = 40$ kG solenoid, for initial supersonic ion injection velocities $v_z^i = -1.5$ cm μs^{-1} (top left), -3 cm μs^{-1} (top right), -6 cm μs^{-1} (bottom left), and -12 cm μs^{-1} (bottom right).

and -12 cm μs^{-1} (corresponding to initial ion Mach numbers of 2.7, 5.5, 11, and 22, respectively). In order to maintain the same initial constant plasma density $n_p \sim 10^{12}$ mentioned above, the current densities are $J_p^i = 0.3$ A cm^{-2}, 0.6 A cm^{-2}, 1.2 A cm^{-2}, and 2.4 A cm^{-2}, respectively. The simulations are executed out to $t = 30$ μs with a time step satisfying the constraints of $\omega_{pe}^{peak}\Delta t < 0.68$ and $\omega_{ce}^{peak}\Delta t < 0.85$ (about 2.5×10^7 total steps). During steady state plasma flow, more than 1.6×10^6 particles are explicitly pushed on the simulation grid at each time step.

Figure 5.19 illustrates $2D$ $\{r, z\}$ isocontours of plasma electron densities n_{pe} from the particle-in-cell simulations during steady state plasma flow. The simulations

indicate that the $B_z = 40$ kG solenoid becomes partially-filled (with $r_p^{fill} < r_{sol}$) by supersonically injected high-density cathodic-arc plasma flowing in steady state, beginning at different times (depends on the ion injection velocity, but corresponds to $t \sim 12$ μs for the slowest speed). As discussed earlier in this Chapter, the initial expansion and acceleration of the ion front occurs. Both species become magnetized as they flow towards the final-focus solenoid, and ambipolar forces play a role in the dynamics. Since the ions become magnetized later in space and time than the electrons, they are able to penetrate farther (in the $-\hat{z}$ direction) before becoming tied to the field lines, and facilitate the penetration of the electrons into the same regions due to space-charge effects. Magnetized plasma continues to flow along field lines and, in some locations, the density is compressed by more than an order-of-magnitude, which helps to achieve the plasma density requirements for neutralization near the simultaneous focal plane. The peak plasma densities in the simulation reach $n_p \sim 10^{14}$ cm^{-3} near the "bottleneck" region (for the cases with higher initial v_z^i), where a majority of the plasma is reflected by the strong magnetic field.

Due to the magnetic mirroring effect, plasma particles streaming into the solenoid generally decelerate due to the force arising in the direction opposite to the field gradient, $\mathbf{F}_\parallel = -\mu \nabla B$. Much of the initial parallel injection energy is transferred into perpendicular energy. The effect dominates the plasma dynamics in this particular scenario because of the ratio of magnetic field strengths involved, and reduces the amount of plasma able to fill the final-focus solenoid. As plasma reaches the edge of the solenoid at $z = +5$ cm, where B_r reaches a maximum, a majority of the plasma is reflected back in the $+\hat{z}$ direction, since only particles with high enough $v_\parallel / v_\perp$ ratios are able to penetrate the high-field region. Most of the particles able to do so are

supersonic ions, and electrons largely follow the ion movement into the solenoid via ambipolar forces; as the supersonic ion injection velocity increases, the amount of electron plasma density able to penetrate the strong solenoid does as well (all cases inject an initial $n_p \sim 10^{12}$ cm^{-3} at the injection plane). In each case, the plasma fills the solenoid for radii $r < 0.6$ cm, indicating that the fill-factor is approximately $r_p^{fill} \sim 0.6$ cm. The "bottleneck" build-up of plasma density near the edge of the final-focus solenoid is simultaneously due to compression along field lines, as well as contributions from reflected plasma. If collisions become important because of the high densities and long time scales, magnetic moment conservation is no longer strictly valid, although the magnetic mirroring effect is nevertheless quite evident.

The presence of the magnetic field and ambipolar forces increases the temperature relative to plasma injection and flow without a field and alters the corresponding density gradients, although temperature is not strictly defined due to the anisotropy of the velocity distributions. As the plasma compresses along field lines and the density increases, the electron and ion temperatures become increasingly coupled. An increase in plasma temperature is typically witnessed in particle-in-cell simulation in the region where plasma encounters greatly increasing magnetic fields, which is also where the most plasma is reflected and gives rise to counter-moving populations.

5.4 Summary and conclusions

Large-space scale and long-time scale numerical simulations were executed in order to study the spatial and temporal evolution of the plasma flow from two different types of source used in the laboratory. Simulations of the plasma injection into the drift region allowed evaluation of the realistic parameters achieved in experiments, so

they can be employed in additionally sophisticated compression simulations. These simulations provide increased confidence that sufficient levels of plasma density are present in the device for longitudinal beam compression experiments.

A filtered cathodic-arc plasma source used a macroparticle debris and neutral atom filter composed of bent solenoids to create and inject supersonic plasma into the system along externally imposed magnetic field lines (Sec. 5.1). Plasma was injected into a $3D$ magnetic topology composed of the two filter coils ($B_z = 2$ kG) and a long guide solenoid ($B_z = 2$ kG) throughout the drift length. The non-uniform magnetic topology complicated the well-known general analytic considerations for evaluating guiding-center drifts, therefore particle-in-cell simulations provided self-consistent evaluation of the physics in an otherwise challenging scenario. Ambipolar forces, perpendicular and parallel ∇B gradient drifts, and curvature drifts were shown to affect the plasma (mostly electron) dynamics. Significant plasma density loss in the filter coils and intermittent region of low magnetic fringe fields was demonstrated, and suggestions for improvement were made. Using parameters relevant for current experiments, 50% coupling efficiency from the sources to the drift region was demonstrated. The efficiency depended on many geometrical factors, as well as the plasma properties and magnetic field configuration. These simulations provide insight into the plasma dynamics from injection to steady state flow.

Numerical simulations of plasma flow from the $BaTiO_3$ ferroelectric plasma source demonstrated that the required plasma densities for longitudinal compression experiments were provided over the drift length (Sec. 5.2). $3D$ simulations of the source indicated that the radially-injected plasma nearly uniformly filled the device, including into the $\Delta z = 5$ cm "gaps" (with reduced densities) for transverse diagnostic access,

in approximately $t \sim 6$ μs, and in good agreement with experimental measurements when $m_i = 3 \times Ba$ and $T_{pe} = T_{pi} = 20$ eV were chosen for the effective plasma ion species and initial plasma temperature, respectively. However, the compelling comparison was qualitative, since the problem did not necessarily have a unique solution, due to the wide range of detected plasma ion constituents, lack of ion temperature measurements, and neglect of other realistic effects in the simulations. Situations involving azimuthally-asymmetric plasma production, using large non-emitting regions at the radial wall, showed that symmetric plasma density profiles were nevertheless achieved at the times of peak on-axis plasma densities, but were reduced in overall density relative to the fully-symmetric case. Lastly, the simulations highlighted that the ferroelectric plasma only expanded upstream on the thermal expansion time scale, and therefore avoided the possibility of allowing plasma to move upstream, partially neutralize the beam, and raise its emittance in the transport and acceleration gap sections.

Strong final-focus solenoids will be used in upcoming experiments in order to transversely focus the axially-compressing beam to a sub-mm spot coincident with the longitudinal focal plane. In order to fill a final-focus solenoid with the requisite amount of high-density plasma for beam neutralization, large-space scale and long-time scale simulations were executed in order to predict the amount of plasma-fill within a solenoid, due to supersonic injection of the plasma from the low-field region (Sec. 5.3). Evidence was shown for significant magnetic mirroring of the injected plasma in the transition region leading up to $B_z = 53$ kG and $B_z = 40$ kG final-focus solenoids in $3D$ and $2D$ models. Plasma partially-filled the solenoid near the $r = 0$ axis to a radius of $r_p^{fill} \sim 0.6$ cm and significant plasma density compression was

evident in the vicinity of the focal plane. Ambipolar forces influenced the dynamics as the solenoid became partially-filled with plasma on-axis, and larger supersonic ion injection velocities corresponded to higher penetrating plasma densities into the final-focus solenoid.

Experiments are planned to measure whether the injected plasma can fill such strong solenoids, and provide quantitative comparisons to the predictions in the simulations. Since the beam radius $r_b(t)$ may be larger than the on-axis plasma fill-factor as it enters the solenoid, whether a partially-filled final-focus solenoid is sufficient for high levels of beam neutralization during simultaneous focusing is an important issue which requires additional research. In addition, whether the plasma that enters the final-focus solenoid has sufficient density and temperature for effective neutralization, which largely depends on design considerations such as the time dependence of the beam density and whether the focal plane resides within or downstream of the final-focus solenoid, should be investigated. Full-fill scenarios involving multiple plasma sources injecting plasma along a variety of field lines are suggested for future research.

Chapter 6

Simultaneous Transverse and Longitudinal Compression

Intense, space-charge-dominated ion beam pulses for warm dense matter and heavy ion fusion applications must undergo simultaneous transverse and longitudinal bunch compression in order to meet the requisite beam intensities desired at the target. As measured in Chapter 2 and studied using reduced models and PIC simulations in Chapter 4, the longitudinal compression of a charge bunch is achieved by imposing an initial axial velocity tilt on the drifting beam and subsequently neutralizing its space-charge and current in a drift region filled with high-density plasma. Very good agreement between experiments, theory, and numerical simulation has been demonstrated for longitudinal current compression [Sefkow and Davidson, 2006]. The models provide physical insights into various limiting imperfections, such as non-ideal velocity tilts, consequences of the finite-size acceleration gap, beam temperature effects, and partial neutralization effects, all of which give rise to decreased compression factors and increased pulse lengths at focus.

At the present time, the compression of intense ion beams in the laboratory has been separately demonstrated in the transverse and longitudinal directions. However, simultaneous focusing to a common focal plane is desired in order to maximize the intensity on the target for a given amount of initial beam charge. The goal for upcoming experiments is to demonstrate the feasibility and study the physical limitations of simultaneous transverse and longitudinal compression of an intense charge bunch [Sefkow *et al.*, 2007, Seidl *et al.*, 2007, Welch *et al.*, 2007].

Beam space-charge, current, and pressure effects are especially important to consider near the simultaneous focal plane of the charge bunch because of the need to evaluate and minimize focusing abberations, arising from temperature effects as well as partial neutralization, and their role in the compression dynamics (via perveance and emittance). The particle-in-cell treatment properly describes the ion beam interaction with the background plasma and self-consistently evolves the beam's self-fields, as well as the plasma response, in situations involving incomplete (partial) charge and current neutralization. All of the particle-in-cell simulation results presented in this Chapter are from $2D$ $\{r, z\}$ LSP simulations, solve the electromagnetic field equations, treat all particle species as explicit and kinetic, resolve ω_{pe} and Ω_{ce} (the electron plasma and cyclotron frequencies, respectively), are not susceptible to the so-called numerical Debye length instability, use the cloud-in-cell model, and conserve energy to good accuracy levels.

The time-dependent radial defocusing effect of the acceleration gap is reviewed in Sec. 6.1, along with a discussion of the "over-focusing" technique for its mitigation. Various numerical simulations are employed in Sec. 6.2 in order to study the dependence of partial neutralization effects on the background plasma density and

temperature. As presented in Sec. 6.3, a strong final-focus solenoid can be situated near the end of the drift region in order to transversely focus the beam to a sub-mm spot size coincident with the longitudinal focal plane, and the compression dependence on beam radius $r_b(t)$ entering the solenoid is explored; certain $r_b(t)$ profiles are shown to alleviate the associated focusing aberration, due to coupling of the transverse and longitudinal dynamics within the solenoid. The design of a near-term simultaneous focusing experiment using existing equipment is shown in Sec. 6.4. In Sec. 6.5, simulations using optimized upgraded equipment show that the current density of an intense ion beam can be compressed over a few meters by factors greater than 10^5 with peak on-axis beam density $n_b^{foc} > 10^{14}$ cm^{-3} at the focal plane. A comparison of simultaneous focusing results involving variations in the final-focus solenoid and background plasma parameters is provided in Sec. 6.6. Depending on the target experiment and diagnostic necessity, the reverse-aligned solenoid configuration for minimizing the magnetic field at the target may be employed for warm dense matter experiments, as discussed in Sec. 6.7. The charge and current neutralization provided by the background plasma is critical in determining the total achievable compression of the beam pulse. The peak beam density sets a lower bound on the local plasma density required near the focal plane for optimal beam compression, since simulations show stagnation of the compression when $n_b > n_p$ before the intended focal plane. Beam-plasma interactions, due to partial neutralization effects in the presence of a strong solenoidal magnetic field near the focal plane, can deleteriously affect the compression physics and lead to the formation of nonlinear wave excitations in the plasma [Sefkow *et al.*, 2007], as simulated and described in Sec. 6.8. A brief summary and discussion of results are provided in Sec. 6.9.

6.1 Radial defocusing effect of the acceleration gap

As mentioned in Chapters 4 and 5, the process of imposing an axial velocity tilt onto a charge bunch for the purpose of longitudinal compression inadvertently contributes a net divergence, in a time-dependent manner, to the otherwise radially converging trajectories of the ions. The time-dependent voltage waveform $V(t)$, imposed across a finite-size acceleration gap, was shown in Chapter 4 to impart velocity spread akin to an effective longitudinal temperature on an otherwise initially cold beam with no space-charge. The origin of the effect was described as the coupling of the transverse and longitudinal phase space of the beam as it traversed the finite-size acceleration gap. Since the equations and boundary conditions describing the induced electric field in the gap necessitate the existence of radial electric field components wherever $\partial E_z(r,z)/\partial z \neq 0$, the time-dependent nature of the voltage waveform, combined with the transit time of the ion particles across the gap, imply an imbalance of integrated $E_r(r,z,t)$ experienced by each particle. It is this radial electric field imbalance across the gap that provides a time-dependent radial defocusing force to both the head *and* tail of the charge bunch intended for longitudinal compression.

During the compressing part of the voltage waveform $[dV(t)/dt < 0]$, beam particles encounter an imbalance of $E_r(r,z,t)$ across the gap and receive a time-dependent net divergence or defocusing angle. As illustrated in Fig. 6.1, particles undergoing time-dependent deceleration in the axial direction early in time [when $V(t) > 0$] encounter $+E_r(r,z,t)$ fields at the entrance of the gap and $-E_r(r,z,t)$ fields at the exit; conversely, particles undergoing time-dependent acceleration in the axial direction late in time [when $V(t) < 0$] encounter $-E_r(r,z,t)$ fields at the entrance of the gap and $+E_r(r,z,t)$ fields at the exit. However, the voltage waveform $V(t)$ decreases on

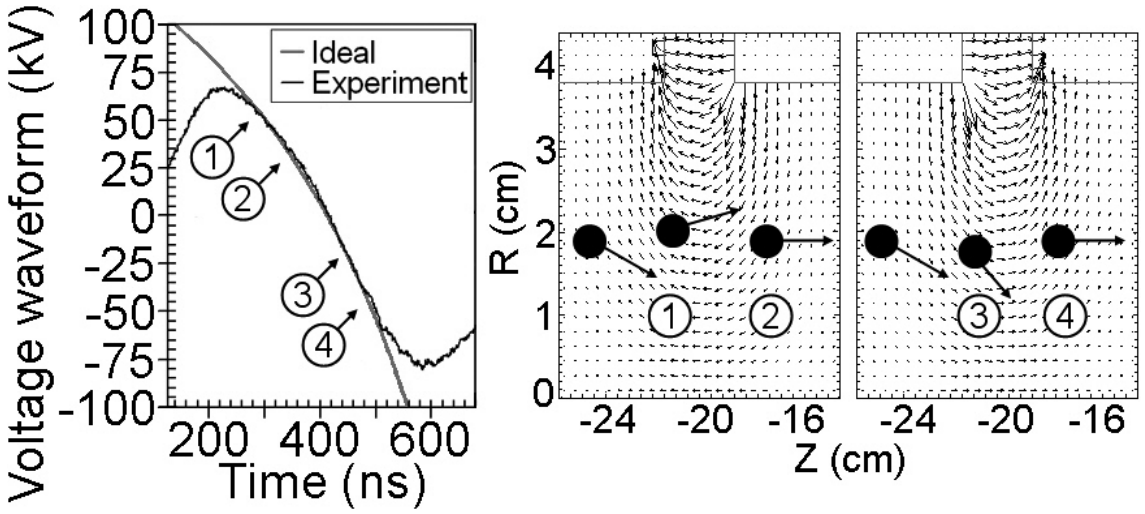

Figure 6.1: Illustration of the radial defocusing effect of the acceleration gap. During the $dV(t)/dt < 0$ portion of the voltage waveform, particles crossing the gap early in time [when $V(t) > 0$, shown as 1 and 2] sample more integrated $+E_r$ at the entrance compared to the exit, whereas particles crossing the gap late in time [when $V(t) < 0$, shown as 3 and 4] sample more integrated $+E_r$ at the exit compared to the entrance. In the center and right frames, electric field vectors are plotted in the background and the black arrows indicating particle velocity vectors are exaggerated. In both cases, a net radial divergence is experienced by the ion trajectories.

a time scale similar to the particle transit time across the gap, which is longer for decelerated particles and shorter for accelerated particles. Therefore, particles in the former case encounter stronger $+E_r$ fields earlier in time and weaker $-E_r$ fields later in time, whereas particles in the latter case encounter weaker $-E_r$ fields earlier in time and stronger $+E_r$ fields later in time, leading to a net radial divergence in *both* cases approximately proportional to $q_b\, E_0(t)^{-1}\, [dV(t)/dt]\, r_b(t)$ during the application of the velocity tilt for longitudinal compression; as similarly discussed in Chapter 4, the time-dependent effect of the finite-size acceleration gap and voltage waveform on the radial and axial beam velocities, which change as functions of time and space within the gap, needs to be evaluated using a model that incorporates the actual

temporal and spatial dependence of the electric field in the gap for each specific case considered, such as a $2D$ warm-fluid treatment or PIC simulation.

The overall $+E_r(r,z,t)$ imbalance felt by all particles undergoing longitudinal compression causes radially converging particles entering the gap to time-dependently lose a significant portion of their convergent trajectory. In order to explicitly illustrate the phenomenon under discussion, a $2D$ $\{r,z\}$ PIC simulation of transverse focusing without an axial velocity tilt is compared to the same with an applied axial velocity tilt. An $E_0 = 300$ keV K^+ beam with an initial radius $r_b = 2$ cm and $I_0 = 18$ mA of beam current is initialized with a Maxwellian $T_b = 0.2$ eV transverse and longitudinal temperature and a convergence angle of $\Delta\theta_r = -15.4$ mrad at the injection plane $z = -30$ cm, just upstream of the acceleration gap. According to Eqs. (1.1) and (1.2), the corresponding normalized effective emittance and perveance are 9.3×10^{-3} cm-mrad and 4.5×10^{-4}, respectively. Recall from Chapter 4 that the application of a radial convergence angle onto the beam causes the $-v_r$ of the beam particles to vary radially as $-v_r(r) = -v_z^0\,(r/r_b)(r_b/L_r)$ for $r = 0$ to $r = r_b$. The initial pulse length of the beam is $t_p = 700$ ns and the experimental waveform, which is shown at the top of Fig. 6.2, imposes an approximate 10% velocity tilt to the beam. In this case, the background plasma from $z = +5$ cm to $z = +110$ cm (the approximate range in experiments) is sufficiently dense and cold to ensure good neutralization throughout the entire drift length.

The particle phase space plots, after the velocity tilt has been applied ($t = 1000$ ns) and the beam enters the plasma, are displayed in Fig. 6.2. The difference in transverse trajectories between using a longitudinally compressing waveform and none at all is clear, and entirely due to the acceleration gap. Application of the velocity tilt

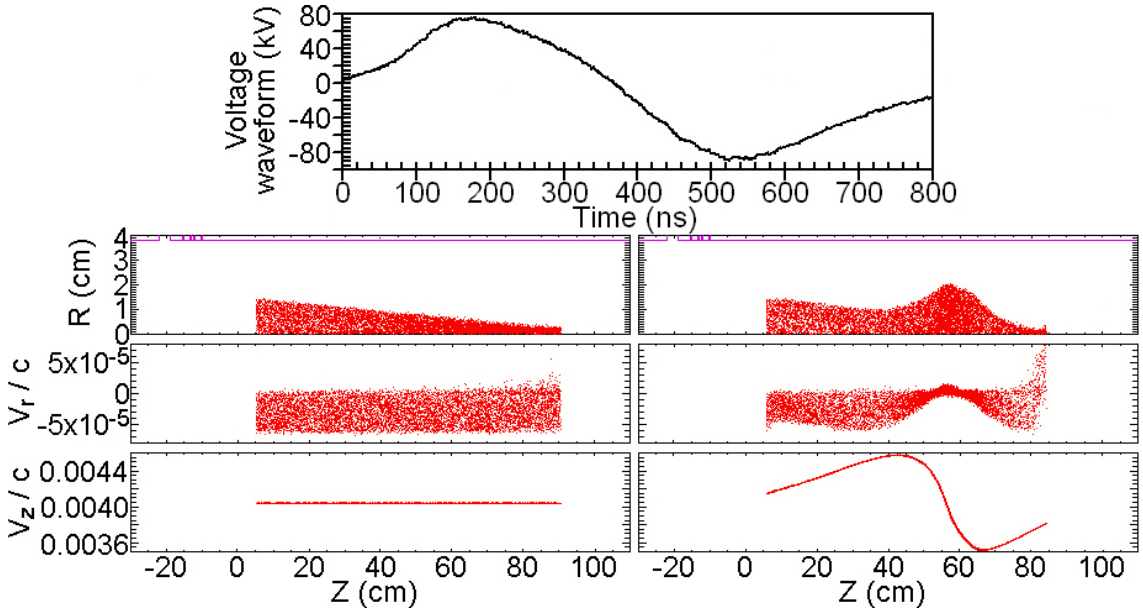

Figure 6.2: (Color) Ion beam phase space comparison between transverse focusing without an axial velocity tilt (left) and with an axial velocity tilt (right) at $t = 1000$ ns shown as particle plots in $\{r, z\}$ (top), $\{z, v_r\}$ (middle), and $\{z, v_z\}$ (bottom) coordinates. The experimental voltage waveform $V(t)$ used in simulation is displayed above the particle plots. The radial defocusing effect imparts excess divergence to the longitudinally compressing portion of the beam in a time-dependent manner.

adds time-dependent divergence [net $+v_r(t)$] to the beam, resulting in a hump-shape in $\{r, z\}$ space around the region of the compressing charge bunch, whose expected $r_b(t)$ at focus is increased considerably compared to the case without a tilt. For the longitudinal compression case, the beam arrives at the axial focal plane $z = +95$ cm ($L_d \sim 115$ cm) at $t = 1320$ ns and achieves a compression ratio of 67 with $t_{fwhm} = 1.7$ ns, in good agreement with some of the most recent experimental measurements. However, the radius at the focal plane is approximately 2 cm, which is the same as the incoming beam radius even though a radial convergence angle was applied, due to the defocusing effect of the acceleration gap. The consequence of the defocusing effect on current density compression, and therefore energy deposition or power of the

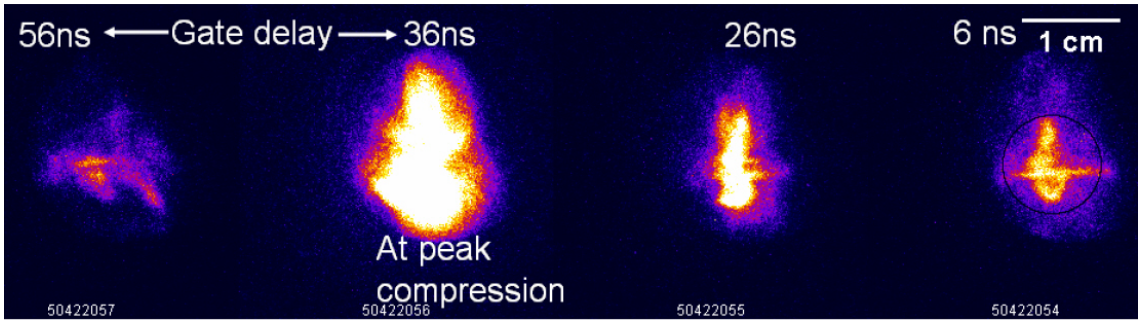

Figure 6.3: (Color) Transverse profiles showing the defocusing effect of the acceleration gap on longitudinal compression, as measured with an aluminum oxide scintillator (placed in the path of the beam) and a gated camera [Roy *et al.*, 2005b].

beam for warm dense matter and heavy ion fusion applications, is striking because of the inverse dependence on the square of the radius [$J_z \sim r_b(t)^{-2}$]. Early longitudinal compression experiments substantiated the existence of the effect, which is evident in Fig. 6.3 [Roy *et al.*, 2005b], and agreed with predictions made by simulations.

Similar to the longitudinal acceleration gap dynamics studied in Chapter 4, the effective transverse temperature (and emittance) of the charge bunch increases relative to the cold beam case, and is manifest in the extra time-dependent radial velocity spread of the beam as it exits the gap. For both the axially decelerating and accelerating portions of the compressing charge bunch, beam particles at larger radii entering the gap receive more of a net $+v_r(t)$ increase than particles initially closer to the $r = 0$ axis at the same entrance time, because the radial electric fields are stronger at larger radii (and zero at the axis). Recall that the entire time-dependent range of various radial velocity spreads will overlap in the axial coordinate near the longitudinal focal plane and appear to be an increase in effective transverse temperature, which gives rise to increased chromatic aberration of the transverse focal plane (and increases the minimum achievable beam radius r_b^{foc} at focus) compared to the case without

a velocity tilt, in an analogous way to the longitudinal temperature smearing of the longitudinal focal plane, as discussed in Chapter 4. Also, the effective transverse temperature increase acquired by the beam is dependent upon the gap geometry, voltage waveform, and beam parameters, such as axial velocity, radius, convergence angle, and emittance. Since the applied convergence angle is usually much larger than the initial transverse beam temperature, as it is in this case, the increase in temperature from the gap is not apparent in the $\{z, v_r\}$ phase space plot of Fig. 6.2, although it is more easily identified in the initially cold beam case.

Note that a constant $dV/dt = 0$ waveform, whether uniformly accelerating or decelerating beam particles across this gap shape, always contributes a net radial convergence ($-\hat{r}$) to the beam. Since decelerated particles spend more relative time near the exit of the gap, they encounter relatively more integrated $-E_r$, and since accelerated particles spend less relative time near the exit of the gap, they encounter relatively less integrated $+E_r$. In either case of constant acceleration or deceleration, alterations to the conducting boundaries of the acceleration gap geometry can change how the total electric field is communicated to the gap, and therefore also the resulting net radial forces on the beam. Linear induction accelerators used for accelerating energetic electron beams are especially susceptible to such radial perturbations, and specially designed contoured [Shope *et al.*, 1987] and coaxial [Prestwich *et al.*, 1983] gap geometries have been successfully employed in order to reduce the integrated E_r fields felt by the beams across the gaps to nearly zero, as well as minimize electron emission and virtual cathode formation in high-current cases.

A similar change in conducting boundaries for the purposes of longitudinal compression would only relieve the problem for half of the beam, since the voltage changes

polarity over the course of the waveform and a gap design that decreases the E_r imbalance for either the positive or negative portion of the voltage waveform only exacerbates the original problem for the other half. Of course, a special gap geometry that reduces some of the imbalance using a longitudinally compressing waveform $[dV(t)/dt < 0]$ that is entirely positive or negative (without the polarity reversal) could work in theory, however it is much less efficient in practice because half of the available Volt-second swing of the induction module isn't used. In addition, the $dV(t)/dt$ of the ideal waveform isn't strictly constant, so the net radial defocusing is time-dependent anyway, resulting in the reality that a fixed gap geometry can't bring to fruition a beam with a time-independent convergence angle as it exits the gap, if it had one while entering. Lastly, an approach under active investigation for mitigating the defocusing effect involves the use of two transverse conducting grids, placed at the upstream and downstream ends of the acceleration gap, in order to minimize the radial electric fields within the gap region. Although the technique shows promise for reducing the defocusing effect described in this Section, it may introduce other deleterious consequences such as unwanted emittance growth of the beam from gas and electron cloud effects, due to beam ion bombardment on the grids.

6.1.1 The "over-focusing" technique

Various separate methods exist to compensate for the defocusing effect in the acceleration gap in order to achieve focused beam radii of a few mm or less at the simultaneous focal plane. The simplest method for recovering the proper transverse beam ion trajectories would be to give the charge bunch too large a convergent angle as it exits the transport section and enters the acceleration gap. An optimized angle

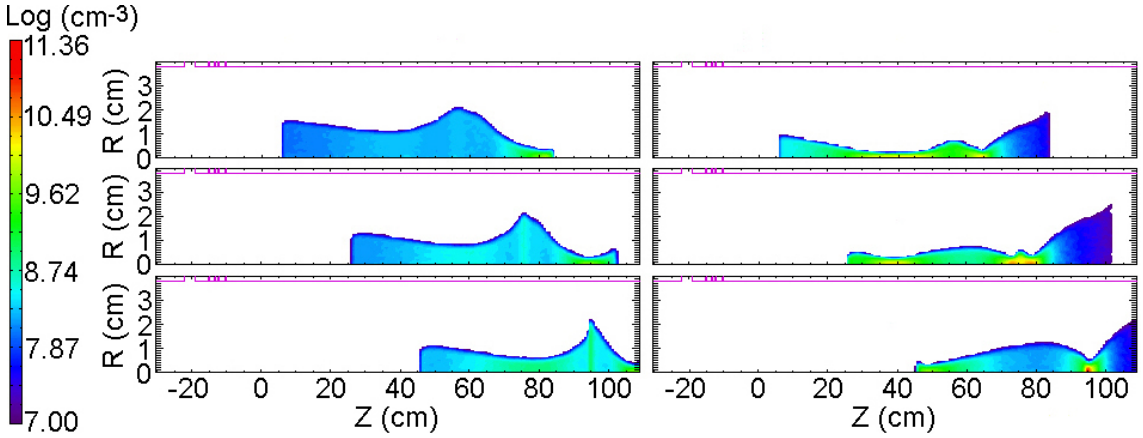

Figure 6.4: (Color) $\{r, z\}$ isocontour plots of beam density n_b at $t = 1000$ ns (top row), $t = 1160$ ns (middle row), and near focus at $t = 1320$ ns (bottom row) for the regular transverse focusing case using $\Delta\theta_r = -15.4$ mrad (left column) and the "over-focusing" case using $\Delta\theta_r = -32.3$ mrad (right column) at the injection plane $z = -30$ cm. All plots are on the same Log scale.

can be found for which the excess amount of focusing is balanced by the defocusing effect, causing the beam to transversely focus to its originally intended location. However, since the excess divergence given to the beam is time-dependent, the so-called "over-focusing" technique can only offset the defocusing effect in an average way. In other words, there will still be a time-dependent range of convergence angles (albeit reduced in magnitude) about the central portion of the compressing charge bunch, with larger discrepancies located near the front of the head and rear of the tail, giving rise to transverse focusing aberration.

The simulation described earlier in this Section is repeated, except with the simple change in radial convergence angle from $\Delta\theta_r = -15.4$ mrad to -32.3 mrad at the injection plane $z = -30$ cm, and the difference in beam density n_b evolution is demonstrated in Fig. 6.4. In the regular focusing case, the $n_b(r) \sim 1.4 \times 10^9$ cm^{-3} is approximately constant at the focal plane $z = +95$ cm with a flat-top radius

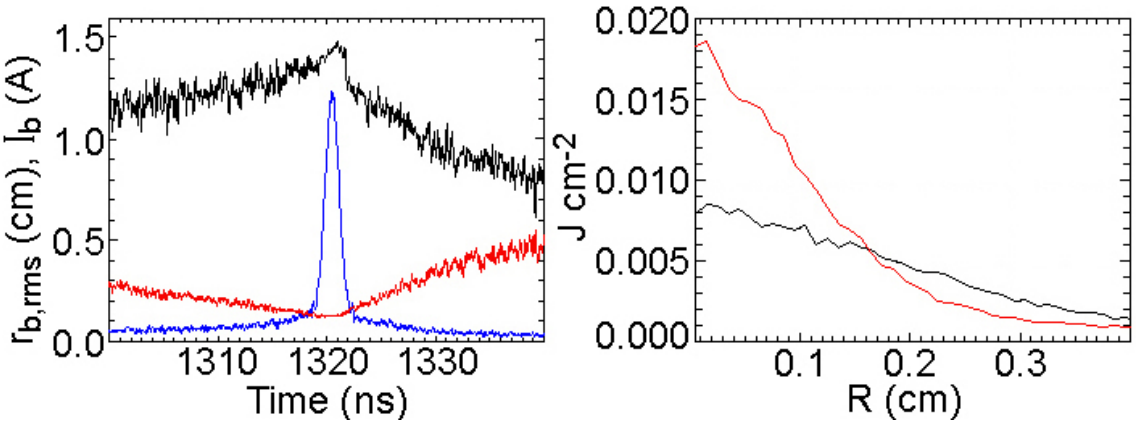

Figure 6.5: (Color) Time history plots (left) of current (blue) and rms beam radius r_b for the convergence angles -15.4 mrad (black) and -32.3 mrad (red) and cumulative energy deposition profiles $E_{dep}(r)$ (right, same color-code) over the entire initial pulse length of 700 ns at the focal plane $z = +95$ cm. Both cases achieve the same longitudinal compression, and the peak current of 1.21 A corresponds to $I_b^{max}/I_0 = 67$.

$r_b^{foc} \sim 2$ cm, whereas the "over-focused" beam reaches a peak on-axis density of $n_b^{foc} \sim 2.3 \times 10^{11}$ cm^{-3} with much smaller radius. Note that the current compression ratio in both cases is 67 with $t_{fwhm} = 1.7$ ns after $L_d \sim 115$ cm around $t = 1320$ ns, as illustrated in Fig. 6.5, but the difference in minimum radius accounts for a factor of approximately 250 in current density. Figure 6.5 shows the striking difference in transverse compression for the two cases; the beam with the -15.4 mrad convergence angle arrives at the intended focal plane with an rms radius of approximately 1.4 cm (not indicative of the constant profile), whereas the "over-focused" beam achieves an rms radius of $r_b^{foc} \sim 0.125$ cm (very close to the $1/e$ radius).

The cumulative energy deposition profiles $E_{dep}(r)$ over the entire duration of the initial pulse length for both convergence angle cases are also presented in Fig. 6.5. Clearly, the beam with the excess initial transverse focusing achieves twice the peak

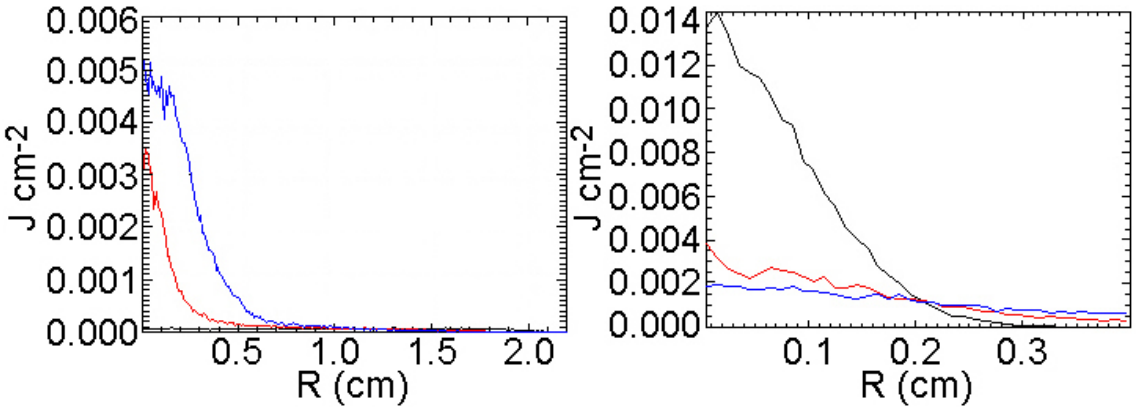

Figure 6.6: (Color) Cumulative energy deposition profiles $E_{dep}(r)$ for the approximate 222 ns of pre-pulse before $t = 1319$ ns (red), 3 ns of main pulse from $t = 1319 - 1322$ ns (black), and 475 ns of post-pulse after $t = 1322$ ns (blue) at the focal plane $z = +95$ cm for the convergence angles -15.4 mrad (left) and -32.3 mrad (right). Note the difference in scales between the two cases, and the main pulse $E_{dep}(r)$ for the case on the left is approximately constant at 6×10^{-5} J cm^{-2} to $r = 2$ cm.

on-axis energy deposition compared to the case suffering from the defocusing effect. However, the proportion of the energy deposition residing within the main compressed pulse itself is vastly different between the two cases, as evident in Fig. 6.6. Apparently, the pre- and post-pulses (the first 222 ns and last 475 ns of beam pulse, respectively) in the regular focusing case contain the overwhelming majority of the time-integrated energy deposition at the focal plane, and the significant relative contrast between them and the main pulse is undesirable for applications involving targets. Conversely, upon comparison of Figs. 6.5 and 6.6, approximately 80% of the peak on-axis cumulative energy deposition in the "over-focusing" case properly resides within the main 3 ns of longitudinally-compressed pulse. The associated amount of pre-heat impinging the target is approximately $20-30$% of that delivered by the main pulse, with 50% of the pre-pulse energy contained in the final 4 ns leading up to the arrival of the main pulse. Whether $20-30$% pre-heat levels are tolerable depends on

the target experiment under consideration. The cases presented here are intended to be illustrative of the mentioned effects and methods, and do not necessarily represent the optimal parameter configuration that can be devised.

The "over-focusing" technique presented here is the simplest time-independent way to partially mitigate the defocusing effect of the acceleration gap. The natural extension of this technique implies the use of time-dependent magnetic focusing, via the last solenoid or quadrupole in the transport section, to separately alter the convergence angles of different portions of the initial beam pulse length in such a way as to completely negate the time-dependent divergence added to the beam by the gap. Clearly, such a method requires careful selection of a group of beam and system parameters, since the optimal application of time-dependent magnetic focusing upstream of the acceleration gap depends on the evaluation of charge bunch propagation involving many variables, including (but not limited to) the beam energy, radius as a function of time, current (perveance), focusing elements, acceleration gap and voltage waveform, location of the background plasma, and device geometry (distances between various components). Currently, time-dependent magnetic focusing enjoys active research as a promising method for relieving the disruption to the transverse ion beam dynamics during the application of velocity tilts. However, the required magnet technology is not currently available, since the magnitude of the involved magnetic field is required to change by as much as 10 kG over periods of time as short as $50 - 100$ ns [$\mathrm{d}\mathbf{B}(\mathrm{t})/\mathrm{dt} \sim 0.2$ TG s^{-1}], for the parameters considered here.

6.2 Neutralization effects on simultaneous focus

The provision that $n_p >> n_b$ throughout the drift length ensures high levels of space-charge and current neutralization as the intense charge bunch transversely and longitudinally compresses. However, in order to quantify the effects of complete neutralization compared to cases of partial neutralization, a series of particle-in-cell simulations are computed in a variety of background plasma conditions. Recall from Chapters 3 and 4 that PIC simulation is the only self-consistent model for properly evaluating conditions of partial neutralization in a background plasma without making limiting assumptions about the form of the beam and plasma. Incomplete neutralization effects are expected to contribute to decreased levels of compression in both directions for cases involving total current density compression factors greater than 10^4. The primary concern for warm dense matter and heavy ion fusion applications is the degradation of the minimum beam radius at simultaneous focus, which occurs for any amount of overall compression involving a high perveance beam, because of the current density's inverse-square dependence on the radius (transverse compression) compared to its linear dependence on line density (longitudinal compression).

The two simultaneous focusing simulations from Sec. 6.1 involving regular and "over-focused" initial radial convergence angles are revisited, except the background plasma is removed from the drift length. In other words, the full self-fields are allowed to self-consistently evolve with the dynamically compressing beam, whose particle velocity distributions change in time due to the self-fields and boundary conditions. The transverse and longitudinal compression results are plotted in Fig. 6.7 as time history plots of rms beam radii r_b and compression ratios $I_b(t)/I_0$, respectively, at the intended simultaneous focal plane $z = +95$ cm. Since the radial electric fields

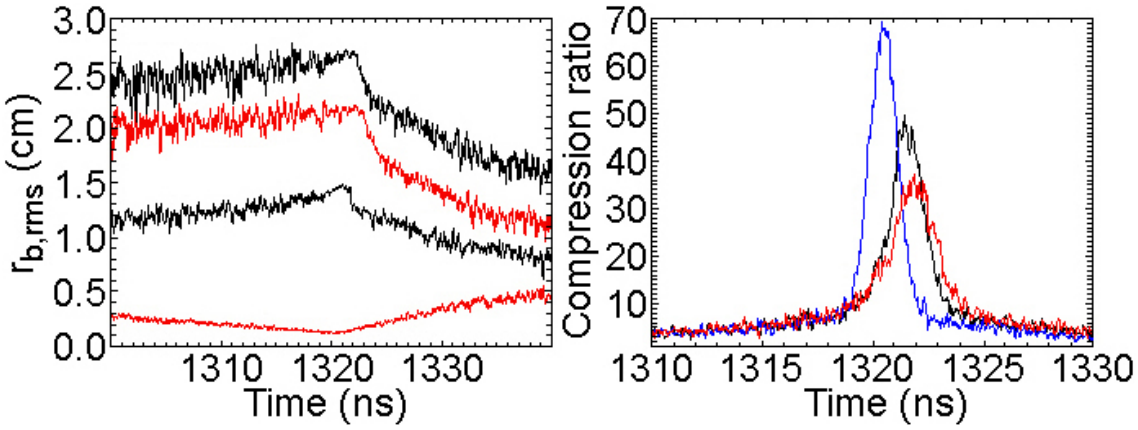

Figure 6.7: (Color) Time history plots of rms beam radius r_b (left, top profiles) and compression ratio $I_b(t)/I_0$ (right) at the intended focal plane $z = +95$ cm without background plasma present in the drift length for the initial convergence angles -15.4 mrad (black) and -32.3 mrad (red). For reference, the completely neutralized color-coded cases from Fig. 6.5 for the rms beam radius (left, bottom profiles) and compression ratio (right, blue) are provided.

are not neutralized in either case, they resist the initial convergence angles and the intense charge bunches begin to radially diverge before reaching the axial location $z = +30$ cm. As shown in Fig. 6.7, the rms beam radii at the intended focal plane are both greater than the initial radius $r_b = 2$ cm, although the rms quantities don't reflect the nearly constant radial density profiles of approximately $r_b \sim 3.5$ cm with $n_b \sim 3.5 \times 10^8$ cm^{-3} ($E_{dep} \sim 1.5 \times 10^{-5}$ J cm^{-2}) for the -15.4 mrad case and $r_b \sim 2.8$ cm with $n_b \sim 5.5 \times 10^8$ cm^{-3} ($E_{dep} \sim 2.3 \times 10^{-5}$ J cm^{-2}) for the -32.3 mrad case. The ranges of expected minimum rms beam radii (for the beam and system parameters under consideration) at $z = +95$ cm and $t = 1320$ ns that cover the spectrum of fully neutralized to unneutralized cases are $r_b^{foc} = \{1.4 \text{ cm}, 2.7 \text{ cm}\}$ for the -15.4 mrad case and $r_b^{foc} = \{0.125 \text{ cm}, 2.2 \text{ cm}\}$ for the -32.3 mrad case. The self-field effects of the beam change the longitudinal dynamics as well, since the longitudinal compression results at the intended focal plane also suffer, as illustrated in Fig. 6.7;

although, the peak compression ratio of 67 is recovered farther downstream from the intended focal plane ($\Delta z = +3$ cm and +5 cm for the -15.4 mrad and -32.2 mrad cases, respectively) because the large beam radius ensures that the self-potential of the charge bunch is too small to significantly alter the axial trajectories of the ~ 300 keV K^+ ions. Such a result also highlights the coupling of the transverse and longitudinal dynamics throughout the drift length.

In order to ascertain the level of neutralization provided by the ferroelectric plasma source for NDCX-relevant parameters, the "over-focusing" simulation from Sec. 6.1 is executed again, except the uniform and constant background plasma is exchanged with the dynamic simulation of radially-injected ferroelectric plasma, as discussed in Sec. 5.2. However, rather than simulating one ~ 20 cm segment with periodic boundary conditions, five 15 cm segments (with four 5 cm transverse diagnostic ports) are modeled between $z = +7$ cm and $z = +102$ cm, in order to align the focal plane within one of the high-density plasma regions. The large-space and long-time scale ferroelectric source plasma flow simulation uses the same input parameters mentioned in Sec. 5.2 (including the initial $T_p = 20$ eV) and the injection dynamics are identical. The timing of the voltage waveform and injection of the beam relative to the beginning of the ferroelectric plasma injection is $\Delta t = +5\,\mu$s, so that the simultaneously compressing beam arrives at the focal plane approximately at the time of peak on-axis plasma density (refer to Fig. 5.13). The simulation results are presented in Fig. 6.8 and show that the beam density does not reach the same peak value at the focal plane (refer to the bottom right frame of Fig. 6.4) in the presence of the ferroelectric source plasma, due to radial focal spot degradation (the longitudinal compression is unaffected).

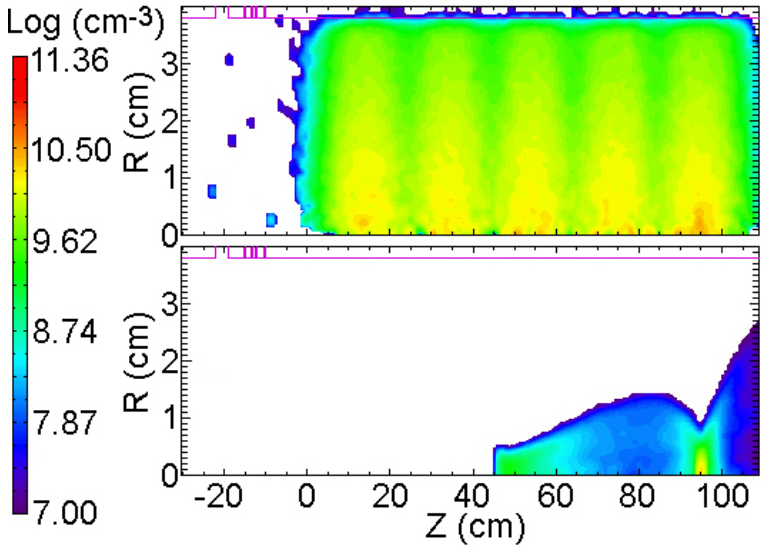

Figure 6.8: (Color) $\{r, z\}$ isocontours of ferroelectric plasma electron density n_{pe} (top) and beam density n_b (bottom) near the simultaneous transverse and longitudinal focal plane at $t = 6320$ ns. Both plots are on the same Log scale.

The intended peak on-axis density of the "over-focused" beam from Sec. 6.1 was $n_b^{foc} \sim 2.3 \times 10^{11}$ cm^{-3} with rms radius $r_b^{foc} \sim 0.125$ cm. As mentioned in Sec. 5.2, the peak on-axis plasma density achievable by the ferroelectric plasma source is approximately $n_p^{foc} \sim 2.5 \times 10^{10}$ cm^{-3} around $t = 6\,\mu$s, so that n_b exceeds the supplied initial n_p near the focal plane, as can be seen in Fig. 6.8 by the extra electrons present near the axis at $z = +95$ cm. Plasma electrons respond to the overabundance of ions and the self-fields of the beam by executing orbits (without a background magnetic field) that minimize the charge perturbation. However, the cumulative effect of the partial neutralization provided by the ferroelectric plasma along the beam's drift length manifests itself in terms of a larger minimum radius and smaller amounts of energy deposition at the intended simultaneous focal plane, as shown in Fig. 6.9. Evidently, the partial neutralization effects of the ferroelectric plasma source on the compression dynamics of the beam doubles the minimum achievable rms radius from

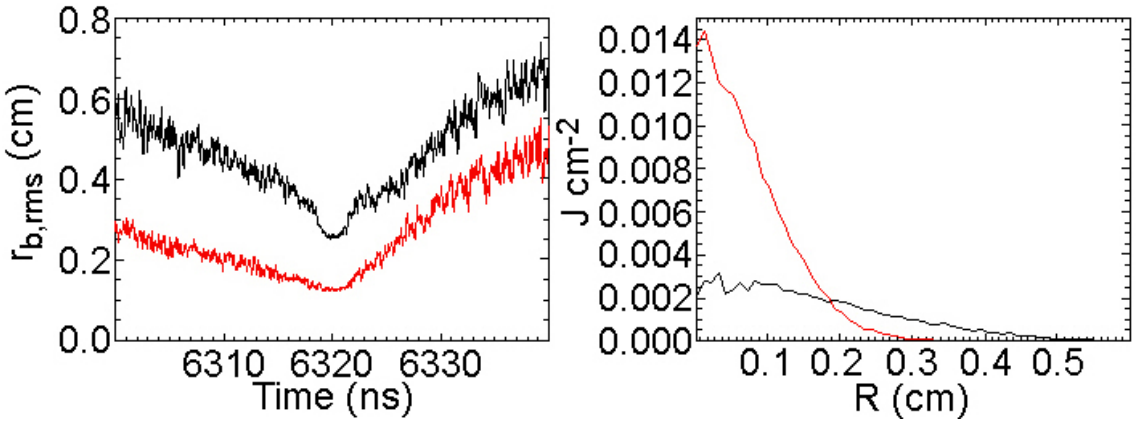

Figure 6.9: (Color) Time history plots of rms beam radius r_b (left) and radial profiles of cumulative energy deposition $E_{dep}(r)$ from the main pulse from $t = 6319 - 6322$ ns (right) at the focal plane $z = +95$ cm using an initial convergence angle of -32.3 mrad, and the ferroelectric plasma source throughout the drift length (black). For reference, the results of the completely neutralized case (red) from Figs. 6.5 and 6.6 are also provided, with the $\Delta t = +5$ μs temporal shift included.

$r_b^{foc} = 0.125$ cm to 0.25 cm, implying reasonable levels of neutralization are achieved since the unneutralized case yields $r_b^{foc} = 2.2$ cm. The peak on-axis cumulative energy deposition steeply decreases from 0.014 J cm^{-2} to approximately 0.003 J cm^{-2} with a radius $(1/e)$ of 0.35 cm, whereas the peak on-axis beam density at the focal plane is $n_b^{foc} \sim 3 \times 10^{10}$ cm^{-3}, almost an order-of-magnitude lower than the completely neutralized case. Clearly, the supplied plasma density ($n_p \sim 2.5 \times 10^{10}$ cm^{-3}) is too low and the plasma temperature ($T_p \sim 20$ eV) is too high to provide the highest levels of neutralization required to asymptote to the fully neutralized case results.

A sequence of PIC simulations is now calculated to quantify the partial neutralization effects from variations in supplied initial plasma density. The "over-focusing" simultaneous compression simulation from Sec. 6.1 is repeated multiple times, with uniform and constant background plasma densities decreasing from $n_p = 10^{12}$ cm^{-3} to $n_p = 10^7$ cm^{-3} (in steps of 10^{-1} cm^{-3}) without initial plasma temperature ($T_p = 0$

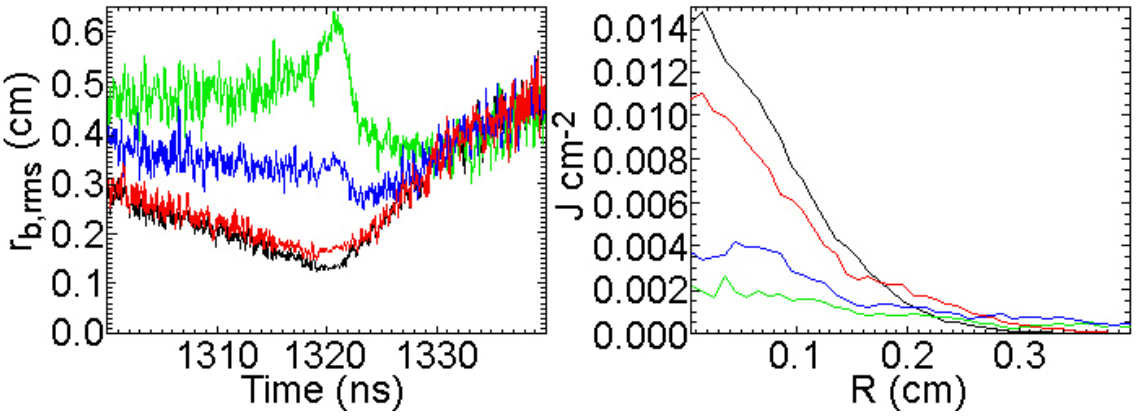

Figure 6.10: (Color) Time history plots of rms beam radius r_b (left) and radial profiles of cumulative energy deposition $E_{dep}(r)$ for the main pulse from $t = 1319 - 1322$ ns (right) at the focal plane $z = +95$ cm using an initial convergence angle of -32.3 mrad and plasma density $n_p = 10^{10}$ cm^{-3} (black), 10^9 cm^{-3} (red), 10^8 cm^{-3} (blue), and 10^7 cm^{-3} (green) with initial $T_p = 0$ eV. The $n_p = 10^{11}$ and 10^{12} cm^{-3} cases (not shown) are identical to the $n_p = 10^{10}$ cm^{-3} case (and completely neutralized case).

eV) and located between $z = +5$ cm and $z = +110$ cm. A cold electron emission model is used in LSP to emit those particles from the conducting wall at $r_w = 3.8$ cm, thereby altering the wall sheath physics and facilitating a more quiescent plasma response to the injected beam. The extra electron population becomes especially important to consider in the two cases involving the lowest plasma densities, since the initial beam density is greater than 10^8 cm^{-3} as it enters the plasma-filled drift length, and the emission electrons participate in the complex interaction process between the beam and plasma for cases where $n_p >> n_b$ is not adequately satisfied.

The simultaneous compression results from the simulations of various plasma densities are plotted in Fig. 6.10. The cases involving $n_p = 10^{10} - 10^{12}$ cm^{-3} with initial $T_p = 0$ eV recover the completely neutralized results (minimum rms beam radius and peak on-axis cumulative energy deposition from the main pulse) initially presented in Sec. 6.1 and Figs. 6.5 and 6.6. Expectedly, as the provided plasma density decreases

below a certain threshold ($n_p = 10^{10}$ cm^{-3} and $T_p = 0$ eV, here), the minimum beam radius and peak on-axis cumulative energy deposition for the main 3 ns pulse decrease as well, although the longitudinal compression ratio of 67 is recovered in each of the cases within a few cm of the intended focal plane (recall the same in the cases lacking plasma). The cumulative partial neutralization effects caused by the partially exposed beam potential within the drift length contribute to emittance growth (up to a factor of ~ 3, here) and ultimately deteriorate the quality of the focal plane.

Note that the $n_p = 10^{10}$ cm^{-3} case traps electrons in the beam potential and recovers the completely neutralized result even though the peak on-axis beam density at focus is over an order-of-magnitude larger ($n_b^{foc} \sim 2.3 \times 10^{11}$ cm^{-3}) than the provided background density. The reason for this result is found in the artificially cold initial $T_p = 0$ eV plasma temperature. A sequence of PIC simulations is calculated to quantify the partial neutralization effects from variations in supplied initial plasma temperature. The "over-focusing" simulation from Sec. 6.1 is repeated multiple times, for uniform and constant background plasma densities of $n_p = 10^{10}$ cm^{-3} and $n_p = 10^9$ cm^{-3} with initial plasma temperatures of $T_p = 10$ eV and $T_p = 50$ eV, and located between $z = +5$ cm and $z = +110$ cm. A warm electron emission model is used in LSP to emit those particles with the same plasma temperature from the conducting wall at $r_w = 3.8$ cm, thereby altering the wall sheath physics and facilitating a more quiescent plasma response to the injected beam (and to replenish depleting electron particle statistics throughout the simulation).

The simultaneous compression results from the simulations of various plasma temperatures for the $n_p = 10^{10}$ and 10^9 cm^{-3} cases are plotted in Fig. 6.11. The case involving $n_p = 10^{10}$ cm^{-3} with initial $T_p = 0$ eV recovers the completely neutralized

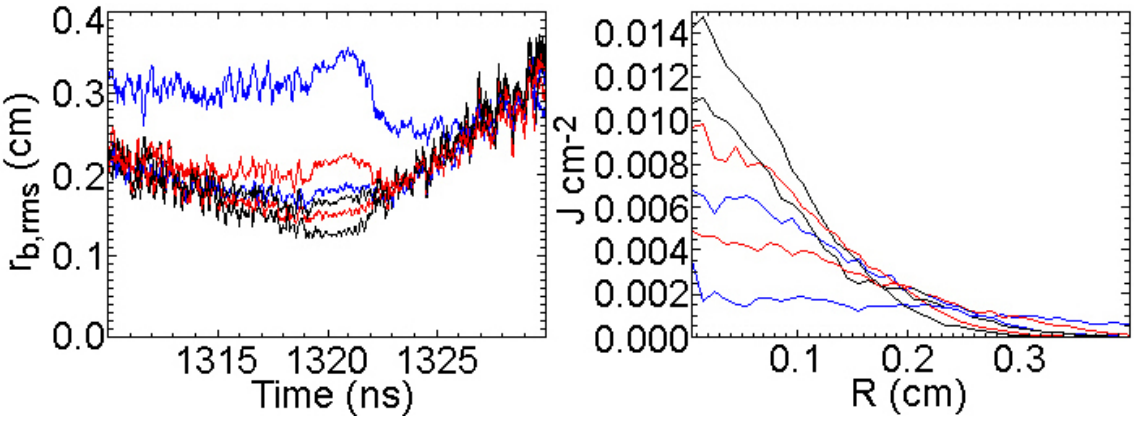

Figure 6.11: (Color) Time history plots of rms beam radius r_b (left) and radial profiles of cumulative energy deposition $E_{dep}(r)$ for the main pulse from $t = 6319 - 6322$ ns (right) at the focal plane $z = +95$ cm using an initial convergence angle of -32.3 mrad and plasma densities $n_p = 10^{10}$ cm^{-3} (bottom profiles on left, top profiles on right) and $n_p = 10^9$ cm^{-3} (top profiles on left, bottom profiles on right) with initial $T_p = 0$ eV (black), $T_p = 10$ eV (red), and $T_p = 50$ eV (blue).

results presented earlier. As the initial plasma temperature increases, the minimum beam radius increases and the peak on-axis cumulative energy deposition for the main pulse decreases, although the longitudinal compression ratio of 67 is recovered in each of the cases within a few cm of the intended focal plane (recall the same in the cases lacking plasma). The cumulative partial neutralization effects caused by the partially exposed beam potential in the plasmas with finite T_p within the drift length contribute to the deterioration of the beam's energy deposition capability.

Table 6.1 presents the approximate minimum rms beam radii at the focal plane for the cases in Fig. 6.11 involving variations in plasma density and temperature. The fourth and fifth columns in the Table evaluate the Debye lengths for each of the cases, as well as the difference between the minimum radii and the Debye lengths. The fifth column demonstrates that partial neutralization effects due to plasma temperature increase the minimum radii from the respective cold plasma cases by approximately

Table 6.1: Simultaneous compression dependence on plasma temperature.

n_p	T_p	r_b^{foc} (rms) at $t = 1320$ ns	λ_D	$r_b^{foc} - \lambda_D$
10^{10} cm^{-3}	0 eV	0.125 cm	0 cm	0.125 cm
10^{10} cm^{-3}	10 eV	0.151 cm	0.024 cm	0.127 cm
10^{10} cm^{-3}	50 eV	0.181 cm	0.053 cm	0.128 cm
10^{9} cm^{-3}	0 eV	0.166 cm	0 cm	0.166 cm
10^{9} cm^{-3}	10 eV	0.220 cm	0.074 cm	0.146 cm
10^{9} cm^{-3}	50 eV	0.334 cm	0.166 cm	0.168 cm

adding to them the corresponding Debye length, for the parameters considered here. In practice, plasma temperatures may take on a wide range in space and time, depending on the circumstances, suggesting that $n_p >> n_b$ should be used in experiments in order to ensure that $r_b^{foc} >> \lambda_D$ and high levels of neutralization are provided. In retrospect, the ferroelectric source provides less neutralization than expected, since the peak densities and temperatures of the plasma are $n_p^{foc} \sim 2.5 \times 10^{10}$ and $T_p = 20$ eV, but the energy deposition from that case ($E_{dep}^{peak} \sim 0.003$ J cm^{-2}, refer to Fig. 6.9) is only as good as the $n_p = 10^9$ cm^{-3} case presented in Fig. 6.11 with a temperature between $T_p = 10$ eV and $T_p = 50$ eV. The assessment of the cause for the excess loss of neutralization in the case of the ferroelectric plasma source requires further research. The three primary differences between the constant density cases presented here and the ferroelectric plasma are the (1) time-dependent nature of the dynamic ferroelectric plasma density, (2) four regions of decreased ferroelectric plasma density due to the transverse diagnostic ports (refer to Fig. 6.8), and (3) significant directed radial momenta of the ferroelectric plasma ions, which are of the same order as the radial momenta of the beam ions.

6.3 Final-focus solenoid for transverse focusing

In addition to the "over-focusing" technique, which only offsets the transverse defocusing effect of the acceleration gap in an average way, and corrective time-dependent magnetic focusing, the technology for which is currently unavailable, a third method is considered involving a strong final-focus solenoid for achieving simultaneous compression to a sub-mm radius at the focal plane. The use of a final-focus solenoid near the end of the drift length controls (and shortens) the effective focal length of the transverse beam compression and therefore helps minimize the amount of high-density plasma required throughout the system, in addition to decreasing the amount of focusing aberration compared to a longer transverse focal length. In addition, a strong axial magnetic field has been shown to dramatically reduce magnetic filamentation of the beam, particularly at high beam densities, due to the fact that plasma electrons are magnetized and constrained to move along field lines [Welch *et al.*, 2003b].

A beam with an axial velocity tilt enters the solenoid with a wide range of beam energies, resulting in aberration of the transverse focal plane. For a static $\mathbf{B}^{sol}(r, z)$, the lower-energy front of the tilted beam transversely focuses earlier in space and time, whereas the higher-energy end of the tilted beam transversely focuses later in space and time; the axial placement of the final-focus solenoid must be precisely positioned so that the longitudinal focal plane is centered near the transverse focal plane of the center of the beam (traveling near v_0), ensuring the optimal amount of simultaneous compression. A smaller fractional tilt f alleviates a portion of the transverse focusing aberration due to the final-focus solenoid, but at the cost of reducing the longitudinal compression. Lastly, in order for time-dependent magnetic focusing by the final-focus solenoid itself (transversely focusing the faster beam tail more than the slower beam

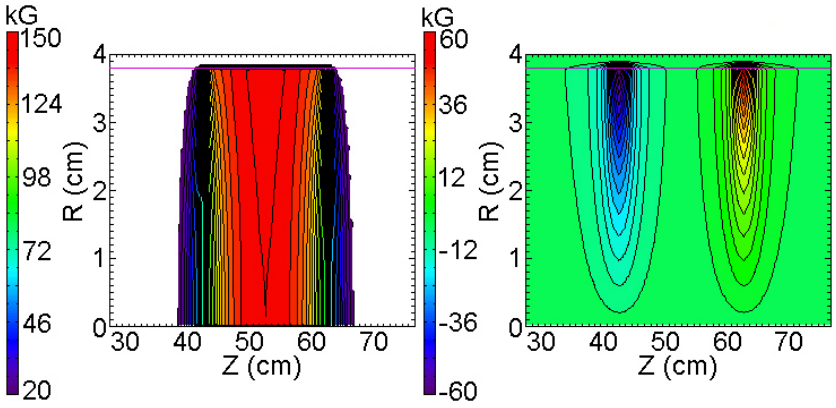

Figure 6.12: (Color) $\{r, z\}$ isocontours of axial B_z (left) and radial B_r (right) magnetic field magnitudes from a 150 kG final-focus solenoid of length $l^{sol} = 20$ cm and radius $r^{sol} = 3.8$ cm, centered at the axial location $z = +52.6$ cm.

head) to be feasible for mitigating some transverse aberration: (1) the beam pulse in the interaction region must be long compared to the length of the solenoid in order to only interact with small, few ns windows of the charge bunch's velocity tilt; (2) the required $d\mathbf{B}^{sol}(t)/dt$ would need to be ≥ 2 TG s^{-1}, for the parameters considered here; and (3) the solenoid must be sufficiently far upstream since the $d\mathbf{B}^{sol}(t)/dt$ would radially expel the magnetized neutralizing plasma from the region.

The magnetic field of a solenoid with finite length and radius is modeled in $2D$ $\{r, z\}$ coordinates in the LSP code by using a power-series expansion of the radial coordinate, which involves only the on-axis $r = 0$ field and its derivatives [Thoma, 2002]. The PIC simulations presented in this Section employ a strong 150 kG final-focus solenoid of length $l^{sol} = 20$ cm and radius $r^{sol} = 3.8$ cm, centered at $z = +52.6$ cm, as illustrated in Fig. 6.12. In general, the location of the intended transverse focal plane (and the degree of its chromatic aberration) depends on the length and strength of the final-focus solenoid, as well as the radius $r_b(t)$ and velocity space distribution $\mathbf{v}(\mathbf{r},t)$ of the beam as it enters the solenoid.

In order to separate and quantify the detrimental effects arising from the final-focus solenoid rather than considering those from within the acceleration gap, the case (from Sec. 4.7.2) of a K^+ ion beam acquiring an ideal velocity tilt, using the "sharp" waveform across an infinitely-thin acceleration gap, with initial parameters $E_0 = 400$ keV, $t_p = 300$ ns, $f = 0.5$, and Maxwellian $T_b = 0.2$ eV of initial temperature, is revisited with the addition of the 150 kG solenoid. The original simulation resulted in a longitudinal compression ratio of $I_b^{max}/I_0 = 400$ with $t_{fwhm} = 0.6$ ns at the focal plane $z = +58.25$ cm at time $t = 950$ ns. Here, $|B_z| \sim 140$ kG at the intended focal plane. In the simulations presented here, the beams are given initial radii of either $r_b = 2$ cm or $r_b = 1$ cm at $z = -30$ cm, without convergence angles, and an initial current of 80 mA, which approximately represent the peak parameters currently available in NDCX experiments. The corresponding perveance in both cases is 1.3×10^{-3}, and the normalized effective emittances are 9.3×10^{-3} cm-mrad and 4.7×10^{-3}, respectively. The background plasma is assumed to be sufficiently dense and cold in order to provide complete charge and current neutralization of the beam throughout the drift length.

The less energetic head of the longitudinally compressing charge bunch arrives at the final-focus solenoid first. As shown in Fig. 6.12, the beam encounters strong $-B_r(r, z)$ fields, which lend the beam additional rotation via the Lorentz force, $-F_\theta = +q[(+v_z)\times(-B_r)] = -m_i\,(\mathrm{d}\mathbf{v}/\mathrm{dt})_\theta$. As found in the acceleration gap, the longitudinal dynamics are coupled to the transverse dynamics, since the $+v_z$ directed ion motion increases the $-v_\theta$ rotation and leads to radial focusing according to $-F_r = +q[(-v_\theta)\times(+B_z)] = -m_i\,(\mathrm{d}\mathbf{v}/\mathrm{dt})_r$. In addition, the $-v_\theta$ responsible for the radial focusing is also the cause of axial deceleration via $-F_z = +q[(-v_\theta)\times(-B_r)] = -m_i\,(\mathrm{d}\mathbf{v}/\mathrm{dt})_z$,

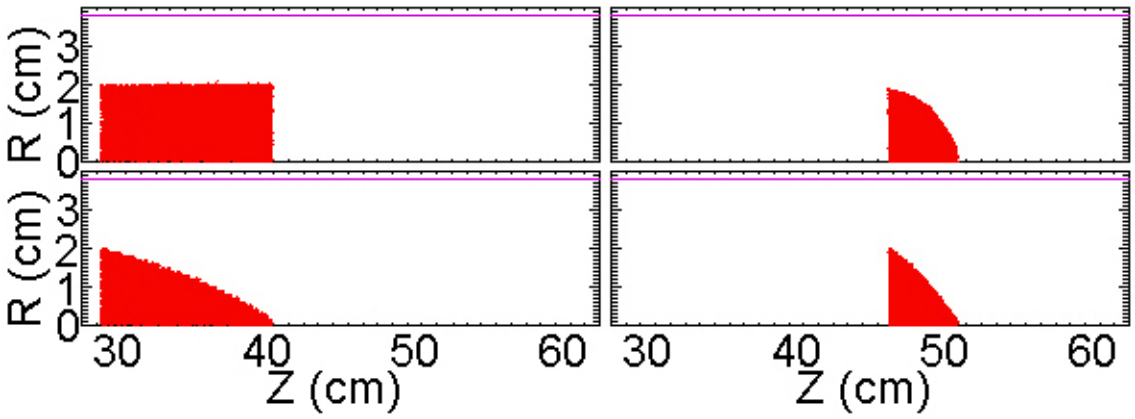

Figure 6.13: (Color) $\{r, z\}$ beam phase space plots for the cases involving constant initial current density with $r_b = 2$ cm (top) and decreasing initial current density $[J_z(t) \sim r_b(t)^{-2}]$ with linearly increasing $r_b(t)$ from $r_b = 0.1$ to 2 cm (bottom) over the initial pulse length $t_p = 300$ ns in the final-focus solenoid simulations at times $t = 785$ ns (left) and $t = 885$ ns (right). The $r_b = 1$ cm cases are similar.

a second order effect. Beam particles at larger radii entering the solenoid encounter stronger $-B_r(r, z)$ fields and acquire more $-v_\theta$, and subsequently more $-v_r$ radial focusing (and $-v_z$ deceleration), than particles relatively closer to the $r = 0$ axis. All of the aforementioned velocities are functions of space and time due to the specific $\mathbf{B}^{sol}(r, z)$. However, beams with larger constant r_b suffer from increased amounts of aberration in both focal planes due to the increased amount of $-B_r(r, z)$ encountered.

In addition to the cases involving beams of constant current density with initial radii of either $r_b = 2$ cm or $r_b = 1$ cm over the duration of the initial pulse length $t_p = 300$ ns, two cases of radially-constant but temporally decreasing current density $[J_z(t) \sim r_b(t)^{-2}]$ with linearly increasing $r_b(t)$ from $r_b = 0.1$ cm to $r_b = 2$ or 1 cm over the duration of the initial pulse length are considered. The resulting total initial current through the $z = -30$ cm plane is 80 mA in all cases. For all of the non-constant $J_z(t)$ cases considered through the remainder of this Section, the optimum position of the center of the final-focus solenoid is moved by $\Delta z = +4$ cm

to $z = +56.6$ cm. Particle plots are provided in Fig. 6.13 for the two types of current density simulations involving the $r_b = 2$ cm case (the $r_b = 1$ cm versions are similar).

The reasoning behind the investigation of this particular case involving a decreasing initial $J_z(t)$ with linearly increasing initial $r_b(t)$ along the initial pulse length is as follows. As mentioned earlier, slower head particles arriving at the solenoid first will normally transversely focus in less space and time compared to the faster tail particles arriving later, contributing to aberration of the transverse focal plane that scales with r for a constant beam radius r_b. In order for slower head particles arriving at the solenoid earlier in time to transversely focus in a *longer* axial distance and amount of time, they must enter the weaker $-B_r(r, z)$ fields at *smaller* radii, and thereby *decrease* the relative amount of $-v_\theta$ rotation and radial focusing force $-F_r$ they experience; conversely, in order for faster tail particles arriving at the solenoid later in time to transversely focus in a *shorter* axial distance and amount of time, they must enter the stronger $-B_r(r, z)$ fields at *larger* radii, and thereby *increase* the relative amount of $-v_\theta$ rotation and radial focusing force $-F_r$ they experience. Since the velocity tilt is nearly linear, and $-B_r$ increases approximately linearly with r for most of the $r < r^{sol}$ (refer to Fig. 6.12), a charge bunch whose radius initially increases linearly from head to tail along the pulse length minimizes the transverse (and longitudinal) aberration associated with the use of a final-focus solenoid.

The $\{z, v_z\}$ beam phase space for the four cases mentioned earlier are shown in Fig. 6.14 at their respective simultaneous focal planes. Recall from Chapter 4 that the original longitudinal focal plane axial location was $z = +58.25$ cm without the final-focus solenoid, about $0.4 - 1.15$ cm downstream of the focal planes in the cases presented here (due to the net $-v_z$ second-order effects). As mentioned, beams with

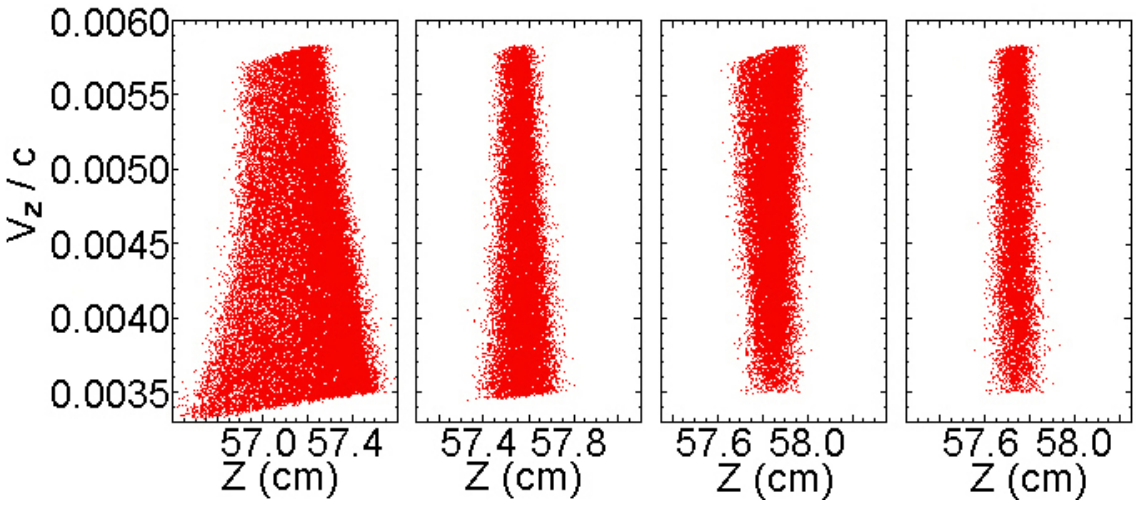

Figure 6.14: (Color) $\{z, v_z\}$ beam phase space plots for the constant $r_b = 2$ cm (left), constant $r_b = 1$ cm (middle left), decreasing $J_z(t)$ with linearly increasing $r_b(t)$ from $r_b = 0.1$ to 2 cm (middle right), and decreasing $J_z(t)$ with linearly increasing $r_b(t)$ from $r_b = 0.1$ to 1 cm (right) cases near the simultaneous focal planes $z = +57.1$ cm at $t = 946.9$ ns, $z = +57.6$ cm at $t = 949.3$ ns, $z = +57.85$ cm at $t = 951.0$ ns, and $z = +57.85$ cm at $t = 950.7$ ns, respectively.

smaller radii suffer less simultaneous focal plane aberration due to the coupled dynamics in the final-focus solenoid, and slower particles acquire an increased proportion of it relative to the faster particles for cases involving constant r_b (the same as in Chapter 4 for longitudinal focusing only). Interestingly, faster tail particles receive more longitudinal aberration in the case involving a linearly increasing r_b to 2 cm due to the increased $-B_r$ they encounter, whereas the original longitudinal compression results are recovered in the case involving a linearly increasing r_b to 1 cm.

When the finite-size acceleration gap effects are included, the resulting $r_b(t)$ profile exiting the acceleration gap can be approximated as having a linear increase over the first half and linear decrease over the second half of the initial pulse length, due to the transverse defocusing effect discussed in Sec. 6.1 (refer to Figs. 6.2 and 6.4). Therefore, such a triangular (or parabolic, due to the velocity tilt) initial pulse shape

is simulated with linearly increasing $r_b(t)$ from $r_b = 0.1$ cm to $r_b = 2$ cm or 1 cm over the first half and linearly decreasing $r_b(t)$ from $r_b = 2$ cm or 1 cm to $r_b = 0.1$ cm over the second half duration of the initial pulse length [with radially-constant $J_z(t) \sim r_b(t)^{-2}$ variation to ensure $I_0(t) = 80$ mA]. Since the second half of the initial pulse lengths in the triangular cases have decreasing $r_b(t)$ profiles, they are not expected to compress as well as the purely increasing initial $r_b(t)$ cases. However, since the first half of the pulse has the appropriate linear $r_b(t)$ increase (for minimizing the aberration) and the second half of the pulse suffers less relative aberration due to the decreasing $r_b(t)$ entering the solenoid (compared to a constant r_b case), the triangular case returns intermediate results between the constant and linearly increasing $r_b(t)$ cases.

Radial profiles of cumulative energy deposition $E_{dep}(r)$ for the six cases discussed in this Section are displayed in Fig. 6.15. The case shown in the middle frame of Fig. 6.15 for the case involving a linear increase from $r_b = 0.1$ cm to $r_b = 1$ cm recovers the original longitudinal compression ratio of 400 with a full-width, half-maximum pulse length of $t_{fwhm} = 0.6$ ns in a simultaneous radius $(1/e)$ $r_b^{foc} = 0.008$ cm, yielding a peak on-axis cumulative energy deposition $E_{dep}^{peak} = 7.7$ J cm^{-2} with approximate peak on-axis intensity 8 GW cm^{-2}. Therefore, this $r_b(t)$ profile entering the final-focus solenoid is better for minimizing the associated aberrations of the focal plane. The results for all of the cases are listed in Table 6.2 in terms of the compression ratio, full-width, half-maximum pulse length, peak on-axis cumulative energy deposition, and minimum simultaneous beam radius $(1/e)$ r_b^{foc}. Note that the triangular cases, which more closely represent present experimental conditions because of the defocusing effect from the finite-size acceleration gap, result in better

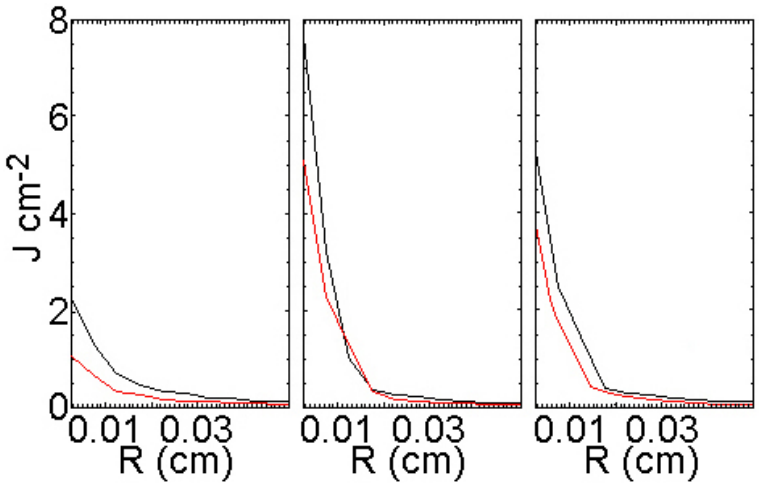

Figure 6.15: (Color) Radial profiles of cumulative energy deposition $E_{dep}(r)$ for compression simulations using a 150 kG final-focus solenoid (refer to Fig. 6.12) and constant J_z (left), decreasing $J_z(t)$ with linearly increasing $r_b(t)$ (middle), and half-decreasing and half-increasing $J_z(t)$ with linearly half-increasing $r_b(t)$ and linearly half-decreasing $r_b(t)$ (right) profiles for the cases involving $r_b = 1$ cm (black) and $r_b = 2$ cm (red) at the respective simultaneous focal planes given in Fig. 6.14.

compression scenarios than the average of the other two types of cases considered because of the reduced $-B_r(r, z)$ experienced by the tail particles compared to the constant r_b cases.

In summary, the transverse defocusing effect of the acceleration gap (described in Sec. 6.1) is beneficial for reducing the transverse and longitudinal aberration normally imposed on a beam with constant $r_b(t)$ entering the final-focus solenoid, because of the particular time-dependent radius $r_b(t)$ created as the beam exits the acceleration gap. Further laboratory improvements for simultaneous focusing using a final-focus solenoid could use time-dependent magnetic focusing upstream of the acceleration gap, in tandem with the calculated defocusing effect, in order to ensure that a beam with a linearly increasing $r_b(t)$ exits the acceleration gap, rather than the approximately triangular (or parabolic) profile presently available. However, the

Table 6.2: Compression dependence on initial $r_b(t)$ profile using a 150 kG solenoid.

Initial $r_b(t)$	I_b^{max}/I_0	t_{fwhm}	E_{dep}^{peak}	r_b^{foc} $(1/e)$
2 cm, constant	100	2.7 ns	1.1 J cm^{-2}	0.011 cm
1 cm, constant	310	0.8 ns	2.3 J cm^{-2}	0.011 cm
2 cm, triangular	275	0.8 ns	3.8 J cm^{-2}	0.010 cm
1 cm, triangular	375	0.7 ns	5.3 J cm^{-2}	0.010 cm
2 cm, linear increase	290	1.0 ns	5.0 J cm^{-2}	0.010 cm
1 cm, linear increase	400	0.6 ns	7.7 J cm^{-2}	0.008 cm

d$\mathbf{B}^{sol}(t)$/dt presently needed exceeds the limits of current technology. Alternatively, recall from Sec. 6.1 that a change in gap conducting boundary geometry to mitigate the defocusing effect would only relieve the problem for half of the beam, since the voltage waveform changes polarity and the E_r imbalance is decreased for one half of the beam, but increased for the other half. Therefore, an alternative gap geometry that decreases the E_r imbalance early in time but exacerbates the defocusing late in time can result in a linearly increasing $r_b(t)$ profile exiting the gap, leading to further reduction of focusing aberration within the final-focus solenoid and the realization of larger energy depositions at the focal plane. Lastly, if the focal plane is chosen to be downstream of the final-focus solenoid (for shorter and/or weaker solenoid choices), the $-v_\theta$ velocities approach their original values as they exit the downstream end of the solenoid due to the presence of the $+B_r(r,z)$ fields. However, due to the inward radial movement within the solenoid, the beam will have a smaller $r_b(z,t)$ as it exits and not sample a balanced amount of $+B_r(r,z)$ at the downstream end compared to the $-B_r(r,z)$ at the upstream end. After the beam leaves the region of strong B_z, and $-v_\theta$ decreases in magnitude, the net radial converging trajectory of the charge bunch remains and transversely propagates the beam to its simultaneous focal plane.

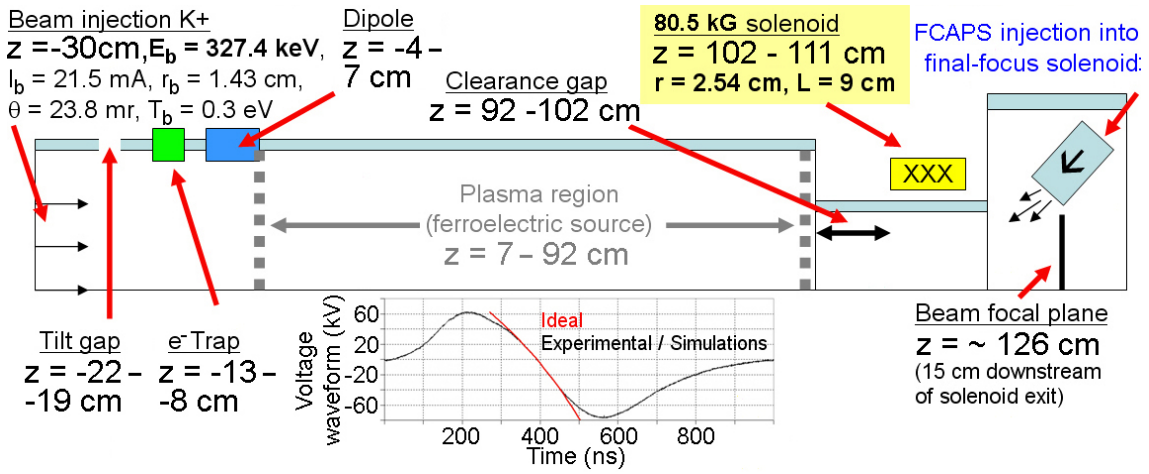

Figure 6.16: (Color) Design schematic of the configuration for simultaneous focusing experiments includes the existing voltage waveform, electrostatic e^- trap, permanent magnetic dipole, ferroelectric plasma source, clearance gap, $B_z = 80.5$ kG final-focus solenoid, and filtered cathodic-arc plasma source (FCAPS) injection into the solenoid.

6.4 Design of a simultaneous focusing experiment

The simultaneous transverse and longitudinal bunch compression of intense ion beam pulses will be studied on NDCX for warm dense matter and heavy ion fusion applications. Near-term experiments will employ existing hardware and a $B_z = 80.5$ kG, 9 cm-long final-focus solenoid, which is currently under construction, for transverse compression of the beam radius to a plane coincident with the longitudinal focus. $2D$ $\{r, z\}$ PIC simulations are used to design experiments involving the existing induction module and modest beam parameters.

Figure 6.16 illustrates the design schematic of the experimental geometry from the injection plane (upstream of the acceleration gap) to the simultaneous focal plane. Downstream of the 3 cm acceleration gap, located from $z = -22$ to -19 cm, are an electrostatic electron trap and permanent magnetic dipole. Originally, the biased (few -kV) trap and dipole ($\sim$ 800 G) were installed to disrupt the upstream flow of

the filtered cathodic-arc plasma source along the $\sim 1-2.5$ m-long guide solenoid, as discussed in Sec. 5.1, in order to suppress electrons from traveling into the transport section and cause emittance growth of the beam due to partial neutralization effects. For consistency, the trap and dipole have remained in the device for near-term experiments, however they will eventually be removed when beams with higher perveances are used, since there are issues associated with the extra axial distance for nonneutral charge bunch transport. The present incarnation of the $BaTiO_3$ ferroelectric plasma source is 85 cm-long and extends to the axial coordinate $z = +92$ cm, beyond which a 10 cm clearance gap for a gate valve is located. The $B_z = 80.5$ kG final-focus solenoid is centered at $z = +106.5$ cm and is responsible for transversely focusing the intense ion beam to the longitudinal focal plane, as discussed in Sec. 6.3, designed to be located at $z = +126$ cm, corresponding to an approximate $L_d \sim 146$ cm. Note the reduction in chamber pipe radius, which alleviates some fabrication cost and mechanical support difficulties associated with high-field solenoids. As discussed in Secs. 5.1 and 5.3, the filtered cathodic-arc plasma source injects supersonic $Al^+ - e^-$ plasma in the upstream direction, into the final-focus solenoid from the off-axis downstream end, in order to provide plasma within the solenoid and near the focal plane for neutralization of the highly compressed charge bunch. Therefore, both types of currently available plasma source, which were both simulated and studied in Chapter 5, are utilized by the experimenter in this configuration.

Similar to previous simulations, an $E_0 = 327.4$ keV K^+ beam with an initial radius $r_b = 1.43$ cm and $I_0 = 21.5$ mA of beam current is initialized with a Maxwellian $T_b = 0.3$ eV transverse and longitudinal temperature and a convergence angle of $\Delta\theta_r = -23.8$ mrad at the injection plane $z = -30$ cm. According to Eqs. (1.1) and

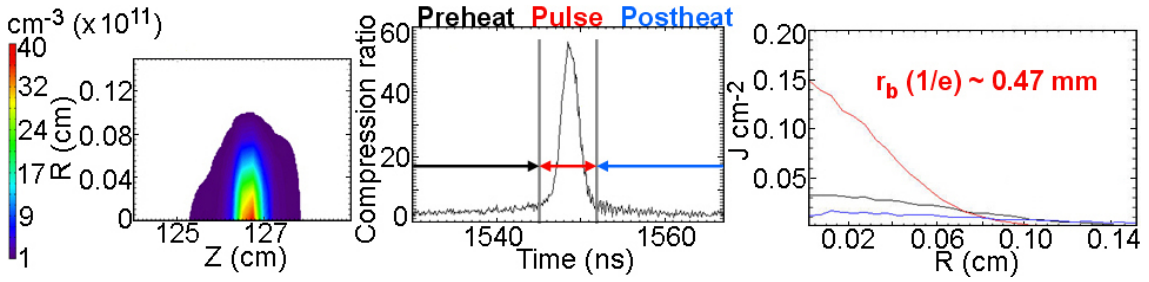

Figure 6.17: (Color) $\{r, z\}$ isocontour of n_b^{foc} (left), compression ratio $I_b(t)/I_0$ (center), and cumulative energy deposition $E_{dep}(r)$ (right) at the simultaneous focal plane $z = +126$ cm using existing hardware and assuming $n_p^{foc} = 2 \times 10^{13}$ cm^{-3} can be provided. The middle and right plots are color coded to show the role of beam pre-heat (200 ns total) on the target in this configuration.

(1.2), the corresponding normalized effective emittance and perveance are 8.2×10^{-3} cm-mrad and 4.7×10^{-4}, respectively. The initial pulse length of the beam is $t_p = 700$ ns and the experimental waveform, which is also shown in Fig. 6.16, imposes an approximate 10% velocity tilt to the beam. Idealized, time- and space-independent parameters are first used for modeling the ferroelectric source plasma ($n_p^{drift} = 5 \times 10^{10}$ cm^{-3}, $T_p^{drift} = 3$ eV) between the magnetic dipole and the clearance gap as well as the cathodic-arc plasma ($n_p^{foc} = 2 \times 10^{13}$ cm^{-3}, $T_p^{foc} = 3$ eV) within and downstream of the strong solenoid, in order to evaluate the expected compression results for the case of nearly complete neutralization. The code predicts a beam radius $(1/e)$ of $r_b = 0.47$ mm with peak on-axis beam density reaching $n_b^{foc} = 4 \times 10^{12}$ cm^{-3} coincident with the longitudinal focal plane, where an approximate 55 compression ratio and $t_{fwhm} \sim 2.4$ ns is achieved when nearly complete neutralization of the large beam space-charge is provided, as shown in Fig. 6.17. The current compression results are in good agreement with the most recent experiments involving only longitudinal focusing.

As previously mentioned, the filtered cathodic-arc plasma source will provide the n_p^{foc} focal region plasma by injecting it with supersonic longitudinal velocity upstream

into the $B_z = 80.5$ kG final-focus solenoid from the downstream end, and the ferroelectric source will provide the n_p^{drift} drift length plasma density. An additional fully-explicit and kinetic $2D$ $\{r, z\}$ large-space and long-time scale simulation (including collisional effects) is carried out in order to assess the realistic flow profiles of both of the plasma source injections at the downstream end of the device ($z = +67$ cm to $z = +127$ cm, refer to Fig. 6.16) in the presence of the strong magnetic fields, as well as to witness the effects of the realistic plasma profiles on the beam compression physics near the downstream end of the configuration. The simulation also investigates whether the 10 cm-long clearance gap, initially devoid of plasma, becomes filled with either ferroelectric plasma drifting downstream and/or cathodic-arc plasma drifting upstream after penetrating the final-focus solenoid.

For the ferroelectric source, located between $z = +67$ cm and $z = +92$ cm at the $r_w = 3.8$ cm wall, the peak injected ion current density is $J_r^i = -10$ mA cm^{-2}, the peak injected ion radial velocity is $v_r^i = -0.375$ cm μs^{-1}, and the initial temperature is $T_p = 20$ eV (as in Sec. 5.2). The cathodic-arc plasma is initialized at $z = +127$ cm with a radially-constant density $n_p^{foc}(r) = 10^{12}$ cm^{-3} and axial ion velocity $v_z^i = -3$ cm μs^{-1}, with electron and ion temperatures $T_e = 20$ eV and $T_i = 1$ eV, respectively, corresponding to an ion Mach number of approximately 3.3. The timing between the two plasma sources is adjusted so the cathodic-arc source injection reaches steady state flow before the ferroelectric source reaches peak density (refer to Fig. 5.13).

The results of the plasma injection simulation are presented in Fig. 6.18 at the time when the ferroelectric source peaks in density and the cathodic-arc plasma source operates in steady state. The cathodic-arc plasma largely follows field lines and partially-fills the final-focus solenoid to approximately $r_p^{fill} = 0.5$ cm, exits the

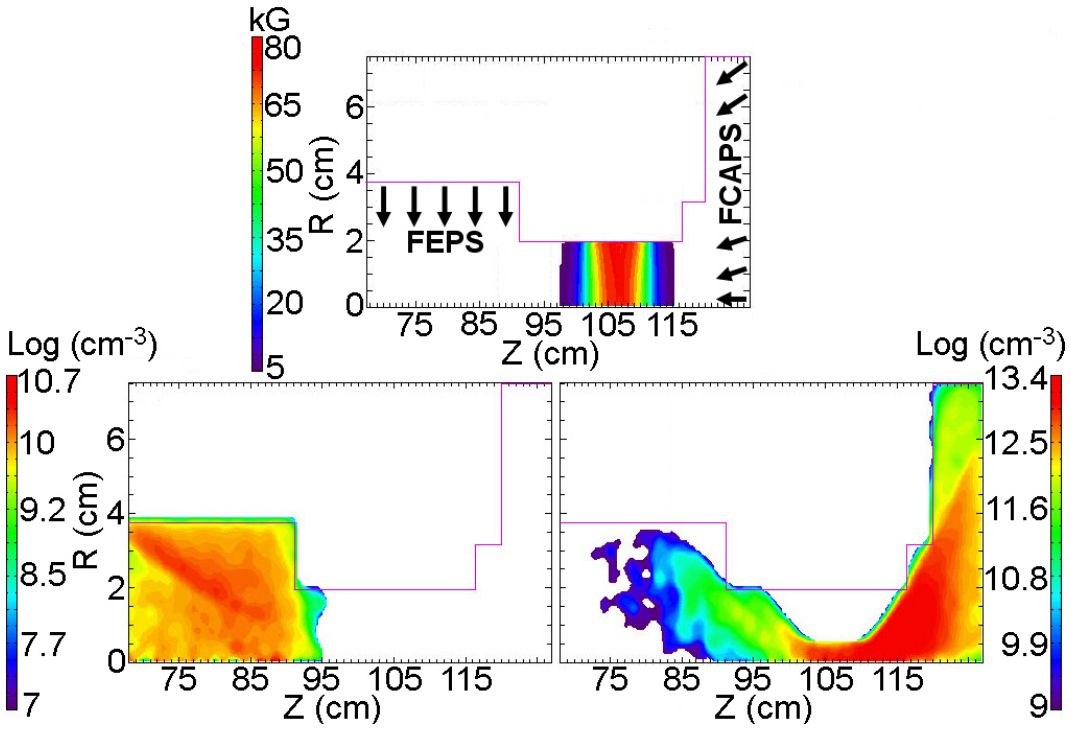

Figure 6.18: (Color) $\{r, z\}$ isocontours of the magnetic field magnitude near the final-focus solenoid (top center), the ferroelectric plasma density n_p^{drift} (Log scale, bottom left), and the cathodic-arc plasma density n_p^{foc} (Log scale, bottom right) in the plasma flow simulation geometry from $z = +67$ cm to $z = +127$ cm (also see Fig. 6.16). Note that the two Log density scales are different.

solenoid, and continues to flow and expand upstream while filling the intermittent clearance gap with plasma. Although most of the cathodic-arc plasma is reflected away from the solenoid, that which is able to penetrate the solenoid is also compressed by an order-of-magnitude and helps to achieve the needed density requirements for beam neutralization. The ferroelectric plasma is significantly affected by the fringe-fields of the solenoid, but nevertheless fills the drift region and penetrates a few cm downstream into the clearance gap. Figure 6.19 illustrates the role of the magnetic fringe-fields on the evolution of the ferroelectric plasma density $n_p^{drift}(r, z)$ upstream of the solenoid, which strongly magnetizes the electrons and prevents the

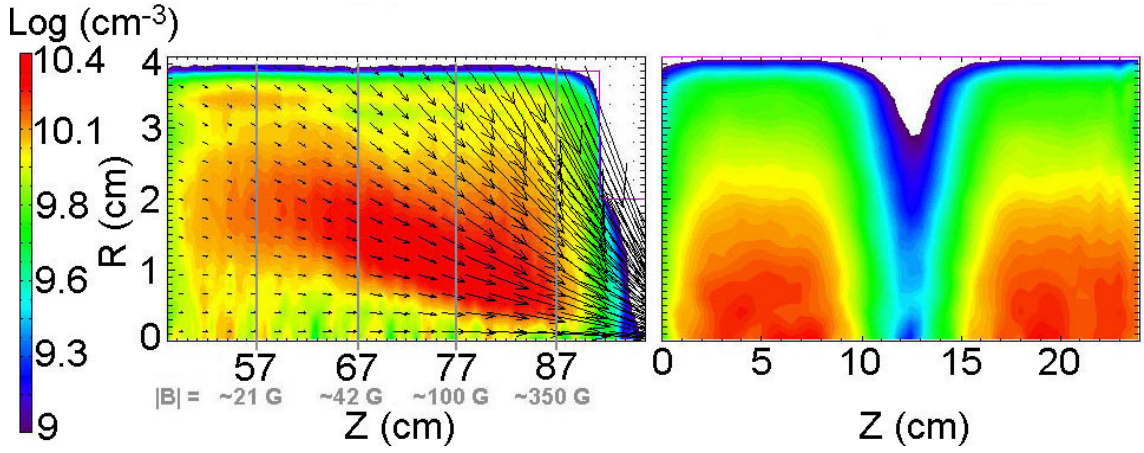

Figure 6.19: (Color) $\{r, z\}$ isocontours of peak ferroelectric plasma electron density (Log scale) in simulations involving the fringe-fields of the nearby $B_z = 80.5$ kG solenoid (left) and without any external magnetic field (right). Magnetic field vectors (black) and approximate magnitudes (gray) overlay the density in the former case. In the latter case, the 5 cm-long transverse port is present (refer to Sec. 5.2).

highest n_p^{drift} from being found on-axis near the downstream end of the source. The two plasma sources are able to effectively overlap in the entire region of interest so that a passing beam won't encounter a region where the expected $n_b > n_p$, except for any beam ions located at $r > 0.5$ cm within the final-focus solenoid.

Future work includes the repetition of the ion beam compression simulation mentioned earlier in this Section in order to investigate whether a difference in beam bunching is evident when using the more realistic plasma profiles, including the associated drift velocities, temperatures, and density variations, in contrast to the stationary plasmas of sufficient density and temperature used earlier. When the beam enters the solenoid, it has a radius of $r_b \sim 0.7 - 0.8$ cm, but neutralization of the majority of the beam by the plasma ($r < r_p^{fill} = 0.5$ cm) diminishes the ability of the beam's self-fields to affect the compression. However, the effects of the supersonic $-\hat{z}$-streaming cathodic-arc plasma and magnetization of its electrons along field lines,

which are at significant angles to the entering beam in the fringe-field region (implying current neutralization may suffer), may cause emittance growth due to partial neutralization or instability and could deleteriously affect the compression physics.

6.5 Simultaneous focusing experiment using upgraded equipment

The maximization of the current density achieved at the simultaneous focal plane, in $2D$ $\{r, z\}$ particle-in-cell simulation, for a given set of experimental constraints using upgraded equipment (relative to existing NDCX hardware) has been carried out as follows [Sefkow *et al.*, 2007]. As in previous simulations, an $E_0 = 400$ keV K^+ beam with an initial radius and beam current of $r_b = 1.8$ cm and $I_0 = 80$ mA, respectively, is initialized with a Maxwellian $T_b = 0.2$ eV transverse and longitudinal temperature and convergence angle of $\Delta\theta_r = -22.5$ mrad at the injection plane $z = -30$ cm. The energy and current are approximately the peak values for an ion beam created using existing NDCX injector technology. According to Eqs. (1.1) and (1.2), the corresponding normalized effective emittance and perveance are 8.4×10^{-3} cm-mrad and 1.3×10^{-3}, respectively. The perveance of the initialized beam is approximately two orders-of-magnitude above the theoretical upper limit for quiescent ballistic beam propagation, and highlights the dominant role of space-charge and self-field effects for these parameters, as well as the need for high levels ($> 95\%$) of neutralization to achieve adequate focusing. The beam is injected into the drift chamber of radius $r_w = 3.8$ cm in the $+\hat{z}$ direction upstream of the 3 cm-wide acceleration gap, located from $z = -22$ cm to $z = -19$ cm, with an initial pulse length of 700 ns.

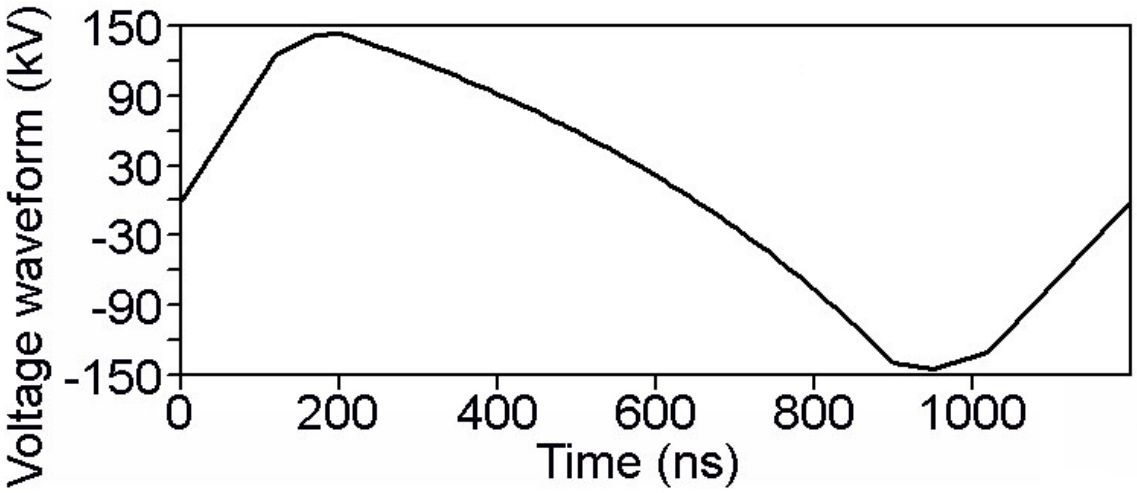

Figure 6.20: The "smooth" voltage waveform (refer to Sec. 4.7) for $E_0 = 400$ keV, $t_p = 750$ ns, and $f = 0.4$ is used to apply an axial velocity tilt to the $t_p = 700$ ns K^+ beam. An upgraded induction module is required to achieve this waveform.

The acceleration gap of the linear induction accelerator imposes a nearly linear velocity tilt to the beam using the voltage waveform illustrated in Fig. 6.20. The total Volt-second capability of the induction module's magnetic flux in this scenario is about twice as much as is presently available in the laboratory. An upgraded induction module expected to contain the requisite Volt-seconds is currently under construction. The injection timing is chosen so the beam encounters only the longitudinally-focusing part of the "smooth" voltage waveform (refer to Sec. 4.7), which is tailored to be ideal and approximately voltage-symmetric from $200 - 900$ ns, according to $E_0 = 400$ keV, $t_p = 750$ ns, and $f = 0.4$ in Eq. (4.22). After its axial velocity is modified, the beam subsequently drifts through a 2.5 m-long plasma column filled with background plasma of density $n_p^{drift} = 10^{11}$ cm^{-3} and temperature $T_p = 3$ eV.

Figure 6.21 displays a schematic of the device geometry, from $z = -30$ cm to $z = +250$ cm, as modeled in the LSP simulations. Also in the figure, note that the beam acquires an effective fractional tilt of $f = 0.37$, comparable to the intended

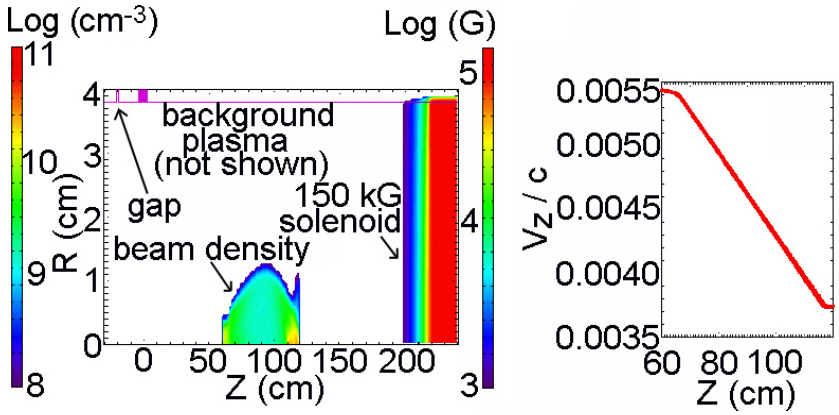

Figure 6.21: (Color) Snapshot of the simulation geometry during longitudinal compression. The model schematic (left) includes the acceleration gap, the ion beam density (Log scale), a uniform background plasma $n_p^{drift} = 10^{11}$ cm^{-3} extending from $z = 0$ cm to $z = +250$ cm (not shown), a 150 kG final-focus solenoid (Log scale) near the end of the chamber, and a high density plasma $n_p^{foc} = 3 \times 10^{14}$ cm^{-3} (not shown) within the solenoid. The $\{z, v_z\}$ beam phase space plot at the same time (right).

tilt $f = 0.4$, due to the long initial pulse length. A multi-Tesla, final-focus solenoid filled with plasma is modeled near the end of the drift region in order to ensure that the ion beam undergoes transverse focusing to a sub-millimeter spot size coincident with the longitudinal focal plane, as discussed in Sec. 6.3. As the beam transversely focuses due to the $v_\theta \times B_z$ Lorentz force, the beam density increases quadratically with decreasing beam radius, and enough plasma must be provided to adequately satisfy $n_p >> n_b$ for neutralization of the beam's rapidly growing charge and current density. For this reason, the initial density of the plasma in the final-focus solenoid is higher than the bulk plasma initialized throughout the drift region ($n_p^{foc}/n_p^{drift} \sim 10^3$), in order to accommodate the fast rise in beam density found near the simultaneous transverse and longitudinal focal plane. The proposed focal plane plasma achieves a density of $n_p^{foc} = 3 \times 10^{14}$ cm^{-3} within the final-focus solenoid and represents another major equipment upgrade in these design simulations (the approximate maximum

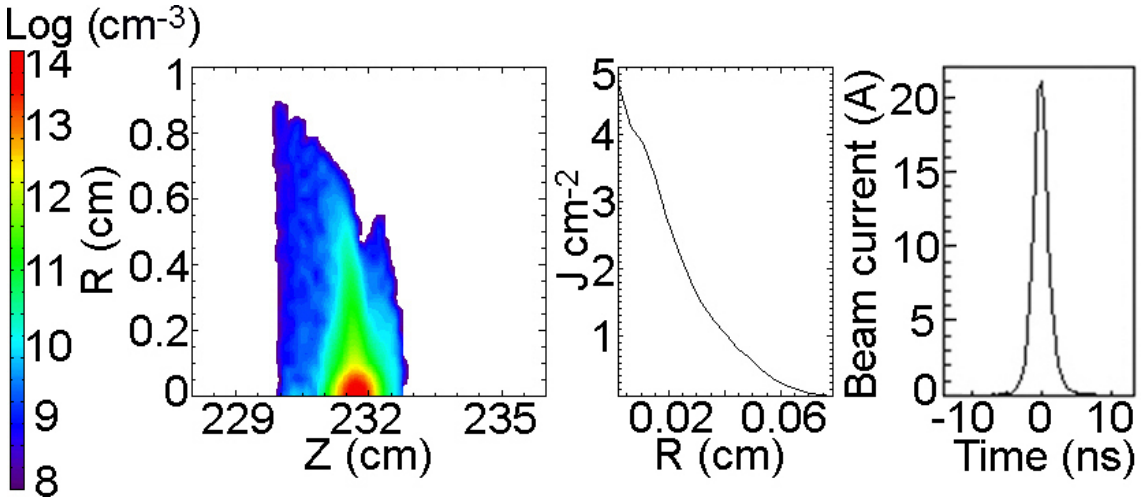

Figure 6.22: (Color) $\{r, z\}$ isocontour of beam density n_b^{foc} (Log scale, left), cumulative energy deposition profile $E_{dep}(r)$ (center), and beam current $I_b(t)$ (right) at the simultaneous focal plane, within a 150 kG final-focus solenoid. The time coordinate has been reset so that $t = 0$ coincides with peak compression [Sefkow *et al.*, 2007].

densities provided by the ferroelectric and cathodic-arc plasma sources are 10^{11} cm^{-3} and 10^{12} cm^{-3}, respectively). Also, such a separation of drift and focal plane plasmas allows smaller densities to be used upstream of the focal plane, where higher plasma densities are not required due to the significantly larger beam radii during neutralized drift compression.

The simulation demonstrates that background plasma of sufficiently high density almost completely neutralizes the charge and current of the compressing ion beam for these parameters, facilitating large amounts of current density compression at the simultaneous focal plane. As presented in Fig. 6.22, a peak beam current of approximately $I_b^{max} = 21$ A with a full-width, half-maximum pulse duration of $t_{fwhm} = 2.3$ ns is achieved at an axial location of $z = +232$ cm, about $L_d \sim 2.5$ m downstream of the acceleration gap for the prescribed beam parameters and "smooth" voltage waveform [Sefkow *et al.*, 2007]. The current compression ratio is determined to be

approximately 260. The radius of the beam as it enters the solenoid in this case is approximately $r_b = 0.7$ cm. The strongest solenoid used in simulation is $B_z = 150$ kG in on-axis magnitude and, when properly situated near the intended simultaneous focal plane, results in a minimum beam radius ($1/e$) of $r_b \sim 0.28$ mm, with a peak on-axis beam density of approximately $n_b^{foc} \sim 1.5 \times 10^{14}$ cm^{-3}, as shown in Fig. 6.22, in a background plasma $n_p^{foc} = 3 \times 10^{14}$ cm^{-3} and $T_p = 3$ eV. The 150 kG solenoid is the third major upgrade not currently available for experiments. The current density of such a highly compressed charge bunch is found to increase more than a factor of 10^5 compared to the initial current density in a focal distance of just a few meters. In particular, the cumulative on-axis peak energy deposition at the simultaneous focal plane increases to almost $E_{dep}^{peak} = 5$ J cm^{-2} over the duration of the pulse.

The peak on-axis current density of the charge bunch at focus in this case is approximately $J_z = 3.4$ kA cm^{-2} (overall compression of 2.7×10^5), assuming an average $E_0 = 400$ keV, and the associated on-axis intensity is approximately 1.34 GW cm^{-2}. In order to provide physical insight and assess the heating capability of ion beams delivering such high intensities for upcoming warm dense matter experiments, $2D$ hydrodynamic simulations using the HYDRA code [Marinak *et al.*, 2001] are used to model the interaction of the simultaneously compressed beam with a 10% solid-density *Al* foam target [Barnard *et al.*, 2007]. The simulations show that the temperature of a thin 10 μm target would reach the highly-coupled warm dense matter regime of $T_{targ} = 2.2$ eV before hydrodynamic disassembly; electromagnetic, fully-implicit LSP simulations corroborate the hydrodynamic estimates of expected target heating [Welch *et al.*, 2007]. Since the initial beam pulse length is $t_p = 700$ ns in this case, and the waveform in Fig. 6.20 is timed to affect the exact amount of

intended charge bunch to undergo longitudinal compression, pre-heat of the target due to pre-pulse (or, pedestal current) is essentially non-existent, and only chromatic aberration from beam temperature contributes to beam current impinging the target before the peak current of the pulse arrives.

When the voltage waveform is nearly ideal (as in this simulation involving an upgraded induction module, final-focus solenoid, and focal plane plasma source), beam temperature, finite-size acceleration gap geometry, and aberration in the final-focus solenoid limit the achievable minimum pulse length and radius at the longitudinal focal plane, as discussed in Secs. 4.7 and 6.3. Also, the results presented in this Section agree with the trends reported in Figs. 4.27 and 4.30, and Tables 4.2 and 4.3. From Table 4.3, a compression ratio of 260 with $t_{fwhm} = 1.0$ ns was achieved at $L_d \sim 1$ m for the "smooth" waveform using the similar parameters $E_0 = 400$ keV, $t_p = 300$ ns, and $f = 0.4$. Here, the initial pulse length is extended to $t_p = 750$ ns, although the beam itself and the pertinent portion of the waveform are only $t_p = 700$ ns long, due to the constraint of voltage symmetry. Recall from Section 4.7.3, that the waveform symmetry requirement arose from a desire to take the most advantage of the available voltage for a given experimental limit (usually hold-off requirements, or Volt-second limitations in the induction module). The longer initial pulse length was chosen in order to increase the achieved fractional tilt ($f = 0.37$, from an intended $f = 0.4$), compression ratio, and integrated total charge at the focal plane for target experiments, at the cost of a longer drift length ($L_d \sim 250$ cm), longer required plasma source, and increased aberration at focus ($t_{fwhm} = 2.3$ ns). Furthermore, waveform accuracy to the ideal is usually sub-optimal in practice near the maximum and minimum voltages, so the use of a longer initial pulse length is a way to (1) increase the

amount of overlap time between the experimental and ideal waveforms, (2) decrease the level of accuracy required per unit time, and (3) mitigate some of the defocusing effect mentioned in Sec. 6.1 by reducing the $-dV(t)/dt$ derivative.

Since shorter pulse lengths may be desired for certain warm dense matter experiments, the $t_p = 300$ ns and $f = 0.4$ waveform from Sec. 4.7.3 (refer to Table 4.3), which results in a similar amount of current compression but $t_{fwhm} = 1.0$ ns over the $L_d \sim 1$ m, may be attempted in future experiments involving waveforms that can mimic the ideal slope with greater fidelity. Note that the case described in Section 4.7.3 required the full, voltage-asymmetric waveform to achieve a compression ratio of 260. For the voltage-symmetric case, where the voltage late in time cannot decrease beyond the peak voltage multiplied by -1, an approximate 15% decrease in compression ratio is expected.

Other waveforms presented in Sec. 4.7 may also be attempted with the upgraded induction module, depending on the desired amount of compression, minimum pulse length, and drift length limitations. Larger fractional tilts may be used, and voltage hold-off issues can be side-stepped, by lengthening the gap by a few cm to reduce the electric field below 100 kV/cm. Simulations of such slightly larger gaps showed relatively little change in longitudinal compression. Alternatively, additional dipole magnetic fields and/or dielectric insulators can be used in the acceleration gap to increase hold-off capabilities and decrease electric field gradients, while reducing the probability of electron emission.

Aberration effects from the finite-size acceleration gap and final-focus solenoid play an important role in determining the upper limit of achievable current density compression when a near-ideal voltage waveform is employed. In addition, the choice

of the neutralizing background plasma profiles as well as the strength and position of the final-focus solenoid are critical factors involved in the realization of large compression factors.

6.6 Dependence on focal plane plasma and final-focus solenoid

In the previous Section, the final-focus solenoid was assumed to be entirely filled with the requisite high-density plasma throughout the region of high magnetic field. A variety of means exist to fill a strong, multi-Tesla solenoid with plasma. As discussed and modeled in Secs. 5.3 and 6.4, one proposed method is to longitudinally inject the plasma with an upstream supersonic directed velocity into the high-field region from the downstream end of the strong magnet. The plasma would then partially fill the solenoid in a certain amount of time and the compressing ion beam would enter the final-focus solenoid from the upstream end.

Recall that simulations indicate a high-field solenoid can become partially-filled by a high-density plasma with characteristics similar to the existing filtered cathodic arc plasma source, in order to provide the necessary charge and current neutralization of the compressing beam, as shown in Sec. 5.3. For the parameters under consideration, the plasma flow equilibrates and fills the solenoid out to a radius $r_p^{sol} = 0.6$ cm after approximately $12\,\mu$s, largely by flowing along magnetic field lines. Most particles are reflected away from the high-field region, but a minority of the plasma particles with large enough $v_\parallel/v_\perp$ velocity component ratios are able to fill the strong final-solenoid

near the $r = 0$ axis. In the process, the plasma density is compressed by an order-of-magnitude, which helps to achieve the background plasma density requirements for neutralization near the simultaneous focal plane.

The simultaneous focusing simulations carried out in the previous Section need to be considered again in order to investigate whether a difference in the beam's compression is evident when the final-focus solenoid is only partially-filled with plasma to a certain radius, which may be less than the beam's radius at the entrance to the solenoid. This case is under consideration here, since an ion beam entering with a smaller radius than the fill value would not encounter a region free of plasma. The simulation of overall current density compression exceeding a factor of 10^5 in a few m are repeated, except with the high-density plasma present in the final-focus solenoid only to the fill radius $r_p^{sol} = 0.6$ cm. The same compression and energy deposition results are obtained when the final-focus solenoid is partially-filled with high-density plasma compared to the fully-filled case when the simultaneous focal plane is located within the length of the solenoid. In both cases, realistic plasma temperature profiles and drift velocities related to the solenoidal plasma injection process were ignored. Evidently, electrons can become trapped in the beam potential in some situations and be dragged by the beam ions into the solenoid along the magnetic field lines such that quasi-neutrality is maintained in the region initially absent of plasma. Whether electrons are dragged along field lines depends on the strength of the solenoid as well as the beam characteristics. In some instances, the beam manipulation throughout the system ensures that the beam radius enters the final-focus solenoid at small radius by design; in such a configuration, neutralization of the on-axis beam space-charge by the high density plasma greatly diminishes the ability of the self-fields to affect

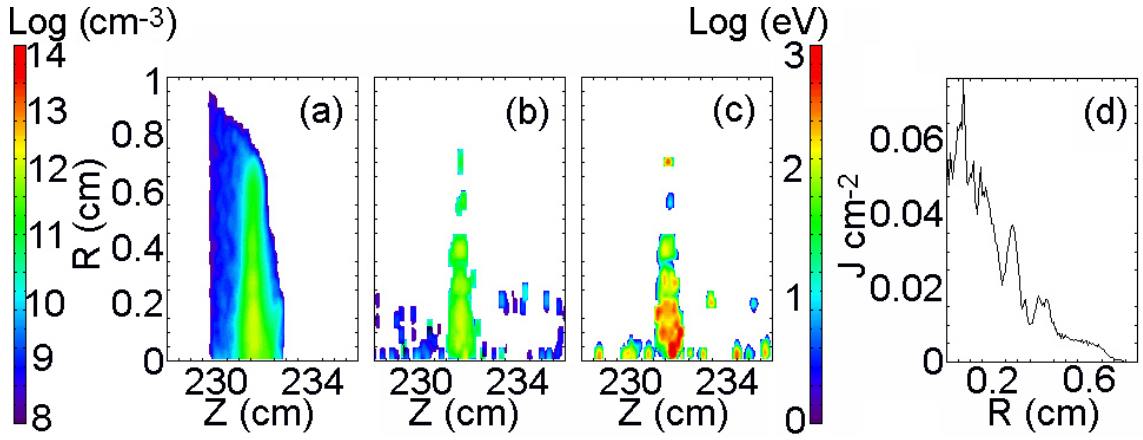

Figure 6.23: (Color) Greatly reduced compression occurs when the final-focus solenoid entirely lacks initial plasma, as evident from the beam density n_b (a), plasma electron density n_{pe} (b), plasma electron temperature T_{pe} (c), and total beam energy deposition $E_{dep}(r)$ through the intended focal plane $z = +232$ cm (d). Significant stagnation and electron heating have already taken place at the location of the intended focal plane. The Log density scale is the same as in Fig. 6.22.

the compression (or drag electrons into the solenoid), since the majority of the beam enters the final-focus solenoid within the plasma fill radius.

It is important to note the difference between final-focus solenoids partially-filled with plasma and not filled with any plasma. Simulations entirely lacking plasma in the region of the simultaneous focal plane show that the bulk of the plasma electrons do not sufficiently penetrate into the $B_z = 150$ kG region and the beam does not compress well, due to the very strong defocusing space-charge forces from with the self electric fields of the partially neutralized beam. The potentials associated with the unneutralized beam densities and radii of interest here are in the tens to hundreds of kV range. In the no-fill limit, only a small population of electrons are pulled into the high field solenoid by the beam's space-charge, as shown in Fig. 6.23. Since the beam is still upstream of the intended focus when it enters the solenoid, the beam will not be able to achieve the intended minimum radius and maximum density at

the focal plane because the trapped electrons satisfy $n_{pe} \sim n_b$ at the entrance to the solenoid and, as the beam continues to compress, the trapped electrons also compress and therefore heat substantially. The electron temperatures associated with such a trapped population are shown in simulations to rise to $0.1 - 1$ keV as the beam tries to focus; the temperatures are higher than would be expected from adiabatic compression, therefore compression and self-field effects from partial neutralization cause electron heating as well as beam emittance growth. The beam's transverse and longitudinal focusing trajectories stagnate under such circumstances due to the strong self-fields resulting from insufficient neutralization by the hot electron population over the remaining distance to focus ($\Delta z > 10$ cm), the beam expands before reaching the intended focal plane, and optimal compression factors are not realized. Such beam stagnation and electron heating, as illustrated in Fig. 6.23, occurs when the simulation described in Sec. 6.5 is attempted without any neutralizing plasma initialized in the final-focus solenoid.

The strength and axial placement of the multi-Tesla final-focus solenoid are two important factors for obtaining optimal compression, since a precise $\mathbf{B}_{sol}(r, z)$ profile is responsible for the coincident transverse compression to the longitudinal focal plane, given a set of beam parameters and sufficient neutralization provided by the background plasma. Although attractive for high amounts of transverse compression, a $B_z = 150$ kG magnetic field situated at the focal plane (which also houses the target) may introduce a number of complications, including undesirable side effects for diagnostics. Therefore, the simulation described in the previous Section is repeated for a variety of final-focus solenoid choices involving the length and strength of the solenoid, including reductions in peak magnetic field magnitude and upstream shifts

Table 6.3: Final-focus solenoid strength and axial placement configurations.

Case	B_z^{peak}	B_z^{foc}	$\mathbf{z}^{sol}$	l^{sol}	n_b^{foc} (cm^{-3})	r_b^{foc}	E_{dep}^{peak}
1	150 kG	131 kG	-5 cm	16 cm	1.5×10^{14}	0.28 mm	5.0 J cm^{-2}
2	150 kG	10 kG	-10 cm	6 cm	1.2×10^{14}	0.37 mm	3.5 J cm^{-2}
3	100 kG	98 kG	-5 cm	26 cm	9×10^{13}	0.46 mm	2.6 J cm^{-2}
4	100 kG	4 kG	-13 cm	10 cm	7×10^{13}	0.53 mm	2.0 J cm^{-2}
5	50 kG	46 kG	-15 cm	40 cm	6×10^{13}	0.49 mm	1.8 J cm^{-2}
6	50 kG	1.5 kG	-22 cm	26 cm	5×10^{13}	0.55 mm	1.4 J cm^{-2}

in axial locations. Simulations involving both types of change increase the achievable spot size and result in reduced cumulative energy deposition profiles and target heating estimates at the simultaneous focus. The axial positions of the solenoids are moved farther upstream in order to reduce the local magnetic (fringe) field values in the region of the simultaneous focal plane. The transverse compression of the beam is not as large in such cases, but sub-mm spot sizes can still be realized.

Table 6.3 categorizes various illustrative final-focus solenoid axial placement configurations by peak solenoidal magnetic field strength (B_z^{peak}), field strength at focus (B_z^{foc}), axial location of the center of the solenoid relative to the focal plane ($\mathbf{z}^{sol}$), total length of the solenoid (l^{sol}), peak on-axis beam density at focus (n_b^{foc}), minimum beam radius ($1/e$) at focus (r_b^{foc}), and peak on-axis energy deposition at focus (E_{dep}^{peak}). All of the final-focus solenoids under consideration have radii $r^{sol} = 3.8$ cm. The odd-numbered cases correspond to solenoids that are situated at the focal plane, whereas the even-numbered cases employ solenoids that do not reside at the focal plane. In other words, the focal plane is chosen to either exist within the interior of the solenoid or downstream of it. The first case in Table 6.3 is the result for the simulation first described in Sec. 6.5. The cumulative beam energy deposition profiles

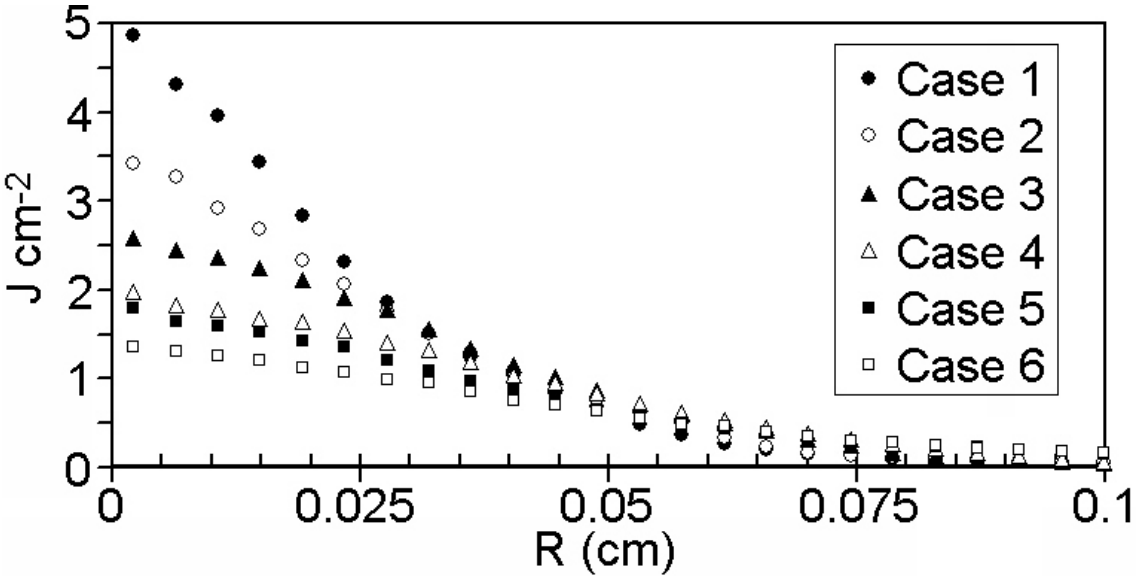

Figure 6.24: Cumulative beam energy deposition profiles $E_{dep}(r)$ for the six cases reported in Table 6.3: 150 kG solenoid at the focal plane (solid circles), 150 kG solenoid upstream of the focal plane (open circles), 100 kG solenoid at the focal plane (solid triangles), 100 kG solenoid upstream of the focal plane (open triangles), 50 kG solenoid at the focal plane (solid squares), and 50 kG solenoid upstream of the focal plane (open squares). All cases contain stationary background plasma $n_p^{drift} = 10^{11}$ cm^{-3}, $n_p^{foc} = 3 \times 10^{14}$ cm^{-3}, and $T_p = 1$ eV.

at the simultaneous focal plane for each of the six cases are shown in Fig. 6.24.

In general, optimization of the beam's trajectory as it enters the final-focus solenoid plays an important role in achieving large amounts of energy deposition for warm dense matter and heavy ion fusion applications. For given experimental constraints, optimal compression depends on many parameters. In the space-charge-dominated limit, the beam's trajectory is especially sensitive to conditions involving nonneutral beam transport, such as transport from the source injector to the exit of the acceleration gap (after which the beam encounters neutralizing plasma). As discussed in Secs. 4.7 and 6.1, the finite-size acceleration gap time-dependently alters the transverse trajectories of the beam ions as the longitudinal velocity tilt is applied and

prevents the beam from entering the final-focus solenoid with a constant temporal radial profile; as mentioned in Sec. 6.3, the velocity tilt can contribute to transverse focusing aberration in the final-focus solenoid. Therefore, the two types of focusing aberration, transverse and longitudinal, are coupled. It is desirable for the beam to have a small radius as it enters the final-focus solenoid in order to reduce transverse focusing aberration originating from the velocity tilt (refer to Sec. 6.3), as well as minimize the amount of beam which encounters regions lacking high-density plasma. Consequently, the beam trajectory needs to be carefully selected for a given acceleration gap geometry and waveform, drift length, and final-focus solenoid placement, in order to balance the sources leading to decreased compression factors and increased final spot sizes and pulse lengths at focus. Both the longitudinal and transverse dynamics are important in determining the optimal compression scenario, especially in circumstances involving such highly compressed ion beams propagating in plasmas whose densities do not necessarily satisfy $n_b \ll n_p$ at all locations in experiments. The sensitivity to so many beam, plasma, and external force parameters is striking.

The presence of the strong magnetic field from the final-focus solenoid affects the neutralization dynamics of the plasma by greatly restricting radial electron movement across field lines, due to their heavy magnetization. The energetic ion beam does not share the same problem because of its high directed velocity and ion mass. Therefore, greater plasma electron densities are required to neutralize the same beam within and around a final-focus solenoid because the electrons can generally only flow along field lines. The simulation presented in Sec. 6.5 and referred to as Case 1 in Table 6.3 is repeated, except the density of the plasma within the final-focus solenoid is allowed to decrease, while the initial plasma temperature remains $T_p = 1$ eV, in

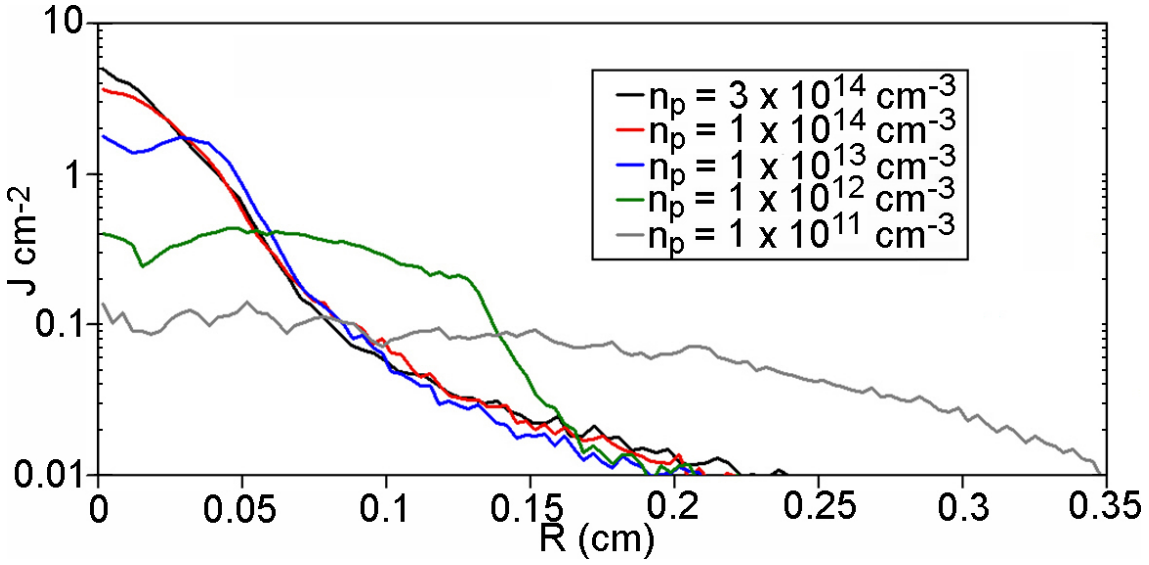

Figure 6.25: (Color) Cumulative beam energy deposition profiles $E_{dep}(r)$ (Log scale) through the intended simultaneous focal plane for $n_p^{foc} = 3 \times 10^{14}$ cm^{-3} (black), 10^{14} cm^{-3} (red), 10^{13} cm^{-3} (blue), 10^{12} cm^{-3} (green), and 10^{11} cm^{-3} (gray). All cases contain stationary drift length plasma $n_p^{drift} = 10^{11}$ cm^{-3} and $T_p = 1$ eV.

order to observe the associated reduction in cumulative energy deposition due to insufficient neutralization. Recall that the expected peak beam density is $n_b^{foc} = 1.5 \times 10^{14}$ cm^{-3} at the simultaneous focal plane for the case of $n_p^{foc} = 3 \times 10^{14}$ cm^{-3} (and is also confirmed by the perfectly neutralized beam case). The results of the plasma density parameter study for this case are plotted as radial cumulative energy deposition $E_{dep}(r)$ profiles through the intended simultaneous focal plane $z = +232$ cm in Fig. 6.25.

As shown in Fig. 6.25, even a modest reduction in plasma density within the final-focus solenoid, where the focal plane resides, from $n_p^{foc} = 3 \times 10^{14}$ cm^{-3} to 10^{14} cm^{-3} results in a decrease in peak energy deposition from 5 J cm^{-2} to 3.69 J cm^{-2}, since the peak expected beam density exceeds the background plasma density in this case. Further decrease in plasma density to $n_p^{foc} = 10^{13}$, 10^{12}, and 10^{11} cm^{-3} causes

the cumulative energy deposition to likewise fall as E_{dep}^{peak} = 1.77, 0.40, and 0.14 J cm^{-2}, respectively, which approximately satisfies a square root dependence on plasma density for cases involving insufficient neutralization levels. Such a result is expected since the neutralization physics depends on the Debye length and $\lambda_D \sim n_p^{-0.5}$ for fixed T_p. Lastly, inhomogeneous radial structures in the beam and plasma densities are apparent in the cases of inadequate neutralization, due to the complex beam-plasma interaction in the presence of the beam's self-fields, including electron inertia effects. The insufficient neutralization case involving $n_p^{foc} = 10^{12}$ cm^{-3} will be presented in greater detail in Sec. 6.8.

6.7 Reverse-aligned solenoid configuration

As mentioned in the previous Section, a wide range of final-focus solenoid design parameters are considered, depending on engineering limitations (e.g. length and strength of the solenoid) and other considerations, such as whether the simultaneous focal plane should be chosen to exist within the interior of the solenoid or not. Two important questions concerning final-focus solenoid design configurations are: (1) How much magnetic field is acceptable at the simultaneous focal plane (where a target would reside); and (2) How much target-impinging background plasma flux can be tolerated in warm dense matter experiments. The diagnosis of some target parameters, such as electrical conductivity or resistivity, will be greatly affected by magnetic fringe-fields and there may be a desire for some experiments to have no remnant magnetic field at the location of the simultaneous focal plane.

An alternative final-focus solenoid concept [Friedman, 2006] under consideration for achieving simultaneous transverse and longitudinal bunch compression involves a

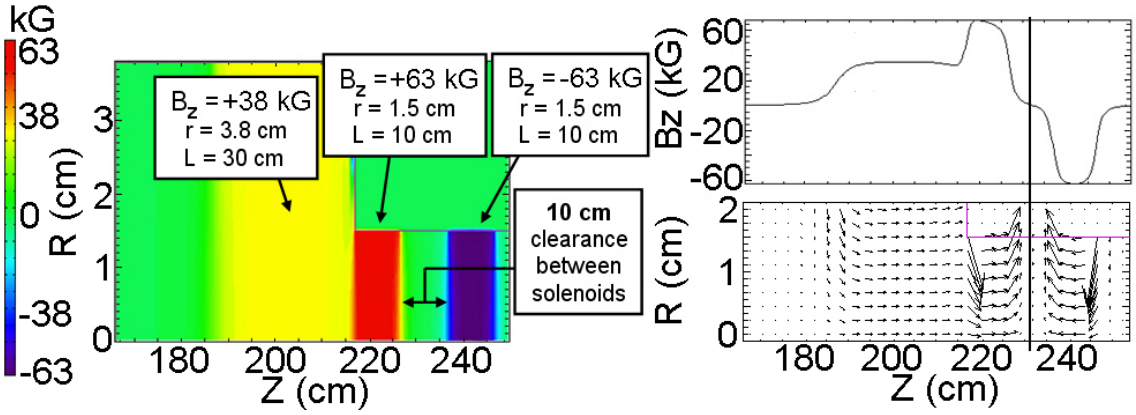

Figure 6.26: (Color) Reverse-aligned solenoid configuration in PIC simulation presented as $\{r, z\}$ isocontours of B_z (left), B_z slice through the $r = 0$ axis (top right), and $\{r, z\}$ **B** vector plot (bottom right). The vertical black lines demarcate the location of the intended simultaneous focal plane, where a target would reside.

configuration of three multi-Tesla solenoids. As illustrated in Fig. 6.26, two identical solenoids ($B_z = 63$ kG, $r^{sol} = 1.5$ cm, $l^{sol} = 10$ cm) are positioned in a reverse-aligned configuration, meaning the direction of the magnetic field of the second downstream solenoid is reversed relative to the first upstream solenoid. The location of the simultaneous focal plane is $z = +232$ cm, and is chosen to exist in between the reverse-aligned solenoids at the location of the magnetic field null. The third solenoid ($B_z = 38$ kG, $r^{sol} = 3.8$ cm, $l^{sol} = 30$ cm) is positioned just upstream of the two solenoids and provides an initial convergent trajectory to the beam in order to reduce the beam's radius as it enters the first of the reverse-aligned solenoids. Note the reduction in chamber pipe radius, which alleviates some fabrication cost and mechanical support difficulties associated with high-field solenoids. In this particular case, the two reverse-aligned solenoids are positioned to provide 10 cm of axial clearance between them, in order to provide access for diagnostics and the target assembly. Note that this configuration

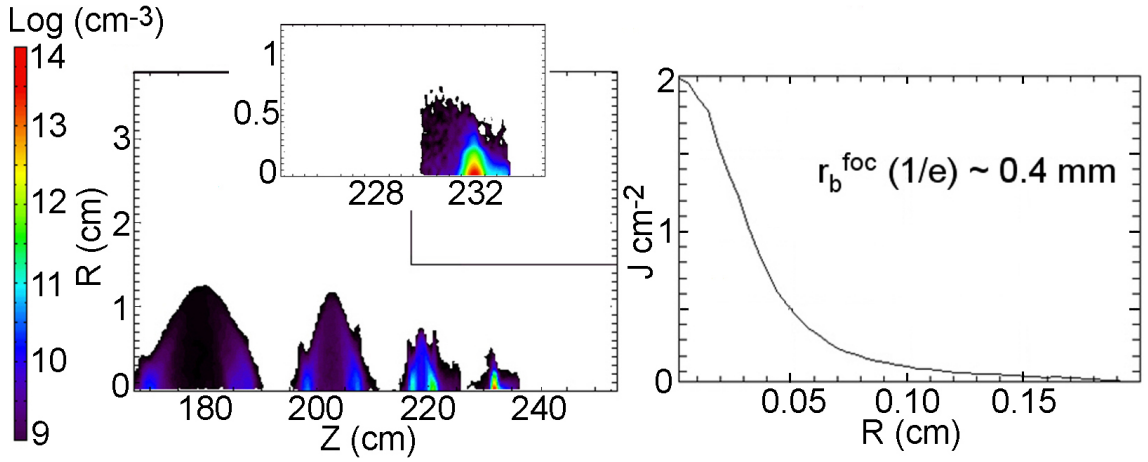

Figure 6.27: (Color) $\{r, z\}$ isocontour of n_b (Log scale, left) at various times before peak compression at the focal plane $z = +232$ cm, and the associated radial profile of the cumulative energy deposition $E_{dep}(r)$ (right). The beam reaches an on-axis peak density of $n_b^{foc} \sim 6.5 \times 10^{13}$ cm^{-3} (inset) with a minimum $r_b = 0.4$ mm.

represents one of many possible combinations, since optimization of the compressing trajectories for a given set of beam and system parameters also depends on the choice of solenoidal magnetic field strengths, lengths, and positioning, implying that technological and engineering limitations need to be considered.

Provided adequate neutralization, the intense ion beam is predicted by simulation to focus well and provide warm dense matter regime heating of the target, located at the focal plane within the region satisfying $\mathbf{B} \sim 0$. The simultaneous focusing beam simulation first described in Sec. 6.5 is executed in this magnetic configuration with the focal plane plasma $n_p^{foc} = 3 \times 10^{14}$ cm^{-3} and $T_p = 3$ eV within the intervening region between the reverse-aligned solenoids, and $n_p^{drift} = 10^{11}$ cm^{-3} elsewhere. As evident in Fig. 6.27, the radius of the center of the beam as it enters the upstream $B_z = 38$ kG solenoid is approximately $r_b = 1.4$ cm, whereas its value entering the first of the reverse-aligned solenoid pair is $r_b = 0.75$ cm and has a converging trajectory.

The peak on-axis cumulative energy deposition of the beam at the focal plane reaches a maximum of $E_{dep}^{peak} = 2.0$ J cm^{-2}, equivalent to the target heating provided by Case 4 in Table 6.3. Although, the minimum beam radius ($1/e$) is $r_b \sim 0.4$ mm here. An interesting positive side-effect of the proposed configuration is the increase in axial tolerance to $\Delta z = \pm 1$ cm in the allowed positioning of the target near the focal plane for the same cumulative energy deposition profile, which eases some experimental engineering restrictions; the origin of the effect is found in the increased level of longitudinal focal plane aberration, but balanced by better transverse focusing, which maintains smaller beam radii for a relatively longer axial distance.

Large-space and long-time simulations of plasma injection and flow into the reverse-aligned solenoid configuration are similar to the simulations of plasma flow into the single final-focus solenoid presented in Sec. 5.3, except for the change in magnetic configuration. Simulation results in Fig. 6.28 indicate that supersonic cathodic-arc plasma can be injected into the $B_z = 38$ kG solenoid in the downstream direction from the upstream end at $z = +170$ cm and $r = 3.8$ cm with an angle of approximately $\pi/8$ radians, and the first solenoid becomes partially-filled with plasma on-axis during flow equilibrium in a manner similar to the discussion in Sec. 5.3. In addition, the plasma will also penetrate into the first of the reverse-aligned solenoids with a slightly reduced radius ($r_p^{fill} \sim 0.5$ cm) relative to the fill-factor of the upstream, weaker solenoid ($r_p^{fill} \sim 0.7$ cm), due to the increased relative field strength. Since a magnetic null, or cusp, region is created in-between the reverse-aligned solenoids in this arrangement, a radially-divergent magnetic field profile is encountered by the injected plasma as it exits the first reverse-aligned solenoid. Subsequently, the substantial plasma flux is largely diverted to the wall of the beam pipe ($r_w = 1.5$ cm)

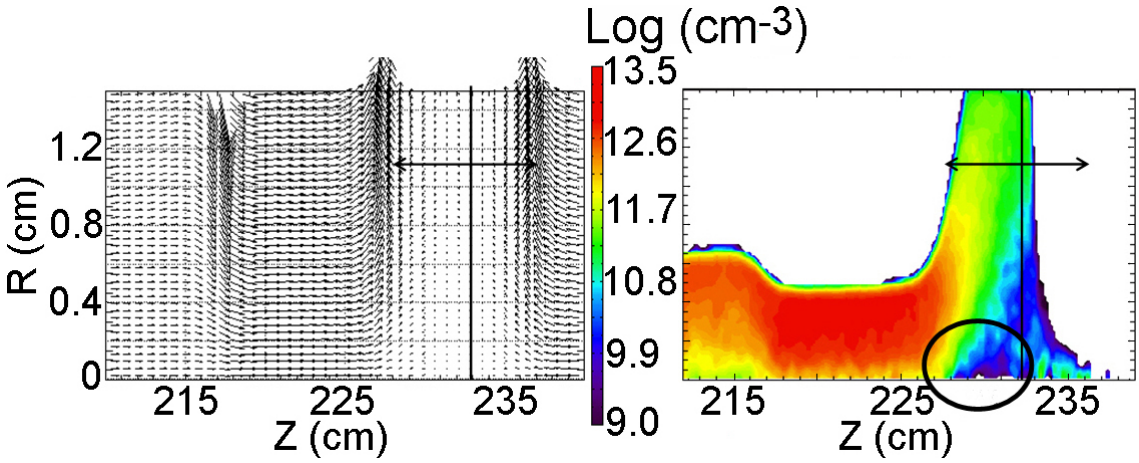

Figure 6.28: (Color) $\{r, z\}$ **B** vector plot (left) and isocontour of n_p at flow equilibrium (Log scale, right) near the simultaneous focal plane $z = +232$ cm. The horizontal and vertical black lines demarcate the locations of the 10 cm axial clearance between the reverse-aligned solenoids and the intended focal plane, respectively. The black circle highlights the location of the "plasma gap", where the expected $n_b > n_p$.

and plasma does not penetrate into the second reverse-aligned solenoid farther downstream. Thus, background plasma flux pre-heat of the target in warm dense matter experiments using this configuration is expected to be greatly reduced compared to the single final-focus solenoid configurations discussed in this Chapter.

Simulations predict an additional beam neutralization challenge is presented by the reverse-aligned solenoid configuration: the divergence of the injected plasma flux to the wall as it exits the first reverse-aligned solenoid results in the formation of a "plasma gap" near the end of the first reverse-aligned solenoid to the focal plane, as indicated in Fig. 6.28, where the expected beam density n_b would greatly exceed the injected background plasma density n_p. Simulation results in Fig. 6.29 of beam compression in the presence of the realistically-injected plasma profile show that, although the beam continues to focus by trapping some electrons as it exits the first reverse-aligned solenoid, the beam does not maintain charge and current neutrality

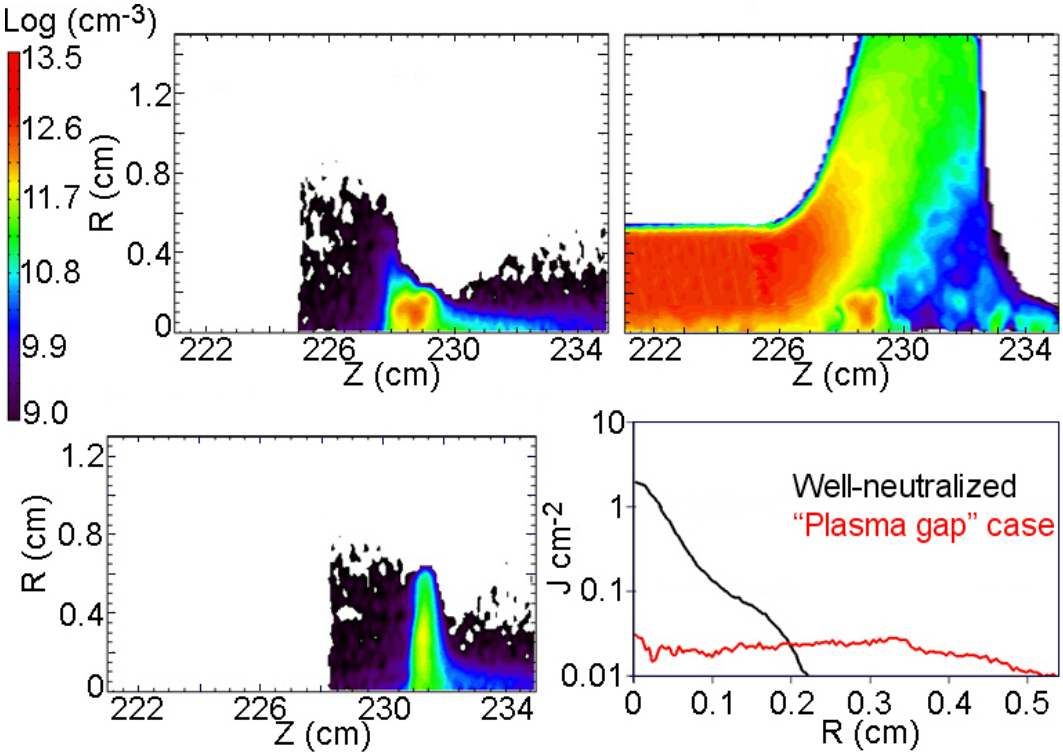

Figure 6.29: (Color) $\{r, z\}$ isocontours of n_b (top left) and n_{pe} (top right) upstream of the intended focal plane near $z = +229$ cm, and n_b (bottom left) near the intended focal plane $z = +232$ cm. All three density plots share the same Log scale. The cumulative energy deposition profile $E_{dep}(r)$ (bottom right) is substantially lower in the "plasma gap" case (red) compared to the well-neutralized case (black).

across the remaining approximate $\Delta z = 7$ cm to the focal plane in such a "plasma gap" region. In fact, the beam compression stagnates due to its intense self-fields once the n_b rises to the level of the local n_p in the "plasma gap", the transverse and longitudinal focal planes no longer coincide (and are not located at the $\mathbf{B} \sim 0$ point), the plasma locally heats, and a large reduction in the beam's energy deposition profile at the intended target/focal plane is the ultimate result. Not only does the radial focusing suffer, but the longitudinal compression decreases from 260 to 220 with an

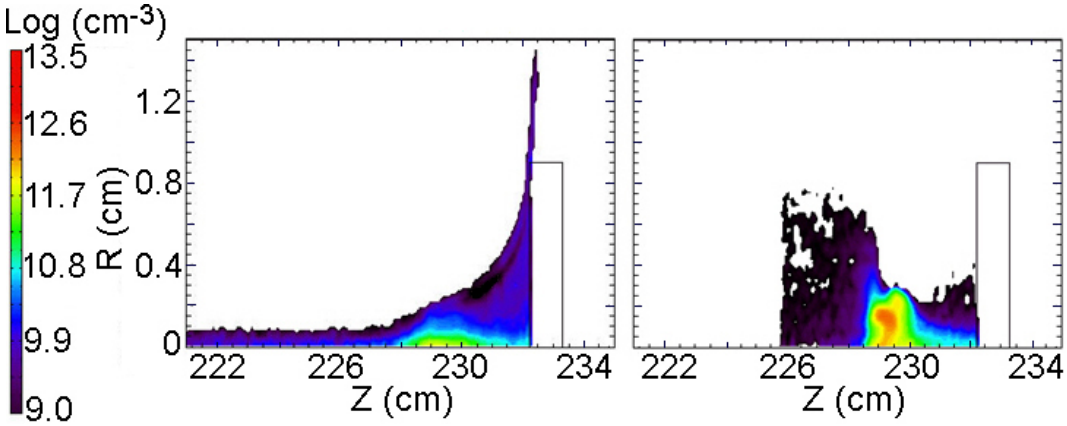

Figure 6.30: (Color) $\{r, z\}$ isocontours of emitted electron density (left) from the beam-target interaction and the resulting n_b (right) upstream of the intended focal plane near $z = +229$ cm. The insufficiently-dense emission electron dynamics are space-charge-limited and restricted by the magnetic fringe-field topology near the target (white rectangle at $z = +232$ cm). The plots share the same Log scale.

increase in pulse length from $t_{fwhm} = 2.3$ ns to 2.8 ns. The focusing trajectories stagnate near $z = +227$ cm, 5 cm upstream of the focal plane, because the neutralization levels provided by the plasma drop to approximately $75 - 85\%$ in this case, and the beam expands under its own self-electric fields.

Further simulations involving the realistically-injected plasma profiles suggest the liberated electrons from the beam-target interaction during target pre-heat will not be adequate to provide the extra neutralization the beam requires in the "plasma gap" region, as illustrated in Fig. 6.30, in order to help realize the intended amount of simultaneous focusing. A Child-Langmuir field-stress model for the electrons from the target, using 100 ns of beam pre-heat, indicates that not enough electron density can be created and transported under space-charge limitations across the $\Delta z = 7$ cm gap region upstream of the focal plane, where they are needed before the arrival of the beam, and the role of the magnetic field configuration on the dynamics of the

additional electron supply is significant.

Additional high-density plasma in the gap region, from $\{r, z\} = \{0, +226\}$ cm to $\{0.5, +232\}$ cm, is required to provide adequate beam neutralization and recover the expected, near-ballistic compression result for a well-neutralized beam, by maintaining a background n_p which is greater than the n_b at all locations in space and time. Simulations suggest a minimum safety factor of $n_p \geq 3\, n_b$ for a constant plasma density profile in the mentioned vicinity of the focal plane; the case for a constant plasma density profile satisfying $n_p = n_b$ suffers a reduction in peak energy deposition by approximately $15 - 20\%$. Possibilities under consideration for additional local plasma density sources include the stimulated desorption and ionization of adsorbed neutrals on the target and the use of a laser-ionized gas jet, among others. However, it is preferred that the plasma have a small stand-off separation distance from the target to prevent electrical connection.

The five noteworthy advantages of the reverse-aligned solenoid configuration are: (1) $\mathbf{B} \sim 0$ in the vicinity of the target/focal plane; (2) the focal plane is not within a final-focus solenoid (affording access by diagnostics, a target assembly, plasma production devices, etc.); (3) pre-heat of the target by supersonically-injected background plasma flux is significantly reduced by diverting the plasma to the wall; (4) short solenoids with $B_z < 65$ kG are arranged in a clever way to achieve warm dense matter-relevant transverse spot sizes (equivalent to the $B_z = 100$ kG Case 4 in Table 6.3, in this example); and (5) the beam's energy deposition profile is less sensitive to axial displacement (up to $\Delta z = \pm 1$ cm) relative to the target/focal plane than in the corresponding single final-focus solenoid case ($\Delta z < \pm 0.5$ cm). For these reasons, the reverse-aligned solenoid configuration is an attractive option for future

warm dense matter experiments, although the experimental challenge of maintaining beam charge and current neutralization in the "plasma gap" region requires additional research. Diagnosis of the plasma parameter profiles in space and time near the focal plane would be critical to understand and simulate the beam compression and neutralization dynamics in this configuration.

As discussed above, when the beam simultaneously focuses transversely and longitudinally near the end of the drift region, the beam density can increase to values above the plasma density if an adequate supply of background plasma is not provided, leading to a lack of charge and current neutrality. Under most circumstances, the beam compression stagnates (and optimal compression is not achieved) due to defocusing self-field forces and the plasma response to the partially-neutralized intense beam, which cannot continue to propagate quiescently. Therefore, the final spot radius of the charge bunch is highly dependent upon the electron population located in the vicinity of the focal plane.

6.8 Nonlinear beam-plasma interaction near simultaneous focus

Provided $n_p >> n_b$ throughout the drift region and near the focal plane, a plentiful supply of electrons is available to neutralize the charge and current of the beam ions, so the compression dynamics are mostly limited by the beam temperature and voltage waveform accuracy. In such cases, the dynamical evolution of the charge bunch can be determined exactly for a prescribed initial distribution function of the beam ions according to a recently developed kinetic formalism [Davidson and Qin, 2005] for

completely neutralized ion beams. However, the beam density can approach values of the plasma density depending on the particular experimental profiles provided for $n_p(\mathbf{r}, t)$, especially near the simultaneous focal plane, and the assumption of complete neutralization may become invalid.

In the case of an inadequate plasma supply, the beam density approaches and surpasses the plasma density during simultaneous compression, beam stagnation ensues due to self-field effects from partial neutralization, and nonlinear beam-plasma interaction occurs [Sefkow *et al.*, 2007]. The resulting amount of compression and energy deposition achieved by the ion beam in such cases will be substantially less than in the case of complete neutralization (refer to Fig. 6.25), primarily due to transverse defocusing by the beam's radial electric self-field for the parameters considered here. Moreover, the longitudinal compression deteriorates as well.

The beam-plasma interaction during simultaneous compression under conditions of inadequate neutralization by the background plasma is complicated by the presence of the external solenoidal magnetic field [Kaganovich *et al.*, 2005], which influences the neutralization process due to the strongly magnetized electrons. The simulation presented here uses the beam and solenoid parameters given in Sec. 6.6, where the background plasma density is $n_p = 10^{12}$ cm^{-3} with temperature $T_p = 1$ eV, and lower than the expected peak beam density at simultaneous focus. The unneutralized perveance and potential of the $E_0 = 400$ keV K^+ beam, associated with the maximum current $I_b^{max} = 21$ A at peak simultaneous compression, are approximately 3.4×10^{-1} [Eq. (1.2)] and -160 kV, respectively. The perveance is more than four orders-of-magnitude above the limit for ballistic charge bunch dynamics (refer to Chapter 1), and highlights the dominant role of space-charge and self-field effects, as well as the

need for high levels ($> 99\%$) of neutralization to achieve the desired focusing.

Simulations indicate that relatively high plasma densities are required to effectively neutralize the beam charge in the presence of a strong magnetic field. Neutralization of the beam becomes harder to provide in the presence of the 150 kG magnetic field, because the plasma skin depth (c/ω_{pe}) is much larger than the electron Larmor radius (ρ_{Le}) for the range of parameters needed here. In addition, the electron plasma frequency ω_{pe} can become comparable to the time scale of the beam density rate of change near simultaneous focus, which also hinders neutralization physics. Lastly, the axial length of the charge bunch decreases to $L_b \sim 0.32$ cm, which is approximately within an order-of-magnitude of its minimum expected radius ($1/e$) $r_b \sim 0.03$ cm near the intended simultaneous focal plane, and both are less the skin depth $c/\omega_{pe} \sim 0.5$ cm. The skin depth is the inertial length over which electrons can effectively neutralize the beam current. Therefore, adequate neutralization is harder to provide for a given amount of plasma, and is not expected in this scenario.

The peak achieved beam density and on-axis cumulative energy deposition occur at the stagnation location 2 cm upstream of the intended focus and are approximately $n_b \sim 1.7 \times 10^{13}$ cm^{-3} and 0.5 J cm^{-2}, respectively, about an order-of-magnitude lower than the expected values (refer to Fig. 6.25). The charge and current density neutralization levels of the beam decrease to the range $85-90\%$ at stagnation, due to the significant overabundance of ions, radial restriction on electron movement due to the large B_z, and low electron plasma frequency. Some of the beam potential becomes exposed as the beam tries to radially focus above $n_b > n_p$ without a plentiful electron population. Due to their restricted radial movement, the plasma electrons must try to neutralize the beam almost exclusively in the axial direction.

When local charge and current neutrality conditions are violated, strong collective excitations are generated in the plasma [Stix, 1992] by beam-plasma interactions in the presence of an applied solenoidal magnetic field. The simulations illustrate that the local charge and current densities can become large in regions where n_b exceeds n_p due to an overabundance of ions and electron dynamics. The beam's transverse and axial electric self-fields grow significantly (along with the beam's emittance), and oppose the transverse and longitudinal focusing trajectories of the ions. In this case, the self E_r field of the beam grows to a peak of approximately 52 kV/cm, whereas the self E_z field is approximately ± 10 kV/cm against the longitudinal compression of the beam. The electric fields resist the compression of the beam in both directions and mostly reduce the beam density through radial defocusing. As the compressing beam stagnates, the local charge and current densities become large as the beam tries to focus and becomes increasingly unneutralized, as plotted in Fig. 6.31, and the local plasma response is greatly modified by the presence of the growing self-fields, to which the background plasma responds via collective excitations, as well as substantial local plasma heating in some cases. In addition to the large ($\delta n/n_p^0 \sim 1-2$) charge density perturbation shown in Fig. 6.31, note the significant lack of current density neutralization near the simultaneous focal plane. The electrons are unable to effectively neutralize the dynamically compressing charge bunch, and significantly alter the surrounding global current density by causing many cm of negative and positive electron current upstream and downstream of the beam, respectively.

Once the beam compression has stagnated, the beam density and self-fields cease to grow and the plasma can support strong electrostatic ($\nabla \times \delta\mathbf{E} \approx 0$) and electromagnetic ($\nabla \times \delta\mathbf{E} \neq 0$) excitations, due to the large charge and current density

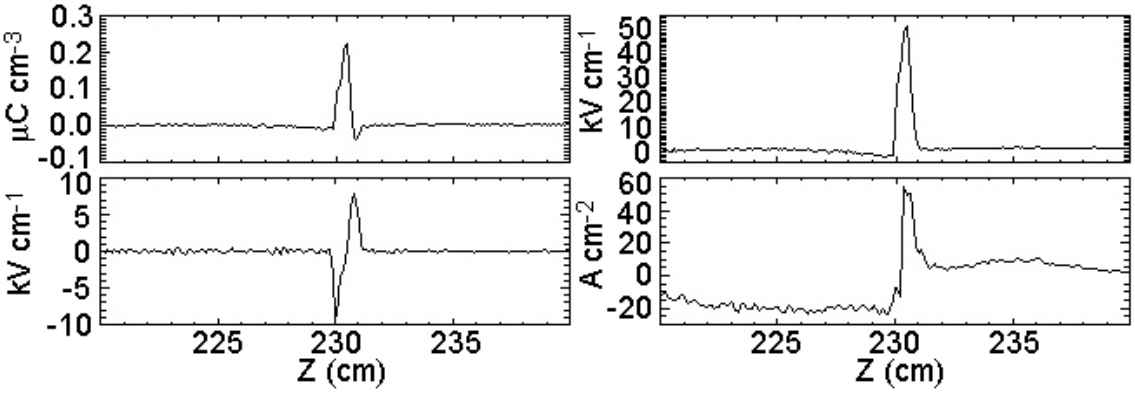

Figure 6.31: Local charge and current neutrality conditions are violated when $n_b > n_p$ near the simultaneous focal plane, providing a large perturbation to the background plasma. Slices of total charge density (top left), radial electric field (top right), axial electric field (bottom left), and axial current density (bottom right). All profiles are slices in z near the axis around the time of the ion beam pulse stagnation. The charge density perturbation approximately satisfies $\delta n/n_p^0 \sim 1 - 2$.

perturbations created during stagnation of the ion beam. The large, nonlinear charge perturbation created by the partial neutralization of the intense beam is responsible for exciting a strong electrostatic wave in the plasma. Figure 6.32 illustrates the effects of the wave on various parameters. The excitation frequency is observed to be $\omega \sim 8 \times 10^8$ rad s^{-1}, which lies within the range $\Omega_{ci} < \omega_{pi} < \omega \ll \omega_{pe} < \Omega_{ce}$. The wave propagates approximately perpendicular to the external $\mathbf{B}_{sol}$ in a carbon plasma ($m_e/m_i \sim 4.5 \times 10^{-5}$) with wave vector $k_\perp \approx 6.3 \times 10^3$ m^{-1}, and a small wave vector component parallel to the external $\mathbf{B}_{sol}$ that satisfies $k_\parallel/k_\perp \sim 4 \times 10^{-3}$ ($< \sqrt{m_e/m_i}$). The excitation appears to be a lower hybrid wave, which can propagate with arbitrary angle relative to the external magnetic field over a broad range of plasma parameters and exhibit a resonance cone [Fisher and Gould, 1971, Stix, 1992]. The solution corresponding to an electrostatic lower hybrid oscillation, whose wave properties depend on both the plasma electron and ion inertial dynamics, is obtained from the

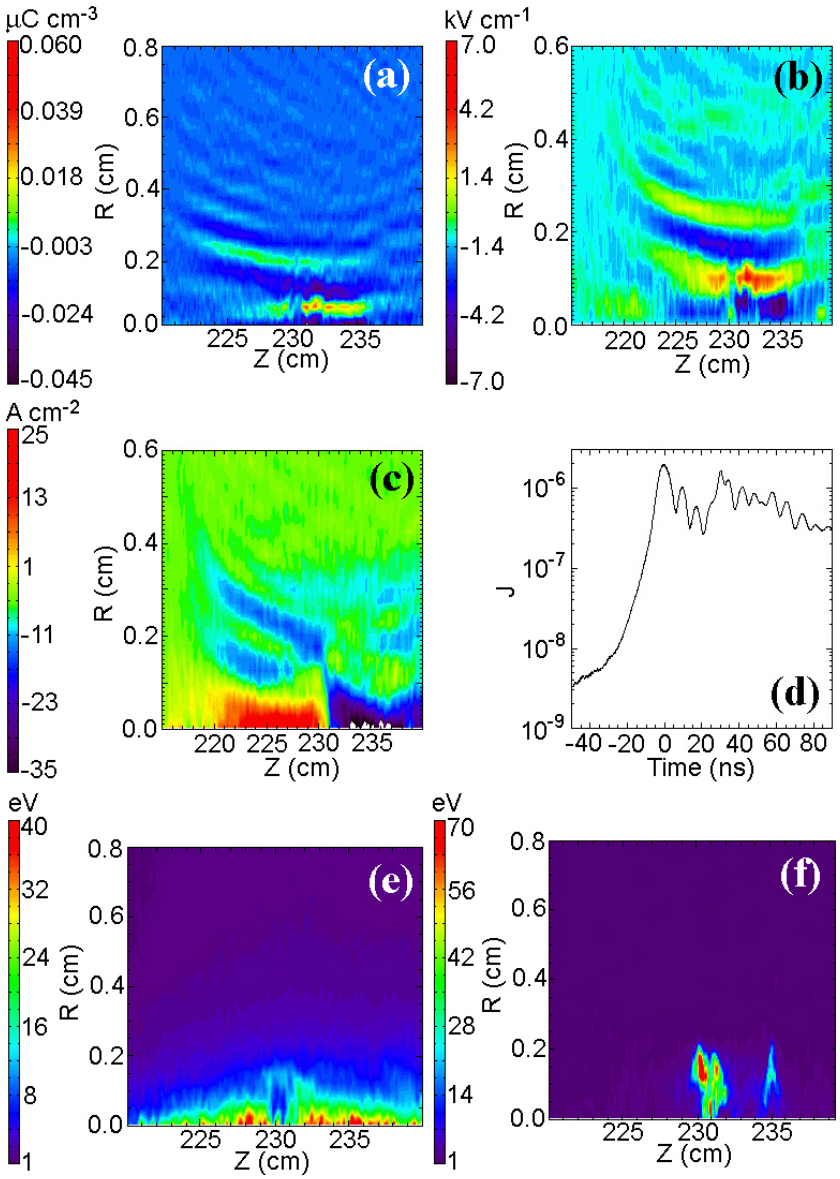

Figure 6.32: (Color) An electrostatic ($\nabla \times \delta\mathbf{E} \approx 0$) wave excited by the beam-plasma interaction for the case $n_b > n_p$ is evident after the ion beam stagnates and passes the intended focal plane. $2D$ $\{r, z\}$ isocontours are shown for the total charge density (a), radial electric field (b), total axial current density (c), plasma electron temperature T_{pe} (e), and plasma ion temperature T_{pi} (f). The snapshots are taken 55 ns after beam stagnation. A temporal history of electric field energy (d) near the focal plane is also plotted, where $t = 0$ corresponds to beam stagnation and defocusing.

cold-plasma dispersion relation including an external magnetic field, and is given by [Lifshitz and Pitaevskii, 1981]

$$\omega^2 \approx \frac{1}{2}\,(\omega_{pe}^2 + \Omega_{ce}^2) - \frac{1}{2}\,\sqrt{(\omega_{pe}^2 + \Omega_{ce}^2)^2 - 4\,\omega_{pe}^2\,\Omega_{ce}^2\,cos^2\theta}, \tag{6.1}$$

where θ is the angle (about $\pi/2 - 4 \times 10^{-3}$) between $\mathbf{k}$ and $\mathbf{B}_{sol}$, and is approximately satisfied for the parameters in these simulations.

Thermal motion of the beam and plasma near the simultaneous focal plane is important for beam compression dynamics, but its inclusion does not inhibit the propagation of the waves created by beam stagnation. Indeed, the modified wave was also observed in simulations using an increased $T_p = 10$ eV. For the cold-plasma waves under discussion, thermal effects are normally treated as small corrections to the dispersion function for small ρ_{Le} and $k_\perp$, Landau damping remains weak, and the propagation of the waves is not hindered. In fact, the background plasma ions (C^+) and electrons are both locally heated by the beam-plasma interaction up to an average temperature of 50 eV in this simulation, with peak temperatures reaching 400 eV near peak beam compression (stagnation) for a short duration. As the beam nears its stagnation point, its electric self-field becomes strongest and radially repels plasma ions from the vicinity of the most intense part of the beam, such that complex inhomogeneous plasma density profiles result in $\{r, z\}$ space, even in the presence of the $B_z = 150$ kG solenoidal field, as displayed in Fig. 6.33. However, a more complete description of the collective processes of the beam-plasma interaction in the situation considered here is quite complex.

A general analysis of nonlinear wave excitation physics during the beam-plasma interaction is difficult because of the non-equilibrium nature of the compressing charge

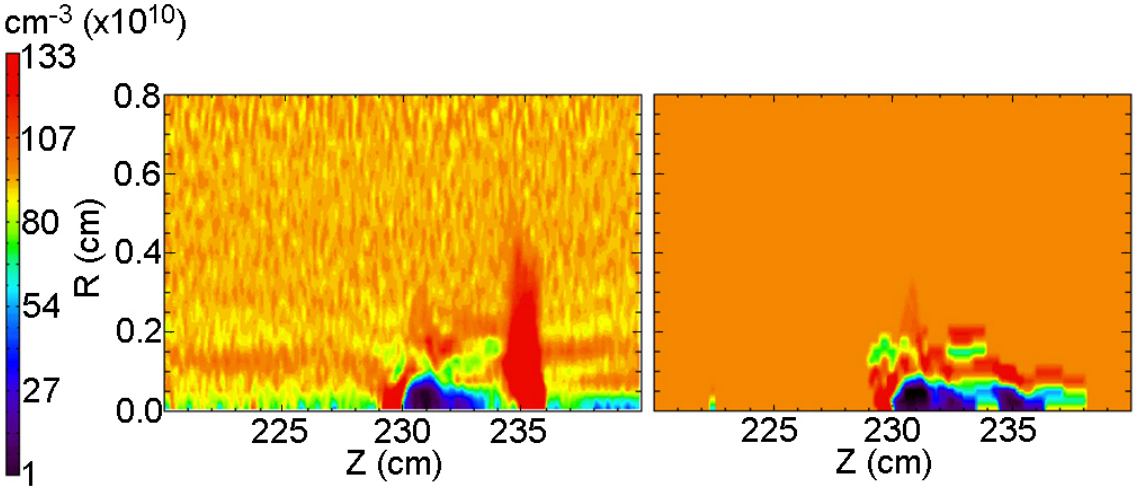

Figure 6.33: (Color) Background plasma electron n_{pe} (left) and ion n_{pi} (right) densities at time $t = +33$ ns after stagnation near the intended simultaneous focal plane of the ion beam. The profiles are non-uniform and substantial local heating occurs because of the beam self-fields. The initial plasma density is $n_p^{foc} = 10^{12}$ cm^{-3}.

bunch near the focal plane, which requires resolution of small size and short time scales in PIC simulation. A more refined analytical model of the plasma response needs to consider corrections involving the inhomogeneous density and self-field profiles of the partially-neutralized ion beam, non-uniform external magnetic field topology, inhomogeneous background plasma ion and electron density profiles, thermal plasma effects (including heating by the self-fields), and scattering effects. On the last point, scattering effects may also alter the compression dynamics of the charge bunch in the presence of such a dense and cold plasma within the final-focus solenoid. Depending on the beam, plasma, and solenoid parameters, a wide variety of electrostatic and electromagnetic collective excitations may be generated in the background plasma by the beam-plasma interaction for the case of inadequate neutralization.

6.9 Summary and conclusions

The finite-size acceleration gap was responsible for time-dependently defocusing the radially-converging trajectories of the beam ions, and the resulting beam radius $r_b(t)$ exiting the gap depended on the beam and gap parameters, as well as the $-dV(t)/dt$ of the voltage waveform (Sec. 6.1). When the beam was given an exaggerated initial convergence angle, the "over-focused" trajectories could offset the defocusing effect in an average way (Sec. 6.1.1). Such a method also ensured that the majority of the cumulative energy deposition resided within the main compressed pulse.

In the absence of background neutralizing plasma, the intense self-fields of the beam caused it to radially expand in the drift region to an unusable spot size for warm dense matter and heavy ion fusion applications. The cumulative effects of partial neutralization on charge bunch compression increased the beam's minimum radius, emittance, and pulse length (to a lesser extent) at the simultaneous focal plane (Sec. 6.2). A range of simultaneous compression results were shown for parameter changes involving the provided background plasma, such as the realistic evolution of the ferroelectric plasma source, as well as global changes in density and temperature. In practice, $n_p >> n_b$ and low plasma temperatures need to be used throughout the drift length in order to ensure high levels of neutralization for charge bunch focusing.

Future experiments seek to transversely focus a beam to sub-mm spot coincident with the longitudinal focal plane using a final-focus solenoid (Sec. 6.3). However, focusing aberrations occurred (in both the transverse and longitudinal directions) due to the spread in beam radius and axial beam energies entering the solenoid. Simulations involving beams with various initial $J_z(t)$ and $r_b(t)$ showed a significant dependence on the phase space of the beam, due to the coupling of the longitudinal

and transverse dynamics within the final-focus solenoid. The transverse defocusing effect of the acceleration gap gave better compression results than the constant $r_b(t)$ case, since it suffered less aberration from the constant solenoidal $\mathbf{B}(r, z)$ fields.

The design of a simultaneous focusing experiment using existing hardware and a $B_z = 80.5$ kG final-focus solenoid has been simulated, in support of near-term experimental efforts (Sec. 6.4). Simulations demonstrated that the ferroelectric and cathodic-arc plasma sources can be used in tandem to provide neutralizing plasma throughout the system for the experiments. However, beam compression simulations involving the realistic experimental plasma profiles, including the associated drift velocities, temperatures, and density variations of both sources, are still under active research.

Simulations indicated that a 400 keV K^+ ion beam can be transversely and longitudinally compressed in current density by factors greater than 10^5 over a distance of a few meters using upgraded hardware, including an induction module with more Volt-second capability, a 150 kG final-focus solenoid, and plasma sources capable of densities $n_p > 10^{14}$ cm^{-3} (Sec. 6.5). Such an intense pulse could be achieved as long as various system components were optimized. The beam's transverse compression was largely determined by the strength and length of the final-focus solenoid, along with its position in the drift region and the amount of plasma provided for neutralization (Sec. 6.6). When the voltage waveform was nearly ideal, the amount of longitudinal compression was largely determined by the beam temperature and the background plasma properties. The transverse and longitudinal beam temperatures contributed to focusing aberrations in both directions, and were limiting factors for achieving small spot sizes and short pulse durations.

If remnant magnetic fields at the target are not desired, the reverse-aligned solenoid configuration was shown to be a viable alternative to the single final-focus solenoid (Sec. 6.7). Although a "plasma gap" region was formed in front of the focal plane during plasma injection (necessitating the use of externally supplied local neutralization), the configuration had many inherent advantages, including diversion of the supersonically-injected plasma to the wall, reduced magnet strength requirements for the same amount of cumulative energy deposition from a single final-focus solenoid, and increased tolerance for axial displacement of the target near the focal plane.

The peak expected beam density set a lower bound on the local plasma density required near the focal plane for optimal beam compression, since simulations showed stagnation of the compression when $n_b > n_p$ before the intended focal plane (Sec. 6.8). Also, lower plasma temperatures provided better neutralization. Beam-plasma interactions, due to partial neutralization effects in the presence of a strong solenoidal magnetic field near the focal plane, deleteriously affected the compression physics and led to the formation of nonlinear wave excitations in the plasma. Therefore, the background plasma was critical for neutralizing the beam throughout the entire process, otherwise the focusing stagnated and optimal compression was not be realized.

Optimization of the simultaneous transverse and longitudinal focusing of an intense ion charge bunch for a given set of experimental conditions was a sensitive function of nearly all of the system parameters. All of the aforementioned realistic aspects of ion beam current density compression need to be carefully considered in an experiment involving simultaneous transverse and longitudinal ion beam focusing, in order to optimize the amount of current density compression (and therefore power density on target) for a given set of conditions.

Chapter 7

Summary and Discussion

7.1 Chapter 1

At the present time, various approaches are concurrently investigated in order to harness the energy production process of nuclear fusion on Earth without the confining aid of gravity. Confinement of the fusion fuel at high densities and temperatures for a significant period of time, enabling net power gain, has been (and continues to be) the primary challenge facing fusion energy scientists within the plasma physics community. The two mainstream paths sharing the goal of fusion power production involve magnetic and inertial confinement. The inertial confinement fusion method (Sec. 1.1) relies on the symmetric implosion of a target capsule and its mass in order to provide confinement. The National Ignition Facility at Lawrence Livermore National Laboratory will house the world's most powerful laser (at 500 TW) and is expected to achieve controlled thermonuclear ignition of an inertial confinement fusion target in the laboratory before 2012, for the first time in human history.

Since current laser technology suffers from low efficiencies and repetition rates,

alternative technologies are under exploration for inertial fusion energy applications. The refurbishment of the pulsed-power Z machine at Sandia National Laboratories will be the world's most powerful x-ray source (at 350 TW) and is expected to perform inertial confinement fusion-relevant experiments beginning in 2008, using the indirect-drive method involving a hohlraum to implode targets. The other main alternative to laser-driven inertial fusion energy is heavy ion fusion (Sec. 1.2), which employs intense and energetic ion beams to implode targets in a similar manner as the other methods. Heavy ion beam drivers are projected to be robust and efficient, achieve the required repetition rates using existing technology, and use non-intercepting magnetics for beam manipulation. Several national review committees evaluated heavy ion fusion as the most viable candidate for inertial fusion energy production in the laboratory. However, at this time, heavy ion driver technology is the least developed of the various inertial confinement driver options.

The most significant drawback of the heavy ion fusion approach is the relative acceleration cost of the ion beam. In order to reduce the cost and size of the accelerator, a shift has been made away from higher-energy emittance-dominated beams towards lower-energy space-charge-dominated beams. As the kinetic energy decreases, the amount of required current for inertial fusion applications increases, requiring higher density beams to offset the slower velocities of the ions. Therefore, the self-fields of the intense nonneutral beams play an increasingly important role on charge bunch propagation, and additional physical and technological challenges are presented. Furthermore, significant levels of current density compression are required in order to achieve the necessary high beam intensities to implode an inertial confinement fusion

target (Sec. 1.3). Simultaneous transverse and longitudinal charge bunch compression to a coincident focal plane is necessary to meet the power demands, where the current density is focused in space by both types of compression and focused in time by longitudinal compression. Intense ion beam focusing to the levels needed for inertial fusion energy applications (few mm in space, few ns in time) is challenging because of the defocusing electric forces of the beam's self-fields, which are much stronger than the focusing magnetic forces for the charge bunch parameters under consideration. Therefore, in order to adequately focus the beams, the majority of the beam's space-charge and current must be neutralized during the final transport stage by a background plasma of sufficiently high density and low temperature.

The Heavy Ion Fusion Science Virtual National Laboratory was established as a consortium of scientists from Lawrence Berkeley National Laboratory, Lawrence Livermore National Laboratory, and Princeton Plasma Physics Laboratory committed to the long-term goal of ion-driven inertial fusion energy. The Neutralized Transport Experiment (Sec. 1.4) and Neutralized Drift Compression Experiment (Sec. 1.5) at Lawrence Berkeley National Laboratory have demonstrated the feasibility of transverse and longitudinal ion beam focusing, respectively, to the required levels for inertial fusion energy applications in scaled, proof-of-principle experiments. Transverse compression was achieved by giving the ion beam a radially-convergent trajectory using the final solenoid or quadrupole in the transport section, and subsequently neutralizing the beam space-charge and current in a background plasma satisfying $n_p >> n_b$ throughout the drift length. Longitudinal compression was achieved by imparting an axial velocity tilt onto the beam as it passed the acceleration gap of a linear induction module, capable of creating a time-dependent longitudinal electric

field in the path of the beam between the final transport magnet and plasma-filled drift section. The physics of current density compression in space and time of high space-charge ion beams has been studied using beam energies and currents far lower than the necessary levels for heavy ion fusion applications. However, the majority of the results are directly relevant to future experiments because important charge bunch quantities, including the perveance and emittance, in the present experiments were chosen to lie within the projected operating regime of a heavy ion fusion driver.

Many of the fundamental physical and technological limitations on simultaneous transverse and longitudinal current density compression were studied in this thesis (Sec. 1.6). The importance of maximizing the achievable current density compression cannot be exaggerated, since it lowers the associated cost and raises the amount of power that can be delivered to the target per unit length of accelerator. The primary uncertainties for a given accelerator design are the minimum achievable transverse spot size and pulse duration, the simultaneous physics of which was quantitatively studied in this thesis for beam and system parameters corresponding to the present experiment (Sec. 1.6). Since the device conducts scaled experiments relevant to future devices involving higher beam energies and currents, this thesis has long-term applicability and value for the heavy ion fusion program.

7.2 Chapter 2

The two main goals of the Neutralized Drift Compression Experiment were to determine the physical and technological limits of current density compression and how accurately the longitudinal compression could be measured in the laboratory. Since simulations predicted final pulse lengths of a few ns at the longitudinal focal plane,

a diagnostic capable of ion beam current, current density, and pulse length measurements with fast temporal resolution needed to be used, and its development was critical for the success of the experiment.

A standard Faraday cup design commonly used in ion beam experiments, that admitted the compressed ion beam in its entirety, was inadequate for the purposes of longitudinal compression measurements, because of the complex plasma and secondary electron behavior within such a probe, the inability to differentiate signals due to the compressed charge bunch alone, and the nominally poor temporal resolution (Sec. 2.1). Therefore, the so-called fast "pinhole" Faraday cup was designed and simulated using the LSP particle-in-cell code (Sec. 2.2). The diagnostic design met all of the key requirements for accurately measuring the absolute ion beam current as a function of time within a plasma environment at the longitudinal focal plane. Essentially, the diagnostic was designed and simulated to remove the longitudinally compressing ion beam from the background plasma, within 0.2 cm of the focal plane, by rejecting the plasma electrons and ions from the collector plate using a series of biased and aligned holeplates within the probe.

The fast Faraday cup diagnostic was fabricated, installed, and calibrated successfully in the Neutralized Drift Compression Experiment (Sec. 2.3). The fast Faraday cup was shown to accurately recover the absolute beam current in the presence of plasma, where the standard Faraday cup diagnostic failed. Experiments confirmed that the fast Faraday cup collector only measured a signal proportional to the ion beam current, without the negative influence of the other particle species in the system, and measurements were corroborated by an optical system using a scintillator and fast phototube arrangement. However, only the fast Faraday cup could measure

the actual ion beam current in the presence of plasma.

Longitudinal compression measurements using the fast Faraday cup demonstrated the successful current compression of intense space-charge-dominated ion beams by ratios of final-to-initial current greater than 50 with full-width, half-maximum pulse lengths less than 5 ns in duration (Sec. 2.4). The diagnostic was further modified to ensure the accurate and fast temporal resolution of compressed ion beam pulses on the few ns time scale (Sec. 2.5). Sophisticated particle-in-cell simulations, involving intense ion beam propagation through a plasma of density $n_p >> n_b$, were in excellent agreement with data acquired by the fast Faraday cup. Early experiments involving an approximate $L_d \sim 2.4$ m drift length revealed a maximum longitudinal compression ratio of 60 with an approximate full-width, half-maximum pulse length of 4.5 ns, corresponding to an overall current density compression factor of 240. The presence of the background neutralizing plasma was vital, notably for transverse confinement and compression. In subsequent experiments, compression ratios greater than 60 with full-width, half-maximum pulse durations of approximately 2 ns were measured, due to various system improvements such as increased voltage waveform accuracy and the use of a ferroelectric plasma source for neutralization.

7.3 Chapter 3

In order to provide valuable insight into laboratory observations and measurements, predict and explain new phenomena, and assess the physical and technological limits of neutralized drift compression, complimentary reduced theoretical models and sophisticated particle-in-cell numerical simulations were employed in this thesis. Charged particle beam physics has a wide range of applications in modern scientific research,

and much of the literature on laboratory-confined nonneutral plasmas, which exhibit complex collective and nonlinear dynamics, is directly relevant to the study of intense ion beam propagation. In support of the neutralized drift compression campaign, previous theoretical models of intense ion beam propagation were expanded upon by accounting for some of the non-ideal parameters and effects found in charge bunch compression experiments.

The Klimontovich equation, Maxwell's equations, and the Lorentz force equation constitute an exact and complete classical kinetic description of a plasma system. The Klimontovich-Maxwell description was derived to show the conservation of microscopic phase space density of all particles in time, as measured along their orbits (Sec. 3.1). The formalism contained all of the exact six-dimensional orbits of each individual particle, and was therefore far more complicated than necessary. The construction of the phase space distribution function and subsequent ensemble-averaging resulted in the derivation of the plasma kinetic equation, a reduced statistical treatment including collective and discrete plasma particle effects. Neglecting collisional effects, the resulting nonlinear Vlasov equation and Maxwell's equations involving ensemble-averaged fields lent an analytically tractable Vlasov-Maxwell description of plasma behavior, which is widely used to study the equilibrium and stability properties of charged particle beams. Such an approximate description provided the tractable determination of average plasma properties over many interparticle spacings, without being encumbered by the inclusion of the exact motion of all the constituent particles.

Even under idealized assumptions, the Vlasov kinetic theory can become quite complex. The macroscopic warm-fluid description was therefore derived as a continuum approximation by evaluating velocity moments of the nonlinear Vlasov equation

(Sec. 3.2). Closure of the hierarchy of equations was achieved by assuming no heat flow in the system, resulting in a reversible set of nonlinear coupled partial differential equations, referred to as the continuity, momentum balance, and energy balance equations. In the fluid approach, velocity space contributions to the kinetic description were ignored, but the system of equations could be solved without the use of macroparticles, as well as yield numerical results containing less noise, more stability, and better energy conservation than traditional particle-in-cell codes.

Nevertheless, particle-pushing routines are incredibly useful in many situations. Particle-in-cell algorithms model complicated charged particle behavior in the presence of collective self electromagnetic fields as well as externally applied fields (Sec. 3.3). Such a code was used to compute the trajectories of many charged particles on a nonphysical spatial grid, on which electromagnetic fields were self-consistently calculated, and within which the particles of each species contributed to the approximation of the corresponding distribution function. Finite-difference techniques were employed to calculate and advance the particle positions and momenta from one time step to the next. Weighting schemes were used to determine the charge and current densities known on the grid, as well as to interpolate the resultant fields to the particles within the grid. When a number of considerations were heeded, energy conservation during the accurate modeling of complex charged particle ensemble behavior throughout space and time was possible. The sophisticated code LSP was used to self-consistently incorporate many effects of beam compression in plasma, and compare to reduced model descriptions. Also, such numerical simulations contributed detailed results to the forefront of ion beam compression research for heavy ion fusion applications, in regimes that require the advanced particle description.

7.4 Chapter 4

There is no theoretical classical upper limit on longitudinal bunch compression for an ion beam with zero temperature, which acquires an ideal velocity tilt across an infinitely thin acceleration gap, since all of the beam particles arrive at the focal plane at the exact same time. The derivation of the ideal velocity tilt, and the induction module voltage waveform that produced it, was outlined (Sec. 4.1). The drift length and time to focus for an ideally-tilted charge bunch was determined to be a function of the initial beam energy, initial pulse length, and intended fractional tilt, where greater fractional tilts and shorter initial pulse lengths led to shorter drift lengths. The experimental voltage waveform was programmed to attempt the application of as near an ideal voltage waveform as possible. In reality, since all beams have finite temperature, any acceleration gap must have finite spatial extent, and other realities must be considered, finite upper bounds on the amount of current density compression exist. The deleterious effects of the finite-size acceleration gap and various origins of longitudinal focal plane aberration were thoroughly investigated and quantified.

The challenge for theoretical models is to realistically and tractably describe the important physics in associated experiments. Reduced theoretical models have been shown to be effective in realistically describing the longitudinal compression of an intense charge bunch in neutralizing background plasma. Many assumptions on solution-type and uniformity were relaxed in the analysis, such as the inclusion of nonuniform and asymmetric density and axial flow velocity profiles, experimental acceleration gap size and voltage waveform, space-charge and perveance, non-zero beam temperature, and propagation through a background plasma which incompletely neutralizes the beam charge and current.

A numerical implementation of the warm-fluid model has been analyzed as a tractable computational tool for realistically predicting the dynamic evolution of the charge bunch and investigating non-ideal effects associated with achieving longitudinal compression across finite-size acceleration gaps (Sec. 4.2). It demonstrated that the inclusion of the actual gap geometry and experimental voltage waveform of the induction module is important in order to make accurate comparisons to the current compression ratio profiles measured in experiments. The main observed features in the profiles from measurements and particle-in-cell simulations were readily recovered with the fluid model, indicating that their origin was in the finite-size nature of the acceleration gap and they did not require kinetic explanations. The applied axial electric field in the gap was observed to act as a means for pulse-shaping not only the axial velocity profile, but also the line density profile in the beam frame. A favorable consequence of the pulse-shaping ability of the gap was that resulting ion beam profiles in some cases acquired a linear velocity tilt, parabolic line density profile, and double-parabolic pressure profile. The generic solution belonged to a family of self-similar drift compression solutions which could be used to transversely focus the entire charge bunch to the same focal plane for warm dense matter and heavy ion fusion applications. Lastly, the warm-fluid model broke down before the focal plane, due to its inability to support multiple-valued functions, since experimental waveform inaccuracies caused regions of the faster tail to surpass the slower head before the focal plane of maximum current compression. Therefore, kinetic treatments that retained the velocity space information of the intense beam were used.

A kinetic formalism for the dynamical evolution of compressing ion beams, based on the Vlasov equation, has also been numerically employed in order to understand

the physics of the central portion of the beam, which acquired a linear velocity tilt with a parabolic line density profile (Sec. 4.3). The kinetic model illustrated that, when using an experimental voltage waveform, the resulting peak in the current profile near longitudinal focus was due to the fact that only the central portion of the beam, which was tilted approximately linearly for the parameters under consideration, contributed effectively to the main compressed pulse. Significant portions of the charge bunch did not reside in the linear region of the velocity profile because of deviations between the experimental and ideal waveforms. In order to study how those regions formed a pedestal of current around the central peak, and decreased the total amount of compression (and increased the pulse duration) achieved at the focal plane, a hybrid combination of the fluid and Vlasov models was developed by propagating a Vlasov solution for the compressing $I(z,t)$ profiles, using the line density and axial velocity profiles from the warm-fluid treatment as initializations, to the focal plane (Sec. 4.4). Such a hybrid implementation combined the main advantages of both methods.

Particle-in-cell simulation contained the richest level of detail of the evolving particle phase space distribution, but at the cost of additional computational resources (Sec. 4.5). Individual current profiles, as well as the envelope of peak current from one profile to the next, were generally not symmetric about the focal plane, due to non-ideal waveform effects, chromatic aberration, and the formation of double-peaks and plateau characteristics, which arose from the reality that more initial beam pulse was used than intended to undergo longitudinal compression. Also, average kinetic energy profiles through fixed axial locations were shown to develop discontinuities near the focal plane, due to multiple-valued axial velocity distributions. Generally, ion beam trajectories must be evaluated numerically by a particle-in-cell code in order

to account for all the (otherwise intractable) complex effects that ultimately determine the quality of the focal plane. The successful comparison between experimental measurements and the various numerical models of neutralized drift compression was very encouraging (Sec. 4.6). In particular, the hybrid and particle-in-cell models very accurately reproduced the measured amount of longitudinal compression and its pulse duration, whereas the kinetic model reproduced the central portion of the beam with an approximately linear velocity tilt.

The detailed physics and implications of acceleration gap effects and focusing aberration (leading to focal plane quality degradation) on optimum longitudinal compression in the laboratory were quantitatively reviewed, with dependency on most of the system parameters examined (Sec. 4.7). Ideal and realistic types of acceleration gap and voltage waveform, the infinitely thin and 3 cm long gap and "sharp" and "smooth" waveforms, respectively, were studied in order to ascertain the origin of various deleterious effects (Sec. 4.7.1). A beam with no initial emittance was demonstrated to achieve the maximum compression achievable (in a simulation involving a discrete time step) by acquiring an ideal velocity tilt over an infinitely thin gap. When the beam pulse is equal to the intended initial pulse length to undergo longitudinal compression, symmetric current profiles in time and space occur without the formation of double-peak and plateau characteristics. In reality, the electric field encountered by the beam has significant spatial and temporal extent relative to the size and pulse length of the beam, and gives rise to a number of complications. The same simulation across the finite-size gap resulted in a significant reduction in longitudinal compression, due to the effective longitudinal temperature imparted to an otherwise cold beam via the coupling of transverse and longitudinal dynamics within

the finite-size gap. In addition, the transit time of the ions across the finite-size gap implied that portions of the charge bunch sampled significant temporal amounts of integrated electric field, but the head and tail extremities of the charge bunch did not encounter the requisite amount of it (with tail particles affected worse), leading to a reduction in intended fractional tilt (without a corresponding change in drift length) as a function of initial pulse length and gap size, and manifested as an apparent increase in effective longitudinal temperature. Therefore, the gap size and transit time of the beam was required to be much smaller than the initial bunch and pulse lengths, respectively, for imparting larger fractional tilts. The inclusion of the extra voltage in the "smooth" compared to the "sharp" waveform increased the relative fractional tilt and compression ratio by approximately 1/3 with only a small increase in minimum pulse duration at focus. The offset in focal plane location between the infinitely thin and finite-size gaps was shown to depend on the bunch lengths compared to the gap length and transit time, but not the intended fractional tilt.

Both transverse and longitudinal focusing were sensitive to initial beam temperature, which led to aberration of the focal planes, increased spot sizes and pulse lengths, decreased amounts of compression, and increased axial tolerance for diagnostic or target positioning (Sec. 4.7.2). Beam temperatures consistent with measurements reduced the achievable compression ratios to < 500 for the parameters under consideration, and caused asymmetric current profiles away from the focal plane. Slower head particles were shown to suffer increased levels of aberration and contributed more current to the pre-pulse for $t < t^{peak}$ compared to faster tail particles, since the thermal velocity is always a greater fraction of the former compared to the latter. An analytical equation for the minimum full-width, half-maximum temporal pulse length

of an ideally-tilted beam with finite beam temperature, accounting for the variation in aberration, was derived. The calculation agreed well with particle-in-cell simulation, when a geometrical constant took into account the effective 45% beam temperature increase due to the "smooth" waveform and finite-size gap, for the parameters under consideration. The compression ratio and pulse length at focus were demonstrated to decrease and increase, respectively, with square root dependence on the initialized beam temperature, which was the limiting physics on longitudinal bunch compression using optimized waveforms and plentiful plasma supply.

The longitudinal compression dependence on initial pulse length and intended fractional tilt was investigated, since they comprise the two induction module waveform parameters adjustable by the experimenter (Sec. 4.7.3). Changes in waveform due to initial pulse length t_p demonstrated an increase in compression ratio with $t_p^{0.8}$ dependence for shorter pulse lengths (100 ns $\leq t_p <$ 300 ns) and $t_p^{0.3}$ dependence for longer pulse lengths (300 ns $\leq t_p <$ 500 ns). A plateau effect occurred at a critical t_p, beyond which aberration due to the longer drift lengths dominated, indicating the presence of a trade-off consideration between high current compression ($\sim t_p^{0.3}$) and minimum pulse duration ($\sim t_p^{1.05}$) at focus for larger initial pulse lengths. Shorter initial pulse lengths achieved reduced fractional tilts from the acceleration gap effects, as the transit times became a significant fraction of t_p, and both the time required and drift length to focus increased with t_p linearly.

Changes in waveform due to intended fractional tilt f illustrated an increase in longitudinal compression and decrease in pulse duration (and aberration) at focus for larger fractional tilts. The compression ratio demonstrated $f^{0.82}$ dependence for smaller fractional tilts ($0.3 \leq f < 0.5$) and $f^{0.51}$ dependence for larger fractional tilts

($0.5 \leq f \leq 0.7$), whereas the minimum achievable pulse length ($f^{-1.23}$), required time to focus ($f^{-0.81}$), drift length to focus ($f^{-1.12}$), and amount of chromatic aberration all decreased with larger f, in agreement with analytic theory. Therefore, larger tilts were desirable for experiments, but were limited by the Volt-second capability and hold-off requirements of the induction module, as well as concerns over increased transverse focusing aberration due to the energy spread. A balance between longer initial pulse lengths and larger fractional tilts was discussed, since both increase the compression ratio, but have opposite effects on the minimum pulse length t_{fwhm}, drift length (and time) to focus, and the amount of aberration. Depending on many experimental constraints, including the induction module capability, an optimum arrangement can be shown to exist for a given set of beam and system parameters.

Quantitative examples were outlined that explored the dependency of longitudinal compression on initial ion beam kinetic energy and thermal distribution, since the slope of the voltage waveform was only ideal for one particular beam energy and assumed a cold beam (Sec. 4.7.4). Small constant differences ($\pm 2.5 - 5\%$) and temporal drifts ($\pm 2\%$) in directed energy, whether due to shot-to-shot variation, systematic uncertainty or inaccuracy, or hardware limitations, caused significant departure from the optimum compression parameters. The constant differences decreased the relative compression ratio by $20 - 40\%$, contributed to significant current pedestal formation, and changed the axial location of the focal plane. It was also demonstrated that experimental beam energy scans to align the plane of the diagnostic with a peak compression result, while holding the waveform fixed, did not necessarily find the true optimum compression achievable; instead, only an axially-moveable diagnostic

in conjunction with a beam energy scan could unambiguously discern the unique optimum compression ratio. The small temporal drifts in initial beam energy resulted in a 22% relative decrease in compression ratio due to deformations of the $\{z, v_z\}$ space from vertical at focus, in addition to current pedestal contributions and alterations of the focal plane location. Lastly, the beam's thermal distribution also affected the temporal shape of the current profiles and amount of aberration at focus. Beams with Waterbag distributions were shown to result in markedly asymmetric current profiles and reduced compression ratios (with peak compression not arriving at the center of the main pulse), compared to the bell-shaped Maxwellian distribution results. However, if an approximate Waterbag distribution could be realized in the laboratory, pre-heat of targets could be substantially reduced because of the low prepulse current pedestals and short elapsed times from low to peak current found just downstream of the actual focal plane.

It was argued that no universally valid analytic model exists for determining the expected maximum longitudinal current compression factor and pulse length at focus, or even the current profile $I_b(t)$ at the focal plane, because of the general intractability of including its dependence on many parameters, such as voltage waveform accuracy and finite-size acceleration gap geometry, beam parameters including its temperature and distribution type, neutralization processes by the background plasma, and other deleterious effects. Therefore, particle-in-cell simulations were employed as the most self-consistent method for investigating most of the major realistic effects that contributed to the physical and technological limits of longitudinal compression in the laboratory; the successful modeling and explanation of the physics involved in imposing velocity tilts provided quantitative understanding of many experimental

limitations regarding longitudinal current compression of intense beams. Numerical models were used to provide physical insights into imperfections such as non-ideal voltage waveforms, consequences of finite-size gaps, beam temperature effects, focusing aberrations, and beam energy uncertainties due to technological limitations, all of which gave rise to decreased compression factors and increased pulse widths at focus.

7.5 Chapter 5

In support of the experimental effort, large-space scale and long-time scale numerical simulations were executed in order to study the spatial and temporal evolution of the plasma flow from two different types of source used in the laboratory, since they were responsible for the achieved degree of beam neutralization within the drift length. Furthermore, the simulations of the plasma injection into the device allowed evaluation of the realistic parameters achieved in experiments, so they can employed in additionally sophisticated compression simulations, which had normally assumed constant profiles and ignored the dynamical nature of the provided plasma. The simulations provided increased confidence that sufficient levels of plasma density were present in the device for longitudinal beam compression experiments.

A filtered cathodic-arc plasma source used a macroparticle debris and neutral atom filter composed of bent solenoids to create and inject highly ionized, supersonic plasma jets into the system along externally imposed magnetic field lines (Sec. 5.1). Two source and filter pairs were installed on opposite off-axis sides on the downstream end of the device, positioned to face the upstream direction, and injected plasma into a $3D$ magnetic topology (due to the lack of adequate symmetry) composed of the two solenoidal filers and a long guide solenoid throughout the drift length (for plasma

confinement purposes). It was argued that the coupling efficiency of the plasma flow from source to drift region depended on many geometrical factors, as well as the plasma properties and magnetic field configuration. Simulations provided insight into the cathodic-arc plasma dynamics from injection to steady state flow, where the electrons were always magnetized but the ion magnetization level varied throughout the configuration. Using parameters relevant for current experiments, 50% coupling efficiency was demonstrated for neutralized beam compression experiments. Ambipolar forces, perpendicular and parallel ∇B gradient drifts, and curvature drifts were shown to affect the plasma (mostly electron) dynamics. Magnetic mirroring of the plasma away from the long guide solenoid ($B_z \sim 2$ kG) was shown to be a factor involving the injection of plasma into higher magnetic field regions. The non-uniform magnetic topology complicated the well-known general analytic considerations for evaluating guiding-center drifts, therefore particle-in-cell simulations provided self-consistent evaluation of the physics in an otherwise challenging scenario. Significant plasma density loss in the filter coils and intermittent region of low magnetic fringe fields was demonstrated, and suggestions for improvement were made.

Numerical simulations of plasma flow from the $BaTiO_3$ ferroelectric source, a large-surface-area emitter capabale of high current densities over large volumes, demonstrated that the required plasma densities for longitudinal compression experiments were provided over the drift length (Sec. 5.2). For simultaneous transverse and longitudinal compression experiments, the ferroelectric source will be used in the main drift length to provide the lower density plasma, compared to the cathodic-arc source planned for higher plasma density use near the simultaneous focal plane. The main advantages of the ferroelectric source were the lack of required magnetic field for plasma

confinement, which can alter the beam ion trajectories and affect neutralization levels, and lack of upstream-directed supersonic plasma (as in the cathodic-arc source), which may penetrate into the acceleration gap and transport sections and raise the beam emittance. $3D$ simulations of the source indicated that the radially-injected ferroelectric plasma nearly uniformly filled the device, including into the $\Delta z = 5$ cm "gaps" (with reduced densities) for transverse diagnostic access, in approximately $t \sim 6$ μs, and in good agreement with experimental measurements when $m_i = 3 \times Ba$ and $T_{pe} = T_{pi} = 20$ eV were chosen for the effective plasma ion species and initial plasma temperature, respectively. However, the compelling comparison was qualitative, since the problem did not necessarily have a unique solution, due to the wide range of detected plasma ion constituents, lack of ion temperature measurements, and neglect of other realistic effects in the simulations. Situations involving azimuthally-asymmetric plasma creation conditions, and large non-emitting regions at the radial wall, showed that symmetric plasma density profiles were nevertheless achieved at the times of peak on-axis plasma densities (when the beam passed through the device), but were reduced in overall density relative to the fully-symmetric case. Lastly, simulations highlighted that the ferroelectric plasma only expanded upstream on the thermal expansion time scale due to its radial, and not axial (as in the cathodic-arc source), injection momentum, and therefore was advantageous for beam compression experiments because it avoided the possibility of allowing plasma to move upstream, partially neutralize the beam, and raise its emittance in the transport and acceleration gap sections.

Strong final-focus solenoids will be used in upcoming experiments in order to transversely focus the axially-compressing beam to a sub-mm spot coincident with

the longitudinal focal plane. In order to fill a final-focus solenoid with the requisite amount of high-density plasma for beam neutralization, $3D$ and $2D$ large-space scale and long-time scale simulations were executed in order to predict the amount of plasma-fill within $B_z = 53$ kG and $B_z = 40$ kG solenoids, respectively, due to supersonically-injected plasma from the low-field region (Sec. 5.3). Significant levels of magnetic mirroring was witnessed in simulations. Also, plasma density compression was evident in the vicinity of the focal plane, which was expected to provide additional neutralization otherwise not achievable from the cathodic-arc source. Ambipolar forces influenced the dynamics as the solenoid became partially-filled with plasma, and the on-axis plasma density dependence on initial injection velocity was demonstrated using plasmas with a variety of Mach numbers. Experiments are planned to measure whether the injected plasma can fill such strong solenoids, and provide quantitative comparison to the predictions made by these simulations.

7.6 Chapter 6

The finite-size acceleration gap was responsible for time-dependently defocusing the radially-converging trajectories of the beam ions, due to an imbalance in integrated electric field across the gap (Sec. 6.1). The resulting beam radius $r_b(t)$ exiting the gap depended on the beam parameters and $-dV(t)/dt$ of the voltage waveform. Nominally, the $dr_b(t)/dt$ increased for the first half of the initial pulse length and decreased for the second half, such that the maximum r_b was found near the central portion of the beam pulse traveling at v_0, in agreement with measurements. By giving the beam an exaggerated initial convergence angle with the final solenoid or quadrupole in the transport section, the "over-focused" trajectories were shown to balance the excess

divergence given to the beam in the gap, and offset the defocusing effect in an average way (Sec. 1.1.1); such a method also ensured that the majority of the cumulative energy deposition resided within the main compressed pulse. Recent "over-focusing" experiments confirmed the validity of the simulated physics and demonstrated simultaneous compression of intense ion beams.

In the absence of background neutralizing plasma, the intense self-fields of the beam would cause it to radially expand in the drift region, and potentially strike the chamber wall. With such a large spot size, such a beam wouldn't be useful for applications involving targets. The cumulative effects of partial neutralization on charge bunch compression, caused by partially exposed beam potential within the drift length, increased the beam's minimum radius, emittance, and pulse length (to a lesser extent) at the simultaneous focal plane (Sec. 6.2). Simultaneous compression simulations, involving parameter changes in the provided background plasma, such as the temporal and spatial evolution of the ferroelectric plasma source, as well as global changes in density and temperature, demonstrated that reduced plasma densities and increased plasma temperatures were harmful to the compression results, since the neutralization physics occurred on the Debye-length scale λ_D. In practice, plasma temperatures may take on a wide range in space and time, suggesting that $n_p >> n_b$ should be used throughout the drift length in experiments, in order to ensure that $r_b^{foc} >> \lambda_D$ and provide high levels of neutralization.

As mentioned in Chapter 4, experiments will attempt to transversely focus intense ion beams to sub-mm spots coincident with the longitudinal focal plane using strong final-focus solenoids placed near the end of the drift length (Sec. 6.3). Such a solenoid shortened the effective transverse focal length and helped minimize the amount of

plasma required throughout the system. However, focusing aberration occurred due to the spread in axial energies entering the solenoid, where slower head particles focused earlier in time and space than faster tail particles. Simulations of simultaneous beam compression involving beams with constant initial $J_z(t)$ and $r_b(t)$ were compared to situations involving beams with linearly increasing $r_b(t)$, as well as those involving realistic beams with half-increasing and half-decreasing $r_b(t)$ over the duration of the pulse. Charge bunches with constant $r_b(t)$ profiles resulted in the lowest amount of compression with the most aberration, whereas those with linearly increasing $r_b(t)$ profiles were shown to compress approximately 4 times better and suffer no additional longitudinal focusing aberration. A beam affected by transverse defocusing in the gap therefore resulted in better compression than the constant $r_b(t)$ case, since the particular $r_b(t)$ profile exiting the gap caused the beam to suffer less aberration within the final-focus solenoid. A linearly increasing $r_b(t)$ profile may be produced by the acceleration gap via time-dependent magnetic focusing (involving future technologies) or a gap with specially-contoured, asymmetric conducting boundaries that offset the defocusing effect for the head of the pulse but exacerbate it for the tail of the pulse.

The design of a simultaneous focusing experiment using existing hardware and a $B_z = 80.5$ kG final-focus solenoid (under construction) was simulated, in support of upcoming experiments (Sec. 6.4). The ferroelectric source was planned for use throughout most of the drift length, and the cathodic-arc source was used to inject supersonic plasma into the final-focus solenoid and focal plane regions. Large-space scale and long-time scale plasma flow simulations demonstrated that plasma of sufficient density was available throughout the system for beam compression experiments, and resulted in current compression ratios > 55, with coincident beam radii < 1 mm

and pulse lengths of approximately 2 ns. However, beam compression simulations involving realistic plasma profiles, including the associated drift velocities, temperatures, and density variations of both sources, were still under active research.

Simulations indicated that a 400 keV K^+ ion beam was transversely and longitudinally compressed in current density by a factor greater than 10^5 over a distance of $L_d \sim 2.5$ m, using upgraded hardware, including an induction module with more Volt-second capability, a $B_z = 150$ kG final-focus solenoid, and plasma sources capable of densities above $n_p \sim 10^{14}$ cm^{-3} (Sec. 6.5). Such an intense pulse was achieved by optimizing various system components; a precisely controlled voltage waveform imparted an axial velocity tilt to the beam with finite temperature, which entered a precisely positioned final-focus solenoid with a specific $r_b(t)$, and was neutralized by a plentiful plasma supply. The optimization of ion beam simultaneous transverse and longitudinal focusing, for a given set of experimental constraints, was a sensitive function of nearly all of the system parameters.

Ultimately, the beam's transverse compression was largely determined by the strength and length of final-focus solenoid, along with its position in the drift region and the amount of plasma provided for neutralization (Sec. 6.6). Weaker solenoids, as well as solenoids positioned farther upstream, resulted in reduced cumulative energy depositions at the focal plane. The transverse and longitudinal beam temperatures contributed to focusing aberrations in both directions, and were limiting factors for achieving small spot sizes with short pulse durations. Neutralization of the on-axis beam within the final-focus solenoid was critical for beam compression, otherwise partial neutralization of the beam led to emittance growth, compression stagnation, and plasma heating.

If remnant magnetic fields at the focal plane are not desired, the reverse-aligned solenoid configuration was shown to be a viable alternative to the single final-focus solenoid (Sec. 6.7); provided adequate neutralization, intense ion beams were predicted to focus well in the three-solenoid set-up. Although a "plasma gap" region was formed in the last $\sim \Delta z = 7$ cm up to the focal plane, and extra externally-supplied local neutralization was required, the reverse-aligned solenoid configuration had many inherent advantages, including diversion of the supersonically-injected plasma to the wall, reduced magnet strength requirements for the same amount of cumulative energy deposition from a single final-focus solenoid, and increased tolerance for axial displacement of the target near the focal plane.

The background plasma must have neutralized the beam's charge and current throughout the entire focusing process, otherwise the beam compression stagnated and optimal compression was not realized (Sec. 6.8). The neutralization provided by the plasma was critical in determining the total achievable compression of the beam pulse. The peak beam density set a lower bound on the local plasma density required near the focal plane for optimal compression, since simulations showed stagnation of the compression when $n_b > n_p$ before the intended focal plane. Beam-plasma interactions, due to partial neutralization effects in the presence of a strong solenoidal magnetic field near the focal plane, deleteriously affected the compression physics and led to the formation of nonlinear wave excitations in the plasma.

7.7 Future work

Suggested future work includes the numerical simulation of $3D$ effects such as the misalignment and aberration from nonlinearities in focusing elements, and the use of permanent magnetic dipoles to employ active correction of beam off-centeredness recently witnessed in experiments. In addition, electron cloud and gas effects in the transport section, from beam scraping (or halo particle production) on apertures or radial walls, should be studied in further quantitative detail relevant for current experiments, since preliminary work suggested small amounts of electron clouds ($n_e \sim 10^6 - 10^8$ cm^{-3}) can be liberated by energetic $K+$ impact in the diode and transport sections and become trapped in the beam, leading to emittance growth (reduced compression) and hollow beam density profiles. Similarly, neutral ionization, scattering, and charge exchange effects in the diode and transport sections would benefit from additional research. Furthermore, high frequency Marx waveform modulations in the injector may affect beam quality and time-dependently alter beam uniformity, and should receive more attention from numerical simulation. Time-dependent magnetic focusing by either the last transport magnet or final-focus solenoid, in order to achieve more desirable $r_b(t)$ profiles, is a field of research that contains high potential for correcting the defocusing effect of the acceleration gap and aberration in the final-focus solenoid, leading to the realization of higher current density compression factors in experiments. Alternatively, specially-contoured acceleration gaps may offset the defocusing effect for the head but exacerbate it for the tail, resulting in desirable $r_b(t)$ profiles. Additional cathodic-arc coupling simulations for other magnetic field topologies, final-focus solenoids, and device geometries under consideration for future experiments should be executed and compared to measurements, in order to assess

and quantify neutralization issues in beam compression experiments. More simulations are necessary in the context of simultaneous beam compression in the presence of plasmas with realistic density, temperature, and directed momentum profiles from the ferroelectric and cathodic-arc sources near the final-focus solenoid and focal plane regions, in order to determine the level of neutralization provided and whether issues such as two-stream instability and filamentation play a role in focal plane degradation. Lastly, future work should include the evaluation of scattering effects for cold, high-density plasmas in the final-focus solenoid region, and the determination of whether they alter the compression dynamics of the charge bunch.

7.8 Epilogue

Heavy ion drivers can deliver more intensity to the target per unit length of accelerator by greatly compressing the intense ion charge bunches over short distances. The associated cost of a heavy ion beam driver dramatically decreases with the amount of current density compression achieved by the beam in the shortest amount of space and time. The physics foundation of neutralized drift compression and simultaneous focusing in experiments provides key insights for the next-step heavy ion beam experiments involving short pulse injectors and larger kinetic energies. Optimization of the current density compression (and therefore intensity on target) under the appropriate experimental constraints allows more compact and cost-effective accelerators and transport lines to be used as heavy ion drivers than previously envisioned, enabling the heavy ion fusion approach to become more competitive with other driver technologies, and ultimately leading to the possible development of reliable, safe, and robust inertial fusion power production on Earth.

Appendix A

The Single-Gap Linear Induction Accelerator

The induction module in the Neutralized Drift Compression Experiment (NDCX) is also known as a linear induction accelerator [Christofilos *et al.*, 1964], the basis for which is the concept of inductive isolation. Linear induction accelerators use a ferromagnetic core as an inductor for broadband isolation of a cavity (via a high-inductance leakage path). The cavity is connected to the beam chamber at the acceleration gap, where electric fields in the presence of conducting boundaries are imposed upon the path of the beam. Rapidly varying magnetic fields $\partial B_\theta(t)/\partial t$ within the core induce strong electric fields E_z in the gap according to Faraday's Law.

The linear induction accelerator is a device that transfers energy from pulse modulators to a charged particle beam. The induction module in the NDCX device contains a pressurized gas region, within which are housed twelve independently driven ferromagnetic cores (stacked longitudinally), that is separated from vacuum by conventional high-voltage insulation. Each core is driven by a high-power thyratron-switched

pulse modulator, and acts as a step-up transformer (the intense charge bunch acts as the secondary). The primary purpose of the cores is to reduce leakage current. Since the load current does not encircle the ferromagnetic cores, the cores' properties set no limitation on the amount of beam that can be accelerated. The induced electric field in the acceleration gap is a result of the changing magnetic flux through the entire core, and the voltage across the gap is electrostatic-like.

Multiple induction cores can be driven at once, and each modulator can be separately programmed and triggered such that each core contributes some electric field to the total electric field in the acceleration gap, as a function of magnitude and time, resulting in an associated voltage waveform $V(t)$. Therefore, a wide range of voltage waveforms is available to the experimenter for creation within the gap, where the inductive electric field modifies the energy of the intense ion beam. The charge bunch encounters the induced electric field *only* within the acceleration gap, and the pulse modulators and cores are external to the beam-plasma-chamber system.

The main application of non-resonant linear induction accelerators is the generation of pulsed, high-current charged particle beams [Humprhries, 1986], which experience a net accelerating field within the acceleration gap. However, electrostatic potential differences in the accelerating structure itself are kept to manageable levels. A sequence of induction modules and gaps can be employed to accelerate charge bunches to high directed energies, although the accelerator involved in a design for heavy ion fusion applications is the most costly component.

For neutralized drift compression experiments involving the longitudinal focusing of an intense ion beam, the linear induction accelerator is used for a different purpose than uniform acceleration. The induced longitudinal electric field in the acceleration

gap is time-dependently pulsed to axially decelerate the beam earlier in time, but changes polarity to accelerate the beam later in time. Therefore, a time-dependent voltage waveform imposes a temporally varying axial electric field such that a head-to-tail increasing velocity tilt is applied to the intense ion beam. As discussed in this thesis, the resulting energy variation acquired by the beam will cause it to longitudinally focus while it drifts through a region filled with high-density plasma, the electrons from which neutralize the space-charge and current of the intense charge bunch and allow it to focus beyond the space-charge limit. The temporal shape of the voltage waveform applied to the beam is directly correlated to the quality of the longitudinal compression according to a force balance equation, as discussed in Chapter 4, and has been demonstrated in experiments [Roy *et al.*, 2005b].

An overview of the technology involved in an induction module is as follows: (1) pulse modulators provide large currents $I(t)$, which pass through high-voltage feedthroughs encircling the ferromagnetic core(s); (2) the current in the feedthroughs creates an amplified magnetic field $B_\theta(t)$ within the ferromagnetic material, and the alignment of atomic currents is equivalent to a macroscopic current flowing on the surface of the material; (3) the time-dependence of the current in the feedthroughs causes the magnetic flux $\Phi_m(t)$ through the ferromagnetic material to also vary in time; (4) the changing magnetic flux induces an electric field $E_z(t)$ along the axis of the induction module according to Faraday's law; and (5) the electric field is communicated from the induction cavity into the path of the beam via the acceleration gap. The major physics principles and technological components of an induction module are provided in Fig. A.1 [HIFS-VNL, 2001, Humprhries, 1986]. The voltage pulse from the modulators is triggered in experiments so that the time-dependent electric

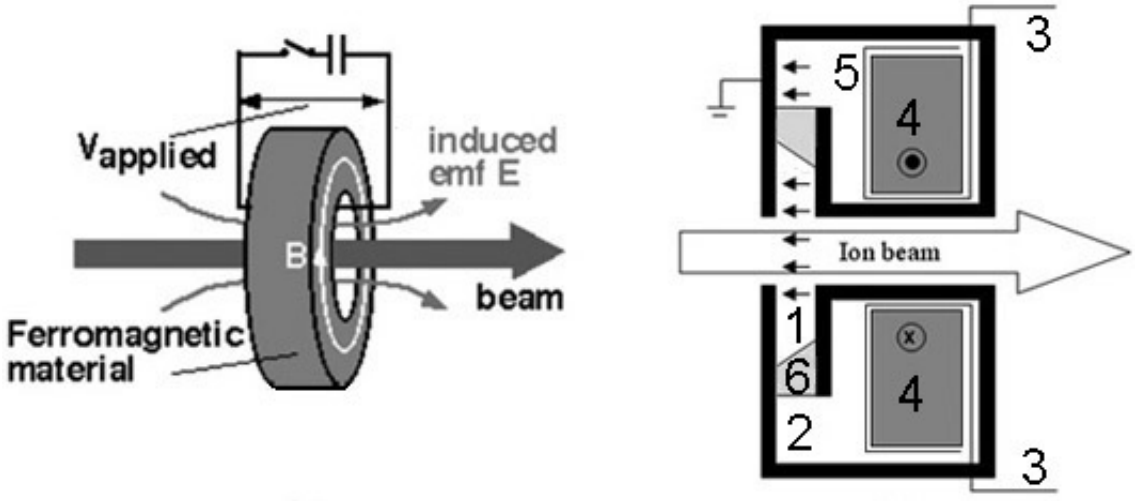

Figure A.1: The physics principles of the induction module (left) [HIFS-VNL, 2001]. A cross-section (right, with ϕ symmetry) of the induction module [Humprhries, 1986]: acceleration gap (load circuit region under vacuum) (1), transformer oil insulation for induction cavity (leakage circuit region) (2), insulated power feed (3), ferromagnetic core (4), exposed face of core (5), and vacuum insulator (6). The E_z field direction in the gap is indicated for the given B_θ field direction in the ferromagnetic core.

field for longitudinal compression is present as the ion beam passes through the gap.

An efficient linear induction accelerator produces its voltage waveform without exceeding the limitations of the ferromagnetic material used in the core(s). Deviations from ideal behavior in an induction cavity can be controlled via laminated core construction to minimize eddy currents in the inductive isolator (which contribute to resistive losses and misalignment of magnetic moments within inner regions of the core), flux forcing to minimize unequal saturation in a core, core reset circuits to maximize flux swing, and compensation circuits to achieve uniform accelerating voltage by reducing leakage current, which also raises the associated efficiency. Those subjects will not be discussed here.

Appendix B

LSP Simulation Code

As discussed in Sec. 3.3, the LSP code [LSP, 1999, Hughes *et al.*, 1999] is an advanced $3D$ electromagnetic particle-in-cell (PIC) code designed for complex, large-scale plasma simulations on parallel and serial platforms; the numerical code supports cartesian, cylindrical, and spherical coordinate systems and can also be used in $1D$ and $2D$ geometries. The technique of particle-in-cell simulation is a powerful computational tool for self-consistently incorporating many effects of charged particle physics and transport into one model; in this thesis, the LSP code is used in order to predict the evolution of the intense ion beam, as it acquires an axial velocity tilt and drifts through the plasma, to the focal plane under a variety of circumstances.

A particle-in-cell code evolves the full distribution functions of all simulated species for given boundary and initial conditions by computing the discrete motions of individual charged particles, which interact with self- and externally applied electromagnetic fields. The numerical method tracks "superparticles" across a nonphysical mathematical grid, which is used at discrete intervals in space, in order to (1) evaluate moments of the distribution function $f(\mathbf{x}, \mathbf{v}, t)$, (2) calculate the macroscopic

electromagnetic fields associated with the charge and current densities of the charged particles within each of the grid cells, and (3) subsequently push the particles to new positions in the grid, over a discrete time step, using the calculated electromagnetic forces. Such an ensemble of particles can be tracked numerically throughout time and space, while maintaining good accuracy, stability, and energy conservation. Therefore, the method was shown in Sec. 3.3 to be an invaluable resource for computational plasma physicists. This Appendix provides further details regarding the LSP code which were not discussed in Sec. 3.3, and the reader should first review that Section.

B.1 Particle and force weighting

Since the fields are known only on the grid and particles move within the grid's cells, the PIC code must use some method of particle and force *weighting* in order to calculate (1) the fields on the grid from the particles and (2) the forces on the particles from the grid. A single particle is labeled by its position and velocity, x_i and v_i. Field quantities are discretely defined on the edges of the grid's cells and are labeled as E_j and B_j (B_j values are defined as normal to the faces of the grid's cells). Particle quantities are connected to field quantities by calculating the charge and current densities on the grid in some manner according to the actual particle positions and velocities within the grid. The process of charge and current density assignment to the grid implies an interpolative weighting to the grid points that is dependent on particle position. Once the new fields are solved on the grid from the grid densities, the field values are then interpolated via another weighting from the grid to the particles in order to apply the appropriate force to each particle.

In nearest grid point (NGP) weighting [Birdsall and Langdon, 1985], also

called zero-order weighting, only the number of particles $N(j)$ with charge q within distance $\pm\Delta x/2$ about the j^{th} grid point X_j are counted and assigned to that point (where Δx is the grid's cell width). Then, the related grid charge density is $q\,N(j)/\Delta x$ in $1D$, and the related grid current density takes into account the average particle velocities for the various species about the same grid point. The resultant electromagnetic fields at X_j will be the same for all particles in the j^{th} cell ($D_j := \{X_j - \frac{\Delta x}{2}, X_j + \frac{\Delta x}{2}\}$), such that the electric field $E(x_i) = E_j$ and the magnetic field $B(x_i) = B_j$ for $j \in D_j$. When a particle crosses through a cell boundary into (or out of) the j^{th} cell, the grid densities of that cell discretely increase (or decrease) and, thus, the densities and fields in a PIC code using NGP weighting can be relatively noisy in space and time if care is not taken. Extension to $2D$ and $3D$ is phenomenologically the same, although extra grid points are present and various techniques may be used for weighting in multiple directions.

LSP can be used with either a first-order (linear) cloud-in-cell (CIC) or particle-in-cell (PIC) weighting algorithm. The CIC model is a first-order weighting scheme that assigns densities to the nearest j and $j+1$ grid points by linear interpolation (or bilinear and trilinear "area weighting" in $2D$ and $3D$, due to its geometric interpretation). The charged particles are then finite-size rigid clouds which may pass through each other. The nominal cloud is one cell wide with its center at x_i (and thus extends through two cells in $1D$, four cells in $2D$, and eight cells in $3D$). The cloud-in-cell weighting scheme then assigns the fraction of the cloud in the j^{th} cell to the X_j grid point and assigns the fraction of the cloud in the $(j+1)^{th}$ cell to the X_{j+1} grid point. This weighting is the same as applying NGP interpolation to each elemental part. The viewpoint called particle-in-cell (PIC), or PIC modeling, is that

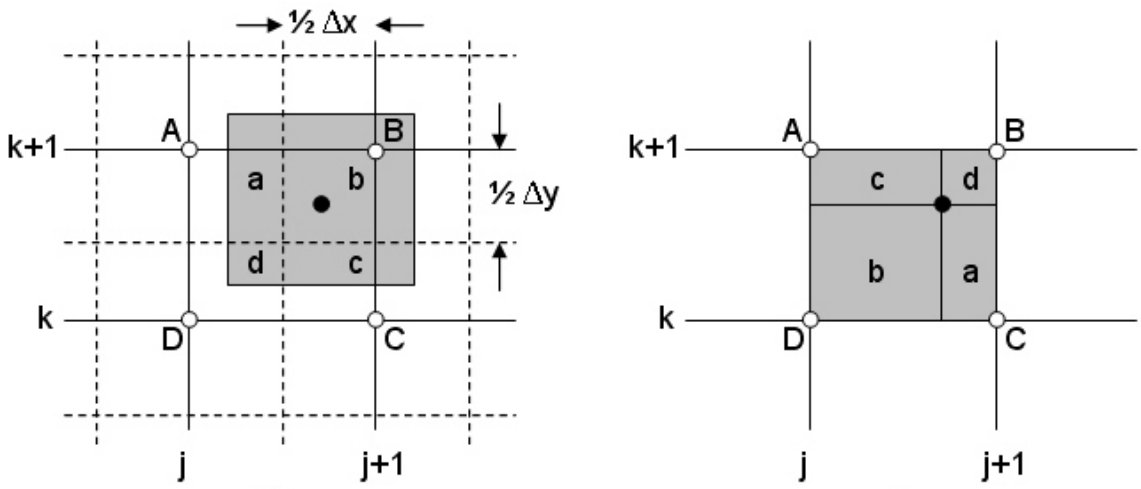

Figure B.1: Charge assignment for linear weighting in $2D$ [Birdsall and Langdon, 1985]. Area labels are assigned to grid points as if by nearest grid point weighting. The black dot is the particle location and the gray area is the spatial extent of the particle's density in the cloud-in-cell (left) and bilinear particle-in-cell (right) interpretations.

assignment of a point charge at x_i to its nearest grid points by linear interpolation would produce the same result as CIC weighting. Thus, the linear PIC method is also a first-order weighting scheme, but without the extra grid point look-ups. Figure B.1 is an adaption from [Birdsall and Langdon, 1985] and illustrates that the particle density extends to four cells (in $2D$) in the cloud-in-cell interpretation, but is confined to one cell in the bilinear particle-in-cell interpretation. The cloud-in-cell model reduces noise in the density and field calculations at the expense of relatively more computational resources (over nearest grid point weighting).

The force weighting back to the location of the particle is done similarly. First-order (and higher-order) weighting methods smooth the "roughness" in particle shape because, as the cloud moves through the grid, it contributes to density much more smoothly than with zero-order weight. Roughness is due to the discrete nature of

particles in a particle-in-cell code and, therefore, noise in the densities and fields can be reduced by employing cloud-in-cell or linear particle-in-cell weighting.

Generally, the grid charge density ρ_j is obtained from the charges q_i located at positions x_i by $\rho_j \equiv \rho(X_j) = \sum_i \, q_i \, S(X_j - x_i)$, where S is the interpolating function of any order, also known as the "weight function" or "assignment function shape" [Birdsall and Langdon, 1985]. The choice of weight function will set the "cloud shape" about the grid point. Care must be taken so that the charge on the grid is the same as the total particle charge (*i.e.*, $\Delta x \, \sum_j \, \rho_j = \sum_i \, q_i$). Also, the contribution to the grid charge density should be the same and correct no matter where the particle is located [*i.e.*, $\Delta x \, \sum_j \, S(X_j - x_i) = 1$ for a particle at x_i].

B.2 Explicit "leap-frog" particle-push algorithm

Once the fields are calculated on the grid and interpolated to the particle positions within the grid's cells, the particle-in-cell code uses a kinematic algorithm to move ("push") particles to new locations according to an equation of motion, with the interpolated forces as known variables. One common (fast) algorithm used to move particles by updating their momenta to new values at every time step is called the explicit "leap-frog" method, as discussed in Sec. 3.3 [Birdsall and Langdon, 1985]. The two first-order differential equations separately integrated for each individual (explicit) particle of mass m are $m \, \mathrm{d}\mathbf{v}/\mathrm{dt} = \mathbf{F}$ and $\mathrm{d}\mathbf{x}/\mathrm{dt} = \mathbf{v}$, where $\mathbf{F}$ is the force. Using finite-difference methods, the two equations are replaced with

$$m \, \frac{\mathbf{v}_{new} - \mathbf{v}_{old}}{\Delta t} = \mathbf{F}_{old} \tag{B.1}$$

$$\frac{\mathbf{x}_{new} - \mathbf{x}_{old}}{\Delta t} = \mathbf{v}_{new} \ , \tag{B.2}$$

where Δt is the discrete time step and must satisfy $\omega_p^{peak}\,\Delta t < 1$ and $\omega_c^{peak}\,\Delta t < 1$ for numerical stability (as in Sec. 3.3), where ω_p^{peak} and ω_c^{peak} are the peak expected plasma and cyclotron frequencies, respectively. A staggered time interval is used such that a given x_i and v_i are not known simultaneously, but are shifted relative to each other by $\Delta t/2$, because $\mathbf{v}_{new}$ is used for the transition between two positions, $\mathbf{x}_{old}$ and $\mathbf{x}_{new}$ (whereas x_i and F_i are known simultaneously). Hence, this integration scheme is known as the "leap-frog" method.

Naturally, the initialization step at the beginning of the simulation must carefully take the time shift into account because of the nature of the time-staggering. For example, consider the $1D$ case for $\mathbf{F} = q\,\mathbf{E} + q\,\mathbf{v} \times \mathbf{B}$ with $\mathbf{B} = B_0\,\hat{z}$ and $\mathbf{E} = E(t)\,\hat{x}$. First, the algorithm calculates $v(t + \frac{\Delta t}{2})$ from $v(t - \frac{\Delta t}{2})$. A centered-in-time and centered-in-space (CTCS) scheme is (with t' and t'' as dummy variables and $t - \Delta t/2 < t' < t'' < t + \Delta t/2$) [Birdsall and Langdon, 1985]:

First half acceleration

$$\begin{bmatrix} v_x(t') \\ v_y(t') \end{bmatrix} = \begin{bmatrix} v_x(t - \frac{\Delta t}{2}) + \frac{q}{m}\,E(t)\,\frac{\Delta t}{2} \\ v_y(t - \frac{\Delta t}{2}) \end{bmatrix} \tag{B.3}$$

Rotation of $\boldsymbol{v}$ *from* $\boldsymbol{B}$

$$\begin{bmatrix} v_x(t'') \\ v_y(t'') \end{bmatrix} = \begin{bmatrix} cos(\omega_c\,\Delta t) & sin(\omega_c\,\Delta t) \\ -sin(\omega_c\,\Delta t) & cos(\omega_c\,\Delta t) \end{bmatrix} \begin{bmatrix} v_x(t') \\ v_y(t') \end{bmatrix} \tag{B.4}$$

Second half acceleration

$$\begin{bmatrix} v_x(t+\frac{\Delta t}{2}) \\ v_y(t+\frac{\Delta t}{2}) \end{bmatrix} = \begin{bmatrix} v_x(t'') + \frac{q}{m}\, E(t)\, \frac{\Delta t}{2} \\ v_y(t'') \end{bmatrix}, \tag{B.5}$$

where q is the particle charge and $\omega_c = q\, B_0/m$ is the electron cyclotron frequency. Second, the algorithm updates the particle position to $x(t+\Delta t)$ from $x(t)$ and $v(t+\frac{\Delta t}{2})$ according to the equation

$$x(t+\Delta t) = \left[x(t) + v\left(t + \frac{\Delta t}{2}\right)\, \Delta t \right]. \tag{B.6}$$

To allow temporal ensemble evolution, this process is then executed in a loop.

B.3 Explicit vs. implicit equation solvers

As discussed in Sec. 3.3, although explicit methods for solving the field equations and equations of motion are the fastest available to particle-in-cell simulation because of their simplicity, *implicit* methods have been developed for field solvers [Welch *et al.*, 2004] and particle-pushing [Friedman, 1990] in order to alleviate some of the restrictions on the choice of time step. The main difference between explicit and implicit schemes for solving systems of differential equations is found in the domain dependence of the problem. In contrast to explicit methods, implicit methods solve for all the quantities simultaneously and require knowledge of those quantities at all grid positions at the preceding time step in order to proceed (rather than only those at adjacent grid points and the preceding time step); the field and

particle equations to be integrated form a large system of coupled nonlinear equations. The domain of dependence for an implicit method is larger than the domain of known quantities at the preceding time step; the boundary conditions are the extra sources of information. Therefore, all the unknown points at the next time step fall within the domain of uniqueness established by the characteristic trajectories beginning from the boundary points. The result is significant: there is no restriction on the computational time step. Thus, implicit methods do not enforce the stringent Courant condition for electromagnetic waves, which usually sets the maximum size of the time step in explicit electromagnetic simulations (the particle Courant condition must still be met). Also, the grid aspect ratio requirement for stability in explicit methods is relaxed substantially for implicit methods.

The most significant advantage of implicit methods is the extension of simulation techniques to kinetic phenomena on slower time scales, so that simulations can take larger time steps. Implicit time integration allows the code to model long-time scale behavior by altering the governing equations in order to eliminate uninteresting high frequency modes, and utilizes finite-differenced equations that are both stable at large time steps and accurate for simulating low frequency phenomena. Implicit techniques typically allow the under-resolution of either ω_p or ω_c (whichever is greatest), but not both simultaneously. Therefore, even modest magnetic field values can hinder the use of a larger time step, which would otherwise allow implicit PIC simulations to compete with other reduced numerical models in terms of required computational resources. However, it is acceptable to solve the fields implicitly while pushing the particles with an explicit integration of the equations of motion, as described earlier [Birdsall and Langdon, 1985]. The time step in such simulations may then be

increased from the electromagnetic wave Courant condition to the particle Courant condition, so long as ω_p and ω_c for each species are still resolved, and the result may be an increase in time step by as much as a factor of 10 to 100, depending on the simulation parameters.

A major issue for implicit techniques is the more complicated time-cycle splitting. As mentioned in Sec. B.2, explicit differencing splits the time-cycle between advancing particles and fields whose calculations alternate (and move forward independently). An implicit numerical simulation, however, must solve a coupled set of nonlinear equations by inverting a large matrix: the future positions $\mathbf{x}_{new}$ depend on the accelerations $\mathbf{a}_{new}$ due to the $\mathbf{F}_{new}$, but the $\mathbf{F}_{new}$ values depend on the new charge and current densities from the new particle positions. Particle boundary conditions in implicit codes can make the situation even more complex. For example, the deletion or emission of particles at (or from) a surface depends on $\mathbf{F}_{new}$ and, therefore, the particle boundary conditions also enter into the implicit equations.

B.4 Implicit field-solving algorithms

Four field-solving algorithms are available in the LSP particle-in-cell code: (1) an electromagnetic, explicit, "leap-frog" algorithm; (2) an iterative, electromagnetic, alternating-direct-implicit (ADI) algorithm; (3) a non-iterative, "unconditionally stable", electromagnetic, implicit ADI algorithm [Welch *et al.*, 2004]; and (4) an iterative, electrostatic successive-over-relaxation (SOR) algorithm. There is also an option to solve the electrostatic fields using the iterative ADI method. Therefore, the LSP simulator has the choice of solving the electrostatic or electromagnetic field equations in an explicit or implicit manner, depending on the situation involved.

Except for the large-space scale and long-time scale plasma flow simulations in Chapters 5 and 6, all of the simulations in this thesis solved the electromagnetic fields with the non-iterative "unconditionally stable" alternating-direct-implicit technique, due to its speed (compared to the iterative ADI method) and the allowed relaxation on time step (increased to the particle Courant condition) and grid aspect ratio (increased up to $\sim 10:1$, in some cases), as discussed in Secs. 3.3 and B.3. The plasma flow simulations solved the electromagnetic fields with the explicit, "leap-frog" technique, because resolution of the large ω_c^{peak} by the time step Δt in strong solenoidal magnetic fields ($B_z \sim 30 - 150$ kG) already ensured satisfaction of the electromagnetic wave Courant condition in those simulations. Also, every simulation in this thesis treated all particle species as explicit and kinetic, resolved ω_{pe} and Ω_{ce} (the electron plasma and cyclotron frequencies, respectively), used the cloud-in-cell model, was not susceptible to the so-called numerical Debye length instability, and conserved energy to good accuracy levels, as mentioned in Sec. 3.4.

When invoked by the LSP simulator with the IMPLICIT_FIELDS compiler directive, the LSP code employs a conventional alternating-direct-implicit procedure in order to solve the electromagnetic field equations. The field solver includes particle currents using an energy- and charge-conserving variation of the traditional alternating-direct-implicit method, and will be described in the following paragraphs. The procedure may also be called upon to solve the electrostatic field equations when the STATIC_FIELDS compiler directive is used in conjunction with the IMPLICIT_FIELDS compiler.

In order to solve the electromagnetic field equations, one implementation is to predict the future field values by linearizing the particle-field equations. The "direct

method" works directly with the particle equations of motion and the equations which couple the particles to the fields. The equations are linearized about extrapolated (estimated) values for the next time step. An interesting class of methods (known as *alternating direction*, *splitting*, or *fractional steps*) can solve a complicated multi-dimensional problem by breaking it down into simpler $1D$ problems for successive solving. The fractional time step method breaks up an equation into a sequence of difference equations using smaller time steps that are fractions of the actual discrete time step, where the fraction is the inverse dimensionality of the problem. To advance from one fractional time to the next, the algorithm must only invert a $1D$ implicit operator of tri-diagonal form. In order to apply a fractional time step method to a steady state problem, the derivative terms in the other directions must be retained at each fractional time step, but evaluated at the previous or otherwise known fractional time level.

First, the alternating-direct-implicit field-solver integrates Maxwell's equations over one time step for numerical stability with an integrating factor, which facilitates the integration because of the fundamental theorem of calculus. The LSP code allows for arbitrary orthogonal coordinate systems, as well as arbitrary electric permittivity and magnetic permeability. Maxwell's equations, once Taylor-expanded to first-order and finite-differenced, yield a set of equations (in cylindrical geometry, here) for (E_r, E_θ, E_z) and (B_r, B_θ, B_z) at time step t^{n+1} in terms of field quantities known at the preceding two time-staggered steps, $t^{n+\frac{1}{2}}$ and t^n (a result related to staggered "leap-frog" particle-pushing, as in Sec. B.2, and *not* to be confused with fractional time steps). Second, the set of field equations are solved iteratively using an energy- and charge-conserving variation on the ADI method. The ADI method

is reasonably fast and does not require large amounts of computer memory because it transforms a large, sparse matrix problem into a simpler, banded matrix problem. Normally, the direct inversion of a $3D$ sparse matrix is quite costly.

In the alternating-direct-implicit method, only the field values in one direction are treated implicitly in each fractional step, and so the runtime is reasonably fast (linear). In each step, there are $i-1$ equations and $i+1$ unknowns for each row of grid points, such that the two boundary conditions for the implicit direction need to be used to solve the system. Then, an inverter algorithm is used to easily solve the tri-diagonal system of equations in each fractional step in about as much computation time as an explicit method. Therefore, evaluation of the fields at t^{n+1} consists only of solving ("sweeping") a succession of tri-diagonal linear systems; each sweep in each direction involves the inversion of one tri-diagonal matrix. In the conventional ADI method, the procedure iterates until convergence to a user-specified tolerance is reached. Since this fractional method solves the fields implicitly in each direction while treating the other directions explicitly, the Courant condition on Δt and grid cell aspect ratio restrictions can be relaxed. The conventional alternating-direct-implicit method is unconditionally stable in $2D$ with second-order accuracy, but unfortunately does not generalize to greater dimensionality in a way that retains unconditional stability and second-order accuracy. In $3D$, the conventional ADI method leads to a conditionally stable and first-order accurate (in time) scheme.

The LSP simulator can also set the convergence acceleration parameter for dynamic alternating-direct-implicit solution, which can increase solving speed. Dynamic alternating-direct-implicit methods also iteratively solve for field quantities by the sweeping method described above, except each sweep requires the inversion of

a matrix which includes two additional higher (second) time derivative terms in the transverse directions (recall that the original finite-differencing retains the first time derivative terms in the transverse directions at each fractional time step). Then, the first derivative terms have an acceleration parameter appended to them to help reach convergence with fewer iterations. The dynamic alternating-direct-implicit solver adjusts the acceleration parameter from one iteration to the next such that the slowest decaying eigenmode of the solution is critically damped (reduces the first derivative for large variations and increases it for small variations). This method can decrease the number of iterations required to reach convergence, as well as decrease the total computational effort involved.

When invoked by the LSP simulator with the EXACT_IMPLICIT compiler directive, the LSP code employs an "unconditionally stable" alternating-direct-implicit procedure to solve the electromagnetic field equations [WELCH *et al.*, 2004]. This implicit field solver involves two half time step field advances with convenient time-centering for the $\nabla \times \mathbf{E}$ and $\nabla \times \mathbf{B}$ terms. While the "unconditionally stable" electromagnetic algorithm makes use of the alternating-direct-implicit technique, certain modifications have been implemented to make it faster by removing the requirement of iteration to reach convergence. The resulting technique has been shown to have unconditional stability without time step satisfaction of the electromagnetic wave Courant condition in $3D$, in the absence of wave-transmitting boundaries (and improved stability with such boundaries). Therefore, the algorithm enables the LSP simulator to execute faster and numerically stable particle-in-cell simulations in an accurate manner.

The procedure is initially similar to the conventional alternating-direct-implicit method in that Maxwell's equations are finite-differenced using a backward-in-time

and centered-in-space (BTCS) scheme. However, in the "unconditionally stable" method, Maxwell's equations are separated into two $\Delta t/2$ pushes, which are found in [Welch *et al.*, 2004]. The second push solves for the full time step field values ($\mathbf{E}^{n+1}$ and $\mathbf{B}^{n+1}$) using the intermediate field values ($\mathbf{E}^{n+\frac{1}{2}}$ and $\mathbf{B}^{n+\frac{1}{2}}$ from the first push). In each set of equations for each half push, the three sets of equations for each direction are solved directly because they are combined into an easily inverted tri-diagonal matrix. The two half sets of equations sum to the original implicit field equations, except for the contribution from off-diagonal terms in the susceptibility tensor, which can be chosen for inclusion or exclusion by the simulator, depending on the problem under investigation. Since no iterations are required, the electromagnetic equations are solved much faster than the traditional alternating-direct-implicit method. Although, for each half time step, the set of equations are not centered in the $\nabla\times$ operators (*e.g.*, B_x^{n+1} and $B_y^{n+\frac{1}{2}}$ terms in the equation for E_z^{n+1}). The lack of centering is suspected to affect high-frequency electromagnetic wave phenomena, which the simulator usually intends to damp anyway, since they generally contribute to nonphysical noise. The conventional iterative alternating-direct-implicit field-solver and the "unconditionally stable" ADI field-solver have yielded nearly identical results in all tests by the LSP authors to date.

B.5 Particle interpolation options

The particle species to be simulated must be specified in the LSP code, and two particle parameters are particularly important for explicit particle-pushing according to a "leap-frog" method similar to the one discussed in Sec. B.2.

First, the choice between linear particle-in-cell and cloud-in-cell interpolation

schemes for particle and force weighting must be made, as discussed in Sec. B.1. The EXTENDED_PARTICLES compiler directive in the LSP code invokes the cloud-in-cell interpolation technique, wherein particles contribute charge and current densities to grids adjacent to the ones in which they reside. When the mentioned compiler directive is not invoked, the linearly weighted particle-in-cell interpolation scheme is used, wherein the particles employ nearest grid point weighting for longitudinal interpolation and bilinear weighting in the transverse directions (an equivalent interpolation for electrostatic simulations is called trilinear weighting). The same is true in the cloud-in-cell scheme, except particle contributions to fields extend over more cells in order to reduce particle noise, the effectiveness of which increases with dimensionality. The use of linear interpolations in all directions for assigning particle contributions to the fields known on the grid is not common in electromagnetic simulations, as it requires additional coding to correct for charge errors.

Second, the choice of a momentum-conserving or an energy-conserving particle-pushing method needs to be made. The important distinction between this and the previous option is that the interpolation now under discussion is the one from the forces on the grid to the particles within the grid, in order to determine the new velocities of the individual particles. Recall from Sec. 3.3 that particle-pushing algorithms can only conserve momentum or energy, but not both at the same time. In the LSP code, electromagnetic simulations always conserve charge via an algorithm that pushes particles such that Poisson's equation is satisfied. In order for energy conservation to occur, the charge-conserving algorithm is required (for symmetry); the same is not true for the momentum-conserving particle forces option.

The AVERAGED particle forces option for particle species in the LSP code employs

spatially-averaged fields from the grid to calculate forces on the particles within the grid. This option is good for momentum conservation since there are no "self-forces" on the particles and self-fields are generated at no cost to the particle's energy, since the interpolation of the forces on the grid to the particles *are the same* in the longitudinal and transverse directions. Since the fields are interpolated linearly in all directions, this interpolation of the forces on the grid to the particles within the grid is called the momentum-conserving linear particle-in-cell method (it is not recommended for use in the cloud-in-cell interpretation). However, this method is subject to the so-called Debye-length numerical instability, which heats particles until their Debye length reaches the size of the grid cell size (so care must be taken during simulation set-up).

The PRIMARY particle forces option in the LSP code employs the fields directly calculated from the electromagnetic solution on the particles, and produces an energy-conserving push that is not susceptible to the Debye-length numerical instability (the simulation is also numerically stable for grid sizes larger than the plasma skin depth). This interpolation of the forces on the grid to the particles within the grid is equivalent to the interpolation of the particle density contributions to the fields on the grid mentioned above, resulting in an energy-conserving algorithm. Species participating in such an energy-conserving particle-push algorithm (whether linear PIC or CIC) generate self-fields by losing energy, and necessarily feel self-forces due to the fact that the interpolation of the grid forces to the particles *are not the same* in the longitudinal and transverse directions. Therefore, momentum is not instantaneously conserved, but self-forces integrate to zero as a particle crosses one cell width. Cloud-in-cell particles experience reduced self-forces compared to linear particle-in-cell particles (by two

in $1D$, four in $2D$, and eight in $3D$) because the forces are integrated over more cells, yielding smaller net forces and better instantaneous momentum conservation; this is the underlying reason why cloud-in-cell weighted particles contribute less particle noise than linear particle-in-cell particles (although both weighting schemes reduce noise by the square root of the number of particles-per-cell compared to nearest grid point weighting alone).

B.6 Other packages

The LSP simulator is also responsible for assigning well-posed simulation conditions, including (but not limited to) setting boundary conditions, creating objects and defining materials' properties in the simulation space, choosing appropriate grid cell sizes and time steps, and implementing diagnostics so that physical insight can be obtained.

Additional complex and sophisticated algorithms implemented in the LSP code include (but are not limited to): direct-implicit particle-pushing and field-solving methods, a hybrid kinetic-fluid electron model, field emission models from object boundaries (stimulated by particle bombardment, field-stress, Child-Langmuir, etc.), auxiliary circuit models, transmission-line boundaries, inclusion of arbitrary electric and magnetic susceptibilities, dispersive magnetic materials, external (applied) electric and magnetic field models, secondary particle generation at surfaces, backscattering, multiple scattering events and energy loss, surface heating and energy deposition, thermal and/or stimulated desorption of neutrals and ions from surfaces, ionization of neutrals, ion stripping, photoionization, and interparticle collisions.

In summary, a generic time step loop in a particle-in-cell simulation includes [Birdsall and Langdon, 1985]:

$\Rightarrow$ Integration of electromagnetic fields on grid (ρ, $\mathbf{J} \rightarrow \mathbf{E}$, $\mathbf{B}$)

$\Rightarrow$ Material effects on electromagnetic fields

$\Rightarrow$ Weighting of forces to particle locations ($\mathbf{E}$, $\mathbf{B} \rightarrow \mathbf{F}$)

$\Rightarrow$ Integration of equations of motion and particle kinematics ($\mathbf{F} \rightarrow \mathbf{v} \rightarrow \mathbf{x}$)

$\Rightarrow$ Particle interactions and sources/sinks (collisions, ionization, material effects, etc.)

$\Rightarrow$ Weighting of densities to grid locations ($\mathbf{x}$, $\mathbf{v} \rightarrow \rho$, $\mathbf{J}$)

$\circlearrowleft \Delta t$

Bibliography

[Anders, 1999] Anders, A. (1999). Approaches to rid cathodic arc plasmas of macro- and nanoparticles: a review. *Surf. Coat. Technol.* **120-121**, 319–330.

[Anders and Yushkov, 1999] Anders, A. and Yushkov, G. Y. (1999). Ion flux from vacuum arc cathode spots in the absence and presence of a magnetic field. *J. Appl. Phys.* **91**, 4824–4832.

[Arfken, 1985] Arfken, G. (1985). *Mathematical Methods for Physicists.* Academic Press, Orlando, FL.

[Ascher and Petzold, 1998] Ascher, U. and Petzold, L. (1998). *Computer Methods for Ordinary Differential Equations and Differential-Algebraic Equations.* SIAM Press, Philadelphia.

[ATI, 2006] ATI (2006). Acree Technologies Incorporated. Private communication.

[Badger *et al.*, 1984] Badger, B., Beckert, K., Bock, R., Boehne, D., Bozsik, I., Brezina, J., Corradini, M., El-Guebaly, L., Engelstad, R., Froehlich, R., Goel, B., Henderson, D., Hoebel, W., Hofmann, I.,

Jahnke, A., Keller, R., Kessler, G., Klein, A., Kreutz, R., Kulcinski, G., Larsen, E., Lessmann, E., Long, K., Lovell, E., von Moellendorff, U., Moritz, N., Moses, G., Mueller, R., Peterson, R., Plute, K., Pong, L., Rungea, H., Sawan, M., Schretzmann, K., Sviatoslavsky, I., Symon, K., Sze, D., Tahir, N., Vogelsang, W., White, A., and Wollnik, H. (1984). HIBALL-II - An Improved Conceptual Heavy Ion Beam Driven Fusion Reactor Study. *University of Wisconsin Fusion Technology Institute Report UWFDM-625* .

[Barnard, 2006] Barnard, J. J. (2006). Private communication.

[Barnard *et al.*, 2007] Barnard, J. J., Friedman, A., Kaganovich, I. D., Logan, B. G., Marinak, M. M., More, R. M., Penn, G. E., Sefkow, A. B., Santhanam, P., Welch, D., , and Wurtele, J. S. (2007). Theory and simulation of warm dense matter targets. *Nucl. Instrum. and Methods A* **577**, 275–283.

[Bashforth and Adams, 1883] Bashforth, F. and Adams, J. C. (1883). *Theories of Capillary Action.* Cambridge University Press, London.

[Beyer, 1987] Beyer, W. H. (1987). *CRC Standard Mathematical Tables.* CRC Press, Boca Raton, Florida.

[Bieniosek *et al.*, 2005a] Bieniosek, F., Baca, D., Roy, P. K., Seidl, P. A., Yu, S. S., Molvik, A. W., Covo, M. K., , and Shiraki, D. (2005a). Diagnostic development for heavy ion based HEDP and HIF experiments. *Bull. Am. Phys. Soc.* **50**, 46, http://meetings.aps.org/Meeting/DPP05/Event/34615.

[Bieniosek *et al.*, 2005b] Bieniosek, F. M., Eylon, S., Faltens, A., Friedman, A., Kwan, J. W., Leitner, M. A., Molvik, A. W., Prost, L., Roy, P. K., Seidl, P. A., and Westenskow, G. (2005b). Diagnostics for intense heavy-ion beams in the HIF-VNL. *Nucl. Instrum. and Methods A* **544**, 268–276.

[Birdsall and Langdon, 1985] Birdsall, C. K. and Langdon, A. B. (1985). *Plasma Physics via Computer Simulation.* McGraw-Hill Book Company, New York.

[Callahan, 1996] Callahan, D. A. (1996). Chamber propagation physics for heavy ion fusion. *Fusion Eng. Des.* **32-3**, 441–452.

[Callahan-Miller and Tabak, 1999] Callahan-Miller, D. A. and Tabak, M. (1999). Increasing the coupling efficiency in a heavy ion, inertial confinement fusion target. *Nucl. Fusion* **39**, 1547–1556.

[Chandrasekhar, 1961] Chandrasekhar, S. (1961). *Hydrodynamic and Hydromagnetic Stability.* Oxford University Press, London.

[Chen, 1984] Chen, F. F. (1984). *Plasma Physics and Controlled Fusion.* Plenum Press, New York.

[Christofilos *et al.*, 1964] Christofilos, N. C., Hester, R. E., Lamb, W. A. S., Reagan, D. D., Sherwood, W. A., and Wright, R. E. (1964). High current linear induction accelerator for electrons. *Rev. Sci. Instrum.* **35**, 886.

[Covo *et al.*, 2006a] Covo, M. K., Molvik, A. W., Friedman, A., Vay, J.-L., Seidl, P. A., Logan, B. G., Baca, D., and Vujic, J. L. (2006a). Absolute measurement of electron-cloud density in a positively charged particle beam. *Phys. Rev. Lett.* **97**, 054801.

[Covo *et al.*, 2006b] Covo, M. K., Molvik, A. W., Friedman, A., Westenskow, G., Barnard, J. J., Cohen, R., Seidl, P. A., Kwan, J. W., Logan, B. G., Baca, D., Bieniosek, F., Celata, C. M., Vay, J.-L., and Vujic, J. L. (2006b). Beam energy scaling of ion-induced electron yield from K^+ impact on stainless steel. *Phys. Rev. ST Accel. Beams* **9**, 063201.

[Cuneo *et al.*, 2006] Cuneo, M. E., Vesey, R. A., Bennett, G. R., Sinars, D. B., Stygar, W. A., Waisman, E. M., Porter, J. L., Rambo, P. K., Smith, I. C., Lebedev, S. V., Chittenden, J. P., Bliss, D. E., Nash, T. J., Chandler, G. A., Afeyan, B. B., Yu, E. P., Campbell, R. B., Adams, R. G., Hanson, D. L., Melhorn, T. A., and Matzen, M. K. (2006). Progress in symmetric ICF capsule implosions and wire-array z-pinch source physics for double-pinch-driven hohlraums. *Plasma Phys. Control. Fusion* **48**, R1–R35.

[Davidson, 2001] Davidson, R. C. (2001). *Physics of Nonneutral Plasmas.* World Scientific, Singapore.

[Davidson *et al.*, 2006] Davidson, R. C., Logan, B. G., Barnard, J. J., Bieniosek, F. M., Briggs, R. J., Callahan, D. A., Covo, M. K., Celata, C. M., Cohen, R. H., Coleman, J. E., Debonnel, C. S., Grote, D. P., Efthimion, P. C., Eylon, S., Friedman, A., Gilson, E. P., Grisham, L. R., Henestroza, E., Kaganovich, I. D., Kwan, J. W., Lee, E. P., Lee, W. W., Leitner, M., Lund, S. M., Meier, W. R., Molvik, A. W., Olson, C. L., Penn, G. E., Qin, H., Roy, P. K., Rose, D. V., Sefkow, A. B., Seidl, P. A., Sharp, W. M., Startsev, E. A., Tabak, M., Thoma, C.,

Vay, J.-L., Waldron, W. L., Wurtele, J. S., Welch, D. R., Westenskow, G. A., and Yu, S. S. (2006). US heavy ion beam research for high energy density physics applications and fusion. *Journal de Physique IV* **133**, 731–741.

[Davidson and Qin, 2001] Davidson, R. C. and Qin, H. (2001). *Physics of Intense Charged Particle Beams in High Energy Accelerators.* World Scientific, Singapore.

[Davidson and Qin, 2005] Davidson, R. C. and Qin, H. (2005). Kinetic description of neutralized drift compression and transverse focusing of intense ion charge bunches. *Phys. Rev. ST Accel. Beams* **8**, 064201.

[Davidson and Startsev, 2004] Davidson, R. C. and Startsev, E. A. (2004). Self-consistent Vlasov-Maxwell description of the longitudinal dynamics of intense charged particle beams. *Phys. Rev. ST Accel. Beams* **7**, 024401.

[Dunaevsky and Fisch, 2004] Dunaevsky, A. and Fisch, N. J. (2004). Measuring the plasma density of a ferroelectric plasma source in an expanding plasma. *J. Appl. Phys.* **95**, 4621–4626.

[Dunaevsky *et al.*, 2001a] Dunaevsky, A., Krasik, Y. E., Felsteiner, J., Dorfman, S., Berner, A., and Sternlieb, A. (2001a). Lifetime of ferroelectric cathodes. *J. Appl. Phys.* **89**, 4480–4485.

[Dunaevsky *et al.*, 2001b] Dunaevsky, A., Krasik, Y. E., Felsteiner, J., and Sternlieb, A. (2001b). Electron diode with a large area ferroelectric plasma cathode. *J. Appl. Phys.* **90**, 3689–3698.

[Efthimion *et al.*, 2007] Efthimion, P. C., Gilson, E. P., Davidson, R. C., Grisham, L., Logan, B. G., Seidl, P. A., Waldron, W. L., and Yu, S. S. (2007). Ferroelectric plasma source for heavy ion beam charge neutralization. *Nucl. Instrum. and Methods A* **577**, 203–206.

[Efthimion *et al.*, 2003] Efthimion, P. C., Gilson, E. P., Grisham, L., Davidson, R. C., Yu, S. S., and Logan, B. G. (2003). RF plasma source for heavy ion beam charge neutralization. In *Proceedings of the 2003 Particle Accelerator Conference*, pages 2661–2663, http://ieeexplore.ieee.org/xpls/abs_all.jsp?arnumber=1289222.

[Efthimion *et al.*, 2005a] Efthimion, P. C., Gilson, E. P., Grisham, L., Davidson, R. C., Yu, S. S., Waldron, W. L., and Logan, B. G. (2005a). Development of a 1-m plasma sorce for heavy ion beam charge neutralization. *Nucl. Instrum. and Methods A* **544**, 378–382.

[Efthimion *et al.*, 2005b] Efthimion, P. C., Gilson, E. P., Grisham, L., Davidson, R. C., Yu, S. S., Waldron, W. L., and Logan, B. G. (2005b). Ferroelectric plasma source for heavy ion beam charge neutralization. In *Proceedings of the 2005 Particle Accelerator Conference*, pages 2452–2454, http://ieeexplore.ieee.org/xpls/abs_all.jsp?arnumber=1591142.

[FEAC, 1993] FEAC (1993). *Advice and Recommendations to the U.S. Department of Energy in Response to the Charge Letter of September 18, 1992.* Fusion Energy Advisory Committee, U.S. Department of Energy, Washington, DC.

[Fisher and Gould, 1971] Fisher, R. K. and Gould, R. W. (1971). Resonance cones in field pattern of a radio frequency probe in a warm anisotropic plasma. *Phys. Fluids* **14**, 857.

[FPAC, 1990] FPAC (1990). *Fusion Policy Advisory Committee Final Report, DOE/S-0081.* U.S. Department of Energy, Washington, DC.

[Friedman, 1990] Friedman, A. (1990). A 2nd-order implicit particle mover with adjustable damping. *J. Comp. Phys.* **90**, 292–312.

[Friedman, 2006] Friedman, A. (2006). Private communication.

[Gilson, 2006] Gilson, E. P. (2006). Private communication.

[Goldston and Rutherford, 1995] Goldston, R. J. and Rutherford, P. H. (1995). *Introduction to Plasma Physics.* Institute of Physics Publishing, Bristol and Philadelphia.

[Griffiths, 1998] Griffiths, D. J. (1998). *Introduction to Electrodynamics (3rd Edition).* Prentice Hall, New Jersey.

[Henestroza, 2006] Henestroza, E. (2006). Private communication.

[Henestroza *et al.*, 2004] Henestroza, E., Eylon, S., Roy, P. K., Yu, S. S., Anders, A., Bieniosek, F. M., Greenway, W. G., Logan, B. G., MacGill, R. A., Shuman, D. B., Vanecek, D. L., Waldron, W. L., Sharp, W. M., Houck, T. L., Davidson, R. C., Efthimion, P. C., Gilson, E. P., Sefkow, A. B., Welch, D. R., Rose, D. V., and Olson, C. L. (2004). Design and characterization of a neutralized-transport experiment for heavy-ion fusion. *Phys. Rev. ST Accel. Beams* **7**, 083501.

[HIFS-VNL, 2001] HIFS-VNL (2001). Figure adapted from the Heavy Ion Fusion Science Virtual National Laboratory webpage. *http://hif.lbl.gov/tutorial/tutorial.html* .

[Higham, 1996] Higham, N. J. (1996). *Accuracy and stability of numerical algorithms.* Society of Industrial and Applied Mathematics, Philadelphia.

[Hughes *et al.*, 1999] Hughes, T. P., Yu, S. S., and Clark, R. E. (1999). Three-dimensional calculations for a 4 kA, 3.5 MV, 2 microsecond injector with asymmetric power feed. *Phys. Rev. ST Accel. Beams* **2**, 110401.

[Humprhries, 1986] Humprhries, S. (1986). *Principles of Charged Particle Acceleration.* John Wiley & Sons, Inc., New York. Digital Edition available at http://www.fieldp.com/cpa/cpa.html.

[Hutchinson, 2002] Hutchinson, I. H. (2002). *Principles of Plasma Diagnostics.* Cambridge University Press, London.

[Jeffreys and Jeffreys, 1988] Jeffreys, H. and Jeffreys, B. S. (1988). *Methods of Mathematical Physics.* Cambridge University Press, Cambridge, England.

[Jung, 2006] Jung, J. Y. (2006). Private communication.

[Juttner, 1987] Juttner, B. (1987). Characterization of the cathode spot. *IEEE Trans. Plasma Sci.* **15**, 474–480.

[Kaganovich *et al.*, 2007] Kaganovich, I. D., Sefkow, A. B., Startsev, E. A., Davidson, R. C., and Welch, D. R. (2007). Effects of finite pulse length, magnetic field, and gas ionization on ion beam pulse neutralization by background plasma. *Nucl. Instrum. and Methods A* **577**, 93–102.

[Kaganovich *et al.*, 2001] Kaganovich, I. D., Shvets, G., Startsev, E., and Davidson, R. C. (2001). Nonlinear charge and current neutralization of an ion beam pulse in a pre-formed plasma. *Phys. Plasmas* **8**, 4180–4192.

[Kaganovich *et al.*, 2005] Kaganovich, I. D., Startsev, E. A., Davidson, R. C., and Welch, D. R. (2005). Ion beam pulse neutralization by a background plasma in a solenoidal magnetic field. *Nucl. Instrum. and Methods A* **544**, 383–388.

[Kikuchi *et al.*, 2006] Kikuchi, T., Someya, T., Kawata, S., Nakajima, M., Horioka, K., and Katayama, T. (2006). Beam dynamics simulation during final bunching and transport for heavy ion inertial fusion. *Nucl. Instrum. and Methods A* **558**, 122–126.

[Klimontovich, 1967] Klimontovich, Y. L. (1967). *The Statistical Theory of Non-equilibrium Processes in a Plasma.* MIT Press, Massachusetts.

[Kutta, 1901] Kutta, M. W. (1901). Beitrag zur naherungsweisen integration totaler differentialgleichungen. *Zeit. Math. u. Phys.* **46**, 435–453.

[Lambert, 1987] Lambert, J. D. (1987). *Numerical Methods for Ordinary Differential Equations.* John Wiley & Sons, Chichester.

[Langdon, 1992] Langdon, A. B. (1992). Reactor chamber propagation of heavy ion beams. *Part. Accel.* **37-38**, 175.

[Lawson, 1958] Lawson, J. D. (1958). Perveance and the Bennett pinch relation in partially neutralized electron beams. *J. Electron. Control* **5**, 146.

[Lifschitz *et al.*, 2006] Lifschitz, A. F., Maynard, G., Vay, J.-L., and Lenglet, A. (2006). Dynamics of neutralizing electrons during the focusing of

intense heavy ion beams inside a HIF reactor chamber. *Journal de Physique IV* **133**, 753–755.

[Lifshitz and Pitaevskii, 1981] Lifshitz, E. M. and Pitaevskii, L. P. (1981). *Physical Kinetics.* Pergamon Press, Oxford.

[Lindl, 1995] Lindl, J. D. (1995). Development of the indirect-drive approach to inertial confinement fusion and the target physics basis for ignition and gain. *Phys. Plasmas* **2**, 3933–4024.

[Lindl, 1998] Lindl, J. D. (1998). *Inertial Confinement Fusion: The Quest for Ignition and Energy Gain Using Indirect Drive.* Springer-Verlag, New York.

[Logan *et al.*, 2006] Logan, B. G., Bangerter, R. O., Callahan, D. A., Tabak, M., Roth, M., Perkins, L. J., and Gaporaso, G. (2006). Assessment of potential for ion-driven fast ignition. *Fusion Sci. Tech.* **49**, 399–411.

[Logan *et al.*, 2004] Logan, B. G., Bieniosek, F. M., Celata, C. M., Henestroza, E., Kwan, J. W., Lee, E. P., Leitner, M., Roy, P. K., Seidl, P. A., Eylon, S., Vay, J.-L., Waldron, W. L., Yu, S. S., Barnard, J. J., Callahan, D. A., Cohen, R. H., Friedman, A., Grote, D. P., Covo, M. K., Meier, W. R., Molvik, A. W., Lund, S. M., Davidson, R. C., Efthimion, P. C., Gislon, E. P., Grisham, L. R., Kaganovich, I. D., Qin, H., Startsev, E. A., Rose, D. V., Welch, D. R., Olson, C. L., Kishek, R. A., O'Shea, P., Haber, I., and Prost, L. R. (2004). Overview of US heavy ion fusion research. *Nucl. Fusion* **45**, 131–137.

[Logan *et al.*, 2007] Logan, B. G., Bieniosek, F. M., Celata, C. M., Kwan, J. W., Henestroza, E., Lee, E. P., Leitner, M., Roy, P. K., Seidl, P. A., Vay, J.-L., Waldron, W. L., Yu, S. S., Barnard, J. J., Cohen, R. H., Friedman, A., Grote, D. P., Covo, M. K., Molvik, A. W., Lund, S. M., Meier, W. R., Davidson, R. C., Efthimion, P. C., Gilson, E. P., Grisham, L., Kaganovich, I. D., Qin, H., Sefkow, A. B., Starsev, E. A., Welch, D. R., and Olson, C. (2007). Recent U.S. advances in ion-beam-drive high energy density physics and heavy ion fusion. *Nucl. Instrum. and Methods A* **577**, 1–7.

[Logan and Callahan, 1998] Logan, B. G. and Callahan, D. A. (1998). Beam charge and current neutralization of high-charge-state heavy ions. *Nucl. Instrum. and Methods A* **415**, 468–472.

[LSP, 1999] LSP (1999). LSP is a software product of ATK Mission Research, Albuquerque, NM 87110.

[Lund and Davidson, 1998] Lund, S. M. and Davidson, R. C. (1998). Warm-fluid description of intense beam equilibrium and electrostatic stability properties. *Phys. Plasmas* **5**, 3028–3053.

[MacGill *et al.*, 1998] MacGill, R. A., Dickinson, M. R., Anders, A., Monteiro, O. R., and Brown, I. G. (1998). Streaming metal plasma generation by vacuum arc plasma guns. *Rev. Sci. Instrum.* **69**, 801–803.

[MacLaren *et al.*, 2002] MacLaren, S. A., Faltens, A., Seidl, P. A., and Rose, D. V. (2002). Results from a scaled final focus experiment for heavy ion fusion. *Phys. Plasmas* **9**, 1712–1720.

[Marinak *et al.*, 2001] Marinak, M. M., Kerbel, G. D., Gentile, N. A., Jones, O., Munro, D., Pollaine, S., Dittrich, T. R., and Haan, S. W. (2001). Three-dimensional HYDRA simulations of National Ignition Facility targets. *Phys. Plasmas* **8**, 2275–2280.

[Meier *et al.*, 1991] Meier, W. R., Monsler, M. J., Bourque, R. F., Stewart, L. D., Sviatoslavsky, I. N., Sawan, M. E., Peterson, R. R., Kulcinski, G. L., MacFarlane, J. J., Wittenberg, L. J., Mogahed, E. A., Rutledge, S. C., Goldman, L. M., Ghose, S. K., and C. W. von Rosenberg, J. (1991). Realistic modeling of chamber transport for heavy ion fusion. In *Proceedings of the 14th IEEE/NPSS Symposium on Fusion Engineering*, pages 631–635, http://ieeexplore.ieee.org/xpls/abs_all.jsp?arnumber=218842.

[Meyertervehn *et al.*, 1990] Meyertervehn, J., Witkowski, S., Bock, R., Hoffmann, D. H. H., Hofmann, I., Muller, R. W., Arnold, R., and Mulser, P. (1990). Accelerator and target studies for heavy ion fusion at the Gesellschaft-fur-Schwerionenforschung. *Phys. Fluids B* **2**, 1313–1317.

[Miller, 1994] Miller, R. B. (1994). *An Introduction to the Physics of Intense Charged Particle Beams*. Plenum Press, New York.

[Mitchell and Griffiths, 1980] Mitchell, A. and Griffiths, D. (1980). *The Finite Difference Method in Partial Differential Equations.* John Wiley & Sons, New York.

[Moir *et al.*, 1994] Moir, R. W., Bieri, R. L., Chen, X. M., Dolan, T. J., Hoffman, M. A., House, P. A., Leber, R. L., Lee, J. D., Lee, Y. T., Shrock, J. C., Tobin, M. T., and Williams, W. H. (1994). HYLIFE-II

- A molten-salt inertial fusion energy power-plant design - Final report. *Fusion Technol.* **25**, 5–25.

[NAS, 1990] NAS (1990). *National Academy of Sciences Review of the Department of Energy's Inertial Confinement Fusion Program, Final Report.* National Academy Press, Washington, DC.

[Nicholson, 1983] Nicholson, D. R. (1983). *Introduction to Plasma Theory.* John Wiley & Sons, New York.

[Nuckolls *et al.*, 1972] Nuckolls, J. H., Wood, L., Thiessen, A., and Zimmerman, G. B. (1972). Laser compression of matter to super-high densities: thermonuclear (CTR) applications. *Nature* **239**, 139–142.

[Olson, 1980] Olson, C. L. (1980). Final transport in gas and plasma. In *Proceedings of the 1979 Heavy Ion Fusion Workshop*, page 403. Lawrence Berkeley National Laboratory Report No. LBL-10301.

[Olson, 2001] Olson, C. L. (2001). Chamber transport. *Nucl. Instrum. and Methods A* **464**, 118–125.

[Orth *et al.*, 1996] Orth, C. D., Payne, S. A., and Krupke, W. F. (1996). A diode pumped solid state laser driver for inertial fusion energy. *Nucl. Fusion* **36**, 75–116.

[Press *et al.*, 1992] Press, W. H., Flannery, B. P., Teukolsky, S. A., and Vetterling, W. T. (1992). *Numerical Recipes in FORTRAN: The Art of Scientific Computing.* Cambridge University Press, Cambridge, England.

[Prestwich *et al.*, 1983] Prestwich, K. R., Hasti, D. E., Miller, R. B., and Sharpe, A. W. (1983). Multistage pulsed-power electron accelerators. In *Proceedings of the 1983 Particle Accelerator Conference*, pages 3155–3158, http://epaper.kek.jp/p83/PDF/PAC1983_3155.PDF.

[Qin and Davidson, 2002a] Qin, H. and Davidson, R. C. (2002a). Longitudinal drift compression and pulse shaping for high-intensity particle beams. *Phys. Rev. ST Accel. Beams* **5**, 034401.

[Qin and Davidson, 2002b] Qin, H. and Davidson, R. C. (2002b). Study of drift compression for heavy ion beams. *Laser Part. Beams* **20**, 565–568.

[Qin *et al.*, 2004] Qin, H., Davidson, R. C., Barnard, J. J., and Lee, E. P. (2004). Drift compression and final focus for intense heavy ion beams with nonperiodic, time-dependent lattice. *Phys. Rev. ST Accel. Beams* **7**, 104201.

[Qin *et al.*, 2005] Qin, H., Davidson, R. C., Barnard, J. J., and Lee, E. P. (2005). Drift compression and final focus options for heavy ion fusion. *Nucl. Instrum. and Methods A* **544**, 255–261.

[Quarteroni and Valli, 1994] Quarteroni, A. and Valli, A. (1994). *Numerical Approximation of Partial Differential Equations.* Springer-Verlag, Berlin.

[Rawnsley, 2000] Rawnsley, W. (2000). Beam Instrumentation Workshop. *AIP Conf. Proc.* **546**, 547.

[Rawnsley, 2005] Rawnsley, W. (2005). Private communication.

[Reif, 1965] Reif, F. (1965). *Fundamentals of Statistical and Thermal Physics.* McGraw-Hill, New York.

[Reiser, 1994] Reiser, M. (1994). *Theory and Design of Charged Particle Beams.* John Wiley & Sons, Inc., New York.

[Richtmeyer and Morton, 1994] Richtmeyer, R. and Morton, K. (1994). *Difference Methods for Initial Value Problems.* Krieger Publishing Company, Florida.

[Rose *et al.*, 2001] Rose, D. V., Welch, D. R., Oliver, B. V., Clark, R. E., Sharp, W. M., and Friedman, A. (2001). Ballistic-neutralized chamber transport of intense heavy ion beams. *Nucl. Instrum. and Methods A* **464**, 299–304.

[Rosenman *et al.*, 2000] Rosenman, G., Shur, D., Krasik, Y. E., and Dunaevsky, A. (2000). Electron emission from ferroelectrics. *J. Appl. Phys.* **88**, 6109–6161.

[Roy *et al.*, 2004] Roy, P. K., Yu, S. S., Eylon, S., Henestroza, E., Anders, A., Bieniosek, F. M., Greenway, W. G., Logan, B. G., Waldron, W. L., Vanecek, D. L., Welch, D. R., Rose, D. V., Davidson, R. C., Efthimion, P. C., Gilson, E. P., Sefkow, A. B., and Sharp, W. M. (2004). Results on intense beam focusing and neutralization from the neutralized beam experiment. *Phys. Plasmas* **11**, 2890–2898.

[Roy *et al.*, 2005a] Roy, P. K., Yu, S. S., Eylon, S., Henestroza, E., Anders, A., Gilson, E. P., Bieniosek, F. M., Greenway, W. G., Logan, B. G., Waldron, W. L., Shuman, D. B., Vanecek, D. L., Welch, D. R., Rose, D. V., Davidson, R. C., Efthimion, P. C., Kaganovich, I. D., Sefkow, A. B., and Sharp, W. M. (2005a). Neutralized transport experiment. *Nucl. Instrum. and Methods A* **544**, 225–235.

[Roy *et al.*, 2005b] Roy, P. K., Yu, S. S., Henestroza, E., Anders, A., Bieniosek, F. M., Coleman, J., Eylon, S., Greenway, W. G., Leitner, M., Logan, B. G., Waldron, W. L., Welch, D. R., Thoma, C., Sefkow, A. B., Gilson, E. P., Efthimion, P. C., and Davidson, R. C. (2005b). Drift compression of an intense neutralized ion beam. *Phys. Rev. Lett.* **95**, 234801.

[Roy *et al.*, 2007] Roy, P. K., Yu, S. S., Henestroza, E., Bieniosek, F. M., Coleman, J., Eylon, S., Greenway, W. G., Anders, A., Leitner, M., Waldron, W. L., Seidl, P. A., Logan, B. G., Welch, D. R., Thoma, C., Sefkow, A. B., Gilson, E. P., Efthimion, P. C., Kaganovich, I. D., and Davidson, R. C. (2007). Neutralized drift compression experiments for high intensity ion beams. *Nucl. Instrum. and Methods A* **577**, 223–230.

[Schiesser, 1991] Schiesser, W. (1991). *The Numerical Method of Lines.* Academic Press, San Diego.

[Sefkow and Davidson, 2006] Sefkow, A. B. and Davidson, R. C. (2006). Theoretical models for describing longitudinal bunch compression in the Neutralized Drift Compression Experiment. *Phys. Rev. ST Accel. Beams* **9**, 090101.

[Sefkow *et al.*, 2006] Sefkow, A. B., Davidson, R. C., Efthimion, P. C., Gilson, E. P., Yu, S. S., Roy, P. K., Bieniosek, F. M., Coleman, J. E., Eylon, S., Greenway, W. G., Henestroza, E., Kwan, J. W., Vanecek, D. L., Waldron, W. L., and Welch, D. R. (2006). Fast Faraday cup to measure neutralized drift compression in intense ion charge bunches. *Phys. Rev. ST Accel. Beams* **9**, 052801.

[Sefkow *et al.*, 2005a] Sefkow, A. B., Davidson, R. C., Efthimion, P. C., Gilson, E. P., Yu, S. S., Roy, P. K., Eylon, S., Bieniosek, F. M., Henestroza, E., Coleman, J. E., Waldron, W. L., Greenway, W. G., Vanecek, D. L., and Welch, D. R. (2005a). A fast Faraday cup for measuring neutralized drift compression. *Bull. Amer. Phys. Soc.* **50**, 49, http://meetings.aps.org/Meeting/DPP05/Event/34629.

[Sefkow *et al.*, 2005b] Sefkow, A. B., Davidson, R. C., Efthimion, P. C., Gilson, E. P., Yu, S. S., Roy, P. K., Eylon, S., Bieniosek, F. M., Henestroza, E., Kwan, J. W., Coleman, J. E., Waldron, W. L., Greenway, W. G., Vanecek, D. L., and Welch, D. R. (2005b). A fast Faraday cup for the Neutralized Drift Compression Experiment. In *Proceedings of the 2005 Particle Accelerator Conference*, page 3765, http://ieeexplore.ieee.org/xpls/abs_all.jsp?arnumber=1591610.

[Sefkow *et al.*, 2007] Sefkow, A. B., Davidson, R. C., Kaganovich, I. D., Gilson, E. P., Roy, P. K., Seidl, P. A., Yu, S. S., Welch, D. R., Rose, D. V., and Barnard, J. J. (2007). Optimized simultaneous transverse and longitudinal focusing of intense ion beam pulses for warm dense matter applications. *Nucl. Instrum. and Methods A* **577**, 289–297.

[Seidl *et al.*, 2007] Seidl, P. A., Armijo, J., Baca, D., Bieniosek, F. M., Coleman, J. E., Henestroza, E., Leitner, M., Logan, B. G., Roy, P. K., Waldron, W. L., Yu, S. S., Friedman, A., Kireeff-Covo, M., Grote, D., Molvik, A. W., Sharp, W. M., Vay, J. L., Haber, I., Sefkow, A. B., Gilson, E. P., Efthimion, P. C., Kaganovich, I. D., Davidson, R. C.,

Rose, D. V., and Welch, D. R. (2007). Plans for neutralized drift compression experiments and initial results from solenoid transport. *Nucl. Instrum. and Methods A* **577**, 215–222.

[Sethian *et al.*, 2004] Sethian, J. D., Myers, M. C., J. L. Giuliani, J., Lehmberg, J. R., Kepple, P. C., Obenschain, S. P., Hegeler, F., Friedman, M., Wolford, M. F., Smilgys, R. V., Swanekamp, S. B., Weidenheimer, D., Giorgi, D., Welch, D. R., Rose, D. V., and Searles, S. (2004). Electron beam pumped krypton fluoride lasers for fusion energy. In *Proceedings of the IEEE, Volume 92, Issue 7*, pages 1043–1056, http://ieeexplore.ieee.org/xpls/abs_all.jsp?arnumber=1306677.

[Shampine, 1994] Shampine, L. F. (1994). *Numerical Solution of Oridinary Differential Equations.* Chapman and Hall, New York.

[Shampine and Gordon, 1975] Shampine, L. F. and Gordon, M. (1975). *Computer Solutions of Ordinary Differential Equations.* W. H. Freeman, San Francisco.

[Sharkov *et al.*, 2005] Sharkov, B. Y., Alexeev, N. N., Basko, M. M., Churazov, M. D., Koshkarev, D. G., Medin, S. A., Orlov, Y. N., and Suslin, V. M. (2005). Power plant design and accelerator technology for heavy ion inertial fusion energy. *Nucl. Fusion* **45**, S291–S297.

[Sharp *et al.*, 2005] Sharp, W. M., Barnard, J. J., Grote, D. P., Celata, C. M., and Yu, S. S. (2005). Simulation of drift compression for heavy-ion fusion. *Nucl. Instrum. and Methods A* **544**, 398–405.

[Sharp *et al.*, 2003] Sharp, W. M., Grote, D. P., Callahan, D. A., Tabak, M., Henestroza, E., Yu, S. S., Peterson, P. F., Welch, D. R., and Rose, D. V. (2003). Realistic modeling of chamber transport for heavy ion fusion. In *Proceedings of the 2003 Particle Accelerator Conference*, pages 2637–2639, http://ieeexplore.ieee.org/xpls/abs_all.jsp?arnumber=1289214.

[Shope *et al.*, 1987] Shope, S. L., Mazarakis, M. G., Miller, R. B., and Poukey, J. W. (1987). The design of the accelerating gaps for the linear induction accelerator RADLAC II. In *Proceedings of the 1987 Particle Accelerator Conference*, pages 978–980, http://epaper.kek.jp/p87/PDF/PAC1987_0978.PDF.

[Stix, 1992] Stix, T. H. (1992). *Waves in Plasmas.* Springer-Verlag, New York.

[Tabak and Callahan-Miller, 1998] Tabak, M. and Callahan-Miller, D. A. (1998). Design of a distributed radiator target for inertial fusion driven from two sides with heavy ion beams. *Nucl. Instrum. and Methods A* **415**, 75–84.

[Tabak *et al.*, 1994] Tabak, M., Hammer, J., Glinsky, M. E., Kruer, W. L., Wilks, S. C., Woodworth, J., Campbell, E. M., Perry, M. D., and Mason, R. J. (1994). Ignition and high-gain with ultrapowerful lasers. *Phys. Plasmas* **1**, 1626–1634.

[Thoma, 2002] Thoma, C. H. (2002). Test of LSP off-axis magnetic field expansion in cylindrical coordinates. *Mission Research Corporation* **MRC/ABQ-R-2070**, 1–16.

[Thoma *et al.*, 2005] Thoma, C. H., Welch, D. R., Yu, S. S., Henestroza, E., Roy, P. K., Eylon, S., and Gilson, E. P. (2005). Comparison of experimental data and three-dimensional simulations of ion beam neutralization from the Neutralized Transport Experiment. *Phys. Plasmas* **12**, 043102.

[VFO-3D, 2005] VFO-3D (2005). Vector Fields Opera-3D is a software product of Vector Fields Inc., Aurora, IL 60505. *http://www.vectorfields.com* .

[Vlasov, 1945] Vlasov, A. A. (1945). On the kinetic theory of an assembly of particles with collective interaction. *J. Phys. (USSR)* **9**, 25.

[Welch *et al.*, 2004] Welch, D. R., Rose, D. V., Clark, R. E., Genomi, T. C., and Hughes, T. P. (2004). Implementation of an non-iterative implicit electromagnetic field solver for dense plasma simulation. *Comput. Phys. Commun.* **164**, 183–188.

[Welch *et al.*, 2005] Welch, D. R., Rose, D. V., Genoni, T. C., Yu, S. S., and Barnard, J. J. (2005). Simulations of neutralized final focus. *Nucl. Instrum. and Methods A* **544**, 236–242.

[Welch *et al.*, 2001] Welch, D. R., Rose, D. V., Oliver, B. V., and Clark, R. E. (2001). Simulation techniques for heavy ion fusion chamber transport. *Nucl. Instrum. and Methods A* **464**, 134–139.

[Welch *et al.*, 2003a] Welch, D. R., Rose, D. V., Sharp, W. M., and Olson, C. L. (2003a). Effects of preneutralization on heavy ion fusion chamber transport. *Laser Part. Beams* **20**, 621–625.

[Welch *et al.*, 2007] Welch, D. R., Rose, D. V., Thoma, C. H., Sefkow, A. B., Kaganovich, I. D., Seidl, P. A., Yu, S. S., and Roy, P. K. (2007). Integrated simulation of an ion-driven warm dense matter experiment. *Nucl. Instrum. and Methods A* **577**, 231–237.

[Welch *et al.*, 2003b] Welch, D. R., Rose, D. V., Yu, S. S., and Olson, C. L. (2003b). Multiple beam interaction studies in heavy ion fusion. In *Proceedings of the 2003 Particle Accelerator Conference*, pages 2685–2687, http://ieeexplore.ieee.org/xpls/abs_all.jsp?arnumber=1289230.

[Wieckert, 1987] Wieckert, C. (1987). A multicomponent theory of the cathodic plasma-jet in vacuum arcs. *Contrib. Plasma Phys.* **27**, 309–330.

[Yu *et al.*, 1979] Yu, S. S., Buchanan, H. L., Lee, E. P., and Chambers, F. W. (1979). Beam propagation through a gaseous reactor: classical transport. In *Proceedings of the 1979 Heavy Ion Fusion Workshop*, page 403, http://www.osti.gov/energycitations/product.biblio.jsp?osti_id=6503091.

[Yu *et al.*, 2003] Yu, S. S., Meier, W. R., Abbott, R. P., Barnard, J. J., Brown, T., Callahan, D. A., Debonnel, C., Heitzenroeder, P., Latkowski, J. F., Logan, B. G., Pemberton, S. J., Peterson, P. F., Rose, D. V., Sabbi, G.-L., Sharp, W. M., and Welch, D. R. (2003). An updated point design for heavy ion fusion. *Fusion Sci. Technol.* **44**, 266–273.

[Yushkov *et al.*, 2000] Yushkov, G. Y., Anders, A., Brown, E. M., and Brown, I. G. (2000). Ion velocities in vacuum arc plasmas. *J. Appl. Phys.* **88**, 5618–5622.